The electronic and geometric structure of [NiFe] hydrogenases studied by theoretical spectroscopy

Dissertation

zur

Erlangung des Doktorgrades (Dr. rer. nat)

der

Mathematisch–Naturwissenschaftlichen Fakultät

der

Rheinischen Friedrich–Wilhelms–Universität Bonn

vorgelegt von

Mario Kampa

aus

Köln

Bonn 2012

Angefertigt mit Genehmigung der mathematisch-naturwissenschaftlichen Fakultät der Rheinischen Friedrich-Wilhelms-Universität Bonn

1. Gutachter: Prof. Dr. Frank Neese

2. Gutachter: Prof. Dr. Thomas Bredow

Tag der Promotion: 20.03.2013

Erscheinungsjahr: 2013

Abstract

In the present PhD thesis, the electronic, geometric and mechanistic features of the active site in [NiFe] hydrogenase were investigated.

[NiFe] hydrogenase catalyzes the reversible oxidative cleavage of molecular hydrogen, H_2, into two electrons and two protons. Due to their ability to produce or cleave H_2 at highly efficient rates, hydrogenases are envisaged to contribute to a putative future hydrogen–based economy by direct use in bioreactors or as inspiration for the development of efficient catalysts.

Several redox–states, which are associated with catalytic steps but also with inhibited structures of the enzyme, were characterized experimentally. The bimetallic [NiFe] core of the enzyme is coordinated by two terminal cysteines, which bind only to the nickel atom, and two bridging cysteines, which form bonds to both metals. A third bridging position is occupied by the variable ligand, of which the nature may change as the enzyme passes through its various redox–states. The coordination shell of the iron atom is unique in nature as it features two CN^- ligands and one CO ligand. The coordination geometries of nickel and iron are distorted square pyramidal and distorted octahedral, respectively.

In the present study, Density Functional Theory (DFT) was employed to investigate the redox–states of [NiFe] hydrogenase. In the recent decades, DFT has become increasingly important in theoretical chemistry, in particular when larger molecular systems, such as active site cluster models of transition metal enzymes, are under investigation, which requires a reasonable compromise between accuracy and computational efficiency. Although in general DFT provides reasonable results, in the case of some molecular systems, DFT calculations are of only mediocre or poor quality. Hence, it is indispensible to assess the accuracy and applicability of DFT to the system under investigation by comparison of the computed results to experimental data. Accordingly, the central approach of the present work is to calculate geometric and spectroscopic properties, such as g–tensors, hyperfine coupling constant and IR–frequencies, and compared them to the available experimental parameters in order to gain reliable insights into the structural and electronic features of the enzyme´s redox–states. Transition metal systems with up to, say, 200 atoms can be fully treated with DFT at suitable accuracy and computational efficiency. In general, transition metal enzymes feature several ten–thousands of atoms. Fortunately, in general it is sufficient to restrict the quantum–mechanical treatment to the active site by means of cluster models to cover the most important properties of the enzyme. Most of the previous DFT studies on [NiFe] hydrogenase employed cluster models which

included the first coordination shell in addition to the bimetallic core, i.e. the four cysteines, the three two–atomic ligands and the variable bridging ligand. We additionally included amino acids of the second coordination sphere, of which the detailed study of the influence on the electronic and geometric structure of the active center was one of the major motivations of the present work.

First, the reliability of DFT for the computation of synthetic Ni^{3+} complexes was evaluated. It turns out that the quality of the computations pronouncedly depends on the complex under investigation. Then, the applicability of the large cluster model was evaluated by studying the experimentally well–characterized Ni–C state of [NiFe] hydrogenase. The agreement of computed and experimental data is good to excellent and clearly encouraged the use of the cluster model for investigations of the less well–known redox–states. Some important features of [NiFe] hydrogenase have been elucidated: The amino acids of the second coordination shell have a profound influence on many properties of the enzyme. Moreover, a stabilizing nickel–iron bond was identified in redox–states which exhibit a vacant bridging position. Furthermore, a reaction mechanism for homolytic hydrogen cleavage at the nickel center, as opposed to the previously suggested heterolytic mechanism at the iron core, is presented. In addition, some of the intriguing features of the active site, as the unique coordination shell of the metals or the role of the iron center, have been shed light on.

Zusammenfassung

In der vorliegenden Dissertation wurden die elektronische und geometrische Struktur sowie die katalytischen Eigenschaften des aktiven Zentrums im Enzym [NiFe] Hydrogenase untersucht. [NiFe] Hydrogenasen katalysieren die reversible oxidative Spaltung von molekularem Wasserstoff, H_2, in zwei Elektronen und zwei Protonen. Hydrogenasen könnten dementsprechend, entweder immobilisiert in Bioreaktoren oder als Inspiration für die Entwicklung neuartiger Katalysatoren, einen vielversprechenden Beitrag zu eine möglichen zukünftigen Wasserstoffwirtschaft leisten.

Verschiedene Redoxzustände des Enzyms wurden experimentell charakterisiert, von denen manche den Reaktionsschritten des Katalyse Mechanismus andere wiederum inhibierten Enzymstrukturen entsprechen. Das [NiFe] Zentrum des Enzyms wird von vier Cystein Resten koordiniert. Zwei terminale Cysteine binden ausschließlich an das Nickelatom, während zwei verbrückende Cystein Reste sowohl an das Nickel als auch an das Eisenatom binden. Eine dritte verbrückende Koordinationsstelle wird durch einen verbrückenden Liganden besetzt, der je nach Redoxzustand unterschiedlich Gestalt annehmen kann. Die Ligandenhülle des Eisenzentrums bestehend aus einem CN^- und einem CO Molekül ist einzigartig. Die Koordinationsgeometrie ist verzerrt quadratisch–pyramidal am Nickelzentrum und verzerrt oktaedrisch am Eisenzentrum.

In der vorliegenden Dissertation wurden die Redoxzustände der [NiFe] Hydrogenase mittels Dichte Funktional Theorie (DFT) untersucht. In den letzten Jahrzehnten, hat sich DFT zu einer der wichtigsten Methoden in der Theoretischen Chemie entwickelt. Letztgenanntes gilt besonders für die Berechnung von größeren molekularen Systemen, wie z.B. von Modellen des aktiven Zentrums in Übergangsmetall Enzymen, welche eine theoretische Methode erforderlich machen, die sowohl ausreichend genau ist als auch eine genügende Effizient aufweist. Obwohl mit DFT im Allgemeinen vernünftige Resultate erreicht werden können, gibt es einige molekulare Systeme, bei denen mit DFT nur Ergebnisse von mittelmäßiger bis unzureichender Genauigkeit erzielt werden. Demnach ist es von besonderer Bedeutung die Genauigkeit und Anwendbarkeit von DFT bei dem untersuchten System durch Vergleich mit experimentell zugänglichen Daten zu überprüfen. Damit in Übereinstimmung, ist der zentrale Ansatz der vorliegenden Arbeit, geometrische und spektroskopische Eigenschaften, wie g–Tensoren, Hyperfine Kopplungskonstanten und IR–Frequenzen zu berechnen und mit den vorhandenen experimentellen Werten zu vergleichen, um dann die elektronische und die geometrische Struktur der Redoxzustände der [NiFe] Hydrogenase im Detail zu verstehen. Übergangsmetallsysteme mit bis zu etwa 200 Atomen können noch zuverlässig und effizient mit DFT berechnet werden. Normalerweise sind Enzyme jedoch aus Zehntausenden von

Atomen aufgebaut. Glücklicherweise ist es normalerweise ausreichend, die quantenmechanische Behandlung auf molekulare Modelle des aktiven Zentrums zu beschränken, um die wichtigsten Eigenschaften des Enzyms zu untersuchen. In den meisten der an der [NiFe] Hydrogenase bereits durchgeführten DFT Studien wurde ein molekulares Modell verwendet welches nur die erste Ligandenhülle der zwei Metalle, d.h. die vier Cysteine, die drei zweiatomigen Eisenliganden und den variablen Brückenliganden beinhaltete. Wir haben zusätzlich die Aminosäuren der zweiten Koordinationssphäre in das Modell aufgenommen. Die detaillierte Untersuchung des Einflusses der zweiten Koordinationssphäre auf die elektronische und geometrische Struktur des aktiven Zentrums war eine der wichtigsten Motivationen der vorliegenden Arbeit.

Zunächst wurde die Zuverlässigkeit von DFT–Rechnungen an synthetischen Ni^{3+} Komplexen untersucht. Es stelle sich heraus dass die Genauigkeit der Rechnungen sehr stark von dem betrachteten Komplex abhängig ist. Im nächsten Schritt wurde die Anwendbarkeit des Modellsystems des aktiven Zentrums für die Berechnung der Redoxzustände der Hydrogenase überprüft. Es wurde der experimentell besonders gut charakterisierte Ni–C Zustand untersucht. Die gut bis sehr gute Übereinstimmung der berechneten mit den experimentellen Daten bestätigt die Anwendbarkeit des Modellsystems für die Untersuchung der weniger gut bekannten Redoxzustände des Enzyms. Einige wichtige Eigenschaften der [NFe] Hydrogenase wurden im Zuge dieser Studie aufgeklärt: Es wurde gezeigt dass sich die Aminosäuren der zweiten Ligandenhüllen des [NiFe] Kerns beträchtlich auf die Eigenschaften des Enzyms auswirken. Weiterhin wurde gezeigt, dass in Zuständen, in denen die verbrückenden Bindungsstelle unbesetzt ist, eine stabilisierende Nickel–Eisen Metallbindung vorhanden ist. Es wurde ein Reaktionsmechanismus vorgeschlagen, in dem der molekulare Wasserstoff homolytisch am Nickelzentrum und nicht, wie bis jetzt postuliert, heterolytisch am Eisenzentrum gespalten wird. Weiterhin wurde die Funktion einer Reihe von einzigartigen strukturellen Eigenschaften des aktiven Zentrums, wie z.B. die außergewöhnliche Ligandenhülle der Metalle oder die Rolle des Eisenzentrums, aufgeklärt.

Acknowledgements

I am deeply grateful to everybody who made the present work possible. I want to thank Prof. Dr. Frank Neese and Prof. Dr. Wolfgang Lubitz for supervision of the project and fundraising. I am most thankful for having been given the opportunity to work in the field of theoretical bioinorganic chemistry and in particular in theoretical spectroscopy as it is a challenging, modern and particularly interesting research area. There are probably not many research groups where it is possible to work on such a wide range of challenging topics. The project was only possible with the financial aid from the Max-Planck-Society, the University of Bonn and the DFG SPP 1319.

I am most grateful for having worked with an outstanding group of highly gifted researchers who helped me in various occasions to get a better understanding of the many questions which have arisen during the project. My special thanks go to PD Dr. Maurice van Gastel whose professional advice helped me to get forward in the publication process of the present work and who has always been both, motivating and inspiring. Thanks to Gemma, Caiyun and Shengfa for sharing the office with me during our time in Bonn and for having such a nice time there. I particularly thank Shengfa for the many helpful explanations and discussions, in particular with respect to theoretical magnetic spectroscopy. I also want to thank Igor, Mihail and Dimitrios for sharing the office with me at the Max-Planck-Institute and for the nice atmosphere. My special thanks go Prof. Dr. Mihail Atanasov for the many fruitful discussions about ligand field theory.

Finally, I want to give my thanks to my dear family and all my friends who never stopped supporting and encouraging me over the years.

STATEMENT OF AUTHORSHIP

The present PhD thesis is entirely the result of my own work. Material from the published or unpublished work of others, in particular in the introductory chapters and sections, is credited to the respective author in the text.

Chapter 4.2: The Ni-C state was previously published in J Biol Inorg Chem. Writing of the Chapter 4.2: The Ni-C state and of the respective publication (J Biol Inorg Chem.) was aided and supervised by Dr. Maurice van Gastel. Maurice van Gastel also proofread Chapter 4.3: The Ni-L state. All calculations were performed by the author of the present thesis.

Content

1. Introduction to [NiFe] hydrogenases

Abstract

In nature, hydrogen biosynthesis and splitting are efficiently catalyzed by enzymes termed hydrogenases. According to the metal content of their active sites, hydrogenases are subdivided into three major classes: [NiFe] hydrogenase, [FeFe] hydrogenase and [Fe]–hydrogenase. In [NiFe] hydrogenases the nickel atom is coordinated by two terminal and two bridging cysteine residues. Most notably, the iron atom features an intriguing coordination shell, which is composed of two cyanide and one carbon monoxide ligand. The ligands which bind to the two remaining coordination sites depend on the redox–states of the enzyme. Various redox–states, some of which are paramagnetic and therefore susceptible to EPR–spectroscopic investigations, have been isolated and characterized. Besides the states which are part of the catalytic cycle of the enzyme, [NiFe] hydrogenases can adopt further redox–states due to its light sensitivity, by CO–binding or by inhibition through oxidation of the nickel center. The various redox–states of the enzyme have been studied in detail by spectroscopic, electrochemical and biochemical as well as computational methods.

1.1. Introduction

H_2 plays a pivotal role in the biosphere by being part of the energy metabolism in a wide range of microorganisms. Reversible biosynthesis of molecular hydrogen is performed by enzymes termed hydrogenases. Although the reaction is disarmingly simple at first sight, the enzymes contain highly complex active sites. In times of dwindling non–renewable energy resources, hydrogen is considered as a promising alternative energy source [1-16]. In this respect, two approaches have been envisaged. Firstly, the enzyme could be immobilized in bioreactors in order to perform large scale hydrogen production from biomass and other organic compounds. In this respect, In a visionary scenario, hydrogenases could produce molecular hydrogen from water by using the energy of sunlight photosynthetically [17]. Unfortunately, direct application of hydrogenases in the production of H_2 is severely undermined by oxidative inhibition [18-19] and inherent enzymatic instabilities to heat and mechanical stress. However, immobilization of hydrogenases on a solid carbon support has proven to improve the stability of the enzyme. A second, possibly more promising, strategy for the use of hydrogenases in large–scale hydrogen production is more indirect. Insights into the structural and electronic factors which govern biosynthesis by H_2 can lead to the design of highly efficient biomimetic H_2 catalysts [20-30]. However, it is probably fair to say that the capability of currently available synthetic compounds to produce H_2 is rather limited [31]. Thus, there is still much research effort to be made by scientists of all sorts of disciplines to make the vision of efficient biomimetic H_2 catalysts to become reality.

1.2. The three classes of hydrogenases

[NiFe] hydrogenases, [FeFe] hydrogenases and [Fe] hydrogenases are the three major classes of the enzymes [32]. The respective designations derive from the metal content of their active sites. [NiFe] hydrogenases contain a bimetallic core of nickel and iron [33-34] in their active sites. The metals are coordinated by the sulfur atoms of four cysteines residues, two cyanide (CN^-) and one carbon–monoxide (CO) molecule. These “standard” hydrogenases can be found for example in sulfate–reducing bacteria from the *Desulfovibrio* genus and are readily inhibited by exposure to an oxidizing agent [18-19]. The subclass of [NiFeSe] hydrogenases [35-39] from the bacterium *Desulfovibrio baculatum* derives structurally from standard [NiFe] hydrogenases by substitution of the terminal Cys546 (*Desulfovibrio vulgaris* Miyazaki F. numbering) by a seleno–cysteine. Although the X–Ray structure of the enzyme shows no major differences to “standard” [NiFe] hydrogenases, [NiFeSe] hydrogenases are less sensitive to oxygen [40-41].

[NiFe] hydrogenases from some bacteria, such as the aerobic bacterium *Ralstonia eutropha*, are oxygen–tolerant. A membrane–bound hydrogenase, a soluble hydrogenase, and a regulatory

hydrogenase have been identified [42-52] in *R. eutropha*. Despite the relatively large number of studies on the [NiFe] hyrogenases, so far it has not been possible to clearly identify the structural or electronic features that govern the oxygen sensitivity in most standard [NiFe] hydrogenases nor has it been possible to explain why the hydrogenases from *R. eutropha* are oxygen–tolerant.

[FeFe] hydrogenases constitute another main class of hydrogenases. Crystal structures of the enzyme are available from *Clostridium pasteurianum* and *Desulfovibrio desulfuricans* [53-54]. The enzymes harbor a metal core with two iron atoms in their active site (Figure 1). Electron transport is mediated by several iron–sulfur clusters [55-56]. Most notably, a [4Fe–4S] iron sulfur cluster is attached via a cysteine sulfur atom to the dinuclear [FeFe] core of the active site. Two cyanide and two carbon–monoxide ligands coordinate to the bimetallic core at the two terminal positions. In addition, the sulfur atoms of a dithiolene ligand bind at the bridging positions between the two metals. The nature of the dithiolene ligand could not be determined unambiguously from the X–Ray structures and a propane–dithiol as well as a di–thiomethyl–amine ligand have been proposed [54, 57].

Despite the structural similarities of [FeFe] and [NiFe] hydrogenases, of which the most notable is certainly the presence of the unusual CN^- and CO ligands, the two enzyme classes are not related phylogenetically [58], which indicates that the CN^- and CO ligands are probably crucial for biosynthetic H_2 formation.

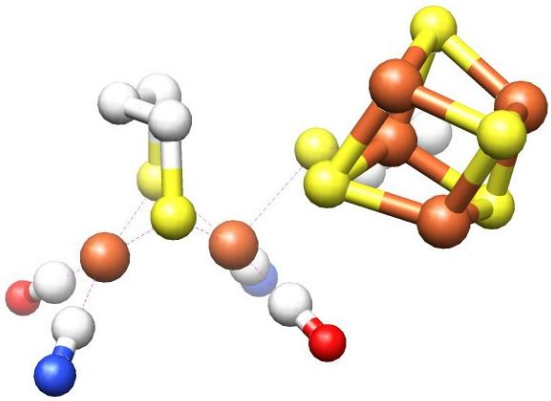

Figure 1: Active site of the [FeFe] hydrogenase from *Clostridium pasteurianum.*

[Fe] hydrogenases form the third major class of hydrogenases [59-60]. The enzyme is isolated from methanogenic bacteria and contains a N5, N10–methylene–tetrahydromethanopterin cofactor in its active site, which mediates the redox–reaction of the enzyme. According to the very different structure of their active site, [Fe] hydrogenases feature a completely different mechanism. Since this

work deals with [NiFe] hydrogenases, a detailed description of [Fe] hydrogenases, which feature a completely different structure, is not give.

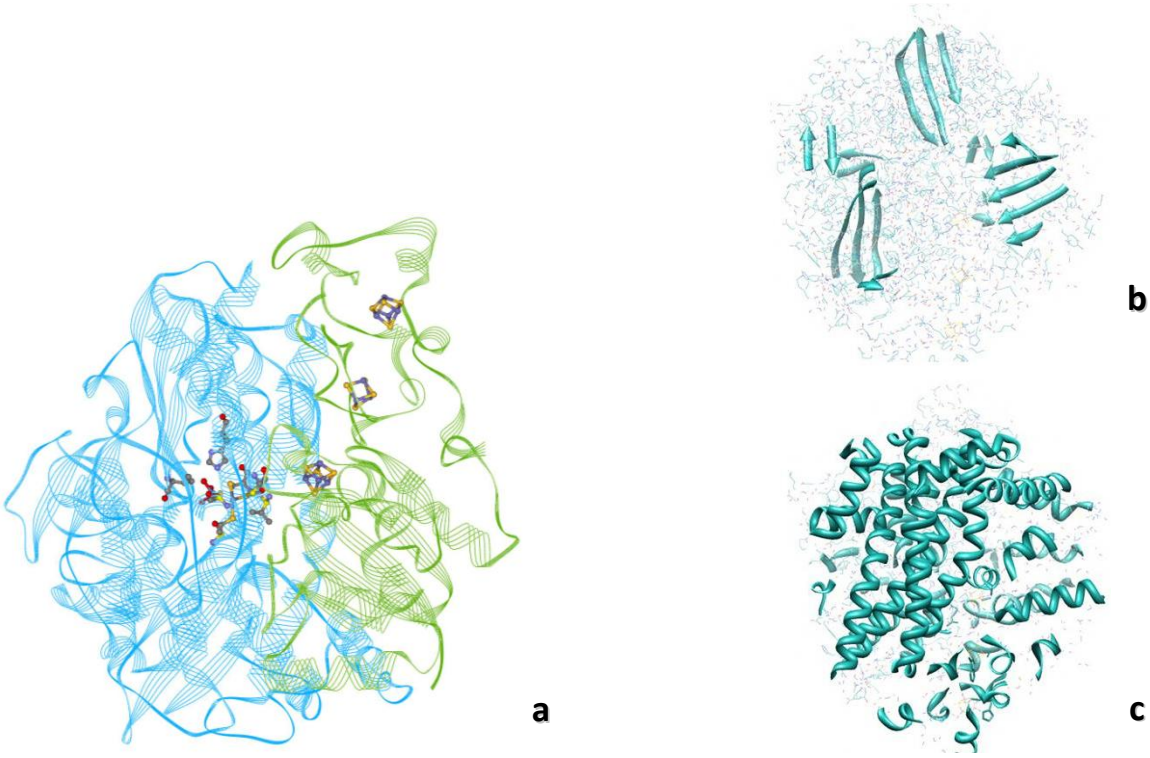

Figure 2: Structures of [NiFe] hydrogenase from *D. vulgaris* Miyazaki F. [61]: (a) the large (blue) and small subunit (green) with the active site and the iron sulfur clusters highlighted as stick models. Secondary structure elements in the enzyme: (b) β–sheets and (c) alpha helices.

1.3. Protein structure

Single crystals of [NiFe] hydrogenase were first obtained by E.C. Hatchikian in 1987 [62]. However, it took seven years more until the first crystal structure of the enzyme was published by Volbeda and co–workers in 1995 [33]. However, for an unambiguous elucidation of the structure of the enzyme´s active center, it took further input from chemical analysis of the metal content of the enzyme and FTIR spectroscopy [63-64]. The amino acid sequence of [NiFe] hydrogenase is highly conserved among different microorganisms [58]. The structure of the enzyme is composed of a large and a small subunit with the former harboring the active site and the latter containing the three iron–sulfur clusters (Figure 2a). In the case of *Desulfovibrio gigas* hydrogenase, the molecular weight of the small and the large subunit is about 28kDa and 60kDa, respectively. Secondary structure elements, namely β–sheets and α–helices, are highlighted for both subunits in Figure 2b and Figure 2c, respectively.

In Figure 3, the structure of the active site from *Desulfovibrio vulgaris* Miyazaki F. is displayed for the well characterized Ni–C state (see also chapter 4.2). The nickel center is coordinated by the sulfur atoms of the two terminal cysteine residues Cys546 and Cys81 and the two bridging cysteines Cys549

and Cys84 which bind to both, nickel and iron. The cysteines are crucial for the stability of the active site and any attempt to substitute them with serine residues resulted in an inactive enzyme [65-66]. A third binding site between the two metals is available and occupied by a variable bridging ligand. The type of ligand, which binds to the bridging position, depends on the catalytic state of the enzyme. In the case of the Ni–C state, the bridging ligand is a hydride. The coordination geometry of the nickel center in the Ni–C state is square–pyramidal. The sulfur atom of Cys549 is found in the apical position while the sulfur atoms of Cys81, Cys84, Cys546 and the bridging ligand bind to the equatorial positions. While the terminal nickel binding site opposite to Cys549 is unoccupied in the Ni–C state there is strong experimental evidence which indicates that this is the position where H_2–coordination takes place [67] during the catalytic cycle (the catalytic cycle is discussed in chapter 4.6).

In addition to the two bridging cysteine residues and the variable bridging ligand, two cyanide ligands and one carbon monoxide molecule coordinate to the iron center, which is a highly unusual coordination shell for a transition metal enzyme. The coordination geometry of the iron in the Ni–C state is a distorted octahedron.

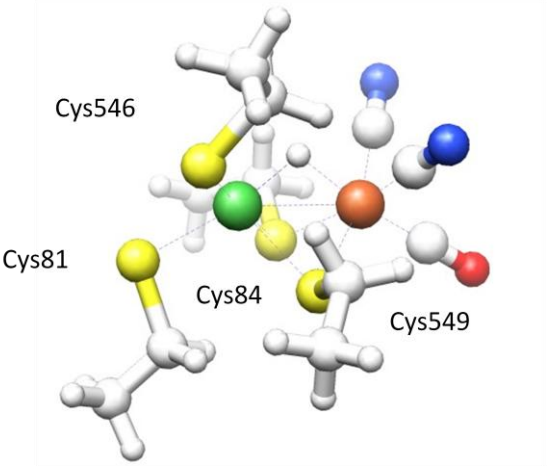

Figure 3: Structure of the active site of *Desulfovibrio vulgaris* [NiFe] hydrogenase in the Ni–C state. Color code for the atoms: nickel (green), iron (brown), sulfur (yellow), nitrogen (green), oxygen (red), hydrogen and carbon (white).

Three iron sulfur clusters are located in the small subunit of the [NiFe] hydrogenase. They are essential to the enzyme's activity as they mediate electron transport. One [4Fe–4S] cluster is located near the active site and another [4Fe–4S] cluster is found in close proximity to the protein surface. Between these clusters, a [3Fe–4S] cluster is located such that the distances between the clusters amount to only about 12 Å, which is suitable for electron transport [68]. In the [NiFeSe] hydrogenase form *D. baculatum* the [3Fe–4S] cluster is replaced by a [4Fe–4S] cluster [36].

Identification of the channel for H_2 and the amino acid cascade by which proton transport is mediated is more challenging. In an intriguing experiment, a hydrophobic gas channel, which ends at the terminal binding site of the nickel center, was mapped out with Xe atoms by crystallization of [NiFe] hydrogenase under high pressure xenon atmosphere [67]. Initial binding of molecular hydrogen to the terminal nickel site was furthermore corroborated by molecular dynamics simulations [67]. In addition, in the X–ray structure of the CO–inhibited enzyme (section, the CO ligand binds to the terminal nickel site of the active center [69] which supports the assignment of the terminal nickel site as position for initial substrate binding.

In addition to the hydrophobic gas channel and the electron transport chain, a pathway for proton transport is required for H_2 biosynthesis. Mainly, two pathways have been suggested for proton transfer. In both, the cysteine residues of the first coordination shell act as initial proton acceptors in oxidative hydrogen cleavage. Firstly, proton transport has been proposed to be initially mediated by the bridging Cys549. In a site–directed mutagenesis study with *R. eutropha* soluble hydrogenase, two nearby histidine and one glutamate residues were mutated [65]. The mutant actually exhibited reduced activity but spectroscopic studies have not been performed. Secondly, Cys546 has been shown to be likely involved in proton transport by experimental [33, 70-71] and theoretical studies [72]. A magnesium ion which was identified in the crystal structure of the enzyme might play a role in proton transfer [73].

1.4. The redox–states

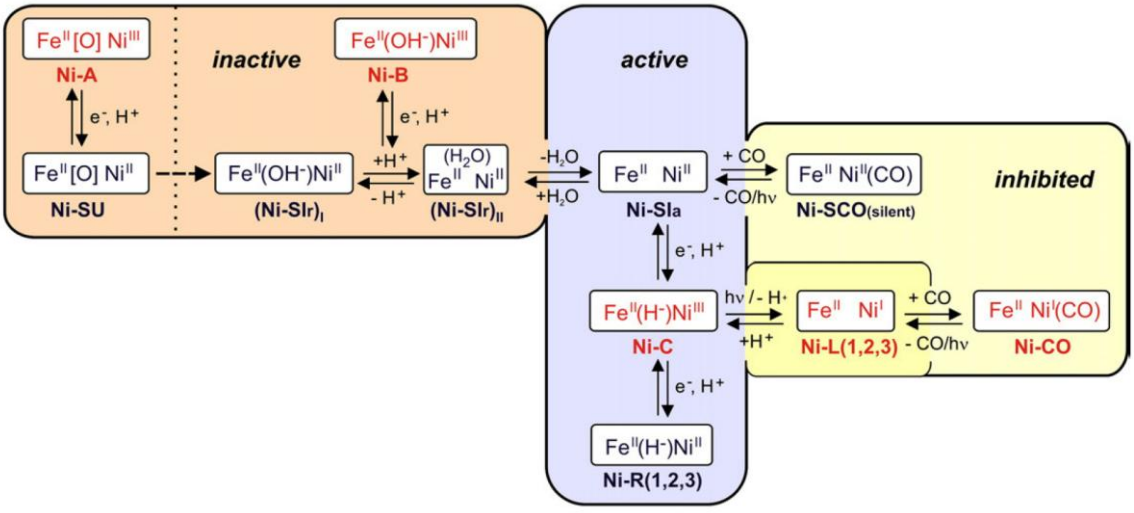

Figure 4: The various redox–states of [NiFe] hydrogenase (from [74]).

[NiFe] hydrogenases have been found to adopt various redox–states (for review see [74-77]). Here, we just present a brief overview (Figure 4). A more detailed introduction to the respective redox–states will be given at the beginning of each chapter.

The redox–states of oxygen–sensitive [NiFe] hydrogenase were initially studied by EPR spectroscopy. After aerobic isolation, two different sets of *g*–values were identified in *D. gigas* [NiFe] hydrogenase. An EPR signal with g–values of 2.31, 2.23 and 2.01 was designated Ni–A, while the signal with g–values of 2.33, 2.16 and 2.01 was designated Ni–B. Upon slow reduction with H_2, the emergence of a third signal was observed with principle g–tensor values of 2.19, 2.16 and 2.01 and designated Ni–C. Later, Ni–A, Ni–B and Ni–C were used as designations for the respective paramagnetic states and not only as terms for the corresponding signals in the EPR spectrum. Additional diamagnetic and paramagnetic states, such as the Ni–SU, Ni–SIa, Ni–SIr, and Ni–R, were identified. Since the EPR–silent states cannot be investigated by EPR–spectrocopy, FTIR spectroscopy is an indispensible tool for their experimental investigation [78-80]. The application of FTIR in the investigation of [NiFe] hydrogenases is especially fruitful as the stretching frequencies of the Fe–bound CO and CN ligands can be easily identified from the FTIR–spectrum of the protein. Ni–SIa, Ni–R and Ni–C form part of the catalytic cycle of the enzyme. The Ni–C state is light–sensitive and upon illumination it readily converts into the Ni–L state. Carbon monoxide is a competitive inhibitor of [NiFe] hydrogenase and an EPR–active and an EPR inactive CO–inhibited state have been identified.

References

1. Melis, A. and T. Happe, *Hydrogen production. Green algae as a source of energy.* Plant Physiology, 2001. **127**(3): p. 740-748.
2. Chornet, E. and S. Czernik, *Renewable fuels - harnessing hydrogen.* Nature, 2002. **418**(6901): p. 928-929.
3. Tamagnini, P., et al., *Hydrogenases and hydrogen metabolism of cyanobacteria.* Microbiology and Molecular Biology Reviews, 2002. **66**(1): p. 1-+.
4. Hallenbeck, P.C. and J.R. Benemann, *Biological hydrogen production; fundamentals and limiting processes.* International Journal of Hydrogen Energy, 2002. **27**(11-12): p. 1185-1193.
5. Tsygankov, A.A., et al., *Hydrogen production by cyanobacteria in an automated outdoor photobioreactor under aerobic conditions.* Biotechnology and Bioengineering, 2002. **80**(7): p. 777-783.
6. Kalia, V.C., et al., *Mining genomic databases to identify novel hydrogen producers.* Trends in Biotechnology, 2003. **21**(4): p. 152-156.
7. Schutz, K., et al., *Cyanobacterial h-2 production - a comparative analysis.* Planta, 2004. **218**(3): p. 350-359.
8. Dante, R.C., et al., *Temporal phenomena of hydrogen photobioproduction.* International Journal of Hydrogen Energy, 2004. **29**(12): p. 1219-1226.
9. Cournac, L., et al., *Sustained photoevolution of molecular hydrogen in a mutant of synechocystis sp strain pcc 6803 deficient in the type i nadph-dehydrogenase complex.* Journal of Bacteriology, 2004. **186**(6): p. 1737-1746.
10. Mertens, R. and A. Liese, *Biotechnological applications of hydrogenases.* Current Opinion in Biotechnology, 2004. **15**(4): p. 343-348.
11. Penfold, D.W. and L.E. Macaskie, *Production of h-2 from sucrose by escherichia coli strains carrying the pur400 plasmid, which encodes invertase activity.* Biotechnology Letters, 2004. **26**(24): p. 1879-1883.
12. Franchi, E., et al., *Metabolically engineered rhodobacter sphaeroides rv strains for improved biohydrogen photoproduction combined with disposal of food wastes.* Marine Biotechnology, 2004. **6**(6): p. 552-565.
13. Kanai, T., et al., *Continuous hydrogen production by the hyperthermophilic archaeon, thermococcus kodakaraensis kod1.* Journal of Biotechnology, 2005. **116**(3): p. 271-282.
14. Prince, R.C. and H.S. Kheshgi, *The photobiological production of hydrogen: Potential efficiency and effectiveness as a renewable fuel.* Critical Reviews in Microbiology, 2005. **31**(1): p. 19-31.
15. Kruse, O., et al., *Improved photobiological h-2 production in engineered green algal cells.* Journal of Biological Chemistry, 2005. **280**(40): p. 34170-34177.
16. Yoshida, A., et al., *Enhanced hydrogen production from formic acid by formate hydrogen lyase-overexpressing escherichia coli strains.* Applied and Environmental Microbiology, 2005. **71**(11): p. 6762-6768.
17. Benemann, J.R., et al., *Hydrogen evolution by a chloroplast-ferredoxin-hydrogenase system.* Proceedings of the National Academy of Sciences of the United States of America, 1973. **70**(8): p. 2317-2320.
18. Hallahan, D.L., et al., *Differential inhibition of catalytic sites in desulfovibrio-gigas hydrogenase.* Biochimie, 1986. **68**(1): p. 49-54.
19. Armstrong, F.A., *Hydrogenases: Active site puzzles and progress.* Current Opinion in Chemical Biology, 2004. **8**(2): p. 133-140.
20. Darensbourg, M.Y., E.J. Lyon, and J.J. Smee, *The bio-organometallic chemistry of active site iron in hydrogenases.* Coordination Chemistry Reviews, 2000. **206**: p. 533-561.
21. Evans, D.J., *Metal-sulfur chemistry relevant to modelling the active sites of some enzymes of environmental importance.* Journal of Chemical Research-S, 2001(8): p. 297-303.
22. Alper, J., *Water splitting goes au naturel.* Science, 2003. **299**(5613): p. 1686-1687.
23. Tard, C., et al., *Synthesis of the h-cluster framework of iron-only hydrogenase.* Nature, 2005. **433**(7026): p. 610-613.
24. Sun, L.C., B. Akermark, and S. Ott, *Iron hydrogenase active site mimics in supramolecular systems aiming for light-driven hydrogen production.* Coordination Chemistry Reviews, 2005. **249**(15-16): p. 1653-1663.
25. Liu, X.M., et al., *Iron-only hydrogenase: Synthetic, structural and reactivity studies of model compounds.* Coordination Chemistry Reviews, 2005. **249**(15-16): p. 1641-1652.
26. Bruschi, M., et al., *Dft investigations of models related to the active site of nife and fe hydrogenases.* Coordination Chemistry Reviews, 2005. **249**(15-16): p. 1620-1640.

27. Bouwman, E. and J. Reedijk, *Structural and functional models related to the nickel hydrogenases.* Coordination Chemistry Reviews, 2005. **249**(15-16): p. 1555-1581.
28. Artero, V. and M. Fontecave, *Some general principles for designing electrocatalysts with hydrogenase activity.* Coordination Chemistry Reviews, 2005. **249**(15-16): p. 1518-1535.
29. Tye, J.W., M.B. Hall, and M.Y. Darensbourg, *Better than platinum? Fuel cells energized by enzymes.* Proceedings of the National Academy of Sciences of the United States of America, 2005. **102**(47): p. 16911-16912.
30. Armstrong, F.A. and P.J. Albracht, *Nife -hydrogenases: Spectroscopic and electrochemical definition of reactions and intermediates.* Philosophical Transactions of the Royal Society a-Mathematical Physical and Engineering Sciences, 2005. **363**(1829): p. 937-954.
31. Gloaguen, F. and T.B. Rauchfuss, *Small molecule mimics of hydrogenases: Hydrides and redox.* Chemical Society Reviews, 2009. **38**(1): p. 100-108.
32. De Lacey, A.L., et al., *Activation and inactivation of hydrogenase function and the catalytic cycle: Spectroelectrochemical studies.* Chemical Reviews, 2007. **107**(10): p. 4304-4330.
33. Volbeda, A., et al., *Crystal-structure of the nickel-iron hydrogenase from desulfovibrio-gigas.* Nature, 1995. **373**(6515): p. 580-587.
34. VanderSpek, T.M., et al., *Similarities in the architecture of the active sites of ni-hydrogenases and fe-hydrogenases detected by means of infrared spectroscopy.* European Journal of Biochemistry, 1996. **237**(3): p. 629-634.
35. Patil, D.S., *Nickel-iron-selenium hydrogenase.* Inorganic Microbial Sulfur Metabolism, 1994. **243**: p. 68-94.
36. Garcin, E., et al., *The crystal structure of a reduced [nifese] hydrogenase provides an image of the activated catalytic center.* Structure, 1999. **7**(5): p. 557-566.
37. Voordouw, G., J.D. Strang, and F.R. Wilson, *Organization of the genes encoding fe hydrogenase in desulfovibrio-vulgaris subsp oxamicus monticello.* Journal of Bacteriology, 1989. **171**(7): p. 3881-3889.
38. He, S.H., et al., *Epr studies with se-77-enriched (nifese) hydrogenase of desulfovibrio-baculatus - evidence for a selenium ligand to the active-site nickel.* Journal of Biological Chemistry, 1989. **264**(5): p. 2678-2682.
39. Eidsness, M.K., et al., *Evidence for selenocysteine coordination to the active-site nickel in the nifese hydrogenases from desulfovibrio-baculatus.* Proceedings of the National Academy of Sciences of the United States of America, 1989. **86**(1): p. 147-151.
40. Berlier, Y., P.A. Lespinat, and B. Dimon, *A gas-chromatographic mass-spectrometric technique for studying simultaneous hydrogen deuteron exchange and para orthohydrogen conversion in hydrogenases of desulfovibrio-vulgaris hildenborough.* Analytical Biochemistry, 1990. **188**(2): p. 427-431.
41. Fauque, G., et al., *The 3 classes of hydrogenases from sulfate-reducing bacteria of the genus desulfovibrio.* Fems Microbiology Reviews, 1988. **54**(4): p. 299-344.
42. Happe, R.P., et al., *Unusual ftir and epr properties of the h-2-activating site of the cytoplasmic nad-reducing hydrogenase from ralstonia eutropha.* Febs Letters, 2000. **466**(2-3): p. 259-263.
43. Kleihues, L., et al., *The h-2 sensor of ralstonia eutropha is a member of the subclass of regulatory [nife] hydrogenases.* Journal of Bacteriology, 2000. **182**(10): p. 2716-2724.
44. Vincent, K.A., et al., *Electrochemical definitions of o-2 sensitivity and oxidative inactivation in hydrogenases.* Journal of the American Chemical Society, 2005. **127**(51): p. 18179-18189.
45. Pierik, A.J., et al., *Characterization of the active site of a hydrogen sensor from alcaligenes eutrophus.* Febs Letters, 1998. **438**(3): p. 231-235.
46. Foerster, S., et al., *Single crystal epr studies of the reduced active site of [nife] hydrogenase from desulfiovibrio vulgaris miyazaki f.* Journal of the American Chemical Society, 2003. **125**(1): p. 83-93.
47. Haumann, M., et al., *Hydrogen-induced structural changes at the nickel site of the regulatory nife hydrogenase from ralstonia eutropha detected by x-ray absorption spectroscopy.* Biochemistry, 2003. **42**(37): p. 11004-11015.
48. Buhrke, T., et al., *Reduction of unusual iron-sulfur clusters in the h-2-sensing regulatory ni-fe hydrogenase from ralstonia eutropha h16.* Journal of Biological Chemistry, 2005. **280**(20): p. 19488-19495.
49. Van der Linden, E., et al., *The soluble nife -hydrogenase from ralstonia eutropha contains four cyanides in its active site, one of which is responsible for the insensitivity towards oxygen.* Journal of Biological Inorganic Chemistry, 2004. **9**(5): p. 616-626.

50. van der Linden, E., et al., *An improved purification procedure for the soluble nife -hydrogenase of ralstonia eutropha: New insights into its (in)stability and spectroscopic properties.* Journal of Biological Inorganic Chemistry, 2006. **11**(2): p. 247-260.
51. Burgdorf, T., et al., *[nife]-hydrogenases of ralstonia eutropha h16: Modular enzymes for oxygen-tolerant biological hydrogen oxidation.* Journal of Molecular Microbiology and Biotechnology, 2005. **10**(2-4): p. 181-196.
52. Muller, A., et al., *Nadh-induced changes of the nickel coordination within the active site of the soluble hydrogenase from alcaligenes eutrophus: Xafs investigations on three states distinguishable by epr spectroscopy.* Angewandte Chemie-International Edition in English, 1997. **36**(16): p. 1747-1750.
53. Peters, J.W., et al., *X-ray crystal structure of the fe-only hydrogenase (cpl) from clostridium pasteurianum to 1.8 angstrom resolution.* Science, 1998. **282**(5395): p. 1853-1858.
54. Nicolet, Y., C. Cavazza, and J.C. Fontecilla-Camps, *Fe-only hydrogenases: Structure, function and evolution.* Journal of Inorganic Biochemistry, 2002. **91**(1): p. 1-8.
55. Nicolet, Y., et al., *A novel fes cluster in fe-only hydrogenases.* Trends in Biochemical Sciences, 2000. **25**(3): p. 138-143.
56. Nicolet, Y., et al., *Desulfovibrio desulfuricans iron hydrogenase: The structure shows unusual coordination to an active site fe binuclear center.* Structure with Folding & Design, 1999. **7**(1): p. 13-23.
57. Nicolet, Y., et al., *Crystallographic and ftir spectroscopic evidence of changes in fe coordination upon reduction of the active site of the fe-only hydrogenase from desulfovibrio desulfuricans.* Journal of the American Chemical Society, 2001. **123**(8): p. 1596-1601.
58. Vignais, P.M., B. Billoud, and J. Meyer, *Classification and phylogeny of hydrogenases.* Fems Microbiology Reviews, 2001. **25**(4): p. 455-501.
59. Thauer, R.K., A.R. Klein, and G.C. Hartmann, *Reactions with molecular hydrogen in microorganisms: Evidence for a purely organic hydrogenation catalyst.* Chemical Reviews, 1996. **96**(7): p. 3031-3042.
60. Klein, A.R., V.M. Fernandez, and R.K. Thauer, *H-2-forming n-5,n-10-methylenetetrahydromethanopterin dehydrogenase - mechanism of h-2 formation analyzed using hydrogen isotopes.* Febs Letters, 1995. **368**(2): p. 203-206.
61. Higuchi, Y., et al., *Removal of the bridging ligand atom at the ni-fe active site of nife hydrogenase upon reduction with h-2, as revealed by x-ray structure analysis at 1.4 angstrom resolution.* Structure with Folding & Design, 1999. **7**(5): p. 549-556.
62. Niviere, V., et al., *Crystallization, preliminary-x-ray study and crystal activity of the hydrogenase from desulfovibrio-gigas.* Journal of Molecular Biology, 1987. **195**(4): p. 969-970.
63. Hatchikian, E.C., M. Bruschi, and J. Legall, *Characterization of periplasmic hydrogenase from desulfovibrio-gigas.* Biochemical and Biophysical Research Communications, 1978. **82**(2): p. 451-461.
64. Volbeda, A., et al., *Structure of the [nife] hydrogenase active site: Evidence for biologically uncommon fe ligands.* Journal of the American Chemical Society, 1996. **118**(51): p. 12989-12996.
65. Massanz, C. and B. Fliedrich, *Amino acid replacements at the h-2-activating site of the nad-reducing hydrogenase from alcaligenes eutrophus.* Biochemistry, 1999. **38**(43): p. 14330-14337.
66. Burgdorf, T., A.L. De Lacey, and B. Friedrich, *Functional analysis by site-directed mutagenesis of the nad(+)-reducing hydrogenase from ralstonia eutropha.* Journal of Bacteriology, 2002. **184**(22): p. 6280-6288.
67. Montet, Y., et al., *Gas access to the active site of ni-fe hydrogenases probed by x-ray crystallography and molecular dynamics.* Nature Structural Biology, 1997. **4**(7): p. 523-526.
68. Page, C.C., et al., *Natural engineering principles of electron tunnelling in biological oxidation-reduction.* Nature, 1999. **402**(6757): p. 47-52.
69. Ogata, H., et al., *Structural studies of the carbon monoxide complex of nife hydrogenase from desulfovibrio vulgaris miyazaki f: Suggestion for the initial activation site for dihydrogen.* Journal of the American Chemical Society, 2002. **124**(39): p. 11628-11635.
70. Matias, P.M., et al., *Nife hydrogenase from desulfovibrio desulfuricans atcc 27774: Gene sequencing, three-dimensional structure determination and refinement at 1.8 angstrom and modelling studies of its interaction with the tetrahaem cytochrome c(3).* Journal of Biological Inorganic Chemistry, 2001. **6**(1): p. 63-81.
71. Dementin, S., et al., *A glutamate is the essential proton transfer gate during the catalytic cycle of the nife hydrogenase.* Journal of Biological Chemistry, 2004. **279**(11): p. 10508-10513.
72. Siegbahn, P.E.M., J.W. Tye, and M.B. Hall, *Computational studies of [nife] and [fefe] hydrogenases.* Chemical Reviews, 2007. **107**(10): p. 4414-4435.

73. Higuchi, Y., T. Yagi, and N. Yasuoka, *Unusual ligand structure in ni-fe active center and an additional mg site in hydrogenase revealed by high resolution x-ray structure analysis.* Structure, 1997. **5**(12): p. 1671-1680.
74. Pandelia, M.E., et al., *Inhibition of the [nife] hydrogenase from desulfovibrio vulgaris miyazaki f by carbon monoxide: An ftir and epr spectroscopic study.* Biochimica Et Biophysica Acta-Bioenergetics, 2010. **1797**(2): p. 304-313.
75. DeLacey, A.L., et al., *Spectroscopic and kinetic characterization of active site mutants of desulfovibrio fructosovorans ni-fe hydrogenase.* Journal of Biological Inorganic Chemistry, 2003. **8**(1-2): p. 129-134.
76. Albracht, S.P.J., *Nickel hydrogenases - in search of the active-site.* Biochimica Et Biophysica Acta-Bioenergetics, 1994. **1188**(3): p. 167-204.
77. Lubitz, W., E. Reijerse, and M. van Gastel, *[nife] and [fefe] hydrogenases studied by advanced magnetic resonance techniques.* Chemical Reviews, 2007. **107**(10): p. 4331-4365.
78. Bleijlevens, B., et al., *The activation of the nife -hydrogenase from allochromatium vinosum. An infrared spectro-electrochemical study.* Journal of Biological Inorganic Chemistry, 2004. **9**(6): p. 743-752.
79. deLacey, A.L., et al., *Infrared spectroelectrochemical characterization of the nife hydrogenase of desulfovibrio gigas.* Journal of the American Chemical Society, 1997. **119**(31): p. 7181-7189.
80. Fichtner, C., et al., *Spectroelectrochemical characterization of the [nife] hydrogenase of desulfovibrio vulgaris miyazaki f.* Biochemistry, 2006. **45**(32): p. 9706-9716.

2.1. Concepts and performance of Density Functional Theory

2.1.1 Introduction

In the recent decades, density functional theory (DFT) has become the major work–horse in theoretical chemistry. In addition, DFT is used more and more by experimentalists, which seek to enrich or facilitate the interpretation of their experimental results. Density functional theory usually combines reasonable accuracy with a computational efficiency that even allows for the quantum–mechanical computation of relatively large molecular systems, such as the active site of metal–enzymes. With modern computational hardware and efficient quantum chemistry program–packages [1-5], it is even possible to perform single point calculations of small proteins with DFT [6]. Despite its enormous success, DFT can unfortunately not be pushed to arbitrary accuracies at the expense of computational efficiencies, as wavefunction–based approaches [6]. Although the accuracy of DFT has been generally assessed by multiple benchmark studies and is sometimes even competitive with wavefunction based approaches, in some cases DFT performs surprisingly bad [7]. Thus, it is indispensible to assess the reliability of the obtained DFT results by comparison with experimental data, such as X–Ray structures and spectroscopic parameters.

Several reviews on the foundations, realization, performance and applications of DFT are available [8-17]. The calculations in the present work have been performed with DFT. Thus, important aspects of modern density functional theory and its foundations shall be outlined briefly. The structure and content of this outline is based on an excellent review on the topic [6].

2.1.2. Quantum–mechanical background:

Starting point for the vast majority of quantum–chemical calculations is the time–independent Schrödinger equation in the Born–Oppenheimer approximation:

$$\hat{H}_{\mathrm{BO}}\Psi(\mathbf{x}_1,\ldots,\boldsymbol{x}_{\mathrm{N}}|\boldsymbol{R}_1,\ldots,\boldsymbol{R}_{\mathrm{M}}) = E\Psi(\boldsymbol{x}_1,\ldots,\boldsymbol{x}_{\mathrm{N}}|\boldsymbol{R}_1,\ldots,\boldsymbol{R}_{\mathrm{M}}) \qquad \textbf{[1]}$$

Here x_i collectively denotes the three spatial and the spin degrees of freedom of the i^{th} electron. H_{BO} denotes the Born–Oppenheimer (BO) operator, which in atomic units reads:

$$
\begin{aligned}
\hat{H}_{\mathrm{BO}} &= T_e + V_{eN} + V_{ee} + V_{NN} \\
&= -\frac{1}{2}\sum_{i=1}^{N}\nabla_i^2 - \sum_{i=1}^{N}\sum_{A=1}^{M}\frac{Z_A}{|\mathbf{r}_i - \mathbf{R}_A|} \\
&\quad + \frac{1}{2}\sum_{i=1}^{N}\sum_{\substack{j=1 \\ j\neq i}}^{N}\frac{1}{|\mathbf{r}_i - \mathbf{r}_j|} + \frac{1}{2}\sum_{A=1}^{M}\sum_{\substack{B=1 \\ A\neq B}}^{M}\frac{Z_A Z_B}{|\boldsymbol{R}_A - \boldsymbol{R}_B|} \\
&\equiv \sum_i h(i) + \frac{1}{2}\sum_{i\neq j} g(i,j) + V_{NN}
\end{aligned}
$$

[2]

The first term T_e corresponds to the kinetic energy and the remaining terms describe the different coulombic interactions between the charged particles of the system: The second term V_{eN} describes the electron–nuclear attraction, the third term V_{ee} the repulsive electron–electron interaction and the fourth term V_{NN} the internuclear repulsion. The time–independent Schrödinger equation is a partial differential equation, which is solved by a multidimensional wavefunction $\Psi(x,R)$. The dimensionality equals the number of degrees of freedom of the respective molecular system, and in the BO approximation, it is assumed that, in a molecular system, the movement of the electrons is much faster than the motion of the nuclei. This leads to a separation of the nuclear and electronic wavefunctions. The nuclei coordinates enter only parametrically into the electronic wavefunction and, hence, the Schrödinger equation is not solved generally but for a given nuclear configuration $R = R_1, R_2, \ldots R_N$. If not stated otherwise, in the following, the term Schrödinger equation (SE) always refers to the electronic time–independent Schrödinger equation. In order to satisfy the Pauli–Principle, the wavefunction needs to be antisymmetric, which means it needs to change its sign when two electrons are interchanged. Physically speaking, the eigenvalues E_i of the SE are the energies of the ground (E_0) and excited states ($E_1, E_2 \ldots$) of the system. By multiplication of the wavefunction by its complex conjugate, one arrives at an expression, which can be physically interpreted as probability density. The probability of finding the system in a certain electronic configuration at given nuclear configuration is described by:

$$
\Psi_I(\mathbf{x}|\mathbf{R})\Psi_I(\mathbf{x}|\mathbf{R})^* \, \mathrm{d}\mathbf{x}
$$

[3]

Solving the SE gives insight into the molecular system in question since it leads to the knowledge of wavefunctions, probability densities, energy eigenvalues and expectation values of physical observables. Unfortunately, even in the BO approximation, the SE can be analytically solved only for the simplest molecular systems. More precisely speaking, the electron–electron repulsion term in the BO operator, prevents a separation of the variables and thereby the exact solution of the SE from many-body systems. This leads the requirement for efficient approaches to approximate solutions.

The general ansatz for finding the most suitable wavefunctions and energy expectation values is based on the variation principle with the expectation value of the energy being an upper–bound to the exact solution:

$$E \leq \frac{\langle \Psi_{\text{trial}} | H | \Psi_{\text{trial}} \rangle}{\langle \Psi_{\text{trial}} | \Psi_{\text{trial}} \rangle} \qquad \textbf{[4]}$$

Hartee–Fock Theory

The fundamental approach to an approximate solution of the SE is the Hartee–Fock ansatz where the wavefunction is set up in the form of a single Slater determinant:

$$\Psi_{\text{SD}}(\boldsymbol{x}_1, \ldots, \boldsymbol{x}_N) = \frac{1}{\sqrt{N!}} \begin{vmatrix} \psi_1(\boldsymbol{x}_1) & \psi_2(\boldsymbol{x}_1) & \cdots & \psi_N(\boldsymbol{x}_1) \\ \psi_1(\boldsymbol{x}_2) & \psi_2(\boldsymbol{x}_2) & \cdots & \psi_N(\boldsymbol{x}_2) \\ \vdots & \vdots & \ddots & \vdots \\ \psi_1(\boldsymbol{x}_N) & \psi_2(\boldsymbol{x}_N) & \cdots & \psi_N(\boldsymbol{x}_N) \end{vmatrix} \qquad \textbf{[5]}$$

Most notably, a wavefunction in the form of a Slater determinant satisfies the Pauli antisymmetry principle, i.e. it changes its sign upon interchanging two electrons. The functions ψ_i shall be interpreted as ortho–normalized, one–electron wavefunctions, termed orbitals. Minimization of the energy expectation value by variation of the orbitals under the constraint of ortho–normality leads to pseudo–one–electron equations of the integro–differential Fock–operator F :

$$\hat{F}\psi_i(\boldsymbol{x}) = \varepsilon_i \psi_i(\boldsymbol{x}) \qquad \textbf{[6]}$$

These equations are solved iteratively to yield, at self–consistency, orbitals ψ_i, from which the wavefunction Ψ_{SD} can be easily obtained. Since in Hartree–Fock Theory, the BO operator is fully incorporated, the only deviation with respect to the exact solution of the BO operator is due to the restriction of the wavefunction to a single Slater determinant. Nevertheless, the Hartree–Fock approach is surprisingly successful since it recovers about 99.9% of the exact ground state energy. Unfortunately, in absolute terms, the error is still in the range of several Hartrees and, even when considering energy differences the errors obtained with Hartree–Fock theory are often still too large for a reliable quantitative treatment of chemical problems. The energy difference between the exact energy and the Hartree–Fock energy has been defined as correlation energy.

In order to go beyond the Hartree–Fock approximatation, multideterminant approaches for the wavefunction are employed. Those “post–Hartree–Fock” approaches [18-25] are capable of recovering significant fractions of the correlation energy but usually are in terms of computational

efficiency highly costly and are generally only applicable to small and medium-sized molecules. Especially, in the field of computational bioinorganic chemistry where relatively large molecular systems are treated quantum–mechanically, the application of post–Hartree–Fock methods is clearly an exception.

Density matrices

The wavefunction Ψ_{SD} is a complex mathematical device depending on the spatial and spin degrees of freedom of all the electrons of the molecular system. In order to gain insights into the system under investigation, it is generally sufficient to operate with a two–electron density distribution since the BO operator contains only one– and two–electron operators. The second–order reduced density–matrix is defined as:

$$\Gamma(\boldsymbol{x}_1, \boldsymbol{x}_2) = \frac{N(N-1)}{2} \int \Psi(\boldsymbol{x}_1, \boldsymbol{x}_2, \ldots, \boldsymbol{x}_N|\boldsymbol{R}) \times \Psi(\boldsymbol{x}_1, \boldsymbol{x}_2, \ldots, \boldsymbol{x}_N|\boldsymbol{R})^* \, \mathrm{d}\boldsymbol{x}_3 \ldots \mathrm{d}\boldsymbol{x}_N \quad \textbf{[7]}$$

The prefactor derives from the requirement that integration over all electronic degrees of freedom needs to yield the number of electrons in the system. In analogy to the second–order density–matrix, a single–particle density–matrix is defined as:

$$\gamma(\boldsymbol{x}_1, \boldsymbol{x}'_1) = N \int \Psi(\boldsymbol{x}_1, \boldsymbol{x}_2, \ldots, \boldsymbol{x}_N|\boldsymbol{R}) \Psi(\boldsymbol{x}'_1, \boldsymbol{x}_2, \ldots, \boldsymbol{x}_N|\boldsymbol{R})^* \mathrm{d}\boldsymbol{x}_2 \ldots \mathrm{d}\boldsymbol{x}_N \quad \textbf{[8]}$$

The diagonal element of *ρ(x,x)* is the electron density *ρ(x)* at configuration *x*. *ρ(x)* can be decomposed into elements stemming from the spin–up and spin–down electrons:

$$\rho(\boldsymbol{r}) = \int \rho(\boldsymbol{x}) \, \mathrm{d}s = \rho^{\alpha}(\boldsymbol{r}) + \rho^{\beta}(\boldsymbol{r}) \quad \textbf{[9]}$$

The spin–density describes the probability for finding the electron spin at a given configuration *x* and reads:

$$\rho^{\alpha-\beta}(\boldsymbol{r}) = \rho^{\alpha}(\boldsymbol{r}) - \rho^{\beta}(\boldsymbol{r}) \quad \textbf{[10]}$$

The spin–density is a particularly useful tool for the description and interpretation of magnetic properties.

2.1.3 The theoretical fundament of Density Functional Theory

The methodological gap between simple Hartree–Fock theory and accurate but computationally highly demanding post–Hartree–Fock methods is filled by density functional theory (DFT), which broadly yields reasonably accurate results at a computational efficiency which even allows for single point calculations of molecular systems with more than say 650 atoms. Hence, DFT enables the quantum–chemical treatment of even large molecular system such as the active sites of metal proteins and therefore it is the method of choice in bioinorganic chemistry.

Theoretically, DFT is based on the theorems of Hohenberg and Kohn, which were already formulated in the 1960s. By knowing the multidimensional wavefunction, the exact energy of the system can be obtained from the SE. The powerful first theorem of Hohenberg and Kohn proves that the energy can be directly derived from the electron density $\rho(x)$ without need to explicitly calculate the highly complex multidimensional wavefunction. More formally speaking, the exact energy is a functional E of the electron density E_{exact}, i.e. $E_{exact} = E[\rho(x)]$.

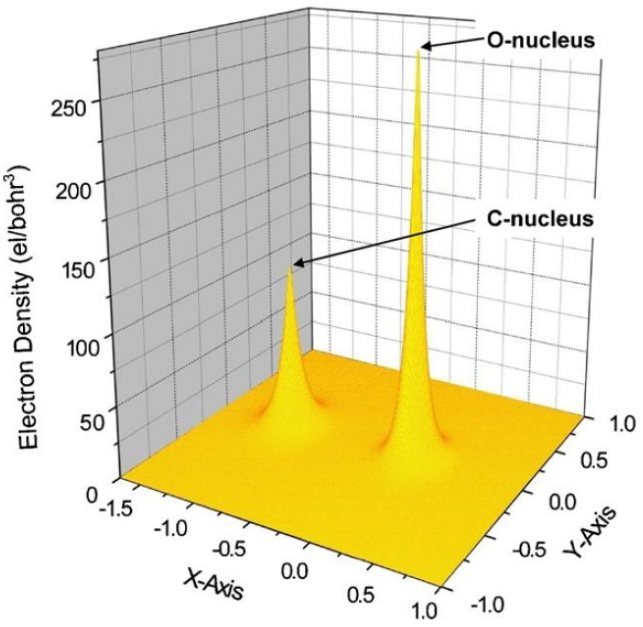

Figure 1: Electron density for carbon monoxide in the xy–plane.

The electron density of the xy–plane of the CO molecule is displayed in Figure 1. At the nuclear positions of the oxygen and the carbon atoms, cusps of the electron density are present. Furthermore, it evident from the Figure 1 that the cusps are finite with values depending on the type of atom. The condition for an electron density cusp at the nucleus reads:

$$\lim_{r\to 0}\left[\frac{\partial}{\partial r}+2Z_A\right]\bar{\rho}(r)=0 \qquad \textbf{[11]}$$

Here the electron density is spherically averaged. The BO Hamiltonian can be set up when the number of electrons and the number, positions and charges of the nuclei are known. Since the nuclear positions and charges can be unambiguously determined from the electron density according to the cusp condition and the number of electrons is obtained by spatial integration of *ρ(x)*, the complete BO Hamiltonian can be set up from the information contained in the electron density. An unique ground state energy is associated with the Born–Oppenheimer Hamiltonian and, consequently, it should in principle be possible to deduce the energy from the spin density via the energy functional *E[ρ(x)]*.

The energy functional E[ρ(x)]

Calculation of the energy without explicitly solving the SE appears advantageous as the electron density *ρ(x)*, which depends only on the degrees of freedom of a single electron, is a much less complex device than the sophisticated multidimensional wavefunction. However, the fundamental problem is that the general energy functional E relating the electron density and the total energy is not known.

Since the nuclear–electron interaction operator V_{eN} in the BO Hamiltonian is a non–differential one–electron operator, the attraction energy of electrons and nuclei can be directly derived from the electron density *ρ(x)*. In contrast, since the operator T_e is a differential operator, calculation of the kinetic energy requires the knowledge of the complete single–particle density matrix *γ(x,x´)*. In addition, the energy of the electron–electron repulsion can only be obtained from the second–order density matrix as the V_{ee} is a two–electron operator. Since the functional for the electron–electron repulsion energy is not known explicitly, one can at least break it down into a known part *J[ρ(x)]*, which represents the self–interaction energy, and an unknown part $E'_{xc}[\rho(x)]$, which represents the exchange–correlation energy. The entire energy expression then reads:

$$E[\rho]=V_{NN}+V_{eN}[\rho]+J[\rho]+T[\rho]+E'_{XC}[\rho] \qquad \textbf{[12]}$$

with J[ρ(x)]:

$$\int\int \rho(\mathbf{r}_1)\rho(\mathbf{r}_2)r_{12}^{-1}\,d\mathbf{r}_1\,d\mathbf{r}_2 \qquad \textbf{[13]}$$

Kohn–Sham equations

Several approaches have been explored to explicitly calculate the kinetic energy T_e from the electron density $\rho(x)$, among which the most famous is clearly the Thomas–Fermi model. Unfortunately, its accuracy is insufficient for a broad application to chemical systems. A more indirect but currently widely employed ansatz for the computation of the kinetic energy is the Kohn–Sham construction, which is founded in the expression for the kinetic energy of Hartree–Fock theory. The wavefunction of N non–interacting electrons is correctly described by a single Slater determinant formed by N Kohn–Sham orbitals. The kinetic energy $T_s[\rho]$ calculated from this single determinant is assumed to be reasonablely close to the actual kinetic energy and reads:

$$T_s[\rho] = -\frac{1}{2}\sum_i \langle \psi_i | \nabla^2 | \psi_i \rangle \qquad \textbf{[14]}$$

The fraction of the kinetic energy $T[\rho]$ which is not covered by $T_s[\rho]$ is absorbed in the correlation–exchange functional:

$$E_{XC}[\rho] = E'_{XC}[\rho] + T[\rho] - T_s[\rho] \qquad \textbf{[15]}$$

The electron density from the Kohn–Sham orbitals equals the exact electron density. The Kohn–Sham orbitals are then given by the Kohn–Sham equations:

$$\left\{-\frac{1}{2}\nabla^2 + v_{\text{eff}}(\boldsymbol{r})\right\}\psi_i(\boldsymbol{x}) = \varepsilon_i \psi_i(\boldsymbol{x}) \qquad \textbf{[16]}$$

The Kohn–Sham equations are single–particle equations and, according to the second Hohenberg–Kohn theorem, can be solved variationally. The effective potential v_{eff} then takes the form:

$$v_{\text{eff}}(\boldsymbol{r}) = -\sum_A Z_A |\boldsymbol{r} - \boldsymbol{R}_A|^{-1} + \int \rho(\boldsymbol{r}')|\boldsymbol{r} - \boldsymbol{r}'|^{-1} \mathrm{d}\boldsymbol{r}' + V_{XC}(\boldsymbol{r}) \qquad \textbf{[17]}$$

With:

$$V_{XC}(\boldsymbol{r}) = \frac{\delta E_{XC}[\rho]}{\delta \rho(\boldsymbol{r})} \qquad \textbf{[18]}$$

This is the famous exchange–correlation potential. The electron density is easily obtained from the Kohn–Sham orbitals:

$$\rho_{KS}(\boldsymbol{r}) = \sum_i \int |\psi_i(\boldsymbol{x})|^2 \, ds \qquad \textbf{[19]}$$

Hence, the only term in the energy expression which is not known is the exchange–correlation potential $V_{xc}(r)$. In contrast to Hartree–Fock theory, where J_{ii} is exactly cancelled out by the exchange interaction K_{jj}, the electron–electron self–interaction is a major problem in DFT. Several attempts to remove the self–interaction haveonly been of limited success, so far [26-28].

From the homogenous electron gas to the local exchange functional

In spite of its existence, the explicit form of the exact exchange–correlation functional is not known. Thus, the main challenge of present day DFT is to find suitable approximate forms of the exchange–correlation functional $V_{xc}(r)$. This is a difficult task and usually involves besides physical reasoning, the fitting of parameters to a large body of empirical data. Sometimes one even has to rely on "chemical and physical intuition" to a certain extend. The homogenous electron gas features a uniformly distributed positive background charge, which results in a homogenous electron density of the N–electrons. It has been an important source of inspiration for the development and improvement of DFT energy functionals. The exchange energy per electron of the homogenous electron gas features a $\rho^{1/3}$ dependence and reads:

$$\frac{E_X}{N} = -\frac{3}{4}\left(\frac{6}{\pi}\right)^{1/3}(\rho_\alpha^{1/3} + \rho_\beta^{1/3}) \qquad \textbf{[20]}$$

To be applicable in DFT, it is assumed that this expression for the total exchange energy of the homogenous electron gas can be applied locally, which gives the local exchange functional E_x:

$$E_X[\rho] = \int \rho(\mathbf{r})\varepsilon_X(\rho)\,d\mathbf{r} = -\frac{3}{4}\left(\frac{6}{\pi}\right)^{1/3}\int(\rho_\alpha^{4/3}(\mathbf{r}) + \rho_\beta^{4/3}(\mathbf{r}))\,d\mathbf{r} \qquad \textbf{[21]}$$

From this expression, the local exchange potential is readily derived:

$$V_X^\alpha(\mathbf{r}) = \frac{\delta E_X}{\delta\rho_\alpha(\mathbf{r})} = -\left(\frac{6}{\pi}\right)^{1/3}\rho_\alpha^{1/3}(\mathbf{r}) \qquad \textbf{[22]}$$

Of course, an analogous equation for the β–electron density ρ_β can be obtained. Despite the crude approximation that the exchange energy of the homogenous electron gas can be applied locally, the local exchange potential is surprisingly successful and yields energies, which are only by about 10%

smaller than the corresponding Hartree–Fock results. Even before the Hohenberg–Kohn theorems were formulated, the local exchange potential had been used in an approximate form of Hartee–Fock theory, known as X_α–method. Since the exchange functional $E_x[\rho]$ already yields suitable results, it is reasonable to take $E_x[\rho]$ as a starting point for the development of more sophisticated forms of the exchange correlation functional $E_{xc}[\rho]$.

Incorporation of the correlation energy in the model

Since only an expression for the exchange interaction has been incorporated so far, terms which cover the electron correlation need to be included in the model.

As for the exchange energy, a suitable starting point for an expression for the correlation energy is the homogenous electron gas. The first expression in this respect was proposed by Wigner and reads:

$$E_C^W[\rho] = \int \rho(\mathbf{r})\varepsilon_C^W[\rho]\,\mathrm{d}\mathbf{r} = -\int \rho(\mathbf{r})\frac{0.44}{r_S + 7.8}\,\mathrm{d}\mathbf{r} \qquad \textbf{[23]}$$

With the Wigner–Seitz–radius being defined as:

$$r_S = (3/(4\pi\rho))^{1/3} \qquad \textbf{[24]}$$

Due to the exchange interaction, electrons of like spin tend to avoid each other more pronouncedly than electrons of opposite spin. As a consequence, electron correlation is stronger for electrons of different spins than for electrons of the same spin. Several parameterizations [29-33] for the local exchange and correlation energy functional are available in the form of the local density approximation (LDA) and its spin–polarized counterparts (LDS).

The generalized gradient approximation and hybrid functionals

The general gradient approximation (GGA) was the next step in the development of suitable energy functional and, in contrast to the LDA and LDS methods, the gradient of the electron density is explicitly included in the energy expression. The exchange correlation functional can then be subdivided into a part which corresponds to the LSD functional and a corrective term which includes the explicit dependency of the energy on the gradient of the electron density:

$$E_{XC}^{GGA}[\rho_\alpha, \rho_\beta, \nabla\rho_\alpha, \nabla\rho_\beta] = E_{XC}^{LSD}[\rho_\alpha, \rho_\beta] + \Delta E_{XC}[\rho_\alpha, \rho_\beta, \nabla\rho_\alpha, \nabla\rho_\beta] \qquad \textbf{[25]}$$

For example, the gradient correction by Becke [34] reads:

$$\Delta E_{XC}[\rho_\alpha, \rho_\beta, \nabla\rho_\alpha, \nabla\rho_\beta] = -\rho^{1/3}(\boldsymbol{r})\frac{\beta x(\boldsymbol{r})^2}{1 + 6\beta x(\boldsymbol{r})\sinh^{-1} x(\boldsymbol{r})} \quad \textbf{[25]}$$

2.1.4 Performance: geometries, energies and molecular properties

Several studies have been devoted to benchmark the performance of DFT in the calculation of parameters relevant to chemical problems, such as geometries, energies and all sorts of spectroscopic parameters. Here, we focus on the computational efficiency and accuracy of DFT for the computation of properties which are most relevant to the present work, i.e. geometries, energies, IR–frequencies and Spin Hamiltonian parameters.

Extensive benchmark studies have been performed to reliably assess the accuracy of DFT in geometry calculations [35-38] showing that the overall performance of DFT in this area is good to excellent. With respect to the basis set, for second row transition metals, a triple–zeta basis set with one, maybe two, polarization functions should already approach the saturation limit. On the other hand, a double–zeta basis set is usually too small for the accurate treatment of transition metal ions [6]. The differences in accuracy between different functionals are mostly negligible such that it is advisable to use computationally less demanding GGA functionals like BP86 instead of hybrid functionals for geometry optimizations [6].

With errors usually below 10%, calculations of vibrational frequencies are astonishingly accurate when GGA functionals are employed (see [17] for an extensive account of benchmark studies). The fairly accurate agreement of computed harmonic frequencies with experimental FTIR measurements can be traced back to a fortuitous cancellation of errors: The systematic underestimation of the harmonic frequencies is compensated by the neglect of anharmonicities in the DFT calculations [39]. On the other hand, harmonic frequencies are usually more accurately obtained with hybrid functionals but the explicit computation of anharmonicity effects is rather involved. Consequently, it is advisable to use GGA functionals for the computation of frequencies with DFT.

The accuracy of the calculations of Spin Hamiltonian parameters, such as g–values, hyperfine couplings, zero–field splitting and quadrupole couplings, depends much more on the system under investigation than in the case of geometries and vibrational frequencies calculations. For organic radicals and biradicals, the results are usually very good. Hybrid functionals, such as B3LYP or TPSSh, perform slightly better than GGA functionals. On the other hand, the computation of magnetic properties of transition metal compounds is more challenging. The g–shifts are usually pronouncedly underestimated by the common functionals [40-42]. This underestimation depends to a certain

extend on the type of metal and the oxidation state. Two major factors have been identified to cause the systematic underrepresentation of the g–shift. Firstly, the metal–ligand bonds are too covalent, which results in a too extensive delocalization of the electron spin from the metal into the ligand orbitals. Secondly, the d–d transitions are usually too large and the system becomes too stiff with respect to an external perturbation. Hybrid functionals reduce the extent of metal–ligand covalency due to the admixture of HF–exchange and, therefore, are generally better suited for the calculation of g–tensors in transition metals. However, too much HF exchange increases the risk of undesirable spin–contamination [41].

The computation of metal hyperfine couplings is quite evolved. Heavy atoms like transition metals feature a significant spin–orbit coupling (SOC) contribution to the hyperfine coupling constant. Particularly challenging is the accurate determination of the Fermi–contact term as spin polarization effect plays a crucial role. The positive spin density in the metal valence orbitals results in an efficient polarization of the core orbitals. The accurate computation of these spin–polarization effects proves difficult and spin–polarization is usually underestimated by DFT [43-44]. In this respect, hybrid functionals give better results than GGA functionals according to the admixture of HF–exchange.

Energies are generally more accurate with hybrid functionals than with GGA functionals. According to benchmark studies on relatively small, closed–shell molecules composed of main–group elements (the so–called G2 set of molecules), energies can be obtained accurately within an error of 2–3 kcal/mol. However, as pointed out by Neese [45], this prediction seems too optimistic in particular when larger and more complex molecular systems, as commonly treated in computational bioinorganic chemistry, are under investigation. Unfortunately, benchmarking of the accuracy of DFT–energies of larger transition metal systems proves difficult due to the lack of a sufficient amount of experimental data.

References

1. van Slageren, J., S. Piligkos, and F. Neese, *Magnetic circular dichroism spectroscopy on the cr antiferromagnetic ring.* Dalton Trans, 2010. **39**(20): p. 4999-5004.
2. Gordon. *Gamess*. Available from: http://www.msg.ameslab.gov/GAMESS/.
3. Frisch. *Gaussian*. Available from: http://www.gaussian.com/.
4. Baerends. *Adf*. Available from: http://www.scm.com/.
5. Ahlrichs. *Turbomole*. Available from: http://www.cosmologic.de/QuantumChemistry/.
6. Neese, F., *Prediction of molecular properties and molecular spectroscopy with density functional theory: From fundamental theory to exchange-coupling.* Coordination Chemistry Reviews, 2009. **253**(5-6): p. 526-563.
7. Grimme, S., *Seemingly simple stereoelectronic effects in alkane isomers and the implications for kohn-sham density functional theory.* Angewandte Chemie-International Edition, 2006. **45**(27): p. 4460-4464.
8. Siegbahn, P.E.M. and T. Borowski, *Modeling enzymatic reactions involving transition metals.* Accounts of Chemical Research, 2006. **39**(10): p. 729-738.
9. Siegbahn, P.E.M., *The performance of hybrid dft for mechanisms involving transition metal complexes in enzymes.* Journal of Biological Inorganic Chemistry, 2006. **11**(6): p. 695-701.
10. Blomberg, M.R.A. and P.E.M. Siegbahn, *Quantum chemistry applied to the mechanisms of transition metal containing enzymes - cytochrome c oxidase, a particularly challenging case.* Journal of Computational Chemistry, 2006. **27**(12): p. 1373-1384.
11. Bassan, A., et al., *Theoretical studies of enzyme mechanisms involving high-valent iron intermediates.* Journal of Inorganic Biochemistry, 2006. **100**(4): p. 727-743.
12. Siegbahn, P.E.M. and M.R.A. Blomberg, *Methods and models for studying mechanisms of redox-active enzymes.* Philosophical Transactions of the Royal Society a-Mathematical Physical and Engineering Sciences, 2005. **363**(1829): p. 847-860.
13. Noodleman, L. and W.-G. Han, *Structure, redox, pk(a), spin. A golden tetrad for understanding metalloenzyme energetics and reaction pathways.* Journal of Biological Inorganic Chemistry, 2006. **11**(6): p. 674-694.
14. Lovell, T., et al., *Density functional methods applied to metalloenzymes.* Coordination Chemistry Reviews, 2003. **238**: p. 211-232.
15. Shaik, S., et al., *Theoretical perspective on the structure and mechanism of cytochrome p450 enzymes.* Chemical Reviews, 2005. **105**(6): p. 2279-2328.
16. Schroder, D., S. Shaik, and H. Schwarz, *Two-state reactivity as a new concept in organometallic chemistry.* Accounts of Chemical Research, 2000. **33**(3): p. 139-145.
17. Koch, W. and M.C. Holthausen, *A chemist's guide to density functional theory*. 2000, Weinheim: Wiley–VCH.
18. Crawford, T.D. and H.F. Schaefer, *An introduction to coupled cluster theory for computational chemists*, in *Reviews in computational chemistry, vol 14*, K.B.B.D.B. Lipkowitz, Editor. 2000. p. 33-136.
19. Bartlett, R.J. and M. Musial, *Coupled-cluster theory in quantum chemistry.* Reviews of Modern Physics, 2007. **79**(1): p. 291-352.
20. Sherrill, C.D. and H.F. Schaefer, *The configuration interaction method: Advances in highly correlated approaches*, in *Advances in quantum chemistry, vol 34*, P.O. Lowdin, et al., Editors. 1999. p. 143-269.
21. Andersson, K., et al., *2nd-order perturbation-theory with a casscf reference function.* Journal of Physical Chemistry, 1990. **94**(14): p. 5483-5488.
22. Andersson, K., P.A. Malmqvist, and B.O. Roos, *2nd-order perturbation-theory with a complete active space self-consistent field reference function.* Journal of Chemical Physics, 1992. **96**(2): p. 1218-1226.
23. Mahapatra, U.S., B. Datta, and D. Mukherjee, *A size-consistent state-specific multireference coupled cluster theory: Formal developments and molecular applications.* Journal of Chemical Physics, 1999. **110**(13): p. 6171-6188.
24. Pal, S., et al., *Multireference coupled-cluster methods using an incomplete model space - application to ionization-potentials and excitation-energies of formaldehyde.* Chemical Physics Letters, 1987. **137**(3): p. 273-278.
25. Pal, S., et al., *Molecular applications of multireference coupled-cluster methods using an incomplete model space - direct calculation of excitation-energies.* Journal of Chemical Physics, 1988. **88**(7): p. 4357-4366.

26. Kummel, S. and J.P. Perdew, *Two avenues to self-interaction correction within kohn-sham theory: Unitary invariance is the shortcut.* Molecular Physics, 2003. **101**(9): p. 1363-1368.
27. Grafenstein, J., E. Kraka, and D. Cremer, *The impact of the self-interaction error on the density functional theory description of dissociating radical cations: Ionic and covalent dissociation limits.* Journal of Chemical Physics, 2004. **120**(2): p. 524-539.
28. Polo, V., et al., *Long-range and short-range coulomb correlation effects as simulated by hartree-fock, local density approximation, and generalized gradient approximation exchange functionals.* Theoretical Chemistry Accounts, 2003. **109**(1): p. 22-35.
29. Perdew, J.P. and Y. Wang, *Accurate and simple analytic representation of the electron-gas correlation-energy.* Physical Review B, 1992. **45**(23): p. 13244-13249.
30. Wang, Y. and J.P. Perdew, *Spin scaling of the electron-gas correlation-energy in the high-density limit.* Physical Review B, 1991. **43**(11): p. 8911-8916.
31. Wang, Y. and J.P. Perdew, *Correlation hole of the spin-polarized electron-gas, with exact small-wave-vector and high-density scaling.* Physical Review B, 1991. **44**(24): p. 13298-13307.
32. Wang, Y., et al., *Exchange potentials in density-functional theory.* Physical Review A, 1990. **41**(1): p. 78-86.
33. Gunnarsson, O. and B.I. Lundqvist, *Exchange and correlation in atoms, molecules, and solids by spin-density functional formalism.* Physical Review B, 1976. **13**(10): p. 4274-4298.
34. Becke, A.D., *Density-functional exchange-energy approximation with correct asymptotic-behavior.* Physical Review A, 1988. **38**(6): p. 3098-3100.
35. Neese, F., T. Schwabe, and S. Grimme, *Analytic derivatives for perturbatively corrected "Double hybrid" Density functionals: Theory, implementation, and applications.* Journal of Chemical Physics, 2007. **126**(12).
36. Buhl, M. and H. Kabrede, *Geometries of transition-metal complexes from density-functional theory.* Journal of Chemical Theory and Computation, 2006. **2**(5): p. 1282-1290.
37. Buhl, M., et al., *Geometries of third-row transition-metal complexes from density-functional theory.* Journal of Chemical Theory and Computation, 2008. **4**(9): p. 1449-1459.
38. Pantazis, D.A., et al., *All-electron scalar relativistic basis sets for third-row transition metal atoms.* Journal of Chemical Theory and Computation, 2008. **4**(6): p. 908-919.
39. Neugebauer, J. and B.A. Hess, *Fundamental vibrational frequencies of small polyatomic molecules from density-functional calculations and vibrational perturbation theory.* Journal of Chemical Physics, 2003. **118**(16): p. 7215-7225.
40. Neese, F., *Prediction of electron paramagnetic resonance g values using coupled perturbed hartree-fock and kohn-sham theory.* Journal of Chemical Physics, 2001. **115**(24): p. 11080-11096.
41. Kaupp, M., et al., *Calculation of electronic g-tensors for transition metal complexes using hybrid density functionals and atomic meanfield spin-orbit operators.* Journal of Computational Chemistry, 2002. **23**(8): p. 794-803.
42. Sun, X.R., et al., *Omicron-iminobenzosemiquinonato(1-) and omicron-amidophenolato(2-) complexes of palladium(ii) and platinum(ii): A combined experimental and density functional theoretical study.* Inorganic Chemistry, 2002. **41**(16): p. 4295-4303.
43. Munzarova, M. and M. Kaupp, *A critical validation of density functional and coupled-cluster approaches for the calculation of epr hyperfine coupling constants in transition metal complexes.* Journal of Physical Chemistry A, 1999. **103**(48): p. 9966-9983.
44. Munzarova, M.L., P. Kubacek, and M. Kaupp, *Mechanisms of epr hyperfine coupling in transition metal complexes.* Journal of the American Chemical Society, 2000. **122**(48): p. 11900-11913.
45. Neese, F., *A critical evaluation of dft, including time-dependent dft, applied to bioinorganic chemistry.* Journal of Biological Inorganic Chemistry, 2006. **11**(6): p. 702-711.

2.2. Ligand Field Theory of Spin Hamiltonian parameters

2.2.1. Introduction to EPR spectroscopy

Early theoretical and experimental contributions to the field of Electron Paramagnetic Resonance (EPR) spectroscopy are usually associated with the names of Zavoisky, Gorter and van Vleck. After World War II, microwave technology became available, which fueled the research of magnetic phenomena. In 1952, the first spectra from organic compounds were reported and in the 1960 first EPR spectrometers became commercially available [1].

The magnetic moment associated with the electron spin is the fundamental physical observable relevant to EPR spectroscopy [2]. Pictorially speaking, the electron spin arises from the rotation of the electron about its axis. It was initially observed by Stern and Gerlach [1] in their infamous experiment, in which a beam of silver atoms in a magnetic field was split into two. The transitions between the non-degenerate energy levels of the electron spin in a magnetic field are investigated by EPR spectroscopy. EPR may yield a detailed picture of the electronic and geometric structure of paramagnetic the compound under investigation. This is in particular true since the magnetic moment of a single unpaired electron spin does not only interact with the applied magnetic field but also with the magnetic moments of nuclear spins and other unpaired electrons from which additional information can be extracted.

Spectroscopic studies on proteins are often hampered by the enormous multitude of signals stemming from the protein matrix. In contrast, EPR spectroscopy is a particularly useful technique in bioinorganic chemistry [3] since it allows for the selective investigation of the unpaired electron found in the active site of the enzyme.

In this chapter, an outline of the physical foundations of g-values and hyperfine coupling constants and a guideline to their calculation in the framework of Ligand Field Theory [4-5] is presented. Present-day DFT calculations use analytic derivative theory for the quantitative computation of magnetic properties [6]. However, a Ligand Field treatment can be very beneficial for a qualitative interpretation of Spin Hamiltonian parameters [6]. Since the computation and interpretation of magnetic properties is a major part of the present work, it seems justified to give an introduction to their theoretical foundations. This overview is based on an excellent in-depth description of the principles and concepts of Spin Hamiltonian parameters [5] (see there for an extensive collection of references).

2.2.2. The concept of the Spin Hamiltonian

EPR spectroscopists make use of a phenomenological Spin Hamiltonian, which is a powerful device in order to extract information from EPR spectra. The concept of the Spin Hamiltonian was introduced by Abragam and Pryce [7]. The Spin Hamiltonian in its common form reads:

$$H = \beta_e \vec{S}_p \cdot \hat{g} \cdot \vec{B}_0 + \sum_j \gamma_j \cdot \vec{I}_j \cdot \vec{B}_0 + \sum_j \vec{S}_p \cdot \hat{A}_j \cdot \vec{I}_j + \sum_j \vec{I}_j \cdot \hat{Q}_j \cdot \vec{I}_j + \sum_k \vec{S}_p \cdot \hat{D}_{pk} \cdot \vec{S}_k + \vec{S}_p \cdot \hat{D}_{pp} \cdot \vec{S}_p \quad \textbf{[1]}$$

This first term represent the electron Zeeman-interaction, i.e. the interaction of the electron spin S with the external magnetic field *B* via the anisotropic g-tensor. In molecular paramagnetic compounds, the g-tensor deviates to a varying degree from the free electron g-value $g_e \approx 2.0023$ due to the coupling of the electron spin to the orbital momentum. In addition, the nuclear Zeeman-interaction of the external magnetic field with the nuclear spin is represented by the second term of the Spin Hamiltonian in equation **[1]**. The electron spin *S* can furthermore couple to the nuclear spin *I* of the atoms in the paramagnetic compounds, which is described by the third term of the Spin Hamiltonian. The parameter of this hyperfine interaction is absorbed in the hyperfine coupling tensor A. The fourth them describes the zero-field splitting and only occurs in paramagnetic compounds with *S>1/2*, i.e. when more than one unpaired electron is present. It describes the magnetic interaction of the unpaired electrons and, as alluded to by its designation, is even observable when no external magnetic field is applied. Finally for nuclear spins with *I>1/2*, the fifth term, which represents the interaction of the electric field gradient with the quadrupole moment of the nucleus under investigation, can become non-zero.

The Spin Hamiltonian operates on the space spanned by the electron and nuclear spin functions of the system:

$$|SM, \mathbf{M}^{(I)}\rangle = |SM\rangle \otimes \prod_{A=1}^{N_A} |I^{(A)} M^{(A)}\rangle \quad \textbf{[2]}$$

The total dimension of this space can be readily obtained by:

$$\dim\left(\left\{|SM, \mathbf{M}^{(I)}\rangle\right\}\right) = (2S+1) \prod_{A=1}^{N_A} (2I^{(A)} + 1) \quad \textbf{[3]}$$

Evaluation of the matrix elements of the Spin Hamiltonian, in the basis spanned by the electron and nuclear spin functions, and subsequent diagonalization leads to the energy levels of the Spin

Hamiltonian, which allows for the extraction of the Spin Hamiltonian parameters from experimental spectra.

2.2.3. The underlying physics of the Spin Hamiltonian parameters

It is probably adequate to remind the reader that the spin Hamiltonian is a phenomenological device, which only operates on the electron and nuclear spin functions. Thus, the parameters in the Spin Hamiltonian, such as the g-tensor and the hyperfine coupling tensor, are no genuine physical observables but fitting-parameters, which facilitate the interpretation of EPR spectra. For the extraction of interpretable parameters from complex EPR spectra, the Spin Hamiltonian is a highly valuable tool. However, for an in-depth theoretical understanding how these parameters depend on the electron structure of the molecule under investigation it is required to study the dependence of the Spin Hamiltonian parameters on physical observables such as magnetic and electric fields.

The Born Oppenheimer Hamiltonian (chapter 2.1) includes the kinetic energies and the electrostatic interactions of the particles in a molecular system. The interactions included in the Born Oppenheimer Hamiltonian account for the major part of the electronic energy. However, smaller contributions are neglected, such as relativistic effects and interactions with magnetic and external electric fields. Usually the neglect of these effects does not introduce major errors but in some cases it is required to include them. Since the additional terms are small compared to the various contributions of the Born Oppenheimer Hamiltonian, they are normally treated by means of perturbation theory. Interactions with the magnetic moment of the electron spin are the origins of the parameters in the Spin Hamiltonian.

The fundamental equation for the coupling of the spin magnetic moment with an external magnetic field, equation **[4]**, and the corresponding relativistic correction term, equation **[5]**, read:

$$\begin{aligned}\hat{H}_{SB} &= \frac{\alpha g_e}{2}\sum_i \mathbf{B}\mathbf{s}_i \\ &= \frac{\alpha g_e}{2}\mathbf{B}\hat{\mathbf{S}}\end{aligned} \qquad \textbf{[4]}$$

$$\hat{H}_{SB}^{RMC} = \frac{\alpha^3 g_e}{2}\sum_i \nabla_i^2 \mathbf{B}\mathbf{s}_i \qquad \textbf{[5]}$$

The Spin orbit coupling (SOC) interaction reads:

$$\hat{H}_{SO} = \sum_A \sum_i \xi(r_{iA}) \mathbf{l}_i^A \mathbf{s}_i \qquad [6]$$

$$\xi(r_{iA}) = \frac{\alpha^2}{2} \frac{Z_{\text{eff}}^A}{r_{iA}^3}$$

Coupling of spin magnetic moments of more than one electron:

$$\hat{H}_{SS} = \frac{\alpha^2}{2} \sum_i \sum_{j \neq i} \frac{\mathbf{s}_i \mathbf{s}_j}{r_{ij}^3} - 3 \frac{(\mathbf{s}_i \mathbf{r}_{ij})(\mathbf{s}_j \mathbf{r}_{ij})}{r_{ij}^5} \qquad [7]$$

Coupling of electron and nuclear spin magnetic moments:

$$\hat{H}_{SI}^{(d)} = \frac{\alpha}{2} g_e \beta_N \sum_A g_N^{(A)} \sum_i \frac{\mathbf{s}_i \hat{\mathbf{I}}^{(A)}}{r_{iA}^3} - 3 \frac{(\mathbf{s}_i \mathbf{r}_{iA})(\hat{\mathbf{I}}^{(A)} \mathbf{r}_{iA})}{r_{iA}^5} \qquad [8]$$

$$\hat{H}_{SI}^{(c)} = \frac{\alpha}{2} \frac{8\pi}{3} g_e \beta_N \sum_A g_N^{(A)} \sum_i \mathbf{s}_i \hat{\mathbf{I}}^{(A)} \delta(r_{Ai}) \qquad [9]$$

$$\hat{H}_{LI} = \frac{\alpha}{2} \beta_N \sum_A g_N^{(A)} \sum_i \frac{\mathbf{l}_i^A \hat{\mathbf{I}}^{(A)}}{r_{iA}^3} \qquad [10]$$

With these perturbing operators, the zero-order wave function and the method of effective Hamiltonians [8-9], expressions for the parameters in the Spin Hamiltonian can be derived. The g-tensor becomes:

$$g_{\mu\nu}^{(OZ/SOC)} = -\frac{1}{S} \sum_{b(S_b=S)} \Delta_b^{-1} \left\{ \left\langle 0SS \middle| \sum_i l_{i\mu} \middle| bSS \right\rangle \left\langle bSS \middle| \sum_{i,A} \xi(r_{iA}) l_{i\nu}^A s_{iz} \middle| 0SS \right\rangle \right. \qquad [11]$$

$$\left. + \left\langle 0SS \middle| \sum_{i,A} \xi(r_{iA}) l_{i\mu}^A s_{iz} \middle| bSS \right\rangle \left\langle bSS \middle| \sum_i l_{i\nu} \middle| 0SS \right\rangle \right\}$$

The isotropic Fermi-contact term of the hyperfine tensor reads:

$$A_{\mu\nu}^{(A;c)} = \delta_{\mu\nu}\frac{8\pi}{3}\frac{\alpha}{2}\frac{1}{S}g_e\beta_N g_N^{(A)}\left\langle 0SS\left|\sum_i s_{zi}\delta(r_{iA})\right|0SS\right\rangle \quad \textbf{[12]}$$

The anisotropic dipolar contribution to hyperfine tensor reads:

$$A_{\mu\nu}^{(A;d)} = \frac{\alpha}{2}\frac{1}{S}g_e\beta_N g_N^{(A)}\left\langle 0SS\left|\sum_i s_{zi}r_{iA}^{-5}\{\delta_{\mu\nu}r_{iA}^2 - 3r_{iA,\mu}r_{iA,\nu}\}\right|0SS\right\rangle \quad \textbf{[13]}$$

Finally one obtains for the SOC term of the hyperfine tensor:

$$\begin{aligned} A_{\mu}^{(A;SO)} = & -\frac{\alpha}{2S}g_e\beta_N g_N^{(A)} \\ & \cdot\sum_{b(S_b=S)}\Delta_b^{-1}\left\{\left\langle 0SS\left|\sum_i l_{i\mu}^A r_{iA}^{-3}\right|bSS\right\rangle\left\langle bSS\left|\sum_{B,i}\xi(r_{iB})l_{iv}^B s_{zi}\right|0SS\right\rangle\right. \\ & \left.+\left\langle 0SS\left|\sum_{B,i}\xi(r_{iB})l_{i\mu}^B s_{zi}\right|bSS\right\rangle\left\langle bSS\left|\sum_i l_{iv}^A r_{iA}^{-3}\right|0SS\right\rangle\right\} \end{aligned} \quad \textbf{[14]}$$

With:

$$\Delta_b = \langle bSS|\hat{H}_{BO}|bSS\rangle - \langle 0SS|\hat{H}_{BO}|0SS\rangle \quad \textbf{[15]}$$

We represent the ground state of a system by a single determinant of total spin S:

$$|0SS\rangle = |\psi_1\overline{\psi}_1\psi_2\overline{\psi}_2\ldots\psi_n\overline{\psi}_n\psi_{o_1}\ldots\psi_{o_m}| \quad \textbf{[16]}$$

Excited states can be represented by single determinants derived from the ground state determinant by promotion of one or several electrons from singly or doubly occupied orbitals into empty orbitals. For the evaluation of the g-values and the hyperfine couplings it is sufficient to consider only the single configuration excited states which arise from the ground state determinant by promotion of an electron from a doubly occupied orbital into a singly occupied orbital as well as those which derive

from the ground state determinant by promotion of an electron from singly occupied orbital into an empty orbital:

$$|I_i^{o_j} SS\rangle = |\psi_1\overline{\psi}_1 \ldots \psi_i\overline{\psi}_{o_j} \ldots \psi_n\overline{\psi}_n\psi_{o_1} \ldots \psi_{o_m}| \quad \textbf{[17]}$$

$$|II_{o_i}^a SS\rangle = |\psi_1\overline{\psi}_1 \ldots \psi_n\overline{\psi}_n\psi_{o_1} \ldots \psi_a \ldots \psi_{o_m}| \quad \textbf{[18]}$$

The energy denominators which become important in the perturbation treatment are:

$$\begin{aligned}\Delta_{I_i^o} &= \varepsilon_O - \varepsilon_i - \langle\psi_i\psi_i|r_{12}^{-1}|\psi_o\psi_o\rangle + \langle\psi_o\psi_o|r_{12}^{-1}|\psi_o\psi_o\rangle \\ &\quad + \tfrac{1}{2}\langle\psi_i\psi_o|r_{12}^{-1}|\psi_i\psi_o\rangle\end{aligned} \quad \textbf{[19]}$$

$$\Delta_{II_o^a} = \varepsilon_a - \varepsilon_o - \langle\psi_o\psi_i|r_{12}^{-1}|\psi_a\psi_a\rangle + \langle\psi_o\psi_a|r_{12}^{-1}|\psi_o\psi_a\rangle \quad \textbf{[20]}$$

The matrix elements of the SOC operator can be obtained by application of the Wigner- Eckhard theorem [8-9]:

$$\left\langle 0SS\left|\sum_{A,i}\xi(r_{iA})l_{i,\mu}^A s_{0,i}\right|I_i^{o_j}SS\right\rangle = -\frac{1}{2}\left\langle\psi_i\left|\sum_A\xi(r_A)l_\mu^A\right|\psi_{o_j}\right\rangle \quad \textbf{[21]}$$

$$\left\langle 0SS\left|\sum_{A,i}\xi(r_{iA})l_{i,\mu}^A s_{0,\mu}\right|II_{o_i}^a SS\right\rangle = +\frac{1}{2}\left\langle\psi_{o_i}\left|\sum_A\xi(r_A)l_\mu^A\right|\psi_a\right\rangle \quad \textbf{[22]}$$

The g-tensor can then be expressed as:

$$g_{\mu\nu}^{(OZ/SOC)} = +\frac{1}{2S}\sum_{i(\text{doubly})}\sum_{o_j(\text{singly})}\Delta^{-1}_{I_i^{o_j}}\{\overline{L}_{2\mu}^{io_j}\overline{L}_{1\nu}^{io_j} + \overline{L}_{1\mu}^{io_j}\overline{L}_{2\nu}^{io_j}\}$$
$$-\frac{1}{2S}\sum_{a(\text{empty})}\sum_{o_j(\text{singly})}\Delta^{-1}_{II_{o_j}^{a}}\{\overline{L}_{2\mu}^{o_j a}\overline{L}_{1\nu}^{o_j a} + \overline{L}_{1\mu}^{o_j a}\overline{L}_{2\nu}^{o_j a}\} \quad \textbf{[23]}$$

For the isotropic and the dipole-dipole contributions to the hyperfine tensor one obtains:

$$A_{iso}^{(A)} = \frac{8\pi}{3}\frac{1}{2S}\frac{\alpha}{2}g_e\beta_N g_N^{(A)}\sum_{pq}P_{pq}^{\alpha-\beta}\langle\varphi_p|\delta(\mathbf{r}-\mathbf{R}_A)|\varphi_q\rangle$$
$$= \frac{4\pi}{3S}P^A\rho^{\alpha-\beta}(\mathbf{R}_A) \quad \textbf{[24]}$$

$$A_{\mu\nu}^{(A;d)} = \frac{1}{2S}P^A\sum_{pq}P_{pq}^{\alpha-\beta}\left\langle\varphi_p|r_A^{-5}\{\delta_{\mu\nu}r_A^2 - 3r_{A,\mu}r_{A,\nu}\}|\varphi_q\right\rangle \quad \textbf{[25]}$$

For convenience the constant factor P^A is introduced:

$$P^A = \frac{\alpha}{2}g_e\beta_N g_N^{(A)} \quad \textbf{[26]}$$

The SOC contribution to the hyperfine tensor is:

$$A_{\mu\nu}^{(A;SO1)} = \frac{1}{2S}P^A\left\{\sum_{i(\text{doubly})}\sum_{o_j(\text{singly})}\Delta^{-1}_{I_i^{o_j}}\{L_{3\mu}^{io_j}L_{1\nu}^{io_j} + L_{1\mu}^{io_j}L_{3\nu}^{io_j}\}\right.$$
$$\left. - \sum_{o_i(\text{singly})}\sum_{a(\text{empty})}\Delta^{-1}_{II_{o_i}^{a}}\{L_{3\mu}^{ao_i}L_{1\nu}^{ao_i} + L_{1\mu}^{ao_i}L_{3\nu}^{ao_i}\}\right\} \quad \textbf{[27]}$$

$$F_{\mu\nu;A}^{ij} = \left\langle\psi_i|r_A^{-5}\{\delta_{\mu\nu}r_A^2 - 3r_{A,\mu}r_{A,\nu}\}|\psi_j\right\rangle \quad \textbf{[28]}$$

A second SOC contribution to the hyperfine tensor, which shall not be discussed here in detail, arises from the cross term of the electron nuclear dipole-dipole interaction and the SOC operator.

2.2.4. Matrix elements over molecular orbitals

Depending on the system under investigation, the expressions for the Spin Hamiltonian parameters can become very complicated. In the following section, the equations for the Spin-Hamiltonian parameters are derived for transition metal ions, and it will become apparent how the corresponding

matrix elements can be simplified by approximations in the spirit of Ligand Field and Crystal Field Theory.

The matrix elements of the SOC operator read:

$$L_{1\mu}^{ij} = \mathrm{Im}\left(\left\langle \psi_i \middle| \sum_A \xi(r_A) l_\mu^A \middle| \psi_j \right\rangle\right) \qquad \textbf{[29]}$$

Here, the sum goes over all atoms of the transition metal complex. Since, the SOC constants for light atoms are fairly small, restriction of the sum to the metal only is a reasonable approximation. In addition, multi-centered integrals can be neglected, since their contributions to the matrix element are usually small due to the r^{-3} dependence of $\xi(r_A)$ and one obtains:

$$\begin{aligned} L_{1\mu}^{ij} &\approx c_{Mi} c_{Mj} \,\mathrm{Im}\left(\langle d_i | \xi(r_M) l_\mu^M | d_j \rangle\right) \\ &= c_{Mi} c_{Mj} \zeta_{ij} \,\mathrm{Im}\left(\langle d_i | l_\mu^M | d_j \rangle\right) \end{aligned} \qquad \textbf{[30]}$$

with:

$$\zeta_{ij} = \langle d_i | \xi(r_M) | d_j \rangle \qquad \textbf{[31]}$$

As further approximation, it is assumed that the metal d-orbitals feature the same radial function. In this case the SOC constant becomes independent of the type of d orbital.

$l_{A,x}$	s	p_z	p_x	p_y	d_{z^2}	d_{xz}	d_{yz}	$d_{x^2-y^2}$	d_{xy}
s									
p_z				i					
p_x									
p_y		$-i$							
d_{z^2}							$i\sqrt{3}$		
d_{xz}									i
d_{yz}					$-i\sqrt{3}$			$-i$	
$d_{x^2-y^2}$							i		
d_{xy}						$-i$			
$l_{A,y}$	s	p_z	p_x	p_y	d_{z^2}	d_{xz}	d_{yz}	$d_{x^2-y^2}$	d_{xy}
s									
p_z			$-i$						
p_x		i							
p_y									
d_{z^2}						$-i\sqrt{3}$			
d_{xz}					$i\sqrt{3}$			$-i$	
d_{yz}									$-i$
$d_{x^2-y^2}$						i			
d_{xy}							i		
$l_{A,z}$	s	p_z	p_x	p_y	d_{z^2}	d_{xz}	d_{yz}	$d_{x^2-y^2}$	d_{xy}
s									
p_z									
p_x				$-i$					
p_y			i						
d_{z^2}									
d_{xz}							$-i$		
d_{yz}						i			
$d_{x^2-y^2}$									$-2i$
d_{xy}								$2i$	

Table 1: Values of the one-center matrix elements of the angular momentum operator for s, p and d orbitals.

	2+	3+	4+	5+	6+
Sc	79				
Ti	118	153			
V	169	206	250		
Cr	229	274	319	376	
Mn	315	351	408	466	540
Fe	427	464	505	578	649
Co	533	619	656	700	
Ni	668	749	858	888	863
Cu	829	911	1009	1139	

Table 2: Empirically determined SOC constants [cm^{-1}] for first row transition metal ions [10].

In contrast to the SOC matrix elements, in the case of the orbital Zeeman matrix elements, the contributions, which arise from ligand orbitals cannot be neglected:

$$L_{2p}^{ij} = \mathrm{Im}\big(c_{Mi}c_{Mj}\langle d_i|l_p^M|d_j\rangle + c_{Mi}c_{Lj}\langle d_i|l_p^M|L_j\rangle + c_{Li}c_{Mj}\langle L_i|l_p^M|d_j\rangle + c_{Li}c_{Lj}\langle L_i|l_p^L - i(\mathbf{R}_{LM}\times\nabla)_p|L_J\rangle\big) \quad \textbf{[32]}$$

In order to avoid the evaluation of two-center integrals, the center of the angular momentum operator of the last term is shifted to the ligands at the expense of the introduction of an additional term:

$$\mathbf{l}^M = \mathbf{l}^L - i\mathbf{R}_{LM}\times\nabla \quad \textbf{[33]}$$

$$\mathbf{R}_{LM} = \mathbf{R}_L - \mathbf{R}_M$$

Even if the overlap of the metal d-orbitals with the ligand orbitals is neglected, the ligand-ligand term cannot be eliminated from the expression, which results in a reduction of the orbital Zeeman matrix element by 20%-25%. The contribution of the ligand-ligand term can be approximately taken into account by introduction of a factor ε_{ij} which in the limiting case of the crystal field becomes unity:

$$L_{2p}^{ij} \approx \mathrm{Im}\big(c_{Mi}c_{Mj}\langle d_i|l_p^M|d_j\rangle\varepsilon_{ij}^p\big) \quad \textbf{[34]}$$

An important influence on the SOC matrix elements arise from metal-ligand covalency. First, the more covalent the metal-ligand bonds of a complex are, the smaller becomes the factor $c_{Mj}c_{Mi}$ and, hence, also the SOC matrix element. This type of covalency has been termed “symmetry restricted covalency” since the symmetry of the complex determines which metal orbitals and ligand orbitals may interact. The covalency effects are usually anisotropic with $c_{Mj} \neq c_{Mi}$. In the limiting case of a crystal field, c_{Mi} becomes one and, hence, the SOC matrix elements are generally overestimated in the framework of Crystal Field Theory.

In addition to the “symmetry restricted covalency”, there is another covalency effect, termed “central field covalency”. When a transition metal ion is placed in a ligand field, the radial distribution functions of the metal d-orbitals may change in comparison to those of the free ion. This effect is in particularly strong for highly covalent bonds. An increase of the electron density leads to more diffuse radial distribution functions and, therefore, accounts for a decrease of the SOC constant of up to 20%. Like the “symmetry restricted covalency”, the “central field covalency” is usually anisotropic.

Due to the r^{-3} dependence of the nucleus-electron dipole-dipole operator, the matrix elements for the metal nucleus can be simplified by neglecting the contributions from the ligand orbitals:

$$\begin{aligned}&\langle\psi_i|r_M^{-5}\{\delta_{\mu\nu}r_M^2-3r_{M,\mu}r_{M,\nu}\}|\psi_j\rangle\\&\quad\approx c_{Mi}c_{Mj}\langle r^{-3}\rangle_d\langle d_i|\delta_{\mu\nu}-3r_M^{-2}r_{M,\mu}r_{M,\nu}|d_j\rangle\end{aligned}\qquad\textbf{[35]}$$

Analogously, the expression for the nucleus-electron dipole-dipole operator of the ligand nuclei reads:

$$\begin{aligned}&\langle\psi_i|r_L^{-5}\{\delta_{\mu\nu}r_L^2-3r_{L,\mu}r_{L,\nu}\}|\psi_j\rangle\\&\quad\approx c_{Li}c_{Lj}\langle r^{-3}\rangle_L\langle L_i|\delta_{\mu\nu}-3r_L^{-2}r_{L,\mu}r_{L,\nu}|L_j\rangle\end{aligned}\qquad\textbf{[36]}$$

Values of the one-center reduced field gradient integrals are found in Table 3.

f_{xx}	s	p_z	p_x	p_y	d_{z^2}	d_{xz}	d_{yz}	$d_{x^2-y^2}$	d_{xy}
s					$-\frac{1}{5}\sqrt{5}$			$\frac{1}{5}\sqrt{15}$	
p_z		$-\frac{2}{5}$							
p_x			$\frac{4}{5}$						
p_y				$-\frac{2}{5}$					
d_{z^2}	$-\frac{1}{5}\sqrt{5}$				$-\frac{2}{7}$			$-\frac{2}{7}\sqrt{3}$	
d_{xz}						$\frac{2}{7}$			
d_{yz}							$-\frac{4}{7}$		
$d_{x^2-y^2}$	$\frac{1}{5}\sqrt{15}$				$-\frac{2}{7}\sqrt{3}$			$\frac{2}{7}$	
d_{xy}									$\frac{2}{7}$

f_{yy}	s	p_z	p_x	p_y	d_{z^2}	d_{xz}	d_{yz}	$d_{x^2-y^2}$	d_{xy}
s					$-\frac{1}{5}\sqrt{5}$			$-\frac{1}{5}\sqrt{15}$	
p_z		$-\frac{2}{5}$							
p_x			$-\frac{2}{5}$						
p_y				$\frac{4}{5}$					
d_{z^2}	$-\frac{1}{5}\sqrt{5}$				$-\frac{2}{7}$			$\frac{2}{7}\sqrt{3}$	
d_{xz}						$-\frac{4}{7}$			
d_{yz}							$\frac{2}{7}$		
$d_{x^2-y^2}$	$-\frac{1}{5}\sqrt{15}$				$\frac{2}{7}\sqrt{3}$			$\frac{2}{7}$	
d_{xy}									$\frac{2}{7}$

f_{zz}	s	p_z	p_x	p_y	d_{z^2}	d_{xz}	d_{yz}	$d_{x^2-y^2}$	d_{xy}
s					$\frac{2}{5}\sqrt{5}$				
p_z		$\frac{4}{5}$							
p_x			$-\frac{2}{5}$						
p_y				$-\frac{2}{5}$					
d_{z^2}	$\frac{2}{5}\sqrt{5}$				$\frac{4}{7}$				
d_{xz}						$\frac{2}{7}$			
d_{yz}							$\frac{2}{7}$		
$d_{x^2-y^2}$								$-\frac{4}{7}$	
d_{xy}									$-\frac{4}{7}$

f_{xy}	s	p_z	p_x	p_y	d_{z^2}	d_{xz}	d_{yz}	$d_{x^2-y^2}$	d_{xy}
s									$\frac{1}{5}\sqrt{15}$
p_z				$\frac{3}{5}$					
p_x			$\frac{3}{5}$						
p_y									$-\frac{2}{7}\sqrt{3}$
d_{z^2}							$\frac{3}{7}$		
d_{xz}						$\frac{3}{7}$			
d_{yz}									
$d_{x^2-y^2}$									
d_{xy}	$\frac{1}{5}\sqrt{15}$				$-\frac{2}{7}\sqrt{3}$				

f_{xz}	s	p_z	p_x	p_y	d_{z^2}	d_{xz}	d_{yz}	$d_{x^2-y^2}$	d_{xy}
s						$\frac{1}{5}\sqrt{15}$			
p_z			$\frac{3}{5}$						
p_x		$\frac{3}{5}$							
p_y									
d_{z^2}						$\frac{1}{7}\sqrt{3}$			
d_{xz}	$\frac{1}{5}\sqrt{15}$				$\frac{1}{7}\sqrt{3}$			$\frac{3}{7}$	
d_{yz}									$\frac{3}{7}$
$d_{x^2-y^2}$						$\frac{3}{7}$			
d_{xy}							$\frac{3}{7}$		

f_{yz}	s	p_z	p_x	p_y	d_{z^2}	d_{xz}	d_{yz}	$d_{x^2-y^2}$	d_{xy}
s							$\frac{1}{5}\sqrt{15}$		
p_z				$\frac{3}{5}$					
p_x									
p_y		$\frac{3}{5}$							
d_{z^2}							$\frac{1}{7}\sqrt{3}$		
d_{xz}									$\frac{3}{7}$
d_{yz}	$\frac{1}{5}\sqrt{15}$				$\frac{1}{7}\sqrt{3}$			$-\frac{3}{7}$	
$d_{x^2-y^2}$							$-\frac{3}{7}$		
d_{xy}						$\frac{3}{7}$			

Table 3: Values of the one-center reduced field gradient integrals. The field gradient integrals can be obtained by multiplication with the corresponding matrix element of the r^{-3} operator.

2.2.5. Ligand field expression of the g-tensor

By combining the equation of the g-tensor, the SOC matrix elements and the orbital Zeeman matrix elements, we are now in the position to derive a ligand field expression of the g-tensor:

$$g_{\mu\nu} = \delta_{\mu\nu} g_e + \frac{1}{2S} \sum_i \sum_j \Delta_{ij}^{-1} c_{Mi}^2 c_{Mj}^2 \zeta_{ij} \left\{ \langle d_i | l_\mu^M | d_j \rangle \varepsilon_{ij}^\mu \langle d_j | l_\nu^M | d_i \rangle + \langle d_i | l_\mu^M | d_j \rangle \varepsilon_{ji}^\nu \langle d_j | l_\nu^M | d_i \rangle \right\} \quad \textbf{[37]}$$

In the case the index i refers to an empty orbital, the negative sign is absorbed in the factors ε_{ij}.

The expression for the g-tensor can be further simplified by neglecting ligand interactions and by absorption of the c_{Mi} and c_{Mj} orbital coefficients into the effective SOC constant:

$$g_{\mu\nu} = \delta_{\mu\nu} g_e + \frac{\overline{\zeta}_{\text{eff}}}{S} \sum_i \sum_j \Delta_{ij}^{-1} (-1)^{p_{ij}} \langle d_i | l_\mu^M | d_j \rangle \langle d_j | l_\nu^M | d_i \rangle \quad \textbf{[38]}$$

The phase factor p_{ij} becomes unity if orbital *i* is doubly occupied and zero if orbital *i* is empty. By using equation **[37]** with the data from Table 2 and Table 1, one can obtain the g-tensor in the framework of ligand-field theory. Expression **[37]** is analogous to the well-known ligand field expression for the g-tensor [1]:

$$g_{\mu\nu}^{LFT} = \delta_{\mu\nu} g_e - 2\lambda \sum_n \frac{\langle 0|L_\mu|n\rangle\langle n|L_\nu|0\rangle}{E_n - E_0} \qquad \textbf{[39]}$$

2.2.6. Ligand field expression of the A-tensor

The Ligand Field expression for the anisotropic electron-nuclear dipole-dipole interaction becomes:

$$A_{\mu\nu}^{(A;d)} = \frac{1}{2S} P_d \sum_i c_{Mi}^2 \langle d_i | f_{\mu\nu} | d_i \rangle \qquad \textbf{[40]}$$

$$P_d = \frac{\alpha}{2} g_e \beta_N g_N^{(A)} \langle r_M^{-3} \rangle_d \qquad \textbf{[41]}$$

The corresponding ligand field expression for the SOC contribution reads:

$$A_{\mu\nu}^{(M;SO)} = \frac{1}{S} P_d \sum_i \sum_j \Delta_{ij}^{-1} (-1)^{p_{ij}} c_{Mi}^2 c_{Mj}^2 \zeta_{ij} \langle d_i | l_\mu^M | d_j \rangle \langle d_j | l_\nu^M | d_i \rangle \qquad \textbf{[42]}$$

The important relation between the SOC contribution to the hyperfine coupling constant and the g-value is then readily identified:

$$A_{\mu\nu}^{(M;SO1)} = P_d \Delta g_{\mu\nu} \qquad \textbf{[43]}$$

The second SOC contribution to hyperfine coupling constants is not be discussed here but is described elsewhere [5].

References

1. Atherton, N., *Principles of electron spin resonance*. 2nd ed., E. Horwood. 1993, New York: Prentice-Hall.
2. Abragam, A. and B. Bleaney, *Electron paramagnetic resonance of transition ions*. 1970, Oxford: Clarendon.
3. Prisner, T., M. Rohrer, and F. MacMillan, *Pulsed epr spectroscopy: Biological applications.* Annual Review of Physical Chemistry, 2001. **52**: p. 279-313.
4. Ballhausen, C.J., *Introduction to ligand field theory*. 1962., NewYork: McGraw-Hill.
5. Neese, F. and E. Solomon, *Interpretation and calculation of spin-hamiltonian parameters in transition metal complexes*, in *Magnetism: Molecules to materials iv*, J.S. Miller and M. Drillon, Editors. 2002, Wiley-VCH p. 345.
6. Neese, F., *Prediction of molecular properties and molecular spectroscopy with density functional theory: From fundamental theory to exchange-coupling.* Coordination Chemistry Reviews, 2009. **253**(5-6): p. 526-563.
7. Pryce, M.H.L., *A modified perturbation procedure for a problem in paramagnetism.* Proceedings of the Physical Society of London Section A, 1950. **63**(361): p. 25-29.
8. McWeeny, *Methods of molecular quantum mechanics*. 1992, London: Academic Press.
9. McWeeny, R., *Spins in chemistry*. 1970, New York: Academic Press.
10. Bendix, J., M. Brorson, and C.E. Schaffer, *Accurate empirical spin-orbit-coupling parameters zeta(nd) for gaseous nd(q) transition-metal ions - the parametrical multiplet term model.* Inorganic Chemistry, 1993. **32**(13): p. 2838-2849.

3. Computational details

3.1. Computational Details

All calculations were performed with the ORCA program package [1]. Geometry optimizations and IR spectra were calculated with the BP86 GGA functional [2-3] given its excellent performance in these areas [4-5]. For the computation of magnetic properties and energies, the hybrid functional B3LYP [6-7] was used owing to its documented good performance in this area [8-9]. The energies of two–dimensional relaxed surface scans were calculated with the BP86 functional for technical reasons. Furthermore, in some cases, properties were computed additionally with the BP86 for comparison with the B3LYP results or for computational reasons. For the same reasons, some were obtained not only with BP86 but also with B3LYP (this is indicated in the respective sections). IR frequency calculations were performed with the BP86 functional.

In the property calculations, the def2–TZVP(–f) basis set [10] was chosen for Ni and Fe and the complete first coordination sphere, which includes all cysteine sulfur atoms as well as the two CN^- and the CO ligand, while a def2–TZVP basis set was used for geometry optimization. For all other atoms, the def2–SV(P) basis sets was employed for geometry optimization and the def2–SVP for the calculation of spectroscopic properties. The def2-SPV/J auxiliary basis set was used in conjunction with the RI [11] approximation and the def2-SPV/J and def2-SVP/C auxiliary basis sets were used with the RIJCOSX [12] approximation in all calculations. Scalar relativistic effects were taken in account in the form of the ZORA approximation [13-14] together with the scalar relativistic recontractions of the def2–basis sets [10]. Except for the calculation of IR–spectra, the COSMO model [15] was used with a dielectric constant of $\varepsilon = 4$, since the use of the COSMO model for vibrational frequency calculations is discouraged by its developer. Central diff was switched off in the IR frequency calculations. For magnetic properties, the picture change was used. Grimme's van der Waals correction VDW06 [16], sometimes called DFT–D2, was employed in all calculations. TightSCF (energy change 10^{-8} E_h) was used as convergence criterion for both, property calculations and geometry optimizations. An integration grid of 4 was chosen. For orbital plots of open–shell systems, quasi–restricted orbitals were employed [17]. As an exception, in the computational treatment of the Ni–L state (chapter 4.3), also magnetic properties and energies were calculated using the BP86 functional due to significant spin contamination when the B3LYP functional was employed. The computational details for the calculation of the synthetic Ni^{3+} models (chapter 4.1) are equivalent to those of the cluster models of [NiFe] hydrogenase. However, in line with the experimental conditions, as COSMO solvent DMF ($\varepsilon = 38$) and as basis set def2–TZVP(–f) was used in geometry optimizations and property calculations. Please note that if for single calculations the methods applied deviate from those given here, this is indicated in the respective sections.

3.2. Cluster Models

The largest cluster model system was constructed from the X–Ray structure of reduced *D. vulgaris* Miyazaki F hydrogenase (pdb: 1H2R) [18]. Consequently, *D. vulgaris* Miyazaki F numbering of amino acids is used consistently throughout this manuscript. The model contains the two metal atoms, a variable bridging ligand, the two CN^- and CO ligands bound to Fe and the four nickel–coordinating cysteines modeled as ethylthiolates. The cysteine residues form a distorted square pyramid at the nickel. Cys549 is found in the apical position whereas Cys84, Cy81 and Cys546 are equatorially coordinated. The terminal nickel coordination site opposite to Cys546 is, in addition to the bridging position between the two metals, the second coordination site for a variable ligand of which the nature depends on the redox state. The model additionally includes the complete second coordination sphere consisting of the residues Glu34, Val83, His88, Asp123, Pro476, Ala477, Arg479, Leu482, Val500, Pro501 and Ser502 (Figure 1). His88 was modeled as imidazole. The amino acids were truncated at a distance larger than 4 Å of the $[NiFeS_4(CO)(CN)_2]$ core, whereby functional groups, e.g., carboxyl groups were retained. The truncated amino acids were saturated with hydrogen atoms. These added hydrogen atoms and the atoms to which they are bound were constrained in the geometry optimization. In this way, the models are balanced such that the restraining influence of residual protein interactions is included by the constraints and the inner region retains sufficient flexibility. The constraints are highlighted with an asterisk in Figure 2.

Glu34 was modeled as propionic acid since it is positioned adjacent to the negatively charged Cys546 which renders the corresponding carboxyl group markedly basic. In agreement with the X–Ray structure, Glu34 forms a hydrogen–bond with the amid–hydrogen of Ala548 in the protein back–bone.

The histidine residue His88 is in hydrogen bonding distance to Cys549 and may give rise to a large effect on the geometric and electronic structure of the [NiFe] center [19]. His88 may exist in three possible protonation and hydrogen–bonding states. The protonation states of His88 were examined by three models called HisHδ, HisHε and HisHδHε, depending on whether the delta, the epsilon or both nitrogen atoms are protonated. Protonation of the ε nitrogen atom results in the formation of a hydrogen bond Hε(His88)$\cdots$Sγ(Cys549).

In chapter 4.2., geometries and spectroscopic parameters were computed with the HisHδ, HisHε and HisHδHε models for the experimentally well–characterized and less controversial Ni–C state, and were compared to a large body of experimental data in order to assess the reliability of the larger cluster model and identify the protonation state of His88. As result of this study, the overall agreement of the HisHε model with experiment is good to excellent and, hence, the HisHε cluster

model is suitable for further computational investigation of the [NiFe] hydrogenase. Please note that, generally, if it is stated that "…the agreement of the calculations with experiment is excellent…", or the like, it is *not* meant that there is a one–to–one numerical correspondence of the calculated with the experimental values, but rather that quantitative agreement is given within the accuracy of the respective experimental and theoretical methods.

How the cluster models for the different redox–states derive from the HisHε model is described in the respective chapters. In addition to the large cluster model, in some cases, a small cluster models is used. The small model includes, in addition to the two metals, only residues of the first coordination shell, i.e. the four cysteines, one or two variable ligands and the diatomic Fe–bound ligands.

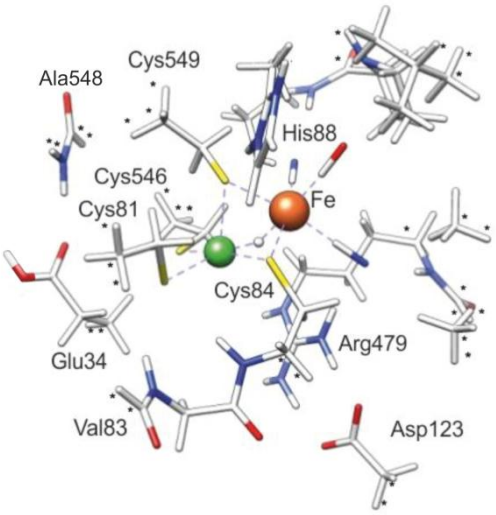

Figure 1. HisHδHε cluster model of [NiFe] hydrogenase. Color code: oxygen (red), nitrogen (blue), sulfur (yellow), nickel (green) and iron (brown). Asterisks indicate the atoms that were constrained during the geometry optimization (see also Figure 2). For clarity, the asterisks at (CH)γ and Nε of His88 have been omitted.

References

1. Neese, F., *Orca, an ab initio, dft and semiempirical scf-mo package*. 2011: University of Bonn.
2. Becke, A.D., *Density-functional exchange-energy approximation with correct asymptotic-behavior.* Physical Review A: Atomic, Molecular, and Optical Physics, 1988. **38**(6): p. 3098-3100.
3. Perdew, J.P., *Density-functional approximation for the correlation-energy of the inhomogeneous electron-gas.* Physical Review B: Condensed Matter, 1986. **33**(12): p. 8822-8824.
4. Buehl, M. and H. Kabrede, *Geometries of transition-metal complexes from density-functional theory.* Journal of Chemical Theory and Computation, 2006. **2**(5): p. 1282-1290.
5. Buehl, M., et al., *Geometries of third-row transition-metal complexes from density-functional theory.* Journal of Chemical Theory and Computation, 2008. **4**(9): p. 1449-1459.
6. Becke, A.D., *Density-functional thermochemistry .3. The role of exact exchange.* Journal of Chemical Physics, 1993. **98**(7): p. 5648-5652.
7. Lee, C.T., W.T. Yang, and R.G. Parr, *Development of the colle-salvetti correlation-energy formula into a functional of the electron-density.* Physical Review B: Condensed Matter, 1988. **37**(2): p. 785-789.
8. Neese, F., *Prediction of electron paramagnetic resonance g values using coupled perturbed hartree-fock and kohn-sham theory.* Journal of Chemical Physics, 2001. **115**(24): p. 11080-11096.
9. Neese, F., *Metal and ligand hyperfine couplings in transition metal complexes: The effect of spin-orbit coupling as studied by coupled perturbed kohn-sham theory.* Journal of Chemical Physics, 2003. **118**(9): p. 3939-3948.
10. Weigend, F. and R. Ahlrichs, *Balanced basis sets of split valence, triple zeta valence and quadruple zeta valence quality for h to rn: Design and assessment of accuracy.* Physical Chemistry Chemical Physics, 2005. **7**(18): p. 3297-3305.
11. Eichkorn, K., et al., *Auxiliary basis sets for main row atoms and transition metals and their use to approximate coulomb potentials.* Theoretical Chemistry Accounts, 1997. **97**(1-4): p. 119-124.
12. Neese, F., et al., *Efficient, approximate and parallel hartree-fock and hybrid dft calculations. A 'chain-of-spheres' algorithm for the hartree-fock exchange.* Chemical Physics, 2009. **356**(1-3): p. 98-109.
13. van Lenthe, E., A. van der Avoird, and P.E.S. Wormer, *Density functional calculations of molecular hyperfine interactions in the zero order regular approximation for relativistic effects.* Journal of Chemical Physics, 1998. **108**(12): p. 4783-4796.
14. van Lenthe, E., J.G. Snijders, and E.J. Baerends, *The zero-order regular approximation for relativistic effects: The effect of spin-orbit coupling in closed shell molecules.* Journal of Chemical Physics, 1996. **105**(15): p. 6505-6516.
15. Klamt, A. and G. Schuurmann, *Cosmo - a new approach to dielectric screening in solvents with explicit expressions for the screening energy and its gradient.* Journal of the Chemical Society, Perkin Transactions 2: Physical Organic Chemistry, 1993(5): p. 799-805.
16. Grimme, S., *Semiempirical gga-type density functional constructed with a long-range dispersion correction.* Journal of Computational Chemistry, 2006. **27**(15): p. 1787-1799.
17. Neese, F., *Importance of direct spin-spin coupling and spin-flip excitations for the zero-field splittings of transition metal complexes: A case study.* Journal of the American Chemical Society, 2006. **128**(31): p. 10213-10222.
18. Higuchi, Y., et al., *Removal of the bridging ligand atom at the ni-fe active site of nife hydrogenase upon reduction with h-2, as revealed by x-ray structure analysis at 1.4 angstrom resolution.* Structure with Folding & Design, 1999. **7**(5): p. 549-556.
19. Agrawal, A.G., et al., *Hydrogen bonding affects the [nife] active site of desulfo vibrio vulgaris miyazaki f hydrogenase: A hyperfine sublevel correlation spectroscopy and density functional theory study.* Journal of Physical Chemistry B, 2006. **110**(15): p. 8142-8150.

Appendix

Cartesian coordinates of the HisHε model:

C	61.346317	52.681264	85.215321
N	60.501766	51.733959	84.706077
C	60.866000	53.302000	83.195000
N	61.601146	53.652037	84.344686
C	60.183609	52.111130	83.417774
H	61.735171	52.620737	86.237124
H	60.827600	53.911400	82.292100
H	59.506513	51.512728	82.801899
H	60.198372	50.859183	85.174455
O	59.042228	49.837104	94.502694
C	58.938426	50.008279	93.276942
N	59.213910	49.026338	92.374936
C	59.558000	47.663000	92.808000
C	59.687172	46.718824	91.601106
O	58.444556	46.402293	91.004777
H	60.475300	47.675100	93.396600
H	59.004317	49.190512	91.378527
H	58.759029	47.277076	93.477099
H	60.388256	47.172778	90.860270
H	60.145618	45.771817	91.954628
H	58.187663	47.192254	90.441057
C	57.164567	52.487642	90.933134
C	58.632240	53.004741	91.013040
H	56.935964	52.129172	89.912507
H	56.445393	53.291895	91.180917
H	59.070346	53.205558	90.015944
H	58.664059	53.963706	91.597366
C	58.462591	51.364471	92.702638
C	57.098216	51.305724	91.951541
H	56.241339	51.377774	92.648979
H	57.028835	50.345117	91.405410
H	58.366047	52.027331	93.602612
N	59.312000	51.906000	91.662000
H	60.368000	51.944500	91.830000
H	53.351200	53.946000	87.696000
C	54.303000	53.479000	87.443000
H	54.259620	52.391277	87.634208
H	55.121493	53.926619	88.040895
H	54.514010	53.634052	86.367398
H	57.957000	40.978700	85.112900
C	57.780000	42.015000	84.825000
H	56.770881	42.110002	84.382498
H	57.833473	42.663765	85.718577
C	58.828518	42.500495	83.749386
C	60.360400	42.353700	83.952800
O	61.022804	42.511486	82.785693
O	60.930963	42.171019	85.020817
H	58.694062	43.600900	83.619270
H	58.595133	42.054168	82.761213
N	54.337658	45.832358	87.572800
C	53.518873	46.179180	86.538628
N	52.806448	45.224261	85.898160
N	52.536097	50.258390	89.361951
C	54.905958	46.809908	88.508610
N	53.426805	47.443247	86.120877
H	50.792100	50.894800	88.466500
C	51.179000	50.370000	89.340000
H	53.090567	50.460604	88.514128
H	53.926460	48.205981	86.601206
H	52.639472	47.705233	85.435313
H	52.727181	44.314300	86.351243
H	51.976483	45.536592	85.291918
H	54.307409	44.859093	87.869137
O	50.416801	50.007821	90.247207
C	53.254931	49.715086	90.518963
C	54.369572	48.731785	90.123933
C	53.823011	47.553885	89.306230
H	55.139064	49.262950	89.532580
H	54.871714	48.378354	91.047840
H	53.281140	46.838069	89.961419
H	53.080487	47.950950	88.586517
H	52.496412	49.223285	91.158870
H	53.694051	50.550616	91.107042
H	55.597294	46.264381	89.176149
H	55.534198	47.527123	87.946175
H	58.527700	56.124000	89.748600
C	58.245000	55.782000	88.753000
C	59.366691	55.870545	87.708473
C	60.605397	55.079040	88.161070
C	58.879795	55.360820	86.339102
H	57.365111	56.377992	88.429019
H	57.905640	54.729000	88.848792
H	61.419742	55.145185	87.410179
H	60.338918	54.007187	88.276876
H	60.989510	55.444431	89.136699
H	59.698102	55.382459	85.590085
H	58.031584	55.971164	85.963567
H	58.538296	54.310234	86.424997
H	59.629800	56.942400	87.595100
H	61.512900	51.424400	89.525100
C	61.182000	50.392000	89.638000
H	61.883817	49.732398	89.090935
H	61.161582	50.110626	90.706599
H	60.157554	50.284575	89.240048
C	60.586000	47.650000	81.309000
H	59.840300	47.712400	80.516500
C	59.920248	47.866577	82.674641
N	55.333305	47.738789	82.222749
C	55.010000	49.125000	82.529000
H	55.548900	49.718100	81.790100
C	55.397516	49.447125	83.984255
H	58.215600	43.795400	89.277400
C	58.668000	44.022000	88.312000
H	59.743400	44.121200	88.459700
C	58.011152	45.276943	87.698302
H	62.366400	46.821300	86.378800

C	62.194000	47.818000	86.785000
C	60.690729	47.937454	87.172438
H	61.417700	48.351700	81.245100
C	54.524478	46.949941	81.469694
O	53.370477	47.234919	81.137034
H	62.819700	47.958500	87.666400
H	55.064087	50.463409	84.267632
H	54.893616	48.730036	84.654065
H	56.305155	47.444173	82.411365
H	56.909458	45.202899	87.773907
H	58.311898	46.187400	88.252290
H	60.682143	47.835742	83.475285
H	59.450366	48.868715	82.724470
H	58.512113	43.139610	87.656663
H	61.021002	46.628101	81.260049
H	62.490500	48.578625	86.034344
H	60.243360	46.941420	87.335823
H	60.537379	48.520390	88.092120
H	53.919444	49.255115	82.398605
H	57.691100	46.389200	78.833300
C	56.680000	46.232000	79.209000
O	55.728768	46.397131	78.436397
N	56.539249	45.792364	80.499832
H	57.337798	45.875324	81.150233
C	55.190000	45.620000	81.069000
H	55.208100	44.957400	81.934300
H	54.545655	45.169213	80.293961
H	51.607500	52.069600	87.183000
H	50.860200	51.339200	85.846100
C	51.735000	51.934000	86.109000
H	51.740813	52.908573	85.587029
H	52.660297	51.359625	85.920036
H	62.661100	43.246700	88.234600
C	63.313000	43.793000	87.553000
O	64.349769	44.296726	88.009504
N	62.922000	43.888000	86.287000
H	63.497000	44.457200	85.556600
H	62.090792	43.390008	85.936881
S	58.647361	46.612307	83.101541
S	57.216990	49.404851	84.336881
S	58.438821	45.436494	85.913866
S	59.680310	48.762083	85.877472
Ni	57.955106	47.395084	85.096645
Fe	57.589173	49.401906	86.606643
C	57.990744	51.032960	87.044868
C	57.890971	48.889205	88.373145
O	58.265351	52.104621	87.418996
N	58.086930	48.606372	89.499253
H	57.170956	47.743814	86.442475
C	55.783795	49.749116	86.964373
N	54.649859	49.987095	87.182324
H	48.470800	47.038700	83.361400
C	49.117000	47.792000	83.812000
C	50.463216	47.250057	84.342939
O	50.560247	45.998887	84.552942
O	51.349099	48.126066	84.570676
H	49.309710	48.601745	83.080303
H	48.570827	48.253744	84.662158
H	61.986743	42.472623	82.983093

Constraints

The following atoms were constraint during the geometry optimizations of the HisHε model.

2, 12, 32, 35, 40, 56, 76, 90, 94, 98, 102, 106, 126, 130, 135, 139, 141, 158, 44, 6, 3, 15, 33, 34, 39, 55, 75, 88, 89, 95, 99, 101, 103, 105, 108, 111, 125, 131, 133, 134, 138, 142, 157

4.1. Synthetic nickel d^7 complexes

The performance of Density Functional Theory in geometry, electronic structure and magnetic property calculations

Abstract

In the present DFT–study, we have examined various paramagnetic nickel 3+ complexes. We demonstrate that some of the complexes feature pronouncedly different electronic structures even if they exhibit similar coordination geometries at the nickel center. For some of the nickel complexes the computed magnetic properties are in excellent agreement with experiment while for other nickel 3+ complexes it becomes evident that DFT cannot be employed for the reliable computation of magnetic properties. In the context of a rising interest in biomimetic catalysts based on the H_2–producing enzyme [NiFe] hydrogenase, new paramagnetic nickel 3+ complexes are likely to evolve in the upcoming years. The present study demonstrates that the application of DFT to such nickel complexes as a black–box procedure, for example with the intention to back experimental characterizations, has to be done with care.

4.1.1. Introduction

Nickel has been identified in the active sites of various transition metal enzymes [1-2], such as the H_2–producing enzyme [NiFe] hydrogenase. In this enzyme, nickel is the redox–active metal center [3-4] of the highly sophisticated bimetallic active site, where it is coordinated by four cysteines residues [5-6]. In the several redox–states [7-8] of the enzyme, the nickel is present in a diamagnetic divalent or paramagnetic trivalent oxidation state. In times of dwindling non–renewable energy resources, H_2 has been envisaged as future energy source [9-10]. Efforts are made to design synthetic compounds which mimic the active site of [NiFe] hydrogenases (for reviews see [11] and [12]). Detailed insights into the geometric and, in particular, the electronic structure of synthetic nickel complexes is of preeminent importance, for an understanding of the factors that govern biochemical H_2 synthesis in [NiFe] hydrogenase enzymes as well as for the design of biomimetic catalysts.

The paramagnetic nickel dithiolene complex $[Ni^{III}(mnt)_2]^-$ is certainly among the best characterized synthetic Ni^{3+} complexes. Maki and Edelstein reported the g–tensor and the orientation of its principal axis obtained by EPR measurements of $[Ni^{III}(mnt)_2]^-$ single crystals [13]. In the same contribution, the ^{61}Ni hyperfine coupling tensor was reported as determined by measurements of isotopically labeled $[Ni^{III}(mnt)_2]^-$ single crystals. Schmitt and Maki investigated the principal values of ^{33}S hyperfine coupling tensors form natural abundance ^{33}S satellites [14]. In a detailed ENDOR and ESEEM study [15], Huyett *el al.* focused on the atoms outside of the $[NiS_4]$ core and reported anisotropic and isotropic hyperfine coupling constants for the two non–equivalent carbon atoms and the N atom of the mnt^{2-} ligand. Density functional studies of $[Ni^{III}(mnt)_2]^-$ were performed by Stein *et al.* in 2001 and by Stadler and co–workers in 2002 [16-17]. In both studies, geometries and EPR parameters were calculated and compared to experiment. At the time, it was not yet possible to perform computations of hyperfine couplings by an unrestricted scalar-relativistic approach including spin orbit coupling (SOC), and hence Stein employed a ROKS approach for the anisotropic contributions in order to incorporate the SOC. Neese [18] calculated the ^{61}Ni hyperfine coupling of the complex in the context of more general study of metal and ligand hyperfine couplings using an unrestricted non-relativistic approach.

In addition to $[Ni^{III}(mnt)_2]^-$, other threevalent nickel complexes with a square planar coordination geometry were reported [19-22]. These complexes contain polydentate thiolate, alkoxyl and amidate chelate ligands. Krüger *et al.* [20] and Hanss *et al.* [22] reported the formation of monoadducts to some of the square planar complexes resulting in a square pyramidal coordination geometry similar to that found for the nickel center some paramagnetic states of [NiFe] hydrogenases [8].

The present DFT–study is similar to the contributions by Stein and Stadler [16-17], who investigated $[Ni^{III}(mnt)_2]^-$. We reevaluated the magnetic properties of $[Ni^{III}(mnt)_2]^-$ by explicitly including spin orbit coupling in the relativistic calculations of $[Ni^{III}(mnt)_2]^-$. The calculated properties of the complex are in an overall very good agreement with experiment. In addition to $[Ni^{III}(mnt)_2]^-$, six other paramagnetic nickel 3+ complexes have been studied (Figure 1). By careful examination of the respective electronic structures and comparison of computed magnetic parameters with experiment, we show for the various nickel complexes that DFT calculations of the electronic structure and magnetic parameters of Ni^{3+} complexes are not in general as reliable as for $[Ni^{III}(mnt)_2]^-$.

Ni^{III} complexes

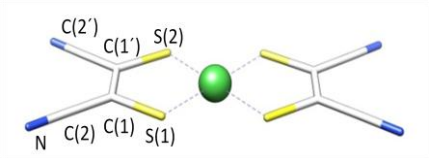

$[Ni^{III}(mnt)_2]^-$

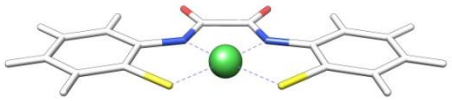

$[Ni^{III}(emb)]^-$

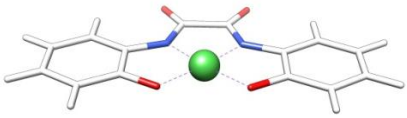

$[Ni^{III}(ehb)]^-$

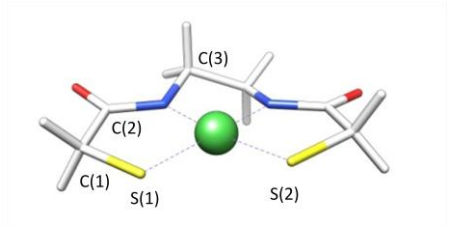

$[Ni^{III}(ema)^-]$

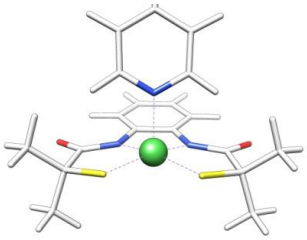

$[Ni^{III}(phmi)(py)]^-$

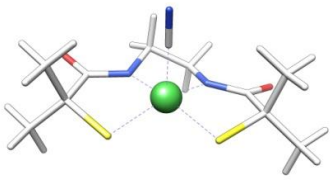

$[Ni^{III}(emi)(CN)]^{2-}$

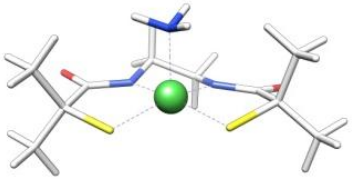

$[Ni^{III}(emi)(NH_3)]^-$

Figure 1: Nickel 3+ complexes: $[Ni^{III}(mnt)_2]^-$, $[Ni^{III}(emb)]^-$, $[Ni^{III}(ehb)]^-$, $[Ni^{III}(ema)]^-$ (square planar) and $[Ni^{III}(phmi)(py)]^-$, $[Ni^{III}(emi)(CN)]^{2-}$ and $[Ni^{III}(emi)(NH_3)]^-$ (square pyramidal). Color code: carbon and hydrogen (white), nitrogen (blue), sulfur (yellow), oxygen (red), nickel (green).

	$Ni^{III}(mnt)_2]^-$	$[Ni^{III}(emb)]^-$	$[Ni^{III}(ehb)]^-$	$[Ni^{III}(ema)]^-$
basis funct.	465	603	593	403
spin cont.	0.01	0.03	0.01	0.01
charge	–1	–1	–1	–1
multiplicity	2	2	2	2

	$[Ni^{III}(phmi)(py)]^-$	$[Ni^{III}(emi)(CN)]^{2-}$	$[Ni^{III}(emi)(NH_3)]^-$
basis funct.	831	601	594
spin cont.	0.03	0.02	0.02
charge	–1	–2	–1
multiplicity	2	2	2

Table 1: The number of contracted basis functions, spin contamination, charge and multiplicity.

The number of contracted basis functions, spin contamination, charge and multiplicity of the Ni^{III} complexes (Figure 1) investigated in the presented study are collected in Table 1. All complexes feature a doublet spin state and a charge of –1 (except for $[Ni^{III}(emi)(CN)]^{2-}$). The spin contamination given in the table is the difference of the actual expectation value of the $\mathbf{S}^2$ operator and the eigenvalue of a pure doublet state, which amounts to 0.75. The spin contaminations are small and do not exceed a value of 0.03.

4.1.2. Geometries

angle [°]	calc.	X–Ray	distance [Å]	calc.	X–Ray
S(1)–Ni–N	89.3	88.4	Ni–N	1.86	1.86
S(1)–Ni–S(2)	85.8	85.6	Ni–S	2.16	2.18
Ni–N–C(2)	124.8	125.4	S(1)–C(1)	1.84	1.81
C(3)–N–Ni	114.7	116.6	C(1)–C(2)	1.52	1.52
C(1)–S(1)–Ni	98.7	98.1	N–C(2)	1.35	1.32
C(2)–C(1)–S(1)	112.8	113.5	N–C(3)	1.47	1.46
C(3)–N–C(2´)	119.8	118	C(3)–C(3´)	1.53	1.50
O–C(2)–N	125.0	126.5	O–C(2)	1.257	1.25
O–C(2)–C(1)	120.9	119			

a

angle [°]	calc.	X–Ray	distance [Å]	calc.	X–Ray
Ni–S(1)–S(2)	92.2	92.5	Ni–S	2.16	2.15
Ni–S(1)–C(1)	104.0	103.0	S(1)–C(1)	1.74	1.72
S–C(1)–C(1´)	119.9	120.0	C(1)–C(1´)	1.39	1.37
C(1)–C(1´)–C(2´)	122.5	121.0	C(1)–C(2)	1.42	1.44
C(1)–C(2)–N	179.02	179.0	C(2)–N	1.17	1.13

Table 2: bond angles [°] and bond lengths [Å] of (a) $[Ni^{III}(ema)_2]^-$ and (b) $[Ni^{III}(mnt)_2]^-$ **b**

Calculated bond angles and bond lengths of $[Ni^{III}(ema)]^-$ and $[Ni^{III}(mnt)_2]^-$ are presented in Table 2. For $[Ni^{III}(ema)]^-$, with values of –1.9°, +1.9° and 0.04 Å, respectively, maximal deviations from experiment are found for the angles Ni–N–C(3), and O–C(2)–C(1) and the N–C(2) bond distance. In the case of $[Ni^{III}(mnt)_2]$, the C(1)–C(1´)–C(2´) bond angle and the C(2)–N bond length exhibit the largest deviations from experiment with values of 1.5° and 0.04 Å. For $[Ni^{III}(ema)]^-$, the mean values of the deviations from the experimental values amount to 0.02 Å and 0.6°. The standard deviations amount to 0.01 Å and 0.6°, respectively. In the case of $[Ni^{III}(mnt)_2]$, one finds mean values of 0.02 Å and 1.1° and standard deviations of 0.01 Å and 0.7°. Thus, bond angles are calculated slightly more accurately for $[Ni^{III}(mnt)_2]$ while the accuracy of the computed distances is the same for both complexes. It is evident from Table 2, that almost all computed bond lengths are slightly overestimated with respect to experiment. In summary, for both complexes, the geometric parameters of the two complexes are described excellently by DFT which confirms the suitability of the BP86 GGA functional in conjunction with a Def2–TZVP(–f) basis set for geometry optimizations of nickel 3+ complexes.

4.1.3 Electronic structure

Ligand field scheme

A ligand field scheme for Ni^{3+}, which features a d^7 electronic configuration, is presented in Figure 2. The coordinate system is chosen such that the x and y axes point in the directions between the in–plane metal–ligand bonds. The z-axis is perpendicular to the molecular plane.

The five degenerate d orbitals split in a square planar ligand field of D_{4h} symmetry while only the d_{yz} and d_{xz} orbitals remain degenerate: e_g (d_{yz}. d_{xz}), a_{1g} (d_{z^2}), b_{2g} (d_{xy}), b_{1g} ($d_{x^2-y^2}$). The d_{xy} orbital is unoccupied, the unpaired electron is found in the $d_{x^2-y^2}$ orbital and the remaining orbitals are doubly occupied. Further symmetry reduction to D_{2h} lifts the degeneracy of the d_{xz} and d_{yz} orbitals: a_g (d_{z^2}, $d_{x^2-y^2}$), b_{1g} (d_{xy}), b_{2g} (d_{xz}), b_{3g}(d_{yz}). In the quasi–planar complexes $[Ni^{III}(mnt)_2]^-$, $[Ni^{III}(emb)]^-$, $[Ni^{III}(ehb)]^-$ and $[Ni^{III}(ema)]^-$ the free electron pairs in the p_z orbitals of the ligand atoms raise the energy of the d_{xz} and d_{yz} orbitals above the energy of the $d_{x^2-y^2}$ orbital. The d_{yz} orbital becomes singly occupied. In $[Ni^{III}(phmi)(py)]^-$, $[Ni^{III}(emi)(CN)]^{2-}$ and $[Ni^{III}(emi)(NH_3)]^-$ an additional ligand is present in z–direction, which raises the energy of the d_{z^2} above that of the d_{xz} and d_{yz} orbitals and, hence, the d_{z^2} orbital becomes singly occupied.

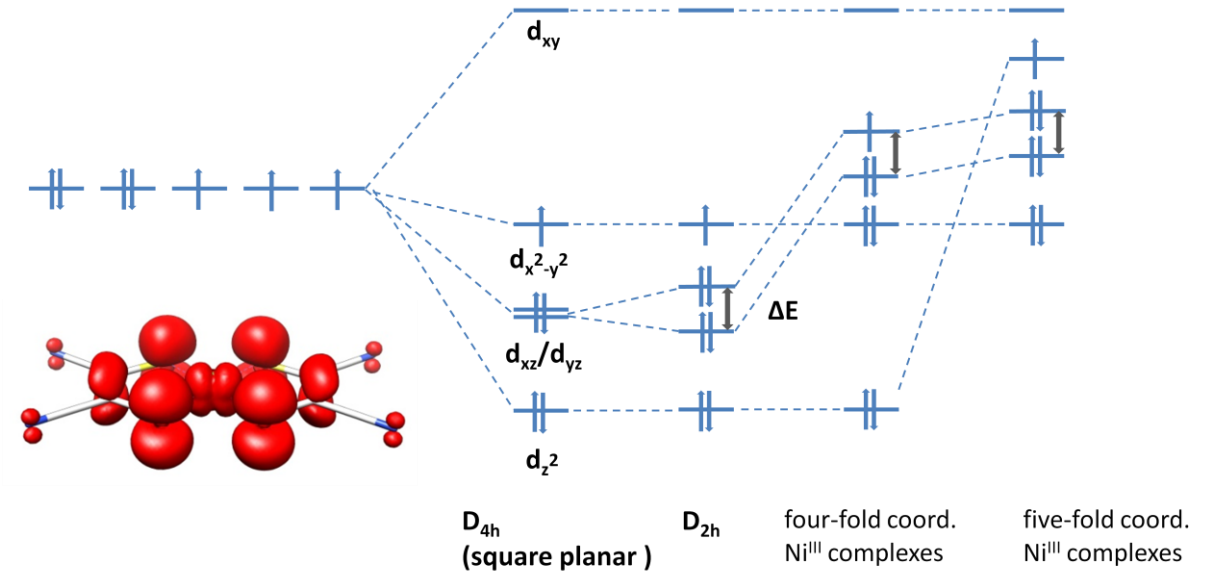

Figure 2: Splitting of the energy levels of a Ni^{3+} d^7 ion in different ligand fields. The spin density distribution (metal d_{yz} character) of $[Ni^{III}(mnt)_2]^-$ is shown as inset.

Electronic excitations

Transition	$[Ni^{III}(mnt)_2]^-$	$[Ni^{III}(emb)]^-$	$[Ni^{III}(ehb)]^-$	$[Ni^{III}(ema)]^-$
1	9069	6520	8078	1832
2	9202	8041	8778	5265
3	11541	12649	11554	11301

Transition	$[Ni^{III}(phmi)(py)]^-$	$[Ni^{III}(emi)(CN)]^{2-}$	$[Ni^{III}(emi)(NH_3)]^-$
1	8580	8719	11329
2	9063	9453	11794
3	12688	14313	12574

Table 3: The three lowest electronic excitations from TD–DFT calculations [cm^{-1}].

In Table 3, TD–DFT transition energies are presented for the three energetically lowest–lying electronically excited states. With excitations between 8600 cm^{-1} and 11400 cm^{-1}, $[Ni^{III}(phmi)(py)]^-$ $[Ni^{III}(emi)(CN)]^{2-}$ and $[Ni^{III}(emi)(NH_3)]^-$ feature a first excited state, which is energetically well–separated from the ground state. The same holds for $[Ni^{III}(mnt)_2]^-$, $[Ni^{III}(emb)]^-$ and $[Ni^{III}(ehb)]^-$ with excitation between 6500 cm^{-1} and 9100 cm^{-1}. In contrast, $[Ni^{III}(ema)]^-$ exhibits a TD–DFT transition of only 1830 cm^{-1} and, accordingly ,features an almost degenerate electronic ground state. With respective squared transition coefficients for $[Ni^{III}(mnt)_2]^-$, $[Ni^{III}(emb)]^-$, $[Ni^{III}(ehb)]^-$ and $[Ni^{III}(ema)]^-$ of 0.86, 0.47, 0.76 and 0.73, the lowest TD–DFT excitation correspond to a promotions of a β–electron from the highest–lying doubly occupied molecular orbital (HOMO) (metal d_{xz} character) into the singly occupied orbital (metal d_{yz} character).

Second order properties, such as g–tensors, of systems with quasi–degenerate ground states cannot be reliably obtained with conventional DFT, which is a genuine single–determinant method (see Chapter 2.1). Consequently, the computation of magnetic properties with DFT is not feasible for $[Ni^{III}(ema)]^-$ and the application of multi–determinant approaches such as complete active space SCF (CAS–SCF) or NEVPT2 is indispensible.

Spin densities and Mulliken spin and charge populations

The spin density of $[Ni^{III}(mnt)_2]^-$ is displayed as inset in Figure 2. In line with the ligand field scheme in Figure 2, the spin at the nickel is found in a d_{yz} orbital. Pronounced delocalization of the spin into the out–of–plane sulfur p_z orbitals of the ligands is observed. The Mulliken population analysis presented in Table 4 confirms that only a minor fraction of the spin is found at the nickel center: a spin population of 0.27 is identified for the nickel ion, whereas at each thiolate a spin population of 0.17 is present. The delocalization of the electron spin reflects the significant covalency of the Ni–S bonds. In addition to spin delocalization, Ni–S bond formation implies the transfer of electron density from

the sulfur atoms to the nickel atom, which results in a Mulliken charge population (Table 5) of 0.02 at the sulfur atoms and an even negative charge population of –0.16 at the nickel. As a word of caution, it has to be remembered that the spin and charge populations are in general no genuine physical quantities [23]. Hence, a negative charge population at the nickel should not be misinterpreted as a genuine nickel anion, but is an indication for the formation of highly covalent Ni–S bonds, which contribute to the Mulliken charge population of the nickel atom. The covalency of the Ni–S bonds is also reflected by the relatively large Mayer Bond orders (Table 6), which are close to unity. Oxygen and amidate nitrogen atoms are harder ligands than sulfur atoms and form relatively ionic bonds in transition metal complexes. Nevertheless, the spin population of the nickel atom in $[Ni^{III}(ehb)]^-$ is only 0.22 as a sizable fraction of the electron spin is delocalization into the extensive π–systems of the ligands.

In $[Ni^{III}(phmi)(py)]^-$, $[Ni^{III}(emi)(CN)]^{2-}$, $[Ni^{III}(emi)(NH_3)]^-$ the spin is found in a d_{z^2} type orbital. The overlap integral of the equatorial ligand p_z orbitals with the metal d_{z^2} vanishes as the p_z and the d_{z^2} orbitals are of *u* and *g* symmetry, respectively. Accordingly, spin populations of the in–plane ligand atoms become virtually zero. On the other hand, a strong σ–type interaction of the metal d_{z^2} with the axial ligand is present. Spin populations of 0.12 and 0.13 and Ni–N bond orders of 0.45 and 0.47 are found for the nitrogen atoms of the neutral axial ligands in $[Ni^{III}(phmi)(py)]^-$ and $[Ni^{III}(emi)(NH_3)]^-$. The negatively charged CN^- ligand in $[Ni^{III}(emi)(CN)]^{2-}$ exhibits a larger Mayer bond order of 0.75 and a larger spin population of 0.2. As spin density is delocalized only into the apical ligand orbitals, spin populations of the nickel atom of $[Ni^{III}(phmi)(py)]^-$, $[Ni^{III}(emi)(CN)]^{2-}$, $[Ni^{III}(emi)(NH_3)]^-$ are relatively large, ranging from 0.8 to 0.9.

	$Ni^{III}(mnt)]^-$		**$[Ni^{III}(emb]^-$**		**$[Ni^{III}(ehb)]^-$**		**$[Ni^{III}(ema)]^-$**
Ni	0.27	Ni	0.28	Ni	0.22	Ni	0.67
S	0.17	S	0.19	O	0.11	S	0.13
S	0.17	S	0.19	O	0.11	S	0.13
S	0.17	N	0.07	N	0.12	N	0.03
S	0.17	N	0.07	N	0.12	N	0.02

	$[Ni^{III}(phmi)(py)]^-$		**$[Ni^{III}(emi)(CN)]^-$**		**$[Ni^{III}(emi)(NH_3]^-$**
Ni	0.91	Ni	0.8	Ni	0.9
S	–0.02	S	–0.01	S	–0.02
S	–0.02	S	0.03	S	0
N	0	N	0.01	N	0
N	0	N	0	N	0
N_{py}	0.12	C_{CN}	0.20	N	0.13
		N_{CN}	–0.04		

Table 4: Mullliken spin populations.

$Ni^{III}(mnt)_2]^-$		$[Ni^{III}(emb)]^-$		$[Ni^{III}(ehb)]^-$		$[Ni^{III}(ema)]^-$	
Ni	–0.16	Ni	–0.28	Ni	0.11	Ni	–0.21
S	0.02	S	–0.14	O	–0.62	S	–0.22
S	0.02	S	–0.14	O	–0.62	S	–0.22
S	0.02	N	–0.16	N	–0.15	N	–0.13
S	0.02	N	–0.16	N	–0.15	N	–0.13

$[Ni^{III}(phmi)(py)]^-$		$[Ni^{III}(emi)(CN)]^{2-}$		$[Ni^{III}(emi)(NH_3)]^-$	
Ni	–0.27	Ni	–0.2	Ni	–0.16
S	–0.3	S	–0.36	S	–0.35
S	–0.3	S	–0.38	S	–0.35
N	–0.21	N	–0.14	N	–0.15
N	–0.21	N	–0.12	N	–0.12
N_{py}	–0.12	C_{CN}	–0.21	N_{NH3}	–0.46
–	–	N_{CN}	–0.39	–	–

Table 5: Mullliken charge populations.

$Ni^{III}(mnt)_2]^-$		$[Ni^{III}(emb)^-$		$[Ni^{III}(ehb)]^-$		$[Ni^{III}(ema)]^-$	
Ni–S	0.93	Ni–S	1.04	Ni–N	0.74	Ni–S	1.1
Ni–S	0.93	Ni–S	1.04	Ni–N	0.74	Ni–S	1.11
Ni–S	0.93	Ni–N	0.68	Ni–O	0.62	Ni–N	0.75
Ni–S	0.93	Ni–N	0.68	Ni–O	0.62	Ni–N	0.74

$[Ni^{III}(phmi)(py)]^-$		$[Ni^{III}(emi)(CN)]^-$		$[Ni^{III}(emi)(NH_3)^-$
Ni–S	0.98	Ni–S	0.94	Ni–S	0.95
Ni–S	0.97	Ni–S	0.94	Ni–S	0.96
Ni–N	0.66	Ni–N	0.68	Ni–N	0.66
Ni–N	0.66	Ni–N	0.68	Ni–N	0.67
$Ni–N_{py}$	0.45	$Ni–C_{CN}$	0.75	$Ni–N_{NH3}$	0.47

Table 6: Mayer bond orders.

Molecular orbital diagrams of $[Ni^{III}(mnt)_2]^-$ and $[Ni^{III}(ema)]^-$

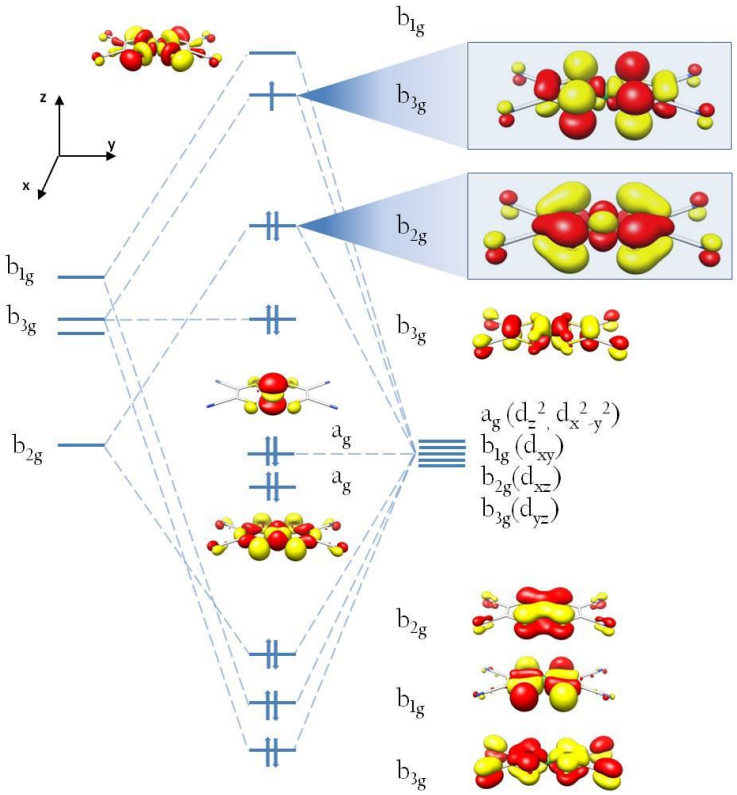

a

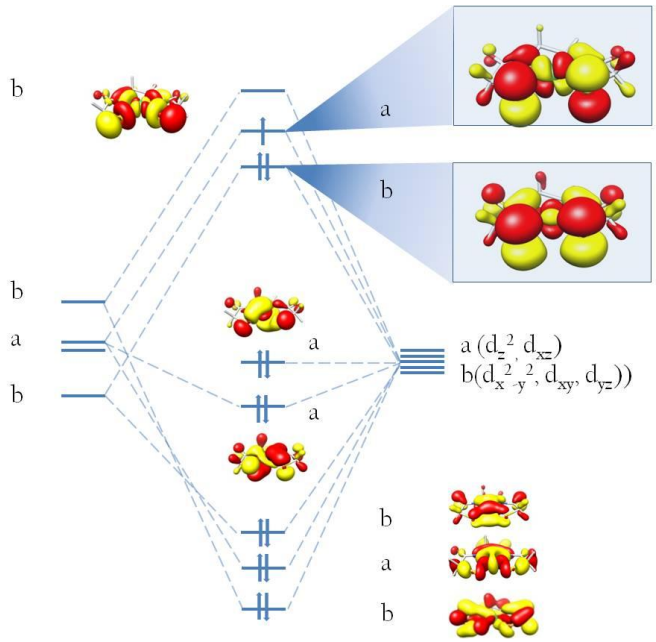

b

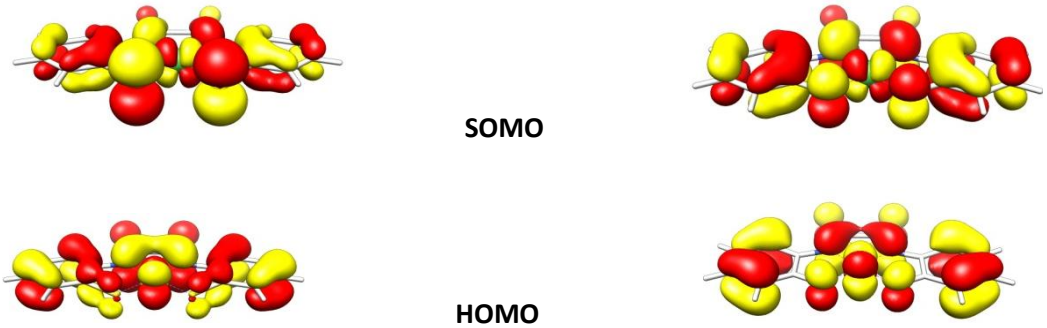

$Ni^{III}(emb)]^-$ $[Ni^{III}(ehb)]^-$ **c**

Figure 3: Molecular orbital diagrams for (a) $[Ni^{III}(mnt)_2]^-$ and (b) $[Ni^{III}(ema)]^-$ with quasi–restricted orbitals. Predominantly ligand–based molecular orbitals are not shown. (c) SOMO and the HOMO of $[Ni^{III}(emb)]^-$ and $[Ni^{III}(ehb)]^-$.

The finding of a quasi–degenerate ground state only for $[Ni^{III}(ema)]^-$ but not for $[Ni^{III}(mnt)_2]^-$ requires further explanation. Molecular orbital diagrams for $[Ni^{III}(mnt)_2]^-$ and $[Ni^{III}(ema)]^-$ from quasi–restricted orbitals are shown in Figure 3a and Figure 3b. For $[Ni^{III}(mnt)_2]^-$, the HOMO, SOMO and LUMO, which feature b_{2g}, b_{3g} and b_{1g} symmetry, contain d_{xz} (29%), d_{yz} (42%) , and d_{xy} (44%) d orbital contributions, respectively. The pronounced mixing with ligand–based orbitals is the result of *π–interactions* in the case of the HOMO and SOMO and due to *σ–interactions* with in the case of the LUMO. In contrast, the doubly occupied d_{z^2} of g symmetry does not interact with the sulfur p_z orbitals of u symmetry and, thereby, the orbital is predominantly metal–based (82%).

The π–interactions of the nickel d–orbitals with the sulfur ligands in b_{2g} and b_{3g} extend to the carbon atoms C(1) and C(1´) thereby connecting the two sulfur atoms of one maleonitriledithiolate ligand by an in–phase combination (b_{3g}) and an out–of–phase (b_{2g}) combination of the corresponding p–orbitals. For the in–phase combination, two nodal planes perpendicular to the molecular plane are found per maleonitriledithiolate ligand while for the out–of–phase combination only one nodal plane is present. As a consequence, the energies of b_{2g} and b_{3g} are well separated. On the other hand, in $[Ni^{III}(ema)]^-$, the sulfur and nitrogen ligand atoms are not connected via an extended π–system and, consequently, both, the (b) HOMO and (a) SOMO feature nearly the same energy.

In conclusion, the planar nickel complexes exhibit an energetically separated SOMO only if the nickel–coordinating atoms are connected via a ligand π–system. In the case of the planar nickel 3+ complexes $[Ni^{III}(emb)]^-$ and $[Ni^{III}(ehb)]^-$, an extended π–system in the form of the phenyl and the amidate moieties is present between the coordinating ligands as shown in Figure 3c and, hence, both

complexes feature a non–degenerate ground state in agreement with the relatively large TD–DFT transition energies (Table 3).

4.1.4 Magnetic spectroscopy

In the present section, we compare calculated g–values and hyperfine coupling constants to the available experimental data. We have analyzed the g–values by means of second order perturbation theory in order to establish a connection to

g–tensor

	g_1	$g_{1\ exptl.}$	g_2	$g_{2\ exptl.}$	g_3	$g_{3\ exptl.}$	g_{iso}	$g_{iso\ exptl.}$
$Ni^{III}(mnt)_2]^-$	2.00	2.00	2.06	2.04	2.11	2.16	2.06	2.07
$[Ni^{III}(emb)]^-$	2.00	2.01	2.01	2.10	2.10	2.30	2.04	2.14
$[Ni^{III}(ehb)]^-$	2.01	2.04	2.04	2.11	2.13	2.29	2.06	2.15
$[Ni^{III}(phmi)(py)^-$	2.03	2.00	2.18	2.28	2.20	2.31	2.14	2.20
$[Ni^{III}(emi)(CN)]^{2-}$	2.03	2.02	2.12	2.17	2.14	2.21	2.10	2.13
$[Ni^{III}(emi)(NH_3)^-$	2.03	2.01	2.18	2.25	2.20	2.31	2.14	2.19

Table 7: g–values. Experimental data is from: [13], [20] and [22].

Calculated g–tensors are presented in Table 7. In the case of $[Ni^{III}(mnt)_2]^-$, the isotropic Δg_{iso} value is by 15% smaller than the corresponding experimental value, which is in accord with the general underestimation of computed g-values (section 2.1). For $[Ni^{III}(emb)]^-$ and $[Ni^{III}(ehb)]^-$, the calculated g–values are pronouncedly underestimated relative to the experimental values as the Δg_{iso} value of each of the two compounds amounts to only 60–70% of the corresponding experimental value. The underestimation with respect to experiment is particularly prominent in the case of the g_2 value. In contrast, with an underestimation of 25–30%, the five–fold coordinated complexes $[Ni^{III}(phmi)(py)]^-$, $[Ni^{III}(emi)(CN)]^{2-}$ and $[Ni^{III}(emi)(NH_3)]^-$ show Δg_{iso} values, which are more compatible with the experiment. In contrast to the square–planar complex $Ni^{III}(mnt)_2]^-$, the tensor geometry is axial, which is correctly reproduced by the calculations.

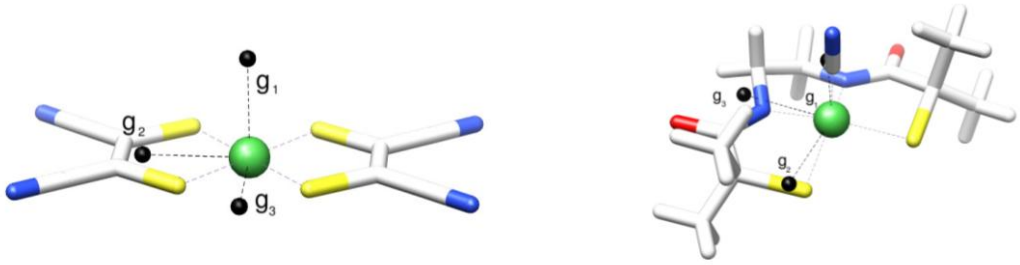

Figure 4: computed g–tensor axes of (a) $[Ni^{III}(mnt)_2]^-$ and (b) $[Ni^{III}(emi)(CN)]^{2-}$.

The orientation of the computed g–tensor axes of $[Ni^{III}(mnt)_2]^-$ are displayed in Figure 4a. The g_1 axis is oriented perpendicular to the molecular plane in the direction of the molecular z–axis while the g_2 and g_3 tensor axes point along the y–axis and x–axis, respectively. The calculated orientations of the g–tensor axes coincide with the experimentally determined orientations [13]. In Figure 4b, it is shown how the computed g–tensor axes of $[Ni^{III}(emi)(CN)]^{2-}$ are oriented with respect to molecular geometry. The g_1 axis is aligned perpendicular to the molecular plane. With $g_2 \approx g_3$, the g–tensor is approximately axial and, thus, the orientation of the g_2 and g_3 axes in the molecular plane is not specified. Analogous orientations of the g–tensor axes are found in $[Ni^{III}(phmi)(py)]^-$ and $[Ni^{III}(emi)(NH_3)]^-$.

An interpretation of the g–tensor in terms of the electron structure is possible by means of second order perturbation theory (see chapter 2.2). In z–direction, the l_z matrix element of the singly occupied d_{yz} orbital with the doubly occupied d_{xy} orbital is non–zero. However, the contribution to Δg_z is limited since the doubly occupied d_{xz} type orbital is by only 42% metal centered. In contrast, with 82%, the d_{z^2} orbital is mainly metal centered since it does not mix with the in–plane ligand p–orbitals. Hence, a major contribution to the g–value derives from the non–vanishing l_x matrix elements of the doubly occupied d_{z^2} orbital with the singly occupied d_{yz} orbital which results in the Δg_x component being the largest of the three Δg components. The interpretation of the g–tensor of $[Ni^{III}(phmi)(py)]^-$, $[Ni^{III}(emi)(CN)]^{2-}$ and $[Ni^{III}(emi)(NH_3)]^-$ is straightforward. There is no non–vanishing l_z matrix–element of the spin–carrying d_{z^2} orbital with the other metal d–orbitals and, hence, the deviation from the free electron g–value in z–direction is (almost) zero. The g–tensor components Δg_2 and Δg_3 arise from the l_x and l_y matrix elements of the d_{z^2} SOMO with the d_{yz} and d_{xz} orbitals. In the ligands of the five–coordinated complexes, the nickel–coordinating atoms are not connected via a delocalized π–system. Hence, the d_{yz} and d_{xz} orbitals are quasi–degenerate, which results in an nearly axial g–tensor.

As evident from Table 7, the computed g–tensor values are generally underestimated relative to the experimentally observed ones. This underestimation of the Δg–values has been related to an

overestimation of the spin–delocalization and an overestimation of the d–orbital transition energies [24]. The major contributions to the g–tensor arise from the transition metal center while lighter ligand atoms can often be neglect according to their smaller SOC constant (see chapter 2.2) and, hence, spin delocalization away from the transition metal into the ligand orbitals results in a decrease of the g–values. In contrast to the transition energy, the *square* of the d orbital coefficients of the molecular orbital *into* which and *from* which an electron is promoted enter the sum–over–states expression (chapter 2.2) for the g–tensor. In the case of the square planar nickel complexes, in which larger amounts of spin density are delocalized into ligand orbitals due to π–interactions with the d_{yz} SOMO, it is seems reasonable that the overestimation of the spin delocalization by DFT is the major reason for the underestimation of the Δg–value. Therefore, the good agreement of the g–values with experiment in the case of $[Ni^{III}(mnt)_2]^-$ indicates that the covalency of the nickel–sulfur π–bonds and, therefore, the spin delocalization are correctly described by DFT. This is corroborated by the overall good agreement of the computed hyperfine coupling constants with the experimental values (*vide infra*). The significant underestimation of the g–values in $[Ni^{III}(emb)]^-$ and $[Ni^{III}(ehb)]^-$ implies that the delocalization of the spin density into the ligand orbitals is strongly overestimated. Common feature of both complexes is the conjugated π–system, which extends over two phenyl moieties. It seems reasonable to assume that the pronounced underrepresentation of the g–values is due to the presence of the extended conjugated π–system, which leads to a particularly pronounced overestimation of spin delocalization (Figure 3c).

Hyperfine coupling constants

	A'_1	A'_2	A'_3	A_{iso}
^{61}Ni	39.4	–18.9	–20.5	–45.2/+6*
^{61}Ni exptl. [13]	32.2 ± 8.8	–21.8 ± 5.8	< –18.8 ± 2.8	+12.6 ± 2.8
^{33}S	–15.1	–20.3	+35.4	+11.1/+8*
^{33}S exptl. [14]	–18.8	–18.8	+37	+5.2
^{13}C(1)	3.9	–2.2	–1.7	–2.7/–2.6*
^{13}C(1) exptl. [15]	5.1	–2.5	–2.5	–2.1
^{13}C(2)	0.6	–0.2	–0.5	–2.1/–2.0*
^{13}C(2) exptl. [15]	0.17	0.27	–0.43	–2.9
^{14}N	–0.1	–0.3	+0.8	+0.2/+0.2*
^{14}N exptl. [15]	–0.2	–0.2	+0.8	+0.1

Table 8: Hyperfine coupling constants [MHz] for $[Ni^{III}(mnt)_2]^-$. A_1', A_2' and A_3' designate the anisotropic contributions to the hyperfine coupling tensor (in contrast to the full hyperfine coupling tensor A). *Full decontraction of the recontracted basis set.

Hyperfine coupling constants of $[Ni^{III}(mnt)_2]^-$ are collected in Table 8. Spin orbit coupling has been included explicitly in the scalar relativistic UKS calculations of the ^{61}N hyperfine coupling constant. Relativistic recontracted basis sets were employed (see chapter 3.1). The computed isotropic ^{61}Ni hyperfine coupling constant amounts to –45 MHz arising from nearly equal contributions of the Fermi contact term and the pseudo contact shift, which are –22 MHz and –23 MHz, respectively. It should be remembered that g_N, i.e. the nuclear g–value of ^{61}Ni, is negative. The electron–nucleus dipole–dipole interactions amount to 60 MHz, –26 MHz and –34 MHz while the anisotropic contributions of the spin–orbit coupling are –21 MHz, 7 MHz and 14 MHz. Hence, the dominant part of the anisotropic contribution to the hyperfine coupling tensor is clearly the first order electron–nucleus dipole–dipole interaction. The hyperfine coupling tensor is approximately axial with the unique tensor axis A_1 pointing in the direction of the x–axis (Figure 5a). Experimentally, the nickel hyperfine coupling constants were obtained by Maki and co–workers [13] by single crystal EPR measurements of ^{61}Ni isotopically labeled diluted single crystals of $[Ni^{III}(mnt)_2]^-$. It was found that the tensor axes are collinear with the g–tensor axes with values of A_{zz} < 6 MHz, A_{yy} = 9 (± 3) MHz and A_{xx} = 45 (± 6) MHz. The isotropic contribution measured in liquid solution amounts to 12.6 ± 2.8 MHz. Unfortunately, the signs of the tensor components were not determined. Stein and co–workers [17] assumed that the anisotropic and the isotropic components should all exhibit a positive sign, while Stadler [16] suggested a positive sign for A_{xx} and A_{yy} and a negative sign for A_{zz}. However, if for the experimental values it is assumed that A_{xx}>0, A_{yy}< 0, A_{zz}<0 and A_{iso}>0, our computed results are in

good agreement with the experimental values of the anisotropic contribution. In contrast, the computed isotropic term which was computed with a scalar relativistic basis set exhibits a negative sign and is therefore not even qualitatively in agreement with the positive sign assigned to the isotropic coupling constant. However, if the recontracted relativistic basis sets are fully decontracted, one obtains a Fermi contact term of +28 and a pseudo contact shift of -22 MHz resulting in an isotropic contribution of +6 MHz which is in suitable agreement with experiment. Hence, while a decontraction of the basis set has almost no effect on the anisotropic contribution, it is clearly mandatory for the computation of the isotropic hyperfine coupling constant.

The computed ^{33}S hyperfine coupling tensor is nearly axial. The orientation $A'_{\perp}$ coincides with the molecular z–axis, which is perpendicular (Figure 5b) to the molecular plane and exhibits a value of 35 MHz. For the in–plane components $A'_{\parallel}$, values of –15 MHz and –20 MHz are found. Thereby, the ratio of the parallel and the perpendicular anisotropic components are consistent with an unpaired electron in the sulfur p_z orbital (chapter 2.2) and the one-center contribution dominantes the A´–values. When the same signs are applied to the experimentally determined values, the computed anisotropic hyperfine contribution is in excellent agreement with experiment. In contrast to ^{61}Ni, the isotropic hyperfine coupling is at least in qualitative agreement with the experimental value in the case of the recontracted relativistic basis set. With 8 MHz the fully decontracted basis set reproduces the experimental value better. However, the improvement is less significant than for the ^{61}Ni isotropic coupling constant. For C(1), C(2) and N, a decontraction of the basis set results in virtually no change of the computed values (Table 9). Conclusively, a fully decontraction of the basis set is only required for the computation of the isotropic coupling constants of heavier atoms, in particular transition metal atoms.

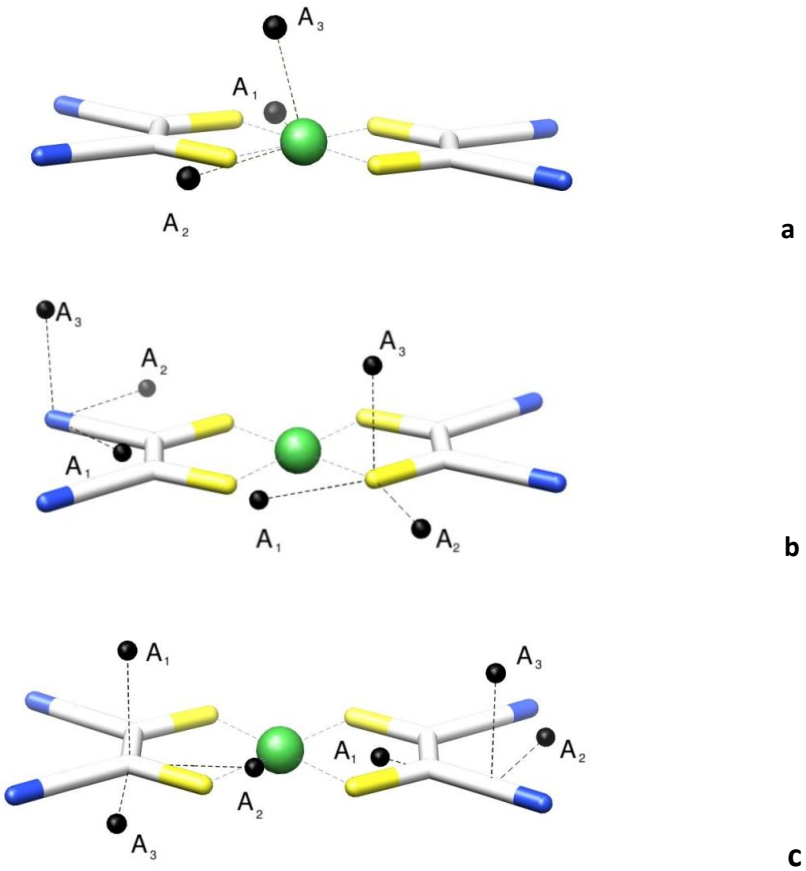

Figure 5: Axes–orientations of the computed (a) ^{61}Ni (b) ^{14}N, ^{33}*S* and (c) ^{13}C1 and ^{13}C2 hyperfine coupling tensors of $[Ni^{III}(mnt)_2]^-$.

The computed hyperfine coupling tensor of C(1) (for atom numbering see, Figure 1) is axial with $A_\perp$ being aligned along the z–axis of the molecule (Figure 5c). As in the case of the sulfur nuclei, the anisotropic contribution to the hyperfine–tensor mainly arises from the one–center contribution of the spin–carrying C(1) p_z orbital. The C(1) hyperfine coupling tensor obtained by orientation selected ENDOR spectroscopy is nicely reproduced by the computed tensor. In particular, even the isotropic contribution of 2.1 MHz is accurately reproduced computationally (2.7 MHz). The calculated hyperfine coupling tensor of the C(2) atoms exhibits only a rather small and nearly isotropic coupling constant of –2.1 MHz which is suitably matched by the experimentally obtained tensor (Figure5c) with a coupling constant of –2.9 MHz.

	$A_{\|}$	$A_{\|}$	$A_{\perp}$	(A_{iso})
$^{14}N_{py}$	58	60	75	65
$^{14}N_{py}$ exptl.	–	–	70	–
$^{14}N_{NH3}$	55	55	72	61
$^{14}N_{NH3}$ exptl.	–	–	67	–

Table 9: ^{14}N hyperfine couplings [MHz] of the axially coordinating ligand of $[Ni^{III}(phmi)(py)]^-$ [22] and $[Ni^{III}(emi)(NH_3)]^-$ [20]. Please note that in contrast to Table 8, the complete A–tensors and not the anisotropic A´–tensor contributions are shown since no isotropic values are available for the extraction of the A´–tensor from the A–tensor.

In Table 9, the ^{14}N hyperfine coupling tensors of the axial ligands in $[Ni^{III}(phmi)(py)]^-$ and $[Ni^{III}(emi)(NH_3)]^-$ are collected. Experimentally, only one the component along the z–axis was extracted from the ESR spectrum. The axial ligand forms an σ–interaction with the spin carrying d_{z^2}–orbital at the nickel. According to the σ–type interaction, the computed hyperfine coupling tensor is axial with a dominant isotropic contribution. The A_{zz} ^{14}N hyperfine coupling constant found for $[Ni^{III}(phmi)(py)]^-$ amounts to 75 MHz, which is only slightly larger and therefore in excellent agreement with the experimentally determined value of 70 MHz. The same holds for the $A_{\perp}$ component of the ^{14}N coupling constant of the axial ligand in $[Ni^{III}(emi)(NH_3)]^-$ which is by only 5 MHz too large with respect to the experimental value of 67 MHz.

4.1.5. Conclusion

The four– and five–coordinated nickel 3+ complexes $[Ni^{III}(mnt)_2]^-$, $[Ni^{III}(emb)]^-$, $[Ni^{III}(ehb)]^-$, $[Ni^{III}(ema)]^-$, $[Ni^{III}(phmi)(py)]^-$, $[Ni^{III}(emi)(CN)]^{2-}$ and $[Ni^{III}(emi)(NH_3)]^-$ were studied by careful comparison of quantum chemistry and spectroscopy. We have revealed that the electronic structures of some complexes strongly vary and are not always correctly described by DFT. In the four–coordinated complexes the unpaired electron is found in the nickel d_{yz} orbital. The singly occupied d_{yz} orbital forms highly covalent π–bonds with the ligand p–orbitals, by which significant amounts of spin density is transferred to the ligand orbitals. In the case of $[Ni^{III}(mnt)_2]^-$, calculated magnetic properties are in very good overall agreement with experiment and indicate that the computed electronic structure is fundamentally correct. However, for $[Ni^{III}(emb)]^-$ and $[Ni^{III}(ehb)]^-$ the determined Δg–values underestimate the experimental values by even more than 50%, which seems to be due to an overestimated delocalization of the electron spin into the extended aromatic π–system of the two complexes. In contrast to $[Ni^{III}(mnt)_2]^-$, $[Ni^{III}(emb)]^-$, $[Ni^{III}(ehb)]^-$, in $[Ni^{III}(ema)]^-$, a quasi–degenerate electronic ground state is present. In $[Ni^{III}(mnt)_2]^-$, $[Ni^{III}(emb)]^-$ and $[Ni^{III}(ehb)]^-$ but

not in $[Ni^{III}(ema)]$ the Ni–coordinating ligand atoms are connected via a conjugated π–system which leads to a lifting of the degeneracy of the d_{xz} and d_{yz} nickel orbitals. However due to the presence of a quasi–degenerate ground state, DFT, which is a genuine single determinant method, cannot be applied for the accurate calculation of magnetic properties such as g–tensors in $[Ni^{III}(ema)]^{-}$.

For the pyramidal nickel complexes $[Ni^{III}(phmi)(py)]^{-}$, $[Ni^{III}(emi)(CN)]^{2-}$ and $[Ni^{III}(emi)(NH_3)]^{-}$, the electronic ground state is non–degenerate with the electron spin at the nickel being present in a d_{z^2} orbital. Spin density is delocalized only into the axial ligand, which is reflected by the relatively large spin density at the nickel. The correct description of the electronic structure of the complexes is confirmed by the good agreement of experiment and computed magnetic properties, such as g–tensors and hyperfine couplings.

In conclusion, in the present study, it has been shown that the treatment of nickel complexes with DFT is of varying quality and should be done carefully. In particular, square planar complex may either be computed accurately with DFT, as $Ni^{III}(mnt)_2]^{-}$ or DFT performs poorly, as in the case of $[Ni^{III}(ehb)]^{-}$ or $[Ni^{III}(ehb)]^{-}$. In Ni–complexes with a quasi–degenerate ground state, such as $[Ni^{III}(ema)]^{-}$, DFT cannot be employed at all for the computation of properties, such as g–tensors, and genuine multi–determinantial methods need to be used.

References

1. Ermler, U., et al., *Active sites of transition-metal enzymes with a focus on nickel.* Current Opinion in Structural Biology, 1998. **8**(6): p. 749-758.
2. Ragsdale, S.W., *Nickel biochemistry.* Current Opinion in Chemical Biology, 1998. **2**(2): p. 208-215.
3. Huyett, J.E., et al., *Fe-57 q-band pulsed endor of the hetero-dinuclear site of nickel hydrogenase: Comparison of the nia, nib, and nic states.* Journal of the American Chemical Society, 1997. **119**(39): p. 9291-9292.
4. Lancaster, J.R., *New biological paramagnetic center - octahedrally coordinated nickel(iii) in the methanogenic bacteria.* Science, 1982. **216**(4552): p. 1324-1325.
5. Albracht, S.P.J., *Nickel hydrogenases - in search of the active-site.* Biochimica Et Biophysica Acta-Bioenergetics, 1994. **1188**(3): p. 167-204.
6. Frey, M., *Nickel-iron hydrogenases: Structural and functional properties*, in *Metal sites in proteins and models: Redox centres*, H.A.O.S.P.J.T.A.J. Hill, Editor. 1998. p. 97-126.
7. Lubitz, W., E. Reijerse, and M. van Gastel, *[nife] and [fefe] hydrogenases studied by advanced magnetic resonance techniques.* Chemical Reviews, 2007. **107**(10): p. 4331-4365.
8. De Lacey, A.L., et al., *Activation and inactivation of hydrogenase function and the catalytic cycle: Spectroelectrochemical studies.* Chemical Reviews, 2007. **107**(10): p. 4304-4330.
9. Coontz, R. and B. Hanson, *Not so simple.* Science, 2004. **305**(5686): p. 957-957.
10. Hoffmann, P., *Tomorrow´s energy. Hydrogen, fuel cells, and the prospects for a cleaner planet*, Cambridge The MIT Press.
11. Halcrow, M.A. and G. Christou, *Biomimetic chemistry of nickel.* Chemical Reviews, 1994. **94**(8): p. 2421-2481.
12. Gloaguen, F. and T.B. Rauchfuss, *Small molecule mimics of hydrogenases: Hydrides and redox.* Chemical Society Reviews, 2009. **38**(1): p. 100-108.
13. Maki, A.H., et al., *Electron paramagnetic resonance studies of electronic structures of bis(maleonitriledithiolato)copper)2) -nickel)3) -cobalt)2) + -rhodium)2) complexes.* Journal of the American Chemical Society, 1964. **86**(21): p. 4580-&.

14. Schmitt, R.D. and A.H. Maki, *Electronic ground state of bis(maleonitriledithiolene)nickel monoanion . Sulfur-33 hyperfine interaction.* Journal of the American Chemical Society, 1968. **90**(9): p. 2288-&.
15. Huyett, J.E., et al., *Pulsed endor and eseem study of bis(maleonitriledithiolato)nickel (-): An investigation into the ligand electronic structure.* Inorganic Chemistry, 1998. **37**(6): p. 1361-1367.
16. Stadler, C., et al., *Density functional calculations for modeling the oxidized states of the active site of nickel-iron hydrogenases. 1. Verification of the method with paramagnetic ni and co complexes.* Inorg Chem, 2002. **41**(17): p. 4417-23.
17. Stein, M., et al., *G- and a-tensor calculations in the zero-order approximation for relativistic effects of ni complexes ni(mnt)(2)(-) and ni(co)(3)h as model complexes for the active center of [nife]-hydrogenase.* Journal of Physical Chemistry A, 2001. **105**(2): p. 416-425.
18. Neese, F., *Metal and ligand hyperfine couplings in transition metal complexes: The effect of spin-orbit coupling as studied by coupled perturbed kohn-sham theory.* Journal of Chemical Physics, 2003. **118**(9): p. 3939-3948.
19. Kruger, H.J. and R.H. Holm, *Stabilization of nickel(iii) in a classical n2s2 coordination environment containing anionic sulfur.* Inorganic Chemistry, 1987. **26**(22): p. 3645-3647.
20. Kruger, H.J., G. Peng, and R.H. Holm, *Low-potential nickel(iii,ii) complexes - new systems based on tetradentate amidate thiolate ligands and the influence of ligand structure on potentials in relation to the nickel site in [nife]-hydrogenases.* Inorganic Chemistry, 1991. **30**(4): p. 734-742.
21. Kruger, H.J. and R.H. Holm, *Stabilization of trivalent nickel in tetragonal nis4n2 and nin6 environments - synthesis, structures, redox potentials, and observations related to [nife]-hydrogenases.* Journal of the American Chemical Society, 1990. **112**(8): p. 2955-2963.
22. Hanss, J. and H.J. Kruger, *First isolation and structural characterization of a nickel(iii) complex containing aliphatic thiolate donors.* Angewandte Chemie-International Edition, 1998. **37**(3): p. 360-363.
23. Mulliken, R.S., *Electronic population analysis on lcao-mo molecular wave functions .1.* Journal of Chemical Physics, 1955. **23**(10): p. 1833-1840.
24. Neese, F., *Prediction of molecular properties and molecular spectroscopy with density functional theory: From fundamental theory to exchange-coupling.* Coordination Chemistry Reviews, 2009. **253**(5-6): p. 526-563.

Appendix

Basis set dependence of bond lengths:

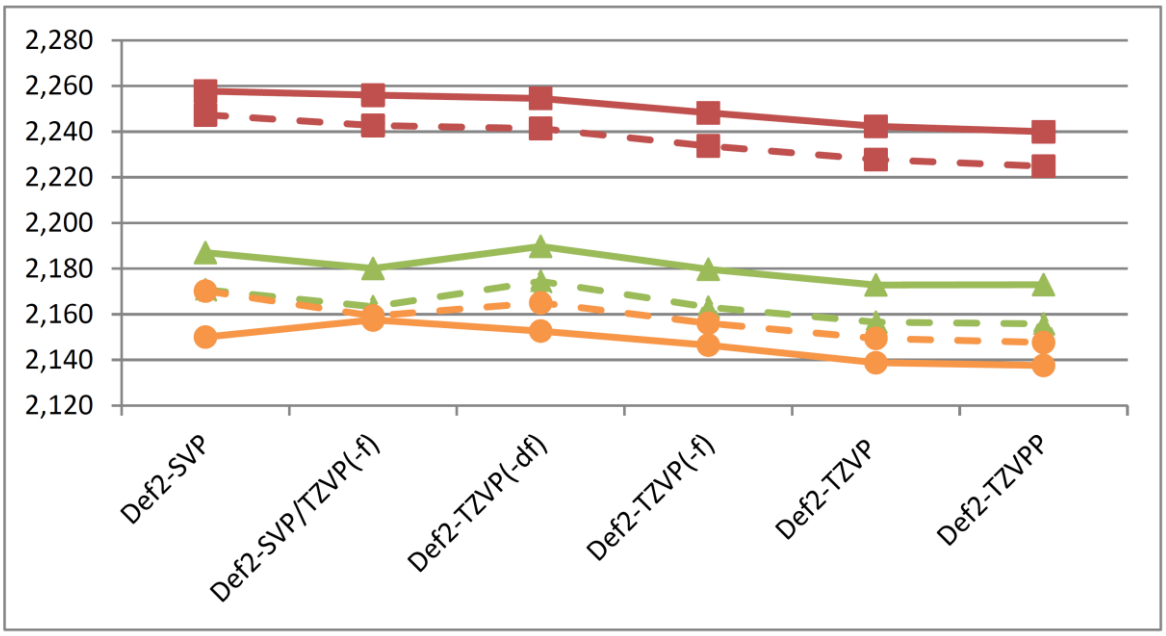

Figure A1: Basis Set dependence of S–Ni bond–lengths.: straight lines (B3LYP), dashed lines (BP86), $N^{III}(mnt)_2^-$ (green), $N^{III}(emi)(CN)^{2-}$(red), $Ni^{III}(ema)^-$ (orange).

Basis set dependence of the g–tensor:

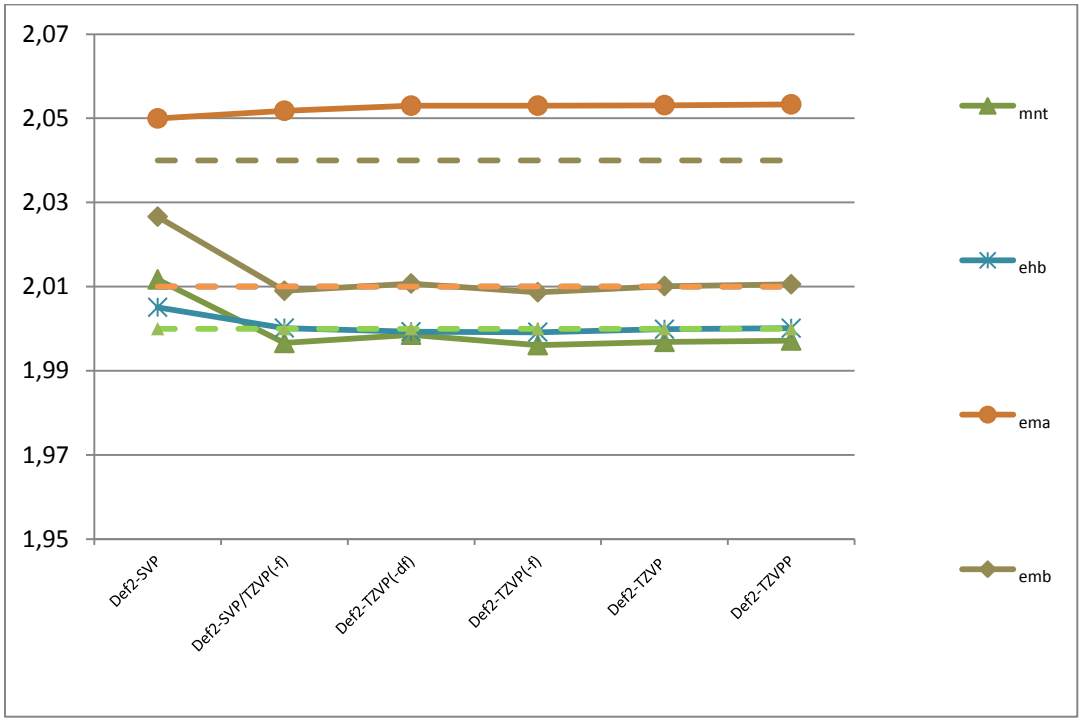

Figure A2: Component of $[Ni^{III}(mnt)_2]^-$ $[Ni^{III}(emb)]^-$ and $[Ni^{III}(ehb)]^-$. Experimental (dotted lines) and computed values (straight lines).

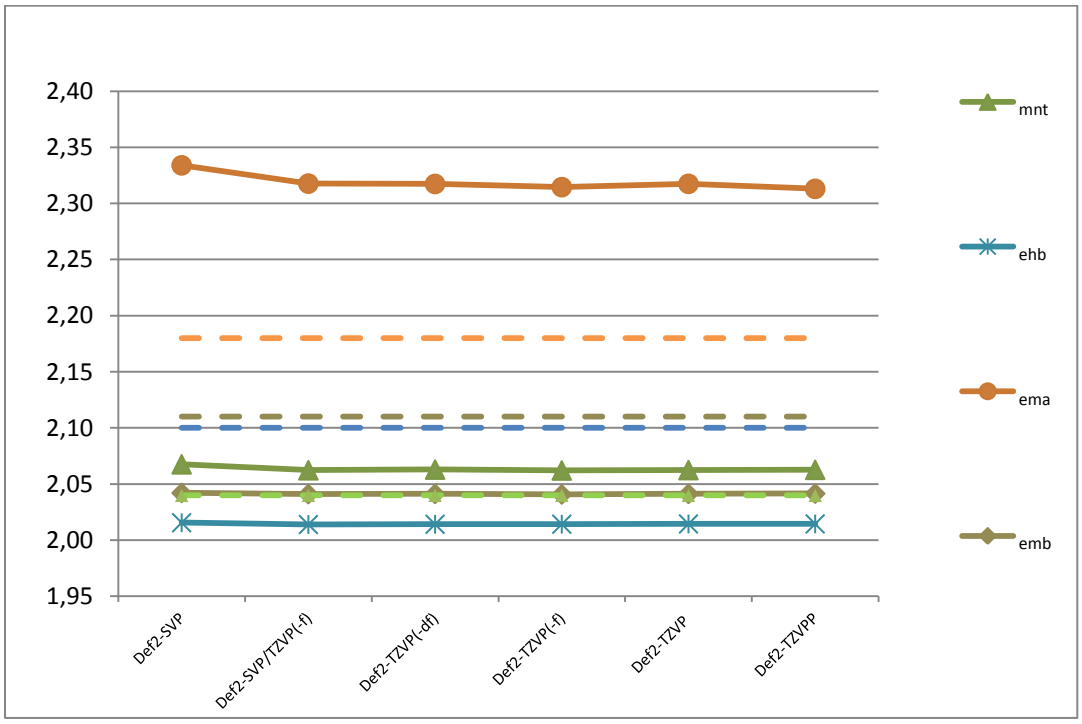

Figure A3: g_2 component of $[Ni^{III}(mnt)_2]^-$ $[Ni^{III}(emb)]^-$ and $[Ni^{III}(ehb)]^-$. Experimental (dotted lines) and computed values (straight lines).

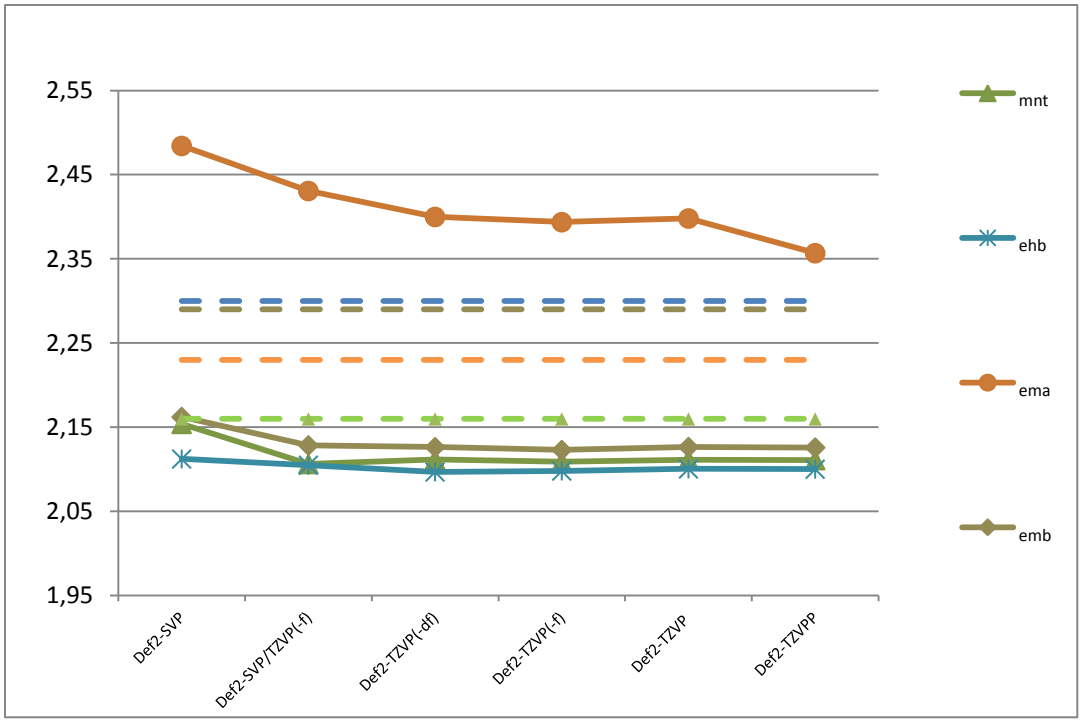

Figure A4: Component of $[Ni^{III}(mnt)_2]^-$ $[Ni^{III}(emb)]^-$ and $[Ni^{III}(ehb)]^-$. Experimental (dotted lines) and computed values (straight lines).

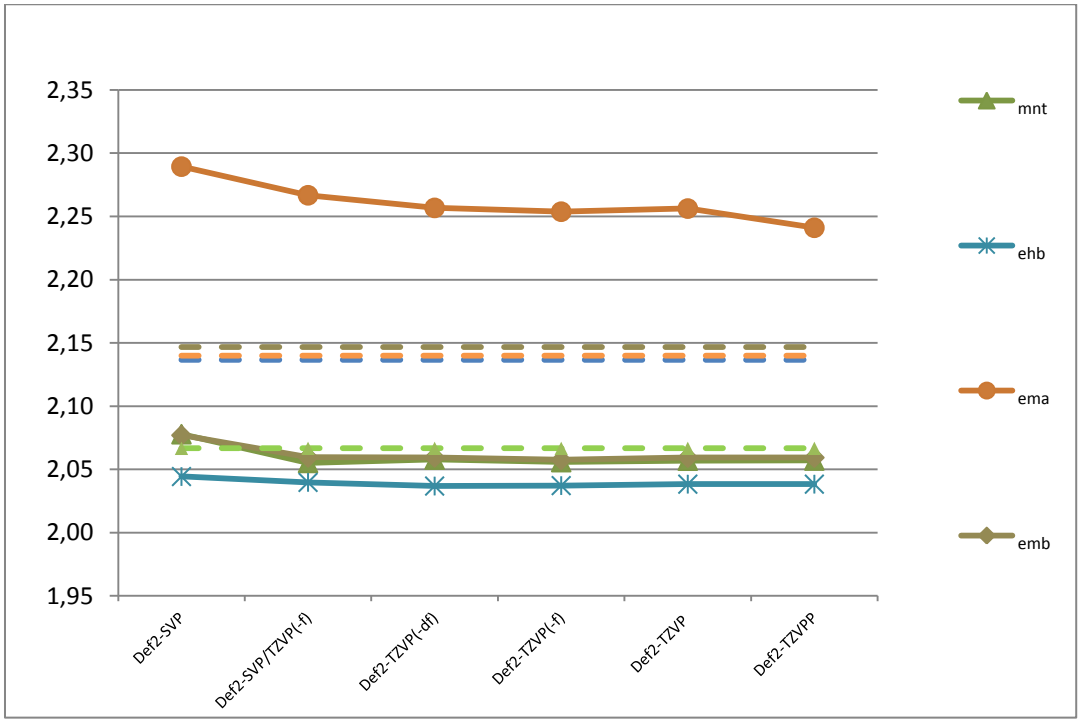

Figure A5: g_{iso} component of $[Ni^{III}(mnt)_2]^-$ $[Ni^{III}(emb)]^-$ and $[Ni^{III}(ehb)]^-$. Experimental (dotted lines) and computed values (straight lines).

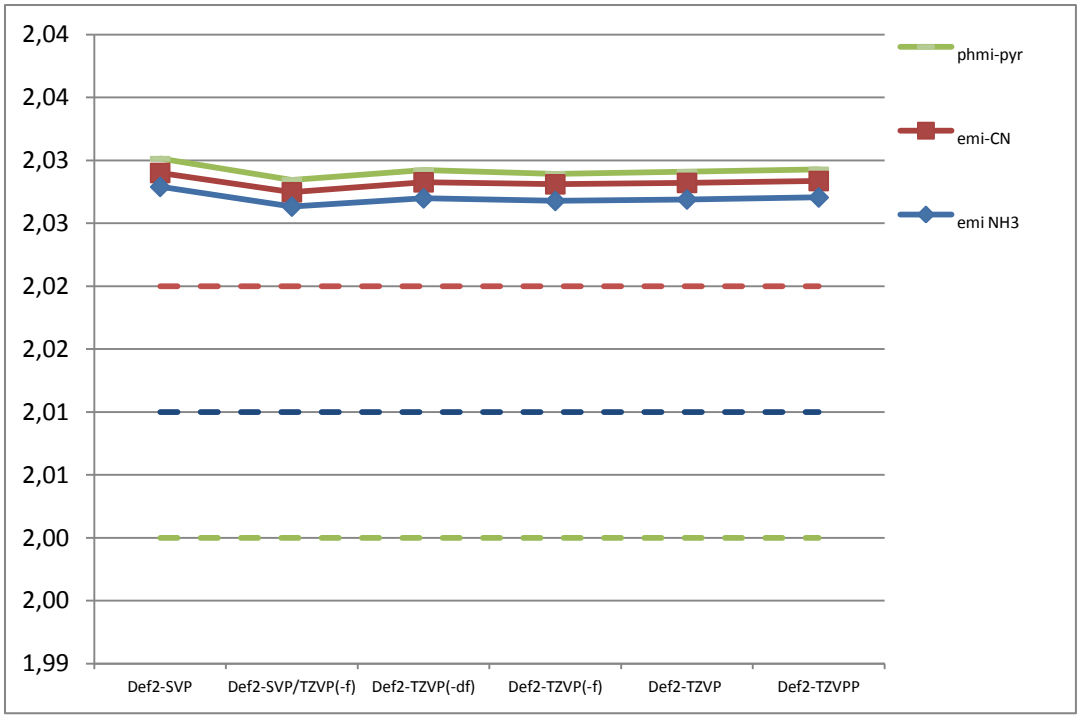

Figure A6: g_1 component of $[Ni^{III}(phmi)(py)]^{-}$ $[Ni^{III}(emi)(CN)]^{2-}$ and $[Ni^{III}(emi)(NH_3)]^{-}$. Experimental (dotted lines) and computed values (straight lines).

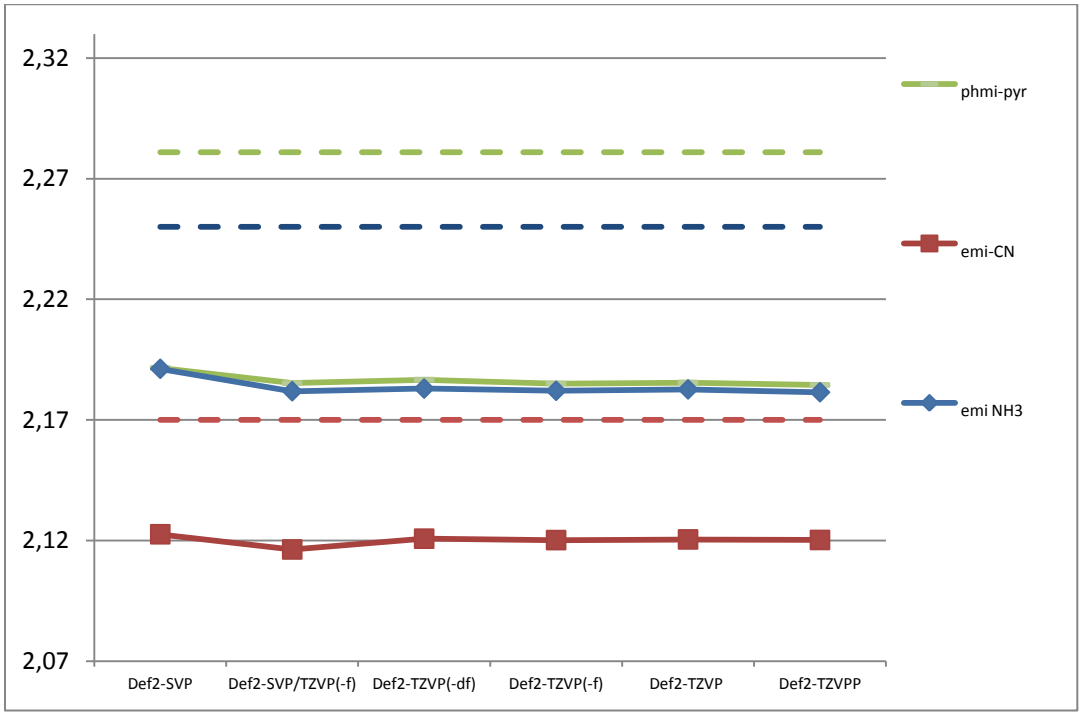

Figure A7: Component of $[Ni^{III}(phmi)(py)]^{-}$, $[Ni^{III}(emi)(CN)]^{2-}$ and $[Ni^{III}(emi)(NH_3)]^{-}$. Experimental (dotted lines) and computed values (straight lines).

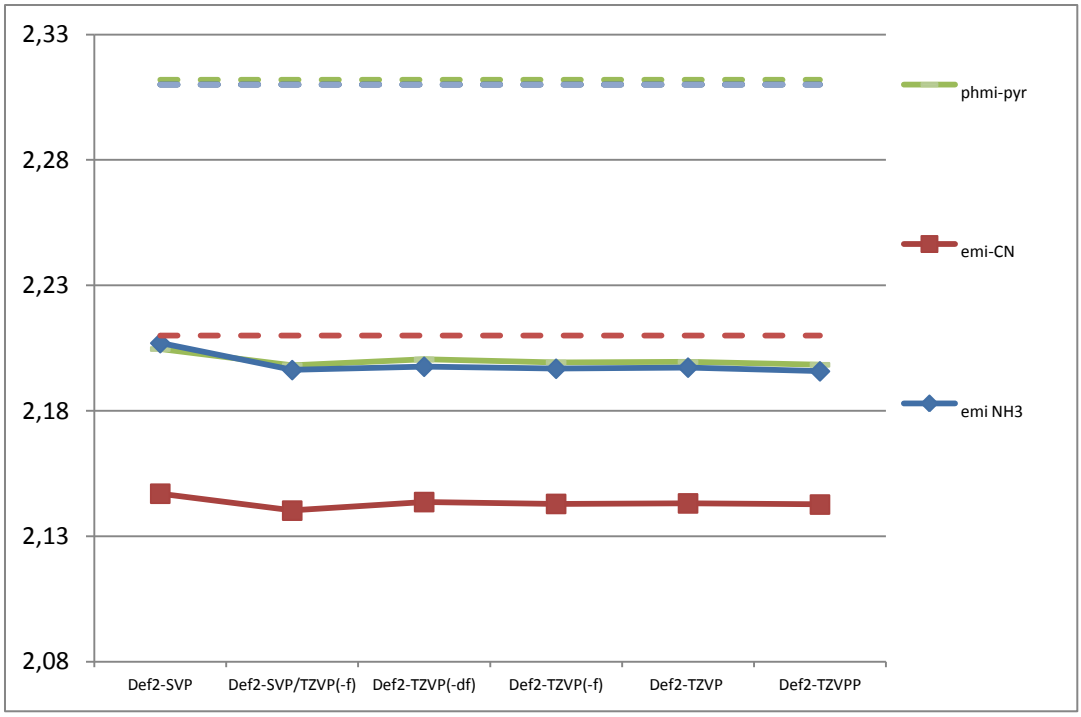

Figure A8: g_3 component of $[Ni^{III}(phmi)(py)]^{-}$, $[Ni^{III}(emi)(CN)]^{2-}$ and $[Ni^{III}(emi)(NH_3)]^{-}$. Experimental (dotted lines) and computed values (straight lines).

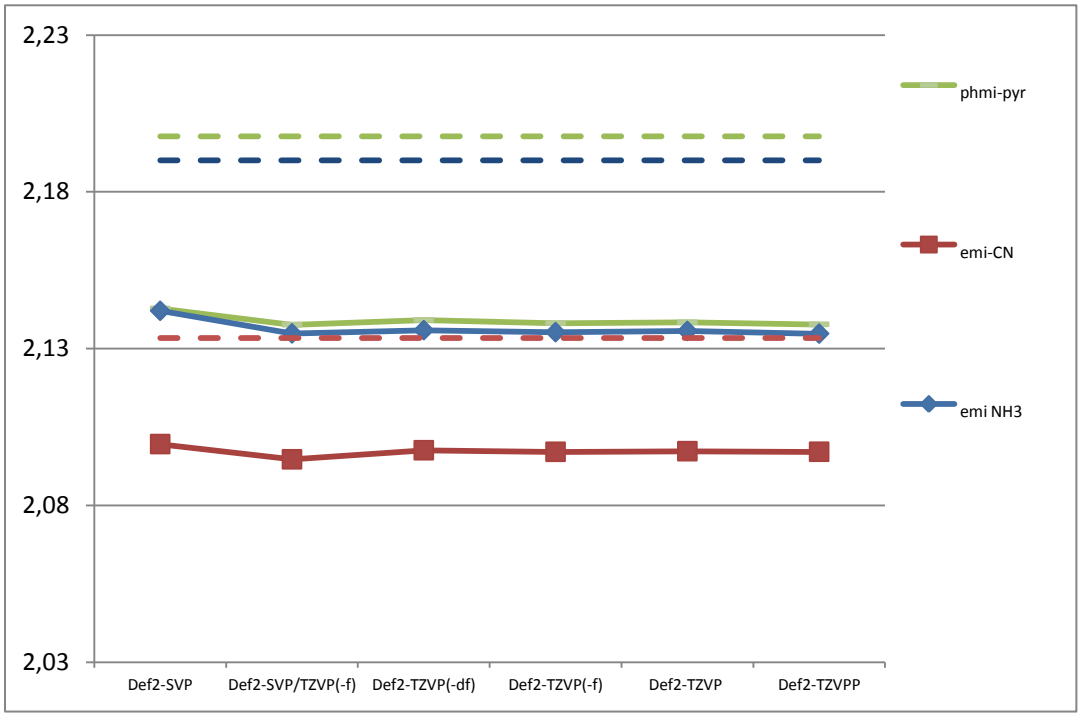

Figure A9: g_{iso} component of $[Ni^{III}(phmi)(py)]^{-}$ $[Ni^{III}(emi)(CN)]^{2-}$ and $[Ni^{III}(emi)(NH_3)]^{-}$. Experimental (dotted lines) and computed values (straight lines).

4.2. The Ni–C state

Electronic structure and magnetic properties including the second coordination shell

Abstract

We have investigated the key catalytic state Ni–C of *Desolfovibrio vulgaris* Miyazaki F hydrogenase using a cluster model that includes the truncated amino acids of the entire second coordination sphere of the enzyme. The optimized geometries, computed g–tensors, hyperfine couplings constants and IR stretching frequencies all agree well with experimental values. For the hydride in the bridging position, only a single minimum on the potential energy surface is found, indicating that the hydride bridges and binds to both nickel and iron. The influence of the second coordination sphere on the electronic structure is investigated by comparing results from the large cluster models with truncated models. The largest interactions of the second coordination sphere with the active site concern the hydrogen bonds to the CN ligands, which modulate the bond between iron and these ligands. Secondly, the electronic structure of the active site is found to be sensitive to the protonation state of His88. This residue forms a hydrogen bond to the spin–carrying sulfur atom of Cys549, which in turn tunes the spin density at the nickel and coordinating sulfur atoms. In addition, the unequal distribution of spin density over the equatorial cysteine residues results from different orientations of the cysteine side chains, which are kept in their particular orientation by the secondary structure of the protein.

4.2.1. Introduction

For the paramagnetic Ni–C state, electron density at the variable bridging position is absent in the X–ray structure [1-3]. However, ENDOR spectroscopy has revealed that the bridging ligand in the Ni–C state is occupied by a hydride [4-7]. The overall spin state of the active site has been determined to be a doublet arising from the d^7 configuration of Ni(III). The iron assumes a low–spin Fe(II) configuration.

A significant number of computational studies has been reported with the main focus being the structural and mechanistic aspects of [NiFe] hydrogenases [8-15]. Several reviews focusing on theoretical studies are available [16-17]. In the computational studies of [NiFe] hydrogenase, density functional theory (DFT) [18-20] on truncated cluster models has been used almost exclusively. The by far most frequently used model system includes only the two metal atoms and their first coordination shell. In a few studies, larger models were employed. Amara et al. [15] treated the [NiFe] active site by making use of the QM/MM procedure and still used the first coordination sphere for the QM part. Another QM/MM study for the oxidized states Ni–A and Ni–B was reported by Jayapal et al. [21] and Söderhjelm [22]. They focused on the geometries in comparison with crystal structures and the presence of either OH^- (Ni–B) or OOH^- (Ni–A) in the bridging position [21] and oxidized thiolate ligands [22]. The most extensive work in terms of cluster models has been reported by Siegbahn et al., who performed calculations using a QM cluster model with 120 atoms. Using this model, the oxygen inhibited states of the enzyme were investigated as well [23]. As opposed to Jayapal, Siegbahn found a discrepancy with experiment, in that the putative OOH^- ligand prefers to bind end–on, i.e., the ligand is monodentate to nickel. A similar model was used for a study on the reaction mechanism of the enzyme [17]. In a more recent contribution, the same group used a large quantum mechanical cluster model in conjunction with a QM/MM approach in order to explore the reaction mechanism of the hydrogenase enzyme [14].

The majority of theoretical studies focus on the calculation of energies. Concerning DFT calculations of EPR parameters, Stein et al. have performed extensive calculations and compared them to experimentally available data. In these studies small cluster models were used without exception [24-30]. Stadler et al. performed calculations on EPR parameters with a model system, which included a His88 and Arg479 fragment (amino acid numbering according to the *Desulfovibrio (D.) vulgaris* Miyazaki F enzyme) [31-32]. Furthermore, DFT calculations of [NiFe] hydrogenase using a small model with one or two additional residues have often been employed in conjunction with spectroscopic measurements to interpret and understand the obtained experimental results [33-35].

Given the seemingly contradictive state of the art in the literature for the oxidized states of the [NiFe] hydrogenase – renewed X–ray experiments for Ni–A for *Allochromatium vinosum* hydrogenase now suggest the presence of a bridging OH^- rather than OOH^- (Ogata, H., personal communication)[36] – and for the influence of the second coordination sphere of the [NiFe] center, we provide a detailed DFT–study of the structurally well characterized and less controversial Ni–C state of [NiFe] hydrogenase. We include the complete second coordination sphere in the calculation up to a total of 165 atoms. The goal of the study is to establish a realistically large cluster model for the Ni–C state that serves as basis for further mechanistic and spectroscopic explorations. To this end, the focus of the study lies on the calculation of spectroscopic parameters rather than on total energies. The computed properties are compared to a large body of available experimental data including those from X–ray diffraction, EPR spectroscopy and FTIR spectroscopy. The influence of the second coordination sphere on the spectroscopic properties of the active site is investigated in detail by using various truncations of the largest cluster model.

The results and discussion section is divided into the following parts: first, the hydride in the bridging position is investigated. Three possible binding modes have been found. Secondly, the influence of the extended coordination sphere on the geometry of the active site is considered. This is followed by an examination of the electronic structure related to the ligand field. Lastly, spectroscopic parameters, i.e., g values, hyperfine and quadrupole coupling constants as well as IR stretching frequencies are compared to experiment. In each section the influence of His88 is examined by comparing the HisHδ model, HisHε and HisHδHε models.

4.2.2. Model Systems

In addition to the HisHδ model, HisHε and HisHδHε models, as described in chapter 3, four truncated models (Figure 1) have been considered for the investigation of the influence of the second coordination sphere. First, a small model is examined which contains the first coordination sphere consisting of the two metals, the CO ligand, the two CN^- ligands, the four cysteine residues and the bridging hydride. Second, the hydrophobic model contains, in addition to the small model, Ala477, Pro478 Leu482, Val500 and Pro501; third, in the polar model, Val83, Arg479, Pro501 and Ser502 have been added to the small model; fourth, the ionic model contains Glu34, His88, Asp123 and Arg479 in addition to the small model. An overview of the number of atoms, charge, spin and basis sets for the different models is given in Table A1 of the supporting information.

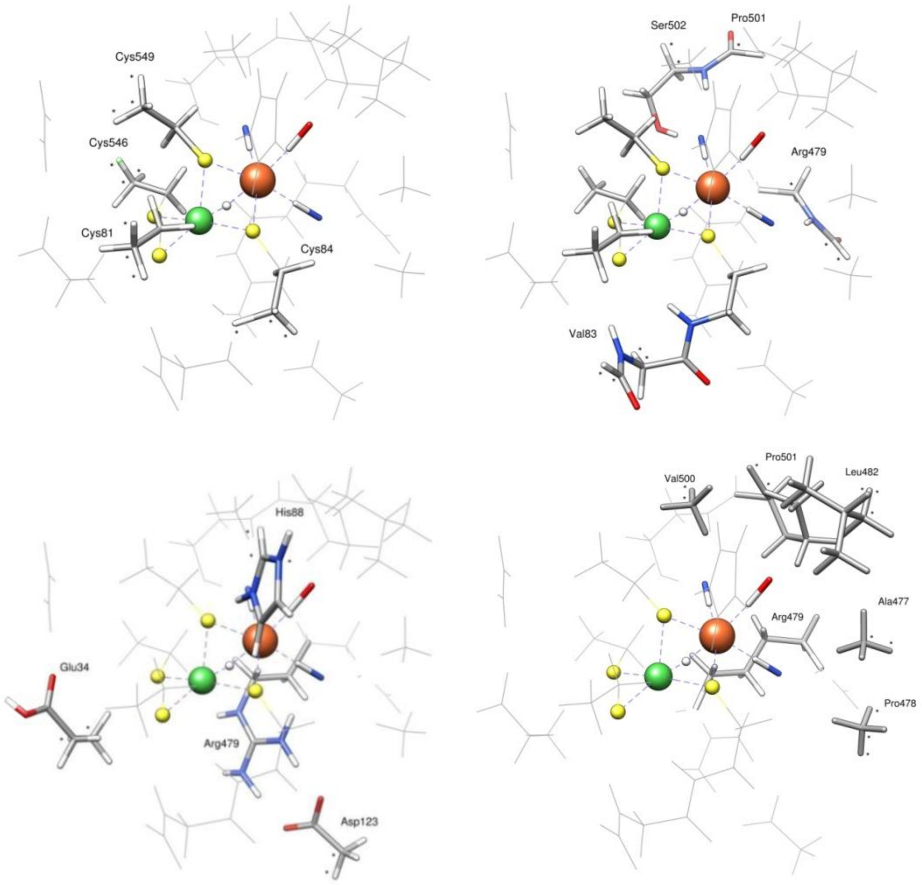

Figure 1: Top: Small model (left) and polar model (right) highlighted as stick diagrams. Bottom: ionic (left) and hydrophobic models (right). Asterisks indicate the atoms that have been constrained during the geometry optimization.

4.2.3. Potential energy surface related to the bridging hydride

Experimentally, the Ni–C state is found to carry a hydride in a bridging position between Ni and Fe [4-7]. In order to assess, whether the hydride actually binds only to nickel, to iron, or to both metal ions, a two–dimensional potential energy surface has been computed. For this computation, the Ni–H distance and H–Ni–Fe angle have been stepwise varied. With exception of the aforementioned Ni–H angle and H–Ni–Fe distance, the hydride ligand has been allowed to fully relax while all other atoms have been fixed. Since only relative energies are of chemical relevance, the absolute energy is set to zero at the energy minimum. The potential energy surface, given in Figure 2a, reveals that only one

minimum is present. The structure that corresponds to this minimum is shown in the supporting information.

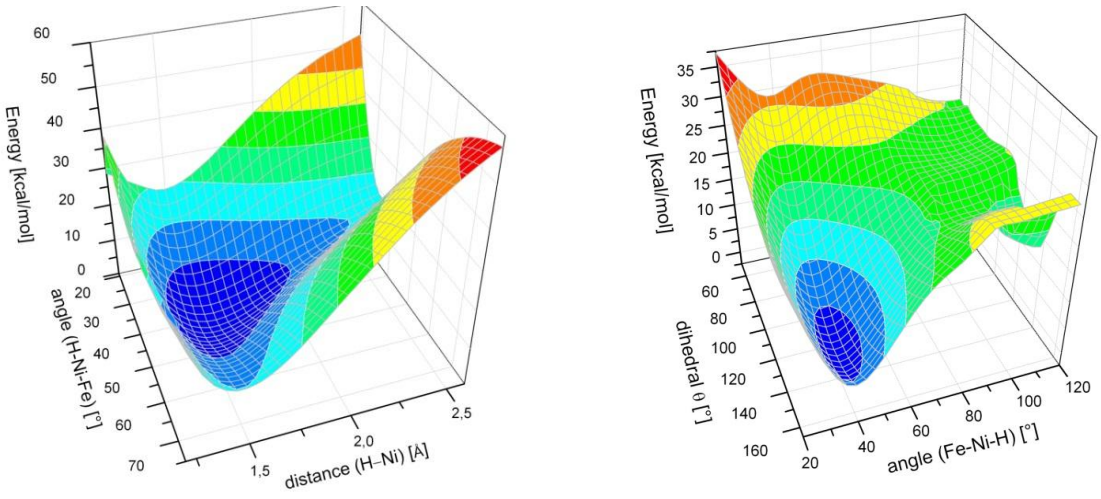

a **b**

Figure 2: (a) Potential energy surface (small model) as a function of the hydride–nickel–iron angle and the hydride nickel bond distance. (b) Potential energy surface (small model) as a function of the iron–nickel–hydride angle and the S(Cys84)–Ni–Fe–hydride dihedral angle. A color coding of the surface is added in order to facilitate the interpretation of the figure. The lowest level (dark blue) concerns an energy window of 0 – 2.5 kcal/mol. Each subsequent color spans a window of 5 kcal/mol (in the order blue, cyan, turquoise, green, yellow, orange, red).

Another potential energy surface is shown in Figure 2b where, along with the H–Ni–Fe angle, the dihedral angle Sγ(Cys84)–Ni–Fe–H (θ) is varied in order to move the hydride out of the equatorial plane towards the free coordination position opposite to Cys549. A total of three local minima can be identified in this plot. First, a minimum is present at θ = 132° and a Fe–Ni–H angle of 41°, corresponding to the minimum of Figure 2a, i.e., with the hydride in the bridging position. This is the lowest of the three minima and corresponds to the global minimum. Secondly, upon increasing the H–Ni–Fe angle to a value of 120° another local minimum is approached. For this minimum, the hydride has entirely moved out of the coordination environment of nickel and iron and binds in form of a proton to Cys546. Hence, in this structure, the nickel is formally reduced from trivalent to monovalent.

The third local minimum is found at θ = 111° and a Fe–Ni–H angle of 63°. In this case, the hydride occupies the axial coordination position at the nickel, i.e., it opposes the sulfur of Cys549. This

structure is by 22 kcal/mol higher in energy than that of the lowest minimum. The energy surface around this minimum is rather flat, i.e., the energy is rather insensitive to small geometric distortions. Hence, the hydride is not confined to the actual minimum. In summary, the Ni–C state is associated with a structure in which the hydride is found in the bridging position between Ni and Fe. Two other minima have been identified that are significantly higher in energy.

4.2.4. Geometries and the influence of the second coordination sphere

Selected computed bond lengths of the bimetallic metal core within the HisHε model and its coordinating ligands are presented in Tables S2 and S17 of the supporting information. The Ni–S distances range from 2.18 Å (Cys546) up to 2.34 Å (Cys549). These distances are inversely related to the corresponding Mayer bond orders [37]. In general, the optimized geometries vary only slightly when the HisHδ and HisHδHε models are considered. The largest difference amounts to only 0.02 Å for the Ni–S(Cys549). The computed Ni–S bond lengths are systematically smaller by about 0.05 Å to 0.1 Å in comparison to the X–Ray data. This effect is especially pronounced for the Ni–S(Cys549) distance. The Ni–Fe distance does not change among these models and is smaller by 0.06 Å than found in the crystal structure. Also, the computed distance of the ε–nitrogen of His88 and the sulfur of Cys549 depends only slightly on the protonation state of His88 (variation of 0.1 Å). Owing to the presence of the additional hydrogen bond of Hε(His88) with Sγ(Cys549), the HisHε model is 13.9 kcal/mol lower in energy than the HisHδ model.

Concerning the orientation of the axial cysteine, the dihedral angle Hβ1(Cys549)–Cβ(Cys549)–Sγ(Cys549)–Ni of −1.5° for the HisHε model matches the value −3.4° from the X–Ray structure rather well. In the case of the small, polar and ionic models the dihedral angle is about −8° and therefore deviates more from experiment. An exception is the hydrophobic model, which yields values similar to the complete models. These findings suggest that the hydrophobic environment influences the orientation of the β–CH_2 group. Careful inspection of the X–ray structure reveals that a valine residue (Val500) is placed in close proximity to the β–CH_2 group with an H–H distance of 2.06 Å from Hβ1(Cys549). This is smaller than the van der Waals distance for two hydrogen atoms (2.2 Å).

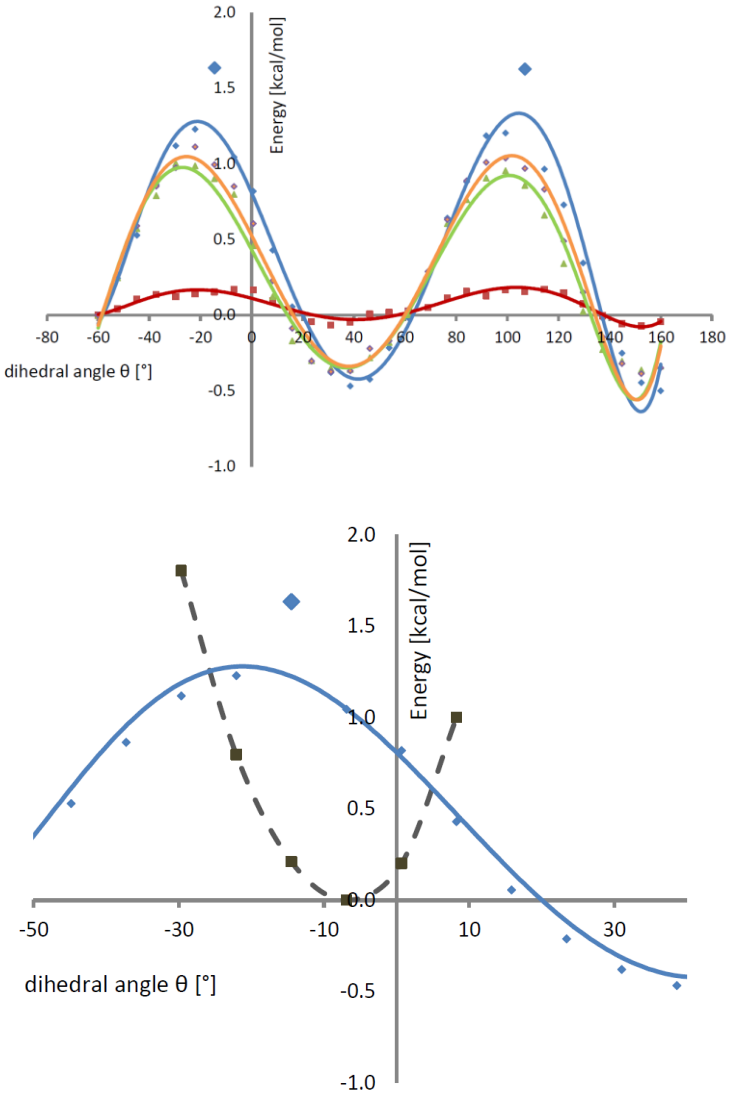

Figure 3: (a) Potential energy scan as a function of the Hβ1(Cys549)–Cβ(Cys549)–Sγ(Cys549)–Ni dihedral angle; the ethyl–group of Cys549 has been replaced with a methyl group. Color code: red (small model), blue (HisHε model), green (Small model with Val500 fragment), orange (Small model with Val500 fragment and van der Waals correction). The energy at −60° has been arbitrarily set to zero. (b) Potential energy surface of the small model with a constrained Cys549 ethyl group (dashed grey line) and of the HisHε model (blue), as in (a).

In order to gain more insight into which factors determine the orientation of Cys549, a scan of Hβ1(Cys549)–Cβ(Cys549)–Sγ(Cys549)–Ni dihedral angle has been performed using the small and the HisHε models (Figure 3a). The Cys549 ethyl group has been replaced by a methyl group, which removes the constraints set on Cα(Cys549) and its protons. Instead, Cβ(Cys549) has been constrained. The energies of the plots have been set to zero at 60° and display a periodicity of about 120°. Strikingly, the nearest energy minimum is reached at a dihedral angle of +40° in all models. Only when Cys549 is modeled as an ethylthiolate group with constraints on Cα(Cys549) and its protons, the energy minimum is reached again at a dihedral angle of −8° in the small model (Figure 3b) and of −1.5° in the HisHε model. These constraints restrain the movement of the thiolate side

chain and are used in the larger models to simulate the restraining influence of the protein environment. Additionally the change of the energy minimum from an angle of −8° to −1.5° upon inclusion of Val500 indicates that this residue has a minor influence on the orientation of Cys549. The energy barriers for rotation are about 2 kcal/mol in all models. The small model augmented with Val500 almost completely restores the barrier found in the HisHε model. Thus, Val500 limits the rotational freedom of Cys549. The thermodynamic equilibrium at room temperature between the structures of minimum and maximum energy can be estimated from their energy difference, neglecting entropic and enthalpic terms, by —— . Hence, it is 40 times more likely to find the system at the minimum at a dihedral angle of +40° than at the maximum at −25°.

4.2.5. Electronic Structure

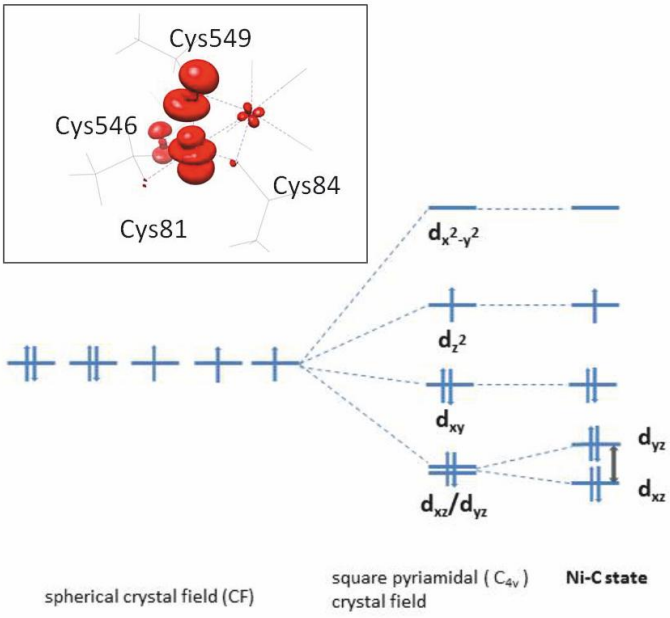

Figure 4: Crystal field splitting of the Ni center in [NiFe] hydrogenases. The inset shows the computed spin density.

A schematic picture of the crystal field splitting for the nickel atom in [NiFe] hydrogenases is shown in Figure 4. The axes system is defined as follows: the z–axis is parallel to the Ni–Sγ(Cys549) bond and the x–axis is chosen such that the Ni–H^- bond is located in the xz plane. The nickel atom is formally in a +3 oxidation state with a $3d^7$ electron configuration. Application of an idealized square planar crystal field (C_{4v} point group) splits the energies of the d–orbitals, such that the d_{xz} and d_{yz} orbitals span a two–dimensional irreducible representation and remain degenerate. The seven electrons

result in a d–orbital configuration $d_{xy}^2\ d_{xz}^2\ d_{yz}^2 d_{z2}^1\ d_{x2-y2}^0$. In [NiFe] hydrogenases, the symmetry is reduces to C_1 and the d_{xz} and d_{yz} orbitals also become non–degenerate. The energy splitting of the d_{xz} and d_{yz} orbitals is reflected by the rhombicity of the g–tensor and the directions of the principal axes (*vide infra*). The inset in Figure 4 displays the spin density of the Ni–C state, calculated from the small model. In agreement with the crystal field scheme in Figure 4 and with earlier calculations using models that include only the first coordination sphere [24-29, 31-32], the spin is indeed predominantly found in a d_{z2} orbital at the nickel. Additionally, there is a significant delocalization of spin into a 3p orbital of the sulfur atom of the apical Cys549 and to a smaller extend, into a 3p orbital of the sulfur atom of the equatorial Cys546. At the iron atom, the inorganic CN^- and CO ligands give rise to a large crystal field splitting. The iron atom therefore resides in the low–spin, Fe(II) oxidation state, in which the 3d orbitals of t_{2g} symmetry are doubly occupied.

	Small	**Polar**	**Hydrophobic**	**Ionic**
Sγ(Cys81)	–0.02	–0.02	–0.02	–0.02
Sγ(Cys84)	–0.01	–0.02	–0.01	–0.02
Sγ(Cys546)	0.05	0.06	0.04	0.06
Sγ(Cys549)	0.26	0.27	0.26	0.23
Ni	0.72	0.71	0.73	0.75
Fe	0.01	0.00	0.01	0.00
H^-	–0.01	–0.01	–0.01	–0.01
	HisHδ	**HisHε**	**HisHδHε**	
Sγ(Cys81)	–0.02	–0.02	–0.02	
Sγ(Cys84)	–0.02	–0.02	–0.02	
Sγ(Cys546)	0.05	0.06	0.07	
Sγ(Cys549)	0.32	0.24	0.19	
Ni	0.67	0.74	0.78	
Fe	0.00	0.00	0.00	
H^-	0.00	–0.01	–0.01	

Table 1: Selected Mulliken spin populations in all employed models for the Ni–C state of [NiFe] hydrogenase.

As evident form a Mulliken spin population analysis given in Table 1, the spin density at Sγ(Cys549) and Ni increases and decreases, respectively, when comparing the models in the order HisHδHε, HisHε and HisHδ. This can be understood, since protonation at Nε of His88 and hydrogen bond formation stabilizes the sulfur 3p orbitals with respect to the nickel 3d orbitals. This is corroborated by the observation that the spin population at Sγ(Cys546) decreases concomitantly with the spin population at Ni. The spin population at Sγ(Cys81), Sγ(Cys84) and the bridging hydride is slightly negative.

The delocalization of unpaired electron density into only two of the four coordinating sulfur atoms, i.e., Sγ(Cys549) and Sγ(Cys546), needs further explanation. Sγ(Cys549) takes the apical position of the square pyramidal coordination sphere and can therefore form a σ–bonding interaction with the d_{z^2} orbital at nickel. Interaction of the unpaired electron with the free electron pair at the sulfur results in a partial bond with a formal bond order of ½ and delocalization of spin into the sulfur $3p_z$ orbital. Among the equatorial ligands, only Sγ(Cys546) displays a π–like interaction of its p_z orbital with one of the lobes and the ring–shaped part of the d_{z^2} orbital. In order to rationalize this finding, the bond order of this interaction, the spin density at Sγ(Cys546) (Figure 5a) and the spin population of Ni (Figure 5b) have been investigated as a function of the Cβ(Cys546)–Sγ(Cys546)–Ni–Sγ(Cys549) dihedral angle. For this purpose, a relaxed surface scan has been performed using the small model system with a methylthiolate group at Cys546 and Sγ(Cys546) has been constrained. When the dihedral angle amounts to 70°, the overlap between the 3p orbital at Sγ(Cys546) and the $3d_{z^2}$ orbital at Ni becomes maximum. Accordingly, the spin density at Sγ(Cys546) and the Sγ(Cys546)–Ni Mayer bond order are largest. On the other hand, when the dihedral angle becomes 170°, poor overlap exists, causing the spin density at Sγ(Cys546) to vanish and the bond order to reach its minimum value. As evident from Figure 5b, the Mulliken spin population of the nickel exhibits the opposite dependence as compared to the spin density at Sγ(Cys546). In the crystal structure, the corresponding dihedral angles for the side chains of Cys81 and Cys84 amount to −18° and −159°, respectively, and that of Cys546 amounts to 77°. Consequently, delocalization of the spin over the equatorial ligands can only occur for Cys546.

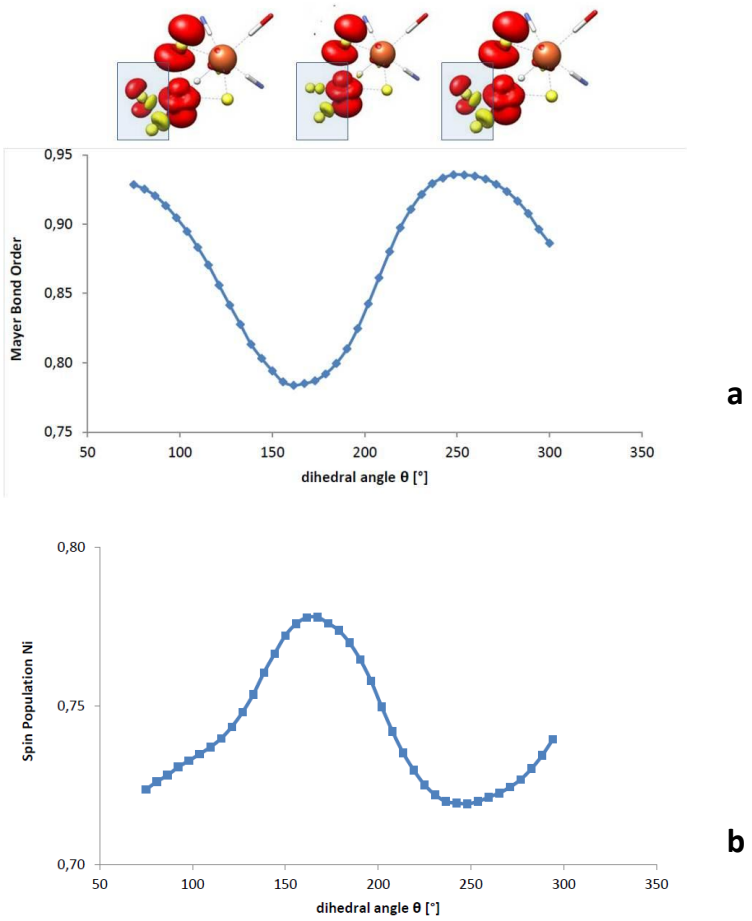

Figure 5: (a) Bond order of the Ni–Sγ(Cys546) bond and (b) spin population at Ni as a function of the Cβ(Cys546)–Sγ(Cys546)–Ni–Sγ(Cys549) dihedral angle. The insets at the top of the figure highlight the spin density at Cys546, i.e. the part of the spin density that changes upon rotation about the dihedral angle.

Mayer bond orders are given in Table A4 of the supporting information. The apical Ni–S(Cys549) bond has the smallest bond order of about 0.6. The corresponding sulfur p_z orbital overlaps with the nickel d_z^2 orbital in an σ–type manner, which results in a doubly occupied bonding orbital (σ) and a singly occupied antibonding orbital (σ*) which corresponds to a formal bond order of ½. The sulfur atoms of the equatorial cysteines Cys81, Cys84 and Cys546 are involved in a σ–bonding interaction with the low–lying d_{x2-y2} orbital at Ni. The largest Mayer Bond order is found for Cys546, since the sulfur atom of this residue additionally has a π–like interaction with the d_z^2 orbital, as described in the previous paragraph. Accordingly, the bond order for the Ni–S bond of Cys546 is largest and the bond length is shortest (Table A2 of the supporting information).

In summary, the protonation state of His88 and its hydrogen bond to Sγ(Cys549) influence the spin density distribution over Ni and Sγ(Cys549). Thus, the spectroscopic properties, especially the g–tensor, and hyperfine coupling constants are expected to depend on the protonation state of His88

as well. *Vice versa*, comparison of these observables with calculations allows a determination of the protonation state of His88. This will be demonstrated in the subsequent section.

4.2.6. Magnetic spectroscopy

g–tensor

Computed and experimental g–values are given in Table 2. For the HisHδ, HisHε and HisHδHε models, the isotropic g_{iso} values are smaller than the experimental values by 30%, 23% and 15%, respectively. Such a systematic underestimation is not uncommon and has been examined before [38]. The tensor is rhombic with $g_1 < g_2 < g_3$ which is reproduced by all models and therefore determined by the first coordination sphere. The largest g shift of the g_3 value is found for the HisHδHε model, which also gives the largest spin population at Ni. The directions of the principal axes of the g–tensor are given in Figure A4 of the supporting information. The g_1 axis is aligned along the z–axis of the d_{z^2} orbital, g_2 approximately along the Ni–Sγ(Cys84) and Ni–Sγ(Cys546) directions and g_3 along the Ni–Sγ(Cys81) and Ni–H directions. Computed and experimental direction cosines are given in Table A5 of the supporting information and agree well.

	g_1	g_2	g_3	g_{iso}
Small	2.03	2.11	2.16	2.10
Polar	2.03	2.11	2.15	2.10
Hydrophobic	2.03	2.11	2.16	2.10
Ionic	2.03	2.14	2.19	2.12
HisHδ	2.03	2.10	2.13	2.09
HisHε	2.03	2.12	2.16	2.10
HisHδHε	2.03	2.13	2.18	2.11
Exp. [39]	2,01	2,15	2,22	2,13

Table 2: Calculated g–values for all models and experimental g–values for the Ni–C state of *D. vulgaris* Miyazaki F hydrogenase in the Ni–C state.

The g values can be interpreted in the framework of ligand field theory by means of second order perturbation theory [40-41]. The z–component equals the free electron g–value as the l_z angular momentum matrix elements between the d_{z^2} orbital and any other d orbital are zero. Positive contributions to the g_y and g_x components arise from excited states in which the spin–down electron is promoted from the d_{xz} and d_{yz} orbitals to the d_{z^2} orbital, respectively. Since the hydride is a weak ligand in terms of ligand field theory, the d_{xz} orbital is lower in energy than the d_{yz} orbital, with the x–

direction being parallel to the Ni–H bond direction. The energy difference $E_{z2} - E_{xz}$ will be larger than $E_{z2} - E_{yz}$. Consequently, the $g_2(g_y)$ value is smaller than the $g_3(g_x)$ value and the g_x axis is parallel to the direction of the weakest ligand field, i.e., along the Ni–H bond direction, in–line with experiment and calculation.

Hyperfine coupling constants

Coupling constants for the hydride, for the β–CH_2 protons of Cys549 and Cys546 and for the ε nitrogen of His88 are considered next. Calculated direction cosines for these hyperfine tensors along with computed ^{61}Ni, ^{57}Fe and ^{33}S hyperfine tensors and experimental ones are given in the supporting information.

Table 3 displays the hyperfine coupling constants of the bridging hydride in all models**.** The computed hyperfine tensor shows a negative isotropic coupling constant of about −25 MHz, in line with the negative spin population found of this atom (Table 1). The experimentally determined coupling is pronouncedly smaller in magnitude with an isotropic value of −3.5 MHz.

A negative isotropic hyperfine coupling constant can be traced back to negative spin density at the nucleus, which is the result of spin polarization induced by the unpaired electron at the nickel: owing to an energetically favorable exchange interaction with the unpaired electron, the electron pair of the Ni–H σ–bond becomes polarized such that the density of the spin–up (α) electron of the electron pair increases at Ni and decreases at H^- and *vice versa* for the spin down (β) electron. The isotropic coupling constant of H^- is less negative for the HisHδ model and more negative for the HisHδHε model. This can be rationalized in terms of the Mulliken spin populations (Table 1). The spin at nickel is smallest for the HisHδ model and largest for the HisHδHε model. The more spin is located at the nickel, the more efficiently the electron pair of the Ni–H bond can be polarized.

The calculated dipolar coupling constants are also systematically larger in magnitude than the experimental coupling constants. In order to investigate whether the B3LYP functional overestimates the spin polarization of the Ni–H bond, a calculation of the HisHε model with the BP86 functional has been performed. This calculation gave an isotropic coupling constant of −2.6 MHz and dipolar coupling constants of 17.2, −6.7, −10.4 MHz, in good agreement with experiment and with earlier calculations which were performed with the BP86 functional and a Slater–type DZP basis set [30]. Indeed, the seemingly significant deviations of the hyperfine tensors calculated with the B3LYP functional as compared to the experimental one mainly arise from a slightly overestimated spin polarization, to which the hydride is very sensitive, given that it is directly coordinated to Ni and located next to the bulk spin density. Additionally, in order to test the sensitivity of the hyperfine coupling constants to the exact position of the hydride, single point calculations have been carried

out, in which the position of the hydride was slightly varied. The calculations demonstrate that the isotropic coupling constant becomes less negative by about 5 MHz if the position of the hydride is changed by about 0.2 Å, at the expense of raising the energy by about 5 kcal/mol. This is insufficient to bring experiment and theory into agreement. Thus, as demonstrated by the good agreement of the hyperfine coupling constants in the test calculation with BP86, and the observation that the difference of 25 MHz between experiment and theory amounts to only 1.7% in terms of 1s spin density at the hydride, which is presently near the limit by which spin densities can be reproduced by DFT calculations, the agreement between experiment and theory for the hyperfine tensor of the hydride is considered quite good. This indicates that the overall spin density distribution near the nickel is well reproduced by the DFT calculations.

		A_{dip}		A_{iso}
Small	25.9	−11.1	−14.9	−25.8
Polar	25.4	−10.7	−14.6	−26.7
Hydrophobic	26.1	−11.0	−15.0	−28.1
Ionic (H^+ His88)	28.2	−12.7	−15.6	−29.6
HisHδ	23.5	−9.6	−13.9	−20.4
HisHε	26.5	−11.4	−15.1	−26.8
HisHδHε	28.2	−12.5	−15.7	−31.9
Exp.[4]	21.9	−7.3	−14.5	−3.5

Table 3: Calculated and experimental ^{1}H hydride dipolar and isotropic hyperfine coupling constants A_{dip} and A_{iso} [MHz].

The ^{1}H hyperfine coupling constants of the β–CH_2 group of Cys549 are given in Table 4. The isotropic component of the first proton H(1) is, in the case of the HisHε model, in agreement with experiment. On the other hand, the corresponding value in the HisHδ model seems to be significantly larger by more than 6 MHz as compared to the experimental value and that of the HisHδHε model too small by more than 4 MHz. The calculated magnitude of the coupling constants correlates with the Mulliken spin populations at the sulfur of Cys549 given in Table 1. Concerning the second proton H(2), the experimental and calculated isotropic values are smaller than those of the first proton H(1). This is especially pronounced for the HisHδ model which gives an isotropic hyperfine coupling of its second proton H(2), which is in excellent agreement with experiment [4]. The HisHε model gives an isotropic value that is slightly smaller (about 2 MHz) compared to experiment but still can be considered satisfactory. The ^{1}H hyperfine tensors of the β–CH_2 protons of Cys549 are axial and dominated by the isotropic components, in agreement with experiment.

H(1)	A_1	A_2	A_3	A_{iso}
Small	10.9	12.6	17.6	13.7
Polar	11.4	13.1	18.0	14.2
Hydrophobic	12.4	14.3	19.5	15.4
Ionic (H^+ His88)	4.1	6.0	11.1	7.1
HisHδ	17.0	18.9	24.0	20.0
HisHε	9.8	11.7	16.7	12.7
HisHδHε	6.2	8.2	13.4	9.2
Exp. [4]	11.3	11.9	17.9	13.7

H(2)	A_1	A_2	A_3	A_{iso}
Small	10.9	11.7	15.5	12.7
Polar	10.8	11.5	15.5	12.6
Hydrophobic	8.2	8.8	12.8	9.9
Ionic (H^+ His88)	6.2	7.1	10.2	7.9
HisHδ	9.8	10.4	15.1	11.8
HisHε	7.9	8.5	12.3	9.5
HisHδHε	5.9	6.7	10.0	7.5
Exp. [4]	10.3	10.7	14.5	11.8

Table 4: Calculated and experimental hyperfine coupling constants [MHz] of the two protons belonging to β–CH_2 group of Cys549.

In order to further analyze the hyperfine couplings of the β–CH_2 protons of Cys549, the isotropic couplings are plotted against the Hβ1(Cys549)–Cβ(Cys549)–Sγ(Cys549)–Ni dihedral angle (Figure 6). The plots show a cosine–squared dependence for all employed models. In general, such a rotational dependence of the isotropic hyperfine coupling of a C–H fragment is found if the atom adjacent to the C atom carries spin density in one of its p–orbitals. In the case of the Cys549 sulfur, spin density is indeed present in a p_z orbital. The maxima of the corresponding plots are found for a parallel alignment of the C–H bond relative to the lobes of the p–orbital. In a model where the spin carrying orbital is a $3p_z$ orbital, this occurs for H(1) at a dihedral angle of 0° and 180°. Minima arise when the C–H bond lies in the nodal plane of the p_z orbital, at 90° and 270° for H(1). Inspection of the plots reveals that a maximum and minimum are found at about 15° and 100° for H(1). Hence, the calculated 3p orbital at Sγ(Cys549) is not completely aligned with the Ni–Sγ(Cys549) axis but rather rotated by about 15° to 20°.

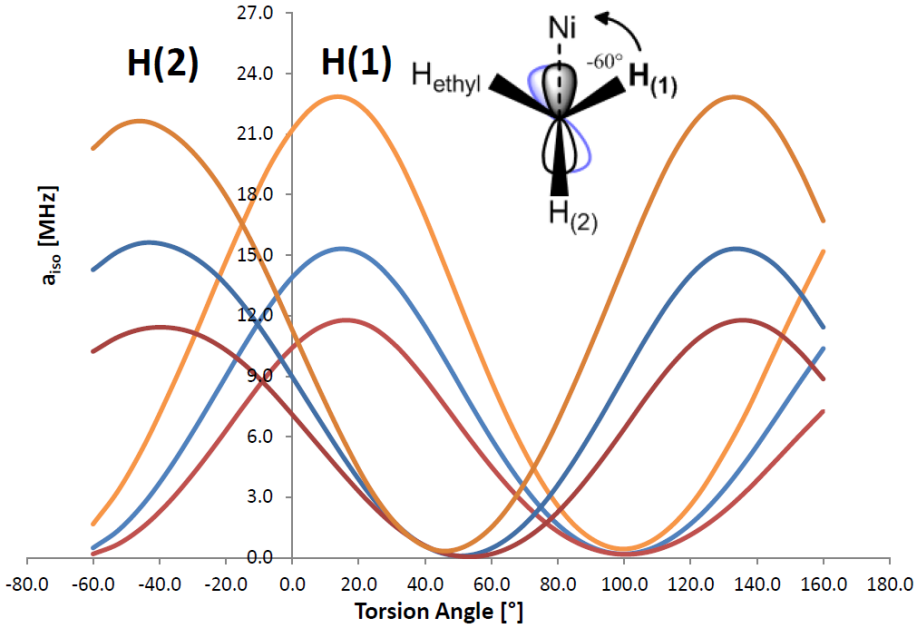

Figure 6: Isotropic hyperfine coupling constant of the β–CH_2 protons of Cys549 as a function of the Hβ1(Cys549)–Cβ(Cys549)–Sγ(Cys549)–Ni dihedral angle. Color Code: small model with cationic His88 (red), small model with neutral His88 and pronotated at Nε (blue), small model with neutral His88 and pronotated at Nδ (orange). Inset: Newman projection along the Cβ(Cys549)–Sγ(Cys549) a dihedral angle of −60° with the idealized orientation (grey) and the actual torsion of the sulfur p_z–orbital (blue).

The amplitudes of the curves differ depending on the protonation state of His88. The largest amplitude is found for the HisHδ model, the smallest for the HisHδHε model. This ordering correlates with the spin populations of Table 1. At −8°, i.e., the equilibrium angle for the small, the polar and the ionic models, the curves for H(1) and H(2) approximately cross. This is in line with the hyperfine coupling constants presented in Table 4. For the hydrophobic model and the HisHε, HisHδ and HisHδHε models, the equilibrium angle is close to zero, resulting in slightly inequivalent hyperfine coupling constants of H(1) and H(2). Overall, the HisHε model gives best agreement with experiment.

For the β–CH_2 protons of Cys546, only a single experimentally determined coupling constant has been reported [4]. The calculated ^{1}H hyperfine couplings of the β–CH_2 protons of Cys546 are presented in Table 5. The isotropic and anisotropic coupling constants for H(1) in the HisHε and HisHδHε models are in good agreement with the experimental findings. The plots for the rotational dependence of Cys546 β–CH_2 (see Figure A6 of the supporting information) are analogous to those in Figure 7. In contrast to Cys549, the 3p orbital at Sγ(Cys546) is oriented perpendicular to the Ni–S bond. Accordingly, a maximum and a minimum are found at about 110° and 20° in the case of H(1). For H(2) the maximum is located at about –10° and the minimum at 80°. At the dihedral angle of the

HisHε model (θ ≈ −35°) the protons H(1) and H(2) have similar coupling constants. For the HisHδHε model, the coupling constants of H(1) and H(2) differ even less.

H(1)	A_1	A_2	A_3	A_{iso}
Small	5.4	6.0	10.4	7.3
Polar	7.0	7.8	11.7	8.8
Hydrophobic	4.5	5.0	9.4	6.3
Ionic (H^+ His88)	7.3	7.9	12.3	9.2
HisHδ	6.2	6.9	10.9	8.00
HisHε	6.8	7.4	11.7	8.6
HisHδHε	7.1	7.8	12.1	9.0
Exp. [4]	7.3	7.3	12	8.9

H(2)	A_1	A_2	A_3	A_{iso}
Small	3.4	3.6	7.5	4.8
Polar	4.5	4.7	8.5	5.9
Hydrophobic	3.5	3.5	7.4	4.8
Ionic (H^+ His88)	7.0	7.3	11.3	8.5
HisHδ	3.5	3.6	7.3	4.8
HisHε	4.5	4.6	8.6	5.9
HisHδHε	6.3	6.5	10.5	7.7

Table 5: Calculated hyperfine coupling constants [MHz] of the two protons belonging to β–CH_2 group of Cys546. An experimental value has only been reported for one of the two hydrogen atoms.

Computed ^{14}N hyperfine tensors of the Nε of His88 and the experimental data obtained by HYSCORE spectroscopy [4] are presented in Table 6. The axiality of the tensor is reproduced by all models. This confirms *a posteriori* the validity of the restriction to an axial tensor imposed in the experimental simulation procedure [4]. For HisHε and HisHδ, the computed perpendicular component of the hyperfine tensor matches the HYSCORE data with a deviation from experiment of +0.8 MHz. The computed parallel components of the axial hyperfine tensor are larger by a factor of about two as compared to experiment. For the HisHδHε model, the absolute values are even significantly larger and in worst agreement with experiment. The HisHδ and HisHε models are in better agreement with experiment.

	A_1	A_2	A_3	A_{iso}	P_1	P_2	P_3
HisHδ	2.9	2.9	3.5	3.1	0.95	1.07	−2.02
HisHε	2.7	2.8	3.5	3.0	0.36	0.66	−1.02
HisHδHε	4.5	4.5	5.3	4.8	0.02	0.66	−0.70
Exp. [4]	1.5	1.5	2.7	1.9	0.28	0.66	−0.94

Table 6: Calculated and experimental ^{14}N hyperfine and quadrupole coupling constants [MHz] for the ε–nitrogen of His88.

Nuclear quadrupole coupling constants

The calculated and experimental quadrupole tensors of the ε–nitrogen of His88 are given in Table 6. From the table, it is apparent that only the HisHε model is able to reproduce the experimental values. The calculated principal values are too large in the case of the HisHδ model, and, in addition, are close to axial, which is not observed experimentally. For the HisHδHε model, the P_1 value is almost zero, which leads to a much more rhombic tensor than experimentally observed. In summary, the nuclear quadrupole coupling constants strongly suggest that histidine 88 is protonated at Nε and deprotonated at Nδ [4, 42].

4.2.7 CN^- and CO stretching frequencies

CN^- and CO stretching frequencies are given in Table 7. DFT systematically underestimates the CO stretching frequencies in metal–carbonyl compounds. Hence, a constant shift of about 28 cm^{-1} has been proposed to account for this deviation [43-44]. With this correction, the HisHε and the HisHδ models accurately reproduce the experimental CO frequencies. The CO frequency in HisHδHε model, on the other hand, is lower than the experimental one by 20 cm^{-1}.

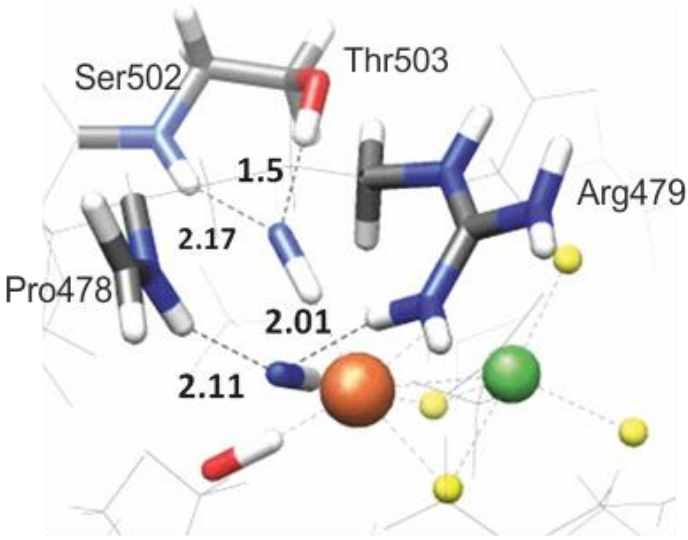

Figure 7: Hydrogen bonding network of the cyanide ligands.

The individual modes of the two cyanides are coupled, resulting in a symmetric and an anti–symmetric stretching vibration of higher and lower frequency, respectively. For the HisHε model, the symmetric mode is in excellent agreement with the experimental findings. The computations for the HisHδ model and the HisHδHε model on the other hand result in frequencies, which are by about 10 cm^{-1} too low and too high, respectively. The anti–symmetric stretching frequency is calculated too small by 10 cm^{-1} in the case of the HisHε model. The deviation from the experimental values for the HisHδ model amounts to more than 20 cm^{-1}. The HisHδHε model gives the correct frequency in this case. In summary, taking into account all three stretching frequencies, the agreement between experiment and theory can be considered best for the HisHε model.

Inspection of the second coordination sphere reveals that the hydroxyl group of Ser503 and the N–H group of the peptide backbone of Pro501 constitute hydrogen–bond donors to one of the cyanides (Figure 7). Hydrogen bonds to the cyanides draw away electron density from Fe to the cyanides and thereby reduce the amount of backbonding to the CO ligand, thus increasing the CO stretching frequency. Hydrogen–bond lengths are 2.17 Å and 1.5 Å, respectively. Arg479 can bind with its guanidinium function and with the N–H group of its peptide bond to the other cyanide with hydrogen–bond distances of 2.01 Å and 2.11 Å, respectively. These asymmetries in the hydrogen bonding seem to contribute to the splitting of the frequencies of the two CN modes. The hydrogen bonds are only fully included in the polar model and the large models (HisHδ, HisHε and HisHδHε). This is especially visible for the CO stretching vibration, which is best reproduced in the polar model and the large models.

	CO	CN^-	CN^-
Small	1928	2071	2081
Polar	1948	2058	2082
Hydrophobic	1826	2074	2087
Ionic	1908	2059	2086
HisHδ	1958	2050	2073
HisHε	1957	2062	2083
HisHδHε	1941	2074	2092
Exp. [45]	1961	2074	2085

Table 7: Calculated and experimental CO and CN^- stretching frequencies [cm^{-1}]; a systematic additive correction of 28 cm^{-1} for the CO frequency has been added.

4.2.8. Conclusion

In this work DFT calculations have been performed on the Ni–C state of [NiFe] hydrogenase with a model system that includes molecular fragments from the complete second coordination sphere. Computations have been performed on models that include three protonation states of the His88 fragment and on four truncated models. Comparison of the calculations amongst the different models and with experimental data has shed light on the influence of the second coordination sphere on the spectroscopic properties of the Ni–C state.

The overall agreement of the spectroscopic parameters with those from experiment is fairly good, even without inclusion of the second coordination sphere. This is in agreement of the earlier calculations of the first coordination sphere [8-20, 24-29, 31-35] and fundamentally confirms the validity of the computed electronic structure of the [NiFe] center in the Ni–C state, as well as the suitability of the employed model system. The best results have been obtained with the HisHε model, in which the His88 residue is protonated at the ε–nitrogen and unprotonated at the δ–nitrogen with a hydrogen bond between Hε and Sγ(Cys549) being present. Hence, this model is most suitable for the computational investigation of [NiFe] hydrogenases, including the second coordination sphere. The HisHδHε is also able to reproduce several experimentally observed spectroscopic properties. In contrast, the agreement of the HisHδ model with experiment is relatively poor. In addition, the model is also energetically unfavorable relative to the HisHε model and, conclusively, it does not represent the Ni–C state very well.

It has been corroborated by our calculations that the bridging position between nickel and iron is occupied by a hydride. Extended potential energy surface scans reveal that only one energy minimum is present, in which the hydride binds to both metals in Ni–C. Additionally, two local minima have been found, for which the hydride either binds to the free coordination position of nickel, opposite to Cys549, or attaches itself as a proton to the sulfur atom of Cys546.

In agreement with literature data [8-15, 24-29], the spin density of the Ni–C state is delocalized. The spin density is distributed over the d_{z2} orbital at nickel, a 3p orbital at Sγ(Cys549) which forms a σ–antibonding combination with the d_{z2} orbital, and a 3p orbital at Sγ(Cys546) which is π–antibonding to d_{z2}. In the latter case, the spin density in the 3p orbital of Sγ(Cys546) has been traced back to the perpendicular orientation of the Cβ–Sγ bond relative to the C_∞ axis of the d_{z2} orbital.

The second coordination sphere has a pronounced influence on the geometry, the electronic structure and, consequently, also on the spectroscopic properties. Firstly, His88 fine–tunes the spin density distribution by the presence of a hydrogen bond to Sγ(Cys549) and, hence, the magnetic properties of the active site. Secondly, Val500 sterically restricts the orientation of the β–CH_2 group of Cys549. Thirdly, hydrogen bonds to the cyanides are formed by the residues Ser503, Pro501 and Arg479, which reduces the electron density at the Fe center and, as a consequence, increases the stretching frequencies of the carbon monoxide ligand.

References

1. Garcin, E., et al., *The crystal structure of a reduced nifese hydrogenase provides an image of the activated catalytic center.* Structure with Folding & Design, 1999. **7**(5): p. 557-566.
2. Garcin, E. 1998, Universite Joseph Foureir-Grenoble 1.
3. Higuchi, Y., et al., *Removal of the bridging ligand atom at the ni-fe active site of nife hydrogenase upon reduction with h-2, as revealed by x-ray structure analysis at 1.4 angstrom resolution.* Structure with Folding & Design, 1999. **7**(5): p. 549-556.
4. Foerster, S., et al., *An orientation-selected endor and hyscore study of the ni-c active state of desulfovibrio vulgaris miyazaki f hydrogenase.* Journal of Biological Inorganic Chemistry, 2005. **10**(1): p. 51-62.
5. Whitehead, J.P., et al., *The hydrogen binding-site in hydrogenase - 35-ghz endor and xas studies of the ni-c active form and the ni-l photoproduct.* Journal of the American Chemical Society, 1993. **115**(13): p. 5629-5635.
6. Fan, C.L., et al., *Detection and characterization of exchangeable protons bound to the hydrogen-activation nickel site of desulfovibrio-gigas hydrogenase - a h-1 and h-2 q-band endor study.* Journal of the American Chemical Society, 1991. **113**(1): p. 20-24.
7. Brecht, M., et al., *Direct detection of a hydrogen ligand in the [nife] center of the regulatory h-2-sensing hydrogenase from ralstonia eutropha in its reduced state by hyscore and endor spectroscopy.* Journal of the American Chemical Society, 2003. **125**(43): p. 13075-13083.
8. Bruschi, M., et al., *A theoretical study of spin states in ni-s-4 complexes and models of the nife hydrogenase active site.* Journal of Biological Inorganic Chemistry, 2004. **9**(7): p. 873-884.
9. Pavlov, M., et al., *Mechanism of h-h activation by nickel-iron hydrogenase.* Journal of the American Chemical Society, 1998. **120**(3): p. 548-555.
10. Fan, H.J. and M.B. Hall, *Recent theoretical predictions of the active site for the observed forms in the catalytic cycle of ni-fe hydrogenase.* Journal of Biological Inorganic Chemistry, 2001. **6**(4): p. 467-473.
11. Siegbahn, P.E.M., et al., *The mechanism of the ni-fe hydrogenases: A quantum chemical perspective.* Journal of Biological Inorganic Chemistry, 2001. **6**(4): p. 460-466.
12. Pardo, A., et al., *Density functional study of the catalytic cycle of nickel-iron nife hydrogenases and the involvement of high-spin nickel(ii).* Journal of Biological Inorganic Chemistry, 2006. **11**(3): p. 286-306.
13. Pardo, A., et al., *Characterization of the active site of catalytically inactive forms of nife hydrogenases by density functional theory.* Journal of Biological Inorganic Chemistry, 2007. **12**(6): p. 751-760.
14. Lill, S.O.N. and P.E.M. Siegbahn, *An autocatalytic mechanism for nife-hydrogenase: Reduction to ni(i) followed by oxidative addition.* Biochemistry, 2009. **48**(5): p. 1056-1066.

15. Amara, P., et al., *A hybrid density functional theory molecular mechanics study of nickel-iron hydrogenase: Investigation of the active site redox states.* Journal of the American Chemical Society, 1999. **121**(18): p. 4468-4477.
16. Bruschi, M., et al., *Dft investigations of models related to the active site of nife and fe hydrogenases.* Coordination Chemistry Reviews, 2005. **249**(15-16): p. 1620-1640.
17. Siegbahn, P.E.M., J.W. Tye, and M.B. Hall, *Computational studies of nife and fefe hydrogenases.* Chemical Reviews, 2007. **107**(10): p. 4414-4435.
18. Argaman, N. and G. Makov, *Density functional theory: An introduction.* American Journal of Physics, 2000. **68**(1): p. 69-79.
19. Baerends, E.J. and O.V. Gritsenko, *A quantum chemical view of density functional theory.* Journal of Physical Chemistry A, 1997. **101**(30): p. 5383-5403.
20. Neese, F., *Prediction of molecular properties and molecular spectroscopy with density functional theory: From fundamental theory to exchange-coupling.* Coordination Chemistry Reviews, 2009. **253**(5-6): p. 526-563.
21. Jayapal, P., et al., *Qm/mm studies of ni-fe hydrogenases: The effect of enzyme environment on the structure and energies of the inactive and active states.* Physical Chemistry Chemical Physics, 2008. **10**(29): p. 4249-4257.
22. Soderhjelm, P. and U. Ryde, *Combined computational and crystallographic study of the oxidised states of nife hydrogenase.* Journal of Molecular Structure-Theochem, 2006. **770**(1-3): p. 199-219.
23. Siegbahn, P.E.M., *Hybrid density functional study of the oxidized states of nife-hydrogenase.* COMPTES RENDUS DE L ACADEMIE DES SCIENCES SERIE II FASCICULE C-CHIMIE, 2007. **10**(8): p. 766-774.
24. Stein, M. and W. Lubitz, *Dft calculations of the electronic structure of the paramagnetic states ni-a, ni-b and ni-c of nife hydrogenase.* Physical Chemistry Chemical Physics, 2001. **3**(13): p. 2668-2675.
25. Stein, M. and W. Lubitz, *Characterization of the paramagnetic intermediates of nife hydrogenase by means of relativistic dft calculations.* Journal of Inorganic Biochemistry, 2001. **86**(1): p. 442-442.
26. Stein, M. and W. Lubitz, *The electronic structure of the catalytic intermediate ni-c in nife and nifese hydrogenases.* Physical Chemistry Chemical Physics, 2001. **3**(23): p. 5115-5120.
27. Stein, M. and W. Lubitz, *Quantum chemical calculations of nife hydrogenase.* Current Opinion in Chemical Biology, 2002. **6**(2): p. 243-249.
28. Stein, M. and W. Lubitz, *Relativistic dft calculation of the reaction cycle intermediates of nife hydrogenase: A contribution to understanding the enzymatic mechanism.* Journal of Inorganic Biochemistry, 2004. **98**(5): p. 862-877.
29. Stein, M., et al., *G- and a-tensor calculations in the zero-order approximation for relativistic effects of ni complexes ni(mnt)(2)(-) and ni(co)(3)h as model complexes for the active center of nife -hydrogenase.* Journal of Physical Chemistry A, 2001. **105**(2): p. 416-425.
30. Pandelia, M.E., et al., *Spectroscopic characterization of the key catalytic intermediate ni-c in the o-2-tolerant nife hydrogenase i from aquifex aeolicus: Evidence of a weakly bound hydride.* Chemical Communications, 2012. **48**(6): p. 823-825.
31. Stadler, C., et al., *Density functional calculations for modeling the oxidized states of the active site of nickel-iron hydrogenases. 1. Verification of the method with paramagnetic ni and co complexes.* Inorganic Chemistry, 2002. **41**(17): p. 4417-4423.
32. Stadler, C., et al., *Density functional calculations for modeling the active site of nickel-iron hydrogenases. 2. Predictions for the unready and ready states and the corresponding activation processes.* Inorganic Chemistry, 2002. **41**(17): p. 4424-4434.
33. Lubitz, W., et al., *Epr and theoretical investigations of nife hydrogenase: Insight into the mechanism of biological hydrogen conversion*. Epr in the 21st century: Basics and applications to material, life and earth sciences, ed. A. Kawamori, J. Yamauchi, and H. Ohta. 2002, Amsterdam: Elsevier. 437-445.
34. van Gastel, M., et al., *A single-crystal endor and density functional theory study of the oxidized states of the [nife] hydrogenase from desulfovibrio vulgaris miyazaki f.* Journal of Biological Inorganic Chemistry, 2006. **11**(1): p. 41-51.
35. van Gastel, M., et al., *Epr experiments to elucidate the structure of the ready and unready states of the [nife] hydrogenase of desulfolvibrio vulgaris miyazaki f.* Biochemical Society Transactions, 2005. **33**: p. 7-11.
36. van Gastel, M., *Structural features of the unready ni-a state of nife hydrogenase revealed by x-ray crystallography and epr spectroscopy.* Applied Magnetic Resonance, 2010. **37**(1-4): p. 207-218.
37. Mayer, I., *Charge, bond order and valence in the abinitio scf theory.* Chemical Physics Letters, 1983. **97**(3): p. 270-274.

38. Neese, F., *Prediction of electron paramagnetic resonance g values using coupled perturbed hartree-fock and kohn-sham theory.* Journal of Chemical Physics, 2001. **115**(24): p. 11080-11096.
39. Foerster, S., et al., *Single crystal epr studies of the reduced active site of nife hydrogenase from desulfiovibrio vulgaris miyazaki f.* Journal of the American Chemical Society, 2003. **125**(1): p. 83-93.
40. Stone, A.J., *Gauge invariance of g tensor.* Proceedings of the Royal Society of London Series a-Mathematical and Physical Sciences, 1963. **271**(1344): p. 424-+.
41. Neese, F. and E.I. Solomon, *Calculation of zero-field splittings, g-values, and the relativistic nephelauxetic effect in transition metal complexes. Application to high-spin ferric complexes.* Inorganic Chemistry, 1998. **37**(26): p. 6568-6582.
42. Buhrke, T., et al., *The h-2 sensor of ralstonia eutropha: Biochemical and spectroscopic analysis of mutant proteins modified at a conserved glutamine residue close to the nife active site.* Journal of Biological Inorganic Chemistry, 2002. **7**(7-8): p. 897-908.
43. Jonas, V. and W. Thiel, *Theoretical-study of the vibrational-spectra of the transition-metal carbonyls m(co)(6) m=cr, mo, w , m(co)(5) m=fe, ru, os , and m(co)(4) m=ni, pd, pt.* Journal of Chemical Physics, 1995. **102**(21): p. 8474-8484.
44. Jonas, V. and W. Thiel, *Density functional study of the vibrational spectra of octahedral transition-metal hexacarbonyls: Neutral molecules (m = cr, mo, w) and isoelectronic ions (m = v, nb, ta; mn, re; fe, ru, os; co, rh, ir; pt; au).* Organometallics, 1998. **17**(3): p. 353-360.
45. Fichtner, C., et al., *Spectroelectrochemical characterization of the nife hydrogenase of desulfovibrio vulgaris miyazaki f.* Biochemistry, 2006. **45**(32): p. 9706-9716.

Appendix

Bond lengths, bond angles and population analysis for the model systems

	Small	*Hydrophobic*	*Polar*	*Ionic*	*HisHε*
Charge	-2	-2	-2	-2	-2
Spin	2	2	2	2	2
number of atoms	41	98	77	84	165/166
contracted basis functions	540	846	828	866	1424

Table A1 Computational details and system size of the model systems.

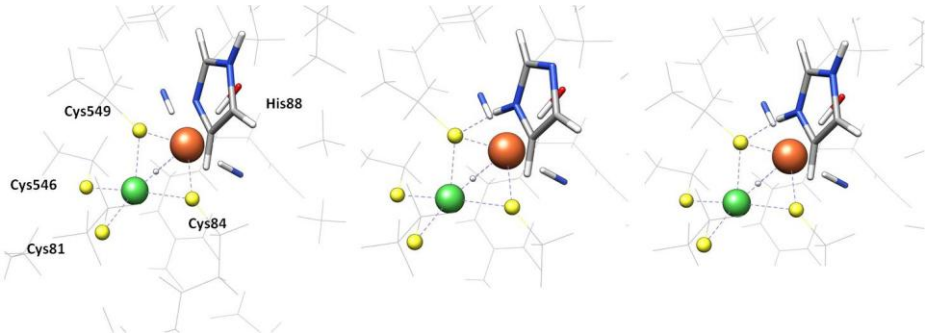

Figure A1: Protonation states and hydrogen bonding of His88 for the HisHδ (left), HisHε (middle) and HisHδHε (right) models.

	Small	Polar	Hydrophobic	Ionic
Ni-S(Cys81)	2.24	2.25	2.24	2.25
Ni-S(Cys84)	2.26	2.27	2.26	2.26
Ni-S(Cys546)	2.18	2.18	2.20	2.18
Ni-S(Cys549)	2.36	2.35	2.35	2.35
Fe-S(Cys84)	2.30	2.29	2.30	2.30
Fe-S(Cys549)	2.30	2.31	2.30	2.31
Ni-H	1.59	1.59	1.59	1.60
Fe-H	1.70	1.72	1.72	
Ni-Fe	2.53	2.54	2.54	2.55
Fe-N(His)	-	-	-	3.12
Fe-CN	1.89	1.87	1.88	1.89
Fe-CN	1.89	1.72	1.89	1.87
Fe-CO	1.73	1.73	1.73	1.72
H(Cys546)-C-S-Ni	-42.6	-44.6	-40.1	-42.5
H(Cys549)-C-S-Ni	-8.5	-7.1	-0.6	-7.7
	HisHδ	**HisHε**	**HisHδHε**	**X-Ray [1]**
S(Cys81)-Ni	2.25	2.25	2.25	2.32
S(Cys84)-Ni	2.27	2.27	2.28	2.33
S(Cys546)-Ni	2.18	2.18	2.17	2.24
S(Cys549)-Ni	2.34	2.34	2.36	2.43
Fe-S(Cys84)	2.30	2.30	2.30	2.28
Fe-S(Cys549)	2.30	2.31	2.31	2.36
Ni-H	1.59	1.60	1.59	
Fe-H	1.72	1.72	1.73	
Ni-Fe	2.54	2.54	2.54	2.60
S(549)-N(His)	3.32	3.30	3.22	3.28
Fe-CN	1.86	1.86	1.87	2.21
Fe-CN	1.88	1.87	1.87	1.86
Fe-CO	1.74	1.74	1.73	1.84
H(1)-Cys546-C-S-Ni	-43.6	-43.2	-42.1	-50.9
H(1)-Cys549-C-S-Ni	0.0	-1.3	-1.5	-3.4

Table A2: Selected bond-lengths [Å] and dihedral angles [°] of the Ni-Fe hydrogenase active site.

	Small	Polar	Hydrophobic	Ionic (H^+ His)
S Cys81	-0.43	-0.42	-0.44	-0.42
S Cys84	-0.13	-0.16	-0.14	-0.12
S Cys546	-0.35	-0.31	-0.37	-0.33
S Cys549	-0.20	-0.18	-0.21	-0.21
Ni	-0.07	-0.10	-0.07	-0.08
Fe	0.05	0.03	0.06	0.10
Hydride	0.00	-0.02	0.05	-0.02

	HisHδ	HisHε	HisHδHε
S Cys81	-0.42	-0.41	-0.39
S Cys84	-0.18	-0.16	-0.17
S Cys546	-0.26	-0.23	-0.21
S Cys549	-0.11	-0.22	-0.27
Ni	-0.12	-0.13	-0.13
Fe	0.05	0.08	0.08
Hydride	0.01	0.03	0.05

Table A3: Selected Mulliken charges.

	HisHδ	HisHε	HisHδHε
S(Cys81)-Ni	0.72	0.74	0.74
S(Cys84)-Ni	0.69	0.68	0.67
S(Cys546)-Ni	0.98	1.01	1.05
S(Cys549)-Ni	0.64	0.61	0.56
H-Ni	0.55	0.54	0.52
H-Fe	0.37	0.38	0.38
S(Cys84)-Fe	0.57	0.59	0.59
S(Cys549)-Fe	0.64	0.55	0.51

Table A4: Mayer bond orders.

Spectroscopic parameters

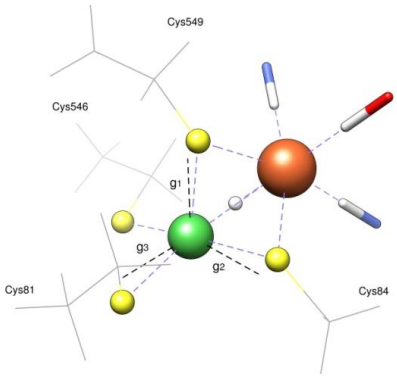

Figure A2: Principal axes of the calculated g-tensor (HisHε model) centered at the nickel atom.

	Cys81	Cys84	Cys546	Cys549
Small Model				
g_1	77	78	78	6
g_2	85	15	12	88
g_3	14	81	90	84
HisHδ				
g_1	78	82	82	7
g_2	83	15	9	91
g_3	14	78	87	84
HisHε				
g_1	78	80	80	7
g_2	81	15	7	95
g_3	14	79	88	84
HisHδHε				
g_1	80	77	76	8
g_2	84	17	14	86
g_3	12	80	89	82
Exptl.[2]				
g_1	78	76	74	5
g_2	90	14	17	88
g_3	12	87	84	85

Table A5: Angles of the principal axes of the g-tensor with the Ni-S_{cys} bonds.

	A_1	A_2	A_3	A_{iso}
Small	-65.9	-104.9	-198.5	-123.1
Polar	-66.7	-97.2	-194.7	-119.5
Hydrophobic	-66.0	-105.1	-199.4	-123.5
Ionic (H^+ His)	-100.5	-125.8	-224.3	-150.2
HisHδ	-56.3	-80.6	-179.9	-106
HisHε	-80.4	-103.9	-206.8	-130.4
HisHδHε	-92.0	-118.1	-218.1	-142.7

Table A6: Calculated principal values [MHz] of the ^{61}Ni hyperfine tensor.

	A_1	A_2	A_3	A_{iso}
Small	-0.4	0.9	-2.1	-0.5
Polar	-0.3	0.8	-2.1	-0.5
Hydrophobic	-0.3	1.1	-2.1	-0.4
Ionic (H^+ His)	0.2	-0.3	-1.5	-0.5
HisHδ	-0.2	1.0	-2.4	-0.5
HisHε	-0.3	0.7	-2.2	-0.6
HisHδHε	0.4	-0.3	-1.9	-0.6

Table A7: Calculated principal values of the ^{57}Fe hyperfine tensor.

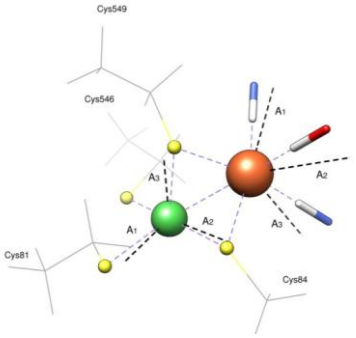

Figure A3: Directions of the principal axes of the ^{61}Ni and ^{57}Fe hyperfine tensors centered at the Ni and Fe atoms, respectively.

Cys-81				
	A_1	A_2	A_3	A_{iso}
HisHδ	1.1	4.3	-6.3	-0.3
HisHε	1.8	5.2	-6.6	0.1
HisHδHε	2.4	5.4	-6.8	0.3

Cys-84				
	A_1	A_2	A_3	A_{iso}
HisHδ	-0.2	6.8	7.0	4.5
HisHε	-1.0	6.6	6.8	4.1
HisHδHε	0.0	6.7	7.1	4.6

Cys-546				
	A_1	A_2	A_3	A_{iso}
HisHδ	0.8	-8.7	27.5	6.5
HisHε	1.2	-9.3	31.7	7.9
HisHδHε	1.5	-10.2	35.7	9.0

Cys-549				
	A_1	A_2	A_3	A_{iso}
HisHδ	0.2	-1.8	88.2	28.9
HisHε	15.8	17.9	80.6	38.1
HisHδHε	21.0	23.3	73.1	39.2

Table A8: Calculated principal values [MHz] of the ^{33}S hyperfine tensors.

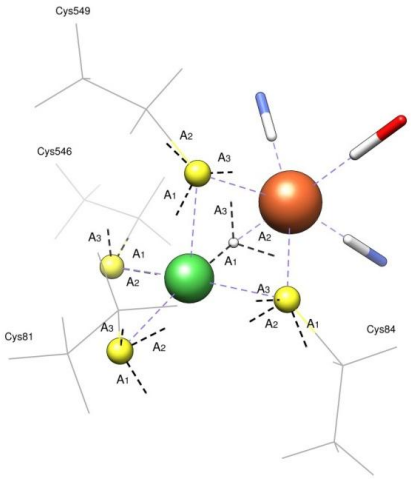

Figure A4: Directions of the principal axes of the ^{33}S and ^{1}H hydride hyperfine tensors centered at the sulfur atoms and hydride respectively.

HisHδ	A_1	A_2	A_3
a axis	-0.46	-0.81	0.37
b axis	0.24	-0.51	-0.83
c axis	0.86	-0.29	0.43

HisHε	A_1	A_2	A_3
a axis	-0.46	-0.81	0.35
b axis	0.24	-0.50	-0.83
c axis	0.85	-0.30	0.43

HisHδHε	A_1	A_2	A_3
a axis	-0.45	-0.82	0.35
b axis	0.25	-0.50	-0.83
c axis	0.86	-0.29	0.43

Exptl.[3]	A_1	A_2	A_3
a axis	-0.63	-0.54	0.55
b axis	0.21	-0.82	-0.55
c axis	0.74	-0.74	0.63

Table A9: Direction cosines of the ^{1}H hydride hyperfine tensor relative to the crystal axis system (a,b,c) given for the complete model systems.

H(1)	**HisHδ**	**HisHε**	**HisHδHε**	**exptl.**
a axis	-0.58	-0.62	-0.65	-0.65
b axis	0.35	0.25	0.16	0.17
c axis	-0.74	-0.75	-0.74	-0.74

H(2)	**HisHδ**	**HisHε**	**HisHδHε**	**exptl.**
a axis	-0.45	-0.47	-0.47	-0.65
b axis	0.03	-0.06	-0.06	-0.21
c axis	-0.89	-0.88	-0.88	-0.73

Table A10: Direction cosines of the A_3 principal axis of the hyperfine tensors of H(1) and H(2) of the Cys549 β-CH_2 group in the crystal axis system (a,b,c).

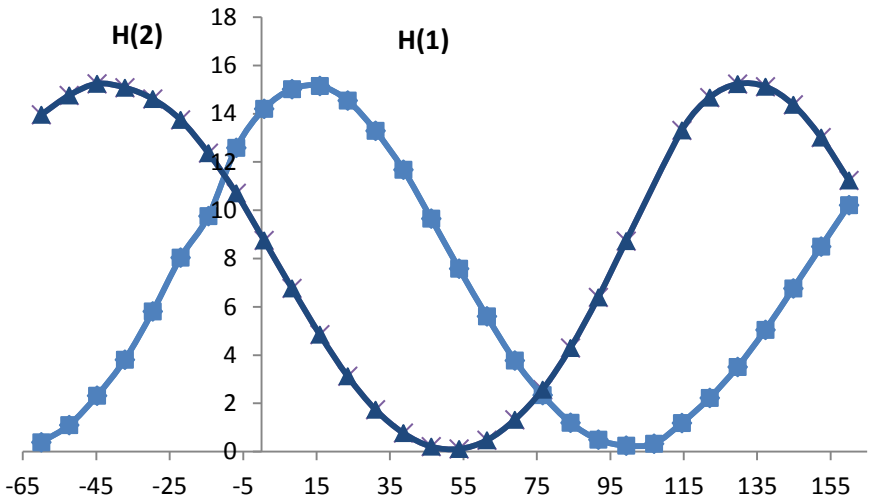

Figure A5: Isotropic ^{1}H Hyperfine coupling constants as a function of the Cys549 β-CH_2 H(1)-C-S-Ni torsion angle. Computations have been performed with the HisHε model.

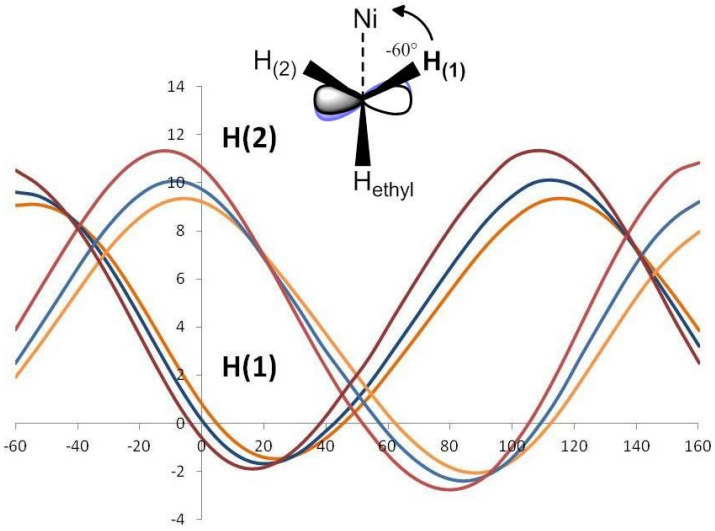

Figure A6: Isotropic ^{1}H Hyperfine coupling tensors as a function of the Cys546 β-CH_2 H(1)-C-Ni-S torsion angle. Color Code: red - small model with His88 HδHε, blue: Hε, orange: His88 Hδ. Inset: Newman projection along the C-S Cys546 bond for the starting angle of Θ = -60° with the idealized orientation (grey) and the actual torsion of the sulfur p_z-orbital (blue).

H(1)	**HisHδ**	**HisHε**	**HisHδHε**	**exptl.**
a axis	-0.34	-0.34	-0.36	-
b axis	-0.54	-0.55	-0.52	-
c axis	0.77	0.76	0.77	-

H(2)	**HisHδ**	**HisHε**	**HisHδHε**	**exptl.**
a axis	0.00	-0.03	0.00	-0.09
b axis	-0.32	-0.35	-0.30	-0.49
c axis	0.95	0.93	0.95	0.87

Table A11: Direction cosines of the principal A_3 axis of the hyperfine tensors of H(1) and H(2) of Cys546 β-CH_2 in the crystal axis system (a,b,c).

HisHδ	P_1	P_2	P_3
a axis	0.53	0.75	0.39
b axis	0.26	-0.58	0.77
c axis	0.81	-0.31	-0.50

HisHε	P_1	P_2	P_3
a axis	-0.35	0.50	-0.79
b axis	-0.85	0.19	0.49
c axis	0.40	0.85	0.36

HisHδHε	P_1	P_2	P_3
a axis	-0.19	0.82	0.54
b axis	-0.84	-0.42	0.33
c axis	0.50	-0.39	0.77

Exptl [3]	P_1	P_2[a]	P_3[a]
a axis	-0.34	0.84	0.41
b axis	-0.90	-0.44	0.12
c axis	0.28	-0.32	0.90

Table A12: Direction cosines of the ^{14}N quadrupole tensor of the ε nitrogen atom of His-88 in the crystallographic axes system.

[a] Note that ,unfortunately, the P2 and P3 axes from the experimental study have likely been incorrect and have to be interchanged, given that the signals barely exceeded the noise level.

HisHδ	**A_1**	**A_2**	**A_3**
a axis	0.36	0.90	0.26
b axis	0.32	-0.38	0.87
c axis	0.87	-0.23	-0.43

HisHε	A_1	A_2	A_3
a axis	0.31	0.92	0.22
b axis	0.34	-0.32	0.88
c axis	0.89	-0.20	-0.42

HisHδHε	A_1	A_2	A_3
a axis	0.46	0.85	0.27
b axis	0.30	-0.44	0.85
c axis	0.83	-0.31	-0.46

Exptl [3]	A_1	A_2	A_3
a axis	-	-	-0.34
b axis	-	-	-0.90
c axis	-	-	0.28

Table A13: Direction cosines of the ^{14}N hyperfine tensor of the ε nitrogen atom of His-88 in the crystallographic axes system.

	A_1	A_2	A_3	A_{iso}
Small	-9.93	13.22	-13.93	-3.55
HisHδ	-5.78	-10.21	15.24	-0.25
HisHε	-9.29	-12.98	14.61	-2.55
HisHδHε	12.28	-13.83	-16.73	-6.09

Table A14: BP86 Calculated principal values [MHz] of the hydride.

H(1)	A_1	A_2	A_3	A_{iso}
Small	15.11	17.33	21.18	17.87
HisHδ	21.20	23.82	27.74	24.25
HisHε	13.25	16.02	19.64	16.31
HisHδHε	8.43	11.51	15.14	11.69
H(2)	A_1	A_2	A_3	**Aiso**
Small	14.47	15.35	19.34	16.39
HisHδ	11.82	12.47	17.24	13.84
HisHε	10.27	11.08	14.79	12.04
HisHδHε	8.21	9.25	12.30	9.92

Table A15: BP86 calculated and experimental hyperfine coupling constants [MHz] of the two protons belonging to β-CH_2 group of Cys549.

H(1)	A_1	A_2	A_3	A_{iso}
Small	7.03	7.45	10.70	8.39
HisHδ	6.78	7.18	10.36	8.11
HisHε	10.07	10.62	14.04	11.57
HisHδHε	14.51	15.19	18.80	16.17
H(2)	A_1	A_2	A_3	A_{iso}
Small	9.60	10.81	13.97	11.46
HisHδ	10.57	11.66	14.78	12.34
HisHε	13.05	14.38	17.59	15.01
HisHδHε	14.58	16.10	19.36	16.68

Table A16: BP86 calculated and experimental hyperfine coupling constants [MHz] of the two protons belonging to β-CH_2 group of Cys549.

	HisHδ	HisHε	HisHδHε
S(Cys81)-Ni	2.27	2.27	2.27
S(Cys84)-Ni	2.32	2.32	2.32
S(Cys546)-Ni	2.20	2.20	2.20
S(Cys549)-Ni	2.38	2.39	2.42
Fe-S(Cys84)	2.34	2.34	2.34
Fe-S(Cys549)	2.34	2.34	2.35
Ni-H	1.57	1.57	1.57
Fe-H	1.73	1.73	1.73
Ni-Fe	2.57	2.58	2.58
S(549)-N(His)	3.33	3.28	3.21
Fe-CN	1.90	1.90	1.90
Fe-CN	1.91	1.90	1.90
Fe-CO	1.76	1.76	1.75
H(1)-Cys546-C-S-Ni	-43.00	-43.50	-43.40
H(1)-Cys549-C-S-Ni	0.81	-0.30	-0.40

Table A17: Selected bond-lengths [Å] and dihedral angles [°] of the Ni-Fe hydrogenase active site in the HisHδ, HisHε and HisHδHε models in B3LYP optimized geometries.

References

1. Higuchi, Y., et al., *Removal of the bridging ligand atom at the ni-fe active site of nife hydrogenase upon reduction with h-2, as revealed by x-ray structure analysis at 1.4 angstrom resolution.* Structure with Folding & Design, 1999. **7**(5): p. 549-556.
2. Foerster, S., et al., *Single crystal epr studies of the reduced active site of nife hydrogenase from desulfiovibrio vulgaris miyazaki f.* Journal of the American Chemical Society, 2003. **125**(1): p. 83-93.
3. Foerster, S., et al., *An orientation-selected endor and hyscore study of the ni-c active state of desulfovibrio vulgaris miyazaki f hydrogenase.* Journal of Biological Inorganic Chemistry, 2005. **10**(1): p. 51-62.

4.3. The Ni–L state

Evidence for a new metal–metal bond

Abstract

The Ni–L state of [NiFe] hydrogenases has been investigated by Density Functional Theory (DFT) calculations of models that include the complete [NiFe] center and parts of the second coordination sphere. The Ni–L state can be obtained by illumination of the Ni–C state at low temperatures. The experimental data, in particular from Electron Paramagnetic Resonance (EPR) and Fourier Transform Infrared (FTIR) spectroscopy indicate that the hydride atom, which is located in the bridging position between nickel and iron in the Ni–C state, dissociates as a proton and binds to a nearby base. Identification of this base, which may play an important functional role, is still an open question. Our calculations suggest that the base is one of the terminal cysteine thiolate ligands of nickel. Additionally, the formation of a nickel–iron bond upon dissociation of the hydride is unequivocally observed in the calculations and is in full agreement with the observed g values, ligand hyperfine coupling constants and FTIR stretching frequencies. This metal–metal bond is possibly also relevant for the stability of intermediates with an empty bridge in the catalytic cycle.

4.3.1 Introduction

Illumination of the Ni–C state at temperatures below 180 K leads to the conversion to the Ni–L state. The formation of the Ni–L state was discovered for the first time in the [NiFe] hydrogenase of *Allochromatium vinosum* [1] and was later found to also occur in other [NiFe] hydrogenases [2-3]. The action spectrum associated with the conversion from Ni–C to Ni–L was found to contain a maximum at 590 nm [4]. By EPR and HYSCORE experiments [4-5], it could be shown that the signal assigned to the bridging hydride in the Ni–C state disappears in the course of the photo–conversion. This has prompted the suggestion that the hydride ligand is removed from the bridging position in the form of a proton, which then binds to a nearby basic amino acid. Although the Ni–L state is not believed to be functionally relevant (e.g., hydrogenases function equally well in the dark) the photodissociated Ni–L state is well suited to investigate the identity of an amino acid base that may function as a proton acceptor in the catalytic cycle. Further evidence for photo–dissociation and re–association of the hydride ligand is available from rapid scan kinetic measurements [6], by which it was demonstrated that binding of the proton to the nearby base is a first–order process. The kinetics of the back–conversion into the Ni–C state was studied in H_2O and D_2O buffer and the primary kinetic isotope effect was found to lie between 5 and 7 [6]. In addition, the light–induced formation of Ni–L was studied with Fourier Transform Infrared (FTIR) spectroscopy by monitoring the changes of the stretching frequencies of the iron–bound CO and CN ligands [7-9].

Formally, the conversion of the hydride into a proton proceeds under concomitant two–electron reduction of the nickel atom from 3+ to 1+. However, XAS experiments at the Ni L–edge[10] are in contrast to this assignment and predict a three–valent nickel as found in Ni–C. Single crystal EPR on the Ni–L state of *Desulfovibrio vulgaris* Miyazaki F by Förster *et al.* [11] furthermore revealed that the orientations of the g–tensor axes of Ni–L are almost equal to those in Ni–C. With g_z = 2.05, g_y = 2.12 and g_x = 2.3, the g–tensor components differ from those obtained for Ni–C, but the smallest g value remains associated with the z direction. The most notable difference concerns the g_z value, which in Ni–C equals 2.01 and is close to the free electron g–value, g_e, while for Ni–L a significantly larger value is found (2.05) [5, 12]. In the study of Förster *et al.* [11], the interpretation of the experimental results was corroborated by DFT–calculations using a Ni–L cluster model, which included the first coordination shell and g–tensor calculations with a formal mono–valent nickel center and a vacant bridge were most compatible with the experimental findings. Analysis of the electronic structure revealed that the singly occupied orbital exhibits mainly nickel d_{z^2} character, as is the case for the Ni–C state, with smaller contributions of the nickel $d_{x^2-y^2}$ orbital. However, it was argued before that since the $d_{x^2-y^2}$ orbital is the lowest unoccupied orbital in the Ni–C state, concomitant two–electron reduction of the nickel center upon Ni–L formation would lead to a singly occupied $d_{x^2-y^2}$ orbital

instead of a singly occupied d_{z^2} orbital. This would imply a g–tensor with the largest instead of the smallest g value pointing along the z direction. This, however, is incompatible with experiment [13].

It is thus still an open question, to which basic amino acid in the vicinity of the [NiFe] core the photo–dissociated proton binds. Also, the oxidation state of nickel is still under debate. In this study, we address these questions by extended DFT calculations using large models for the [NiFe] center that include the second coordination sphere. Computed g–tensors, hyperfine coupling tensors and stretching frequencies of the CN and CO ligands have been compared to experimental data and indeed shed light on the geometric and electronic structure of the Ni–L state.

	H^+81–A	**H^+81–B**	**H^+84**	**H^+546–A**	**H^+546–B**	**H^+549**	**HisHε**	**deprot**
Atoms	165	165	165	165	165	165	165	164
Basis functions	1424	1424	1424	1424	1424	1424	1424	1418
Charge	2–	2–	2–	2–	2–	2–	2–	3–
<S2> BP	0.77	0.77	0.77	0.77	0.77	0.77	0.76	0.78
<S2> B3LYP	0.86	0.88	1.14	0.88	0.87	1.12	0.77	1.15

Table 1: Number of atoms and contracted basis functions, total charge, and spin contaminations.

4.3.2 Model systems

Cluster models for the Ni–L state have been derived from the HisHε model, which has been shown to provide an accurate description of the geometric and electronic structure of the Ni–C state (see chapter 4.2). The HisHε model has been constructed from the X–ray structure of reduced *D. vulgaris* Miyazaki F hydrogenase (pdb: 1H2R)) [14]. Accordingly, *D. vulgaris* MF numbering of amino acids is used consistently throughout this manuscript.

The model contains the [NiFe] core, which consists of nickel, iron, the four nickel–coordinating cysteine residues modeled as ethylthiolates, the CN and CO ligands to iron and amino acid fragments of the second coordination sphere as specified before [15]. The hydride ligand has been removed from the bridging position in the Ni–L cluster models and one cysteine sulfur atom has been protonated. For the terminal cysteines Cys81 and Cys546, two orientations of the proton are possible and, hence, two models (A, B) have been created for each cysteine. Thus, six cluster models have been used, denoted as H^+81–A, H^+81–B, H^+84, H^+546–A, H^+546–B and H^+549. The structures of the first coordination shell of these models are presented in Figure 1. In addition, a seventh model, in which the proton has not been included, is designated as ‘deprot’ model (not shown).

The Ni–L cluster models contain 164 atoms and 1424 contracted basis functions (Table 1). All cluster models are spin ½ systems. The total charge of the cluster models is 2– while it is 3– for the deprot model. All calculations have been performed with the ORCA program package.[16] Geometry optimizations and IR spectra have been calculated with the BP86 GGA functional [17-18] due to its

well–documented good performance in these areas [19-20]. In contrast to the HisHε model for the Ni–C state, the spin contamination of the wavefunction is significant when the hybrid functional B3LYP is used. With spin contaminations of almost 0.4, this holds especially true for H^+84 and H^+549. In contrast, since Hartree–Fock exchange is absent in the BP86 functional, the spin contamination for the BP86 functional is negligible. Accordingly, not only geometry optimizations and IR spectra but also magnetic properties and energies calculations have been performed with the BP86 functional.

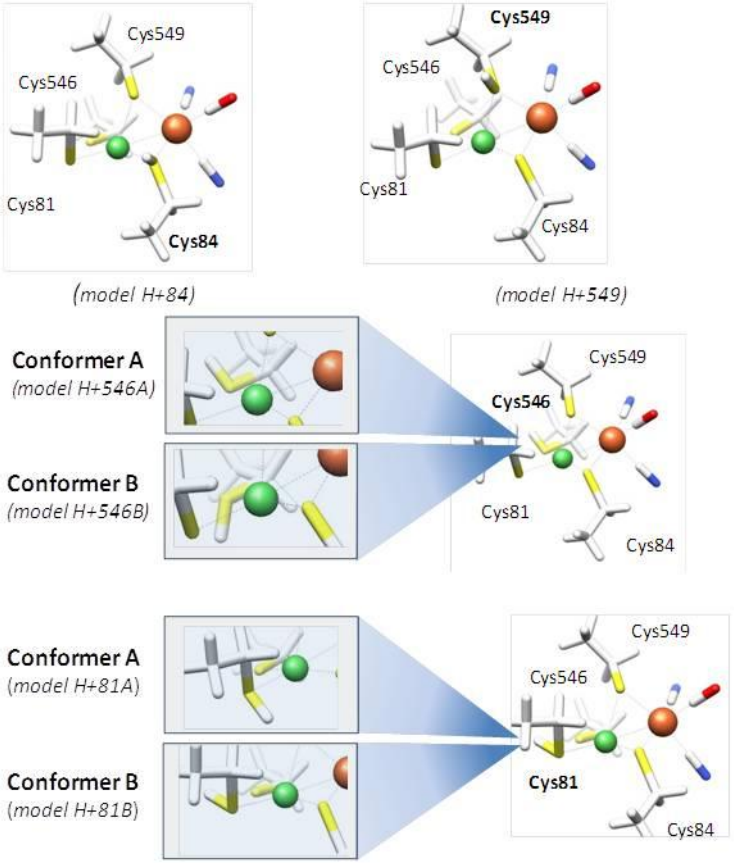

Figure 1: Cluster models for the Ni–L state. The models feature an unoccupied bridging position and one protonated cysteine residue. In the cluster models H^+84 and H^+549, Cys84 and Cys549 are protonated. Two orientations of the proton are possible for protonation at Cys546 and Cys81. The corresponding model clusters are called H^+546–A, H^+546–B, H^+81–A and H^+81–B. Not shown is the deprot model in which the photo–dissociated proton has not been included.

4.4.3. Geometries

A crystal structure of the Ni–L state has not been reported so far. Geometries are therefore only shortly discussed. In Table 2, selected geometric parameters of the geometry–optimized Ni–L models and the HisHε model are collected. The Ni–S distances show no systematic variation with the different Ni–L cluster models. Exceptions are the H^+84 and the H^+549 cluster models, in which a bridging thiolate is protonated. For these models, the distance between metal and protonated bridging sulfur atom becomes shorter.

The Ni–Fe distance of the other models is slightly larger than that found for HisHε. Interestingly, the spread of Hβ(1)(Cys546)–Cβ(Cys546)–Sγ(Cys546)–Ni torsion angles in the various Ni–L models with values of −29.6° to −49.5° indicates a degree of flexibility of the terminal ligand Cys546. The torsion angle βH(1)(Cys549)–βC(Cys549)–γS(Cys549)–Ni varies less strongly among the multiple Ni–L models than the corresponding angle for Cys546, which is presumably due to the stabilizing hydrogen bond betweenSγ(Cys549) and H(ε) of His88.

	H^+81–A	H^+81–B	H^+84	H^+546–A	H^+546–B	H^+549	HisHε
Ni–S(Cys81)	2.31	2.28	2.30	2.32	2.33	2.31	2.25
Ni–S(Cys84)	2.25	2.26	2.17	2.22	2.22	2.26	2.27
Ni–S(Cys546)	2.17	2.17	2.14	2.21	2.21	2.17	2.18
Ni–S(Cys549)	2.28	2.27	2.28	2.26	2.28	2.19	2.34
Fe–S(Cys84)	2.29	2.29	2.19	2.28	2.28	2.29	2.3
Fe–S(Cys549)	2.29	2.29	2.29	2.28	2.28	2.22	2.31
Ni–Fe	2.56	2.56	2.66	2.58	2.58	2.64	2.54
Ω_{546}	−29.6	−34.0	−35.0	−30.4	−49.5	−33.5	−43.2
Ω_{549}	1.2	0.4	−2.5	−2.3	−4.3	−6.3	−1.3

Table 2: Selected bond distances [Å] and torsion angles Ω_{546} (Hβ(1)(Cys546)–Cβ(Cys546)–Sγ(Cys546)–Ni) and Ω_{549} (Hβ(1)(Cys549)–Cβ(Cys549)–Sγ(Cys549)–Ni) [°] from the geometry–optimized Ni–L cluster models.

4.4.4. Electronic structure

Upon illumination of the Ni–C state, the hydride leaves the bridging position as a proton and may bind to one of the cysteines. This would correspond to a formal two–electron reduction of the d^7 Ni^{3+} to a d^9 Ni^{1+} center. In the Ni–C state the d_{z^2} orbital is singly occupied whereas the $d_{x^2-y^2}$ orbital is unoccupied. Hence, two–electron reduction of the nickel center would then lead to a doubly occupied d_{z^2} orbital and a singly occupied $d_{x^2-y^2}$ orbital with significantly changed g values and ligand hyperfine interactions. Since the spin–orbit coupling matrix element of $d_{x^2-y^2}$ and d_{xy} would give rise to a dominant contribution to second order to the g_z value (e.g., in Cu(II) complexes with a singly occupied $d_{x^2-y^2}$ orbital the g_z value attains values typically between 2.2 and 2.3),[21] one would expect

the largest g–tensor component in the z–direction. This, however, is not observed experimentally [11]. In addition, XAS experiments have not confirmed the presence of a reduced nickel center but rather indicate an oxidation state similar to that in Ni–C [10].Therefore, the available experimental data do not seem to confirm the presence of the unpaired electron in the $d_{x^2-y^2}$ orbital, indicative of a d^9 Ni^{1+} species. The question thus arises: where do the two electrons of the former hydride go upon photodissociation?

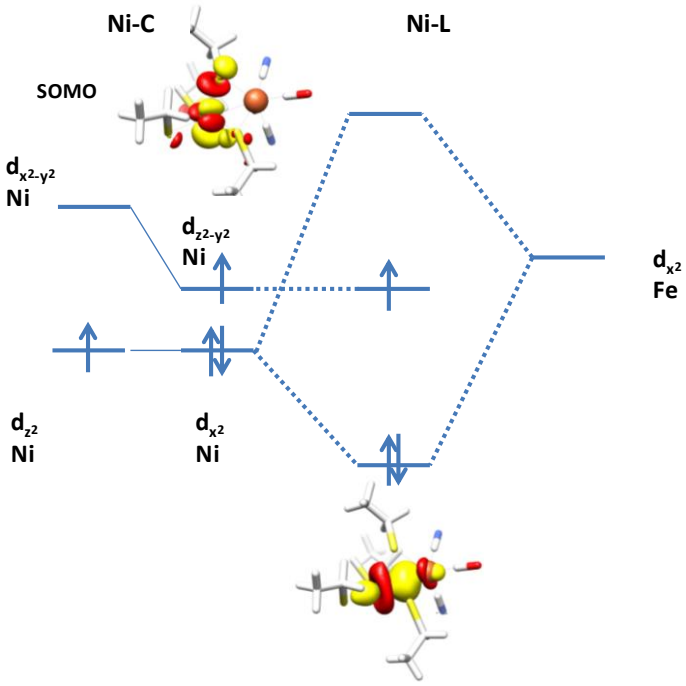

Figure 2: Frontier orbital diagram for the Ni–C (leftmost levels only) and Ni–L states. The insets show orbitals for Ni–L, which have been obtained from a quasi–restricted wave function in the H^+Cys546–A model. The orbital corresponding to the Ni–Fe bond has been obtained by localization [22].

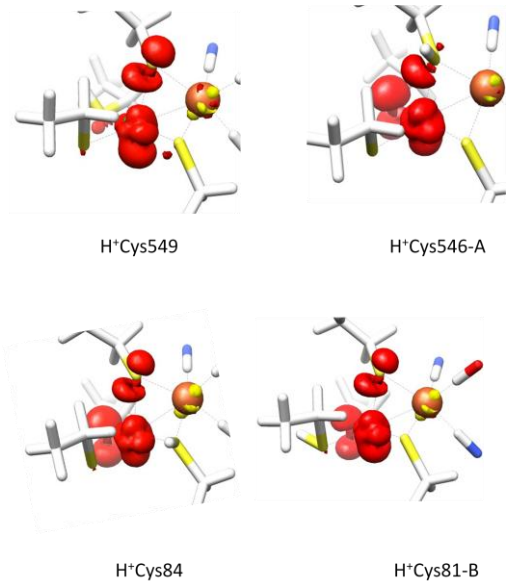

Figure 3: Spin density plots for the Ni–L models (a) H^+549, (b) H^+546–A, (c) H^+84 and (d) H^+81–B.

In Figure 2, the orbital diagram is presented for the frontier orbitals of the Ni–C and Ni–L states. The diagram has been restricted to only the $d_{x^2-y^2}$ and d_{z^2} orbitals, since consideration of these orbitals will turn out to suffice for understanding the changes in electronic structure upon photodissociation from Ni–C to Ni–L. As a coordinate system, the g tensor principal axes system has been chosen [11]. In this axes system the z–axis points approximately along the Ni–Sγ(Cys549) bond and the x–axis along Ni–Sγ(Cys81) and orthogonalized to z. Since the hydride ligand is removed from the equatorial plane, the $d_{x^2-y^2}$ orbital is lowered in energy relative to the one in Ni–C. In order to interpret the bonding interactions of nickel for Ni–L, it turns out to be practical to consider the d_{x^2} and $d_{z^2-y^2}$ orbitals, which can be trivially formed by a linear combination of the d_{z^2} and the $d_{x^2-y^2}$ orbitals:

[1a]

[1b]

The lobes of the d_{x^2} orbital approximately point along the Ni–Sγ(Cys81) bond and towards the vacant bridging position. The lack of a hydride ligand opens the possibility to form a bent metal–metal σ interaction by bonding and anti–bonding combinations of the nickel d_{x^2} orbital and the iron d_{x^2} orbital (both orbitals are of course not perfectly aligned along the x axis. The C_∞ symmetry axis of each orbital forms a small angle with respect to the x axis, but we retain this nomenclature in order to prevent overly complicated labeling of the involved orbitals). The DFT calculation reveals that the corresponding localized Ni–Fe orbital is centered by 81% at nickel and by 15% at iron (see inset of Figure 2). The anti–bonding combination of the nickel d_{x^2} orbital and the iron d_{x^2} orbital is unoccupied while the singly occupied molecular orbital (see inset of Figure 2) has $d_{z^2-y^2}$ character. The finding of

the $d_{z^2-y^2}$ orbital as the dominant contribution of nickel to the singly occupied orbital is corroborated by the Mulliken spin populations presented in Table 3. Significant mixing of the d_{z^2} and $d_{x^2-y^2}$ orbitals is observed, with the d_{z^2} orbital being the dominant contribution. The coordination of a hydride to both nickel and iron in the Ni–C state can thus be viewed as a protonation of the electron pair that forms the nickel–iron bond. In Ni–C, the electron pair is counted to the hydride and a metal–metal bond is formally absent, whereas upon photodissociation to Ni–L, the base becomes deprotonated and the electron pair formally forms a nickel–iron bond. Hence, back–conversion of Ni–L to the Ni–C state can be interpreted as a protonation of the bimetallic center of the hydrogenase. Mayer bond orders (Table 4) corroborate the formation of a nickel–iron bond in the Ni–L state with bond orders of about 0.4 for all models. This is larger by 0.1 than the corresponding value for the HisHε model. However, despite the finding of a Ni–Fe bond order of about 0.3 for the HisHε model, the interaction of the two metals and the hydride in Ni–C is best described as Ni–H–Fe three–center bond while, in the case of Ni–L, a genuine two–center metal–metal bond is present. Possibly, the formation of Ni–L occurs only due to the stabilization of the active site by this Ni–Fe bond, which partly compensates for the loss of the favorable interactions of the hydride with the two metals. The bond order for the S–H bond formed by the protonated sulfur atom of one of the cysteines and the former hydride is 0.9 for the terminal cysteines and 0.8 for the bridging cysteines indicating a normal covalent sulfur–hydrogen bond. Since electron density is shared with the proton, formation of a covalent S–H bond results in a smaller absolute Mulliken charge of the sulfur atom in question, i.e., the sulfur becomes more charge–neutral. The Mulliken charge for the remaining sulfur atoms becomes more negative as compared to the HisHε model. For the Ni–L models, the Mulliken charge at the nickel atom is similar to the one in the HisHε model. The finding of a formal charge of 3+ instead of 1+ in L–edge XAS experiments for the Ni–L state [10] can be rationalized by this transfer of electron density from the nickel center to the sulfur ligands and, in addition, to the iron center via the metal–metal bond. On a side note, the extreme difference between the formal charge of 3+ at nickel and the actual Mulliken charge of about −0.1 is an indication that the formal charge is only useful for bookkeeping purposes when counting the number of electrons.

	$\mathbf{d_{z^2}}$	$\mathbf{d_{x^2-y^2}}$
H^+81–A	0.25	0.16
H^+81–B	0.39	0.19
H^+84	0.37	0.16
H^+546–A	0.43	0.14
H^+546–B	0.40	0.14
H^+549	0.43	0.12

Table 3: Mulliken spin populations of the nickel d_{z^2} and $d_{x^2-y^2}$ orbitals.

The spin population at the nickel atom, ranging from 0.6 to 0.7, is larger than in the HisHε model with a value of 0.5. Concomitantly, spin delocalization is reduced and the sulfur atom of Cys549 exhibits a Mulliken spin population between 0.17 and 0.22 whereas the spin population at this sulfur atom is 0.3 in the HisHε model. For the H^+549 model the spin population even decreases to a value of 0.1. The spin population of the sulfur atom of Cys546, on the other hand, increases relative to the HisHε model, except, of course, when the residue itself is protonated.

	H^+81–A	H^+81–B	H^+84	H^+546–A	H^+546–B	H^+549	deprot	HisHε
Ni–S(81)	0.50	0.48	0.60	0.60	0.60	0.61	0.52	0.75
Ni–S(84)	0.70	0.68	0.71	0.74	0.74	0.68	0.69	0.70
Ni–S(546)	0.99	0.98	1.04	0.70	0.68	1.04	0.85	1.04
Ni–S(549)	0.62	0.63	0.63	0.67	0.65	0.66	0.63	0.60
Fe–S(81)	0.69	0.68	0.67	0.68	0.68	0.72	0.58	0.64
Fe–S(546)	0.60	0.62	0.61	0.61	0.62	0.64	0.90	0.60
S–H	0.89	0.90	0.82	0.92	0.92	0.81	–	–
Fe–H	–	–	–	–	–	–	–	0.39
Ni–H	–	–	–	–	–	–	–	0.51
Ni–Fe	0.37	0.38	0.38	0.38	0.38	0.37	0.40	0.29

Table 4: Mayer bond orders of selected bonds.

	H^+81–A	H^+81–B	H^+84	H^+546–A	H^+546–B	H^+549	deprot	Ni–C
S(81)	–0.14	–0.18	–0.43	–0.48	–0.51	–0.41	–0.48	–0.37
S(84)	–0.21	–0.23	0.04	–0.18	–0.19	–0.16	–0.19	–0.10
S(546)	–0.30	–0.35	–0.21	–0.03	–0.03	–0.21	–0.35	–0.20
S(549)	–0.22	–0.24	–0.21	–0.18	–0.21	0.03	–0.22	–0.15
Ni	–0.15	–0.13	–0.11	–0.11	–0.11	–0.11	–0.04	–0.24
Fe	0.09	0.10	0.03	0.10	0.11	0.00	0.11	–0.10
H^+	0.09	0.11	0.09	0.12	0.11	0.08	–	0.25

Table 5: Mulliken charges. H^+ designates the photo–dissociated proton.

	H^+81–A	H^+81–B	H^+84	H^+546–A	H^+546–B	H^+549	deprot	Ni–C
S(81)	0.01	0.01	0.02	0.04	0.03	0.01	0.02	0.00
S(84)	0.04	0.04	0.04	0.05	0.05	0.02	0.05	0.00
S(546)	0.19	0.17	0.26	0.05	0.03	0.23	0.13	0.15
S(549)	0.18	0.19	0.17	0.22	0.22	0.11	0.18	0.29
Ni	0.63	0.65	0.59	0.68	0.70	0.63	0.71	0.51
Fe	–0.07	–0.08	–0.09	–0.06	–0.05	–0.03	–0.10	0.02
H^+	0.00	0.00	–0.01	0.00	0.00	0.00	–0.01	0.00

Table 6: Mulliken spin populations. H^+ designates the photo–dissociated proton.

Spin density plots for the H^+549, H^+546–A, H+84 and H^+81–B models are displayed in Figure 3. The plots for H^+546–B and H^+81–A are similar to those for H^+546–A and H^+81–B, respectively, and are therefore not shown. In agreement with the orbital diagram (Figure 2), the contours of the spin density at the nickel center indicate that the relevant orbital at nickel is best classified as a $d_{z^2-y^2}$ orbital. Significant amounts of spin density are found in 3p orbitals of Sγ(Cys549) and Sγ(Cys546). For H^+546–A, the spin density at Sγ(Cys546) almost vanishes, in agreement with the Mulliken spin populations in Table 6. Close inspection of the spin density plot for H^+549–A reveals that the singly occupied orbital at Sγ(Cys549) is not a pure 3p orbital but also contains s–orbital contributions. In contrast to second row elements, like carbon, the 3s and 3p valence–orbitals of sulfur are energetically more separated and s–p mixing occurs to a smaller degree. However, for protonation and thereby the formation of a fourth bond, the sulfur 3p orbitals of Cys549 mix with the 3s orbital, i.e. the 3p orbitals become hybridized, which is also reflected by a change of the sulfur bond angles. For example, the Ni–Sγ(Cys549)–Fe bond angle increases from 66° to 74°, which is accommodated by an elongation of the Ni–Fe distance and a contraction of the Sγ(Cys549)–Fe and Sγ(Cys549)–Ni bonds. The same reasoning holds for the sulfur atom of Cys84 in H^+Cys84.

In summary, the electronic structure of the Ni–L models differs markedly from that of the HisHε model for the Ni–C state. In the Ni–C state the metal contribution to the singly occupied molecular orbital is the nickel d_{z^2} orbital with its C_∞ axis pointing approximately along the Ni–Sγ(Cys549) bond. In the Ni–L state, a bond is formed between nickel and iron. Rehybridization of the nickel d–orbitals occurs, such that the d_{x^2} orbital, which points in the direction of the unoccupied bridging position, forms a metal–metal bond with the iron d_{x^2} orbital. Thus, the interaction of the nickel and iron centers in Ni–L is different from that in Ni–C where a three–center two–electron bond is present formed by the Fe d_{x^2}, the Ni $d_{x^2-y^2}$ and the hydride s–orbital. As opposed to the Ni–C state, the singly occupied molecular orbital is not a d_{z^2} orbital but a $d_{z^2-y^2}$ orbital, which results in significantly altered magnetic properties, in particular g–tensors (*vide infra*). In addition, the Mulliken spin populations at the sulfur atoms of Cys549 and Cys546 are smaller and larger, respectively, as compared to the values for Ni–C and, hence, also ^{1}H hyperfine tensors of the β–CH_2 groups of Cys549 and Cys546 are different from those of Ni–C (*vide infra*).

4.4.5 Energies

Energies for the conversion from Ni–C to Ni–L are collected in Table 7. All energies are positive which means that the conversion from Ni–L back to Ni–C is energetically favorable for all cluster models. The Ni–L models H^+549 and H^+84 have the highest energies and, hence, protonation at the bridging ligand is energetically more costly than protonation of the terminal cysteines. The two conformers

H^+81–A and H^+81–B exhibit almost equal energies. On the other hand, the conversion energy for H^+546–B is larger by more than 10 kcal/mol than that of H^+546–A. With only 8 kcal/mol, the latter model features the lowest energy for Ni–L formation amongst the Ni–L models.

	ΔE
H^+81–A	17
H^+81–B	15
H^+84	26
H^+546–A	8
H^+546–B	20
H^+549	27

Table 7: Energies ΔE [kcal/mol] for the conversion from Ni–C to Ni–L.

The conversion energies exhibited by all Ni–L cluster models are positive, which matches the experimental finding that the Ni–L state is only accessible by a photochemical reaction but not a thermal reaction. Furthermore, the energies are in line with the finding that the Ni–L state readily converts back to the Ni–C state above an enzyme dependent annealing temperature. Apparently, at lower temperatures, the enzyme is kinetically trapped. Due to their similar energy, the two conformers H^+81–A and H^+81–B would possibly occur in a thermal equilibrium. The prevalence of one of the two structures would be possible only if one conformer is formed exclusively upon illumination and the conversion into the other conformer is sufficiently slowed down by a large energy barrier. Similarly, observation of H^+546–B is only possible if a sufficiently large energy barrier prevents its conversion into the energetically more stable conformation H^+546–A.

Since the potential energy surface of the excited state on which the photochemical formation of Ni–L takes place is not known, it cannot be determined by consideration of the energy alone which of the cysteines likely becomes protonated. Hence, in order to come to a structural assignment of the Ni–L state, and to see whether protonation of the cysteine residue is compatible with the observed g values and hyperfine couplings, a comparison of computed and experimental spectroscopic data is indispensable and is considered next.

4.3.6. Magnetic spectroscopy

Calculated and experimental g values are summarized in Table 8. As evident from the table, the computed g–values for the multiple cluster models accurately reproduce the experimentally observed difference between the g_z values of Ni–C and Ni–L. As is well known from reference calculations, the largest g shift for various metals in certain oxidation states, including Cu(II) and Ni(I)/Ni(III), is usually underestimated by up to 30% [23]. Indeed, the same is found here – the calculated g_x values are systematically smaller than the experimental ones. This systematic underestimation has been attributed partly to an overestimated spin delocalization into ligand

orbitals [23]. Compared to the hybrid B3LYP functional, the spin delocalization is even stronger for the BP86 used here due to the lack of Hartree–Fock exchange. Therefore, the underestimation of the g–tensor relative to experiment is very pronounced. Experimentally, a smaller g_y and a larger g_x component have been observed in the Ni–L state with respect to Ni–C. This trend is reproduced at least qualitatively except for the H^+549 and H^+84 models, where bridging thiolates are protonated. Thus, with given accuracy of the calculated g values, cluster models H^+81–A, H^+81–B, H^+546–A and H^+546–B are most compatible with experiment.

	g_z	g_y	g_x	g_{iso}
H^+81–A	2.04	2.05	2.11	2.07
H^+81–B	2.04	2.05	2.12	2.07
H^+84	2.04	2.06	2.09	2.06
H^+546–A	2.04	2.06	2.12	2.07
H^+546–B	2.04	2.06	2.12	2.07
H^+549	2.04	2.08	2.12	2.08
Deprot	2.05	2.07	2.12	2.08
HisHε	2.01	2.07	2.10	2.06
Ni–C[11]	2.01	2.14	2.20	2.12
Ni–L[11]	2.05	2.12	2.30	2.15

Table 8: Computed g–values for models of Ni–L and Ni–C (HisHε) and experimental g–values.

H^+81–A	g_z	g_y	g_x	H^+81–B	g_z	g_y	g_x
a–axis	–0.94	0.11	0.33		–0.81	0.45	0.37
b–axis	–0.23	–0.90	–0.36		–0.57	–0.72	–0.39
c–axis	–0.26	0.42	–0.87		–0.09	0.53	–0.84
H^+84				**H^+546–A**			
a–axis	–0.71	0.49	0.51		–0.77	0.13	0.63
b–axis	–0.67	–0.70	–0.26		–0.45	–0.81	–0.38
c–axis	–0.23	0.53	–0.82		–0.46	0.57	–0.68
H^+546–B				**H^+549**			
a–axis	–0.86	0.05	0.51		–0.82	0.54	0.19
b–axis	–0.30	–0.85	–0.43		–0.57	–0.80	–0.20
c–axis	–0.42	0.52	–0.74		–0.04	0.28	–0.96
Deprot				**HisHε**			
a–axis	–0.79	0.47	0.40		–0.79	0.37	0.48
b–axis	–0.60	–0.73	–0.32		–0.55	–0.77	–0.32
c–axis	–0.14	0.49	–0.86		–0.26	0.52	–0.81
Ni–C[11]				**Ni–L[11]**			
a–axis	–0.76	0.46	0.46		–0.75	0.36	0.56
b–axis	–0.59	–0.78	–0.20		–0.59	–0.74	–0.33
c–axis	–0.27	0.43	–0.86		–0.30	0.57	–0.77

Table 9: Orientations of the principal axes of the calculated and experimental g–tensors.

Fortunately, not only the g–values but also the directions of the principal axes are known experimentally. In Table 9, the orientations of the principal axes of the g–tensor are summarized. Experimentally, the orientations of the g–tensor axes of Ni–L were found to be similar to those of the Ni–C state with the g_z axis pointing approximately along the Ni–Sγ(Cys549) bond, g_y along Ni–Sγ(Cys546) and g_x along Ni–Sγ(Cys81). Indeed, the orientations of the g–tensor are suitably reproduced by all models. Upon comparison of the calculated directions with the experimental ones for Ni–L, best agreement is reached with H^+546–A and H^+546–B and worst agreement with H^+549. The orientations of the g_z and g_y components are less accurately reproduced. However the direction cosines lose their meaning owing to the near axiality of the calculated g tensor (cf. Table 8).

In the framework of second order perturbation theory, all spin–orbit coupling matrix elements in the z–direction vanish for the Ni–C state and the g_z component equals the free electron g–value. In contrast, in the Ni–L state, a positive contribution to g_z comes from an excited state which arises from the transition of an electron from the d_{xy} orbital into the $d_{z^2-y^2}$ singly occupied orbital. Since g_z is the smallest g value, it can be deduced that d_{xy} is lower in energy than d_{xz} and d_{yz}. Contributions to g_y and g_x arise from matrix elements between the $d_{z^2-y^2}$ orbital and the d_{xz} and d_{yz} orbitals, respectively. For the Ni–C state the d_{yz} orbital is found higher in energy than the d_{xz} orbital resulting in a g–tensor with $g_x > g_y$. The removal of the hydride ligand, which lies along the x–axis in the Ni–C state stabilizes the d_{xz} orbital. Consequently, also in the Ni–L state, d_{xz} should be found at lower energy than d_{yz}

which results in a g–tensor with $g_x > g_y$ and essentially unchanged principal axes, which is indeed found both experimentally and computationally. Also, the angular momentum matrix elements of d_{yz} with the $d_{z^2-y^2}$ singly occupied orbital for Ni–L is larger by a factor of ¯ than the matrix element of d_{yz} with the d_{z^2} orbital for Ni–C. The larger matrix element is in agreement with the finding of a larger g_x component in the Ni–L state relative that in the Ni–C state.

In summary, the g–tensor orientations of Ni–L are equal to those of the Ni–C state. However, the g–values for the Ni–L state differ significantly from those for the Ni–C state. The most prominent deviation is found for the g_z component which for Ni–L (2.05) differs significantly from the free electron g value (g_e). This can be attributed to the finding of the non–vanishing matrix element of the $d_{z^2-y^2}$ orbital with the d_{xy} orbital in the Ni–L state. Furthermore, the g_x component is larger than for Ni–C. The g values and direction of the principal axes are best reproduced by the H^+546–B model.

The ^{1}H hyperfine coupling constants of the two protons of the βCH_2–group of Cys549 are presented in Table 10. The magnitude of the ^{1}H isotropic hyperfine couplings is largely determined by the spin density at the sulfur atom of Cys549. For the HisHε model, the isotropic hyperfine couplings in Table 10 are larger than those obtained for Ni–C with the B3LYP functional [15]. This is in line with the finding of a larger spin population at the sulfur atom of Cys549 (Table 6) compared to the corresponding values obtained with B3LYP. The computed isotropic hyperfine coupling for H(1) in the HisHε model for Ni–C is slightly larger than the experimentally observed value but the value for H(2) is in accurate agreement with the experimental one. In the Ni–L models, the isotropic hyperfine coupling constants of H(1) range between 9 and 14 MHz with H^+546–A and H^+546–B yielding the largest values. An exception is clearly the H^+549 model with a hyperfine coupling of only 3 MHz which is in agreement with the observed reduction of the spin density at the sulfur atom of Cys549 upon protonation relative to HisHε. Therefore, the isotropic hyperfine coupling constants of the Ni–L models are smaller than the corresponding ones obtained with HisHε. For H(2) the Ni–L models yield isotropic hyperfine coupling constants which range from 6 to 10 MHz. They are all smaller than the corresponding values for H(1), with the exception of the H^+549 model

H(1)	A_1	A_2	A_3	A_{iso}
H^+81–A	8	10	15	11
H^+81–B	8	10	15	11
H^+84	6	8	13	9
H^+546–A	12	13	18	14
H^+546–B	11	13	17	14
H^+549	0	2	7	3
Deprot	9	11	16	12
HisHε	13	16	20	16
Ni–C [12]	11	12	18	14

H(2)	A_1	A_2	A_3	A_{iso}
H^+81–A	5	6	9	7
H^+81–B	5	6	9	7
H^+84	4	5	8	6
H^+546–A	7	7	11	8
H^+546–B	8	9	12	10
H^+549	6	7	9	7
deprot	6	7	10	7
HisHε	10	11	15	12
Ni–C[12]	10	11	15	12

Table 10: ^{1}H hyperfine coupling constants [MHz] of the two protons of the βCH_2–group of Cys549.

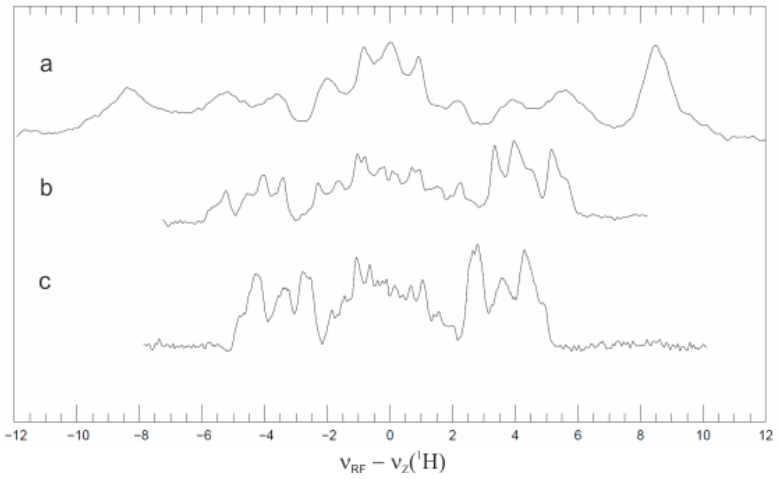

Figure 4. Orientation–selected ^{1}H Davis–ENDOR spectra of the regulatory hydrogenase from *Ralstonia eutropha*: (a) Ni–C state, (b) Ni–L state and (c) Ni–L_A state. The spectra have been recorded at the g_y canonical orientation (data reproduced from reference [24]).

H(1)	A_1	A_2	A_3	A_{iso}
H^+81–A	15	15	19	16
H^+81–B	11	11	15	13
H^+84	19	20	24	21
H^+546–A	−1	−1	3	0
H^+546–B	−1	−2	2	0
H^+549	19	19	23	21
Deprot	11	12	15	13
HisHε	10	11	14	12
Ni–C[12]	7	7	12	8.9

H(2)	A_1	A_2	A_3	A_{iso}
H^+81–A	13	14	18	15
H^+81–B	13	14	18	15
H^+84	18	19	24	20
H^+546–A	2	3	7	4
H^+546–B	0	0	4	1
H^+549	14	15	20	16
Deprot	8	9	13	10
HisHε	13	14	18	15

Table 11: ^{1}H hyperfine coupling constants [MHz] of the two protons of the βCH_2-group of Cys546.

	A_1	A_2	A_3	A_{iso}
H^+81–A	0	−7	−7	−5
H^+81–B	2	−5	−5	−3
H^+84	−6	−12	−13	−10
H^+546–A	3	4	11	6
H^+546–B	8	9	11	9
H^+549	17	21	26	21

Table 12: Computed ^{1}H hyperfine couplings [MHz] of the photo-dissociated proton.

Computed ^{1}H hyperfine coupling constants for the protons H(1) and H(2) of the β–CH_2 group of Cys546 are presented in Table 11. The coupling constants for the cluster models H^{+}546–A and H^{+}546–B are small, which is in line with the relatively small Mulliken spin population at Sγ(Cys546) found for these models (Table 11). The hyperfine tensors of the other Ni–L models are dominated by the isotropic contributions, which are comparable in magnitude or larger than the corresponding value for the HisHε model. In particular, H^{+}549 and H^{+}84 exhibit fairly large isotropic values up to 21 MHz. The deprot model gives an isotropic coupling for H(2), which is smaller by 5 MHz than the corresponding value for HisHε, while the value of H(1) is similar to that found in the HisHε model. These differences are relatively small and the result of a slight reorientation of the Cys546 residue, as described in the geometries section.

In Figure 4, orientation selected spectra of the oxygen tolerant regulatory hydrogenase (RH) from the aerobic bacterium *Ralstonia eutropha*, recorded with a modified Davis–ENDOR sequence are displayed. In this enzyme, two Ni–L states have been observed with slightly different g values.[5] These states have been denoted by the labels Ni–L and Ni–L_A. The spectroscopic properties of the active site of RH are otherwise almost identical to those of oxygen–sensitive hydrogenases.[12] In *R. eutropha,* by raising the temperature for 20 min to 200K, the Ni–L state converts to the Ni–L_A state. Upon further increase of the temperature, the enzyme converts back to Ni–C. Inspection of the ENDOR spectra immediately reveals that the signals with largest hyperfine shifts in Ni–C, assigned to the βCH_2 protons of Cys549 signals appear at reduced RF shifts in Ni–L and Ni–L_A. Thus, the ENDOR spectra also indicate that the spin density at Cys549 is significantly reduced in Ni–L as compared to Ni–C. Given that the anisotropy of these signals, as measured by orientation–selected ENDOR spectra, is similar in Ni–L and Ni–C, the ENDOR spectra also confirm that the directions of principal axes of the g tensor as well as the orientation of the Cys549 residue are identical in Ni–C and Ni–L.

Upon photoconversion of the Ni–C state to the Ni–L state, the signal corresponding to the bridging hydride disappears. A proton bound to one of the thiolates is expected to have smaller ^{1}H hyperfine coupling constants than the hydride. The computed ^{1}H hyperfine coupling constants of the thiolate–bound proton are presented in Table 12. The isotropic hyperfine coupling constant in the H^{+}81–A, H^{+}81–B and H^{+}84 models are negative whereas it is positive in the H^{+}546–A, H^{+}546–B and H^{+}549 models. The largest absolute values are found for H^{+}84 and H^{+}549 with the latter amounting to even more than 20 MHz which is clearly incompatible with the ENDOR experiment. The values in the models with protonated terminal thiolates are much smaller and would give rise to signals with hyperfine shifts between 0 and 5.5 MHz, which is compatible with the ENDOR experiments in Figure 4.

4.3.7. CN^- and CO stretching frequencies

Stretching frequencies of the CO and CN ligands bound to iron center are collected in Table 13. Since the CO stretching frequencies are systematically underestimated in DFT calculations of metal–carbonyl compounds, a constant shift of 28 cm^{-1} has been proposed to correct the calculated frequency.[25-26] The experimentally found CO stretching frequency for Ni–L is 50 cm^{-1} smaller than that for Ni–C. All Ni–L cluster models yield a CO stretching frequency smaller than that for HisHε, by about 30 cm^{-1}. The CO frequencies for the models H^+81–A, H^+81–B, H^+546–A and H^+546–B are almost equal and are about 15 cm^{-1} larger than the experimental Ni–L value. The H^+84 model yields a value that is even 30 cm^{-1} larger than the experimental one. On the other hand, the value for the deprot model is by almost 15 cm^{-1} smaller compared to experiment.

The two experimentally determined CN modes exhibit smaller stretching frequencies compared to those found for Ni–C, which is also reproduced by the Ni–L cluster models with protonated terminal thiolates. The computed values for the Ni–C state using the HisHε model are in accurate agreement with experiment for the higher–frequency anti–symmetric stretching mode but underestimate the lower–frequency symmetric mode by about 12 cm^{-1}. The CN frequency shifts from Ni–C to Ni–L are again best reproduced by the H^+81–A, H^+81–B, H^+546–A and H^+546–B models, in which a terminal thiolate becomes protonated.

	CO	**CN^-**	**CN^-**
H^+81–A	1925	2032	2055
H^+81–B	1925	2033	2055
H^+84	1940	2047	2067
H^+546–A	1924	2031	2052
H^+546–B	1923	2031	2053
H^+549	1924	2049	2065
Deprot	1896	2006	2031
HisHε	1957	2062	2083
Ni–C[27]	1961	2074	2085
Ni–L[6]	1911	2048	2061

Table 13. IR stretching frequencies [cm^{-1}] of the CO and CN ligands bound to the Fe atom. The CO frequencies have been adjusted by an additive systematic correction of +28 cm^{-1}.[25-26]

4.3.8. Conclusion

In this work, we have performed a systematic quantum chemical study for the Ni–L state of [NiFe] hydrogenases. The Ni–L state arises from the Ni–C state by illumination which results in the photo–dissociation of the bridging hydride and formal reduction to monovalent oxidation state. The photodissociated proton is expected to bind to a basic residue in the vicinity of the active site since upon raising the temperature the Ni–L state is readily converted back to Ni–C state.

Multiple models have been used, which feature a vacant bridging position. The photodissociated proton bound has been attached to one of the cysteines or left out of the calculation completely. The electronic structure of the Ni–L state differs markedly from that of the Ni–L state. The LUMO $d_{x^2-y^2}$ and the SOMO d_{z^2} orbital of Ni–C re–hybridize into a $d_{z^2-y^2}$ and d_{x^2} orbital in the Ni–L state The SOMO is mainly composed of the $d_{z^2-y^2}$ orbital, which results in a g–tensor with different g_x and g_z values as compared to the Ni–C state. The C_∞ orbital axis of the doubly occupied d_{x2} orbital points in the direction of the unoccupied bridging position and forms a metal–metal bond with the d_{x^2} orbital of the Fe center. Formally, upon photoconversion of Ni–C to Ni–L, the nickel center adopts a d^9 Ni^{1+} electron configuration. However, the Mulliken charge population of the nickel is even slightly more positive with respect to Ni–C, which is accommodated by the accumulation of significant amounts of additional negative charge at the cysteines. This is in agreement with XAS measurements predicting a Ni^{3+} instead of a Ni^{1+} oxidation state. In this respect, the nickel and iron atoms can be viewed as a base with the Ni–Fe bond being the electron pair, which is protonated for Ni–C and unprotonated for Ni–L. The formation of the Ni–Fe bond is probably essential for the occurrence of the Ni–L state at low temperatures as it partly compensates for the loss of the favorable interactions of the hydride with the two metals. The formation of a metal–metal bond is not only relevant for the stabilization of the Ni–L state, but might also be important for intermediates in the catalytic cycle, which also feature a vacant bridging site. Computational spectroscopic parameters, i.e., g–tensors, hyperfine couplings and IR–frequencies, all agree with the presence of the metal–metal bond between nickel and iron.

Concerning the identity of the base that binds the proton upon photodissociation of the hydride, the models with protonated bridging thiolates match the experimental findings worst. Best, and in some cases quantitative agreement is obtained with the cluster models in which one of terminal cysteines is protonated, i.e., H^+546–A, H^+546–B, H^+81–A and H^+81–B. Since, according to our investigation, the terminal cysteines act as basic residues which become protonated in the Ni–L state, it is conceivable that these residues also act as nucleophiles for hydrogen abstraction in the course of the catalytic mechanism. This is in agreement with the conclusion drawn from various experimental and computational studies [28-38] of the reaction mechanism of [NiFe] hydrogenase.

References

1. van der Zwaan, J.W., et al., *Mono-valent nickel in hydrogenase from chromatium-vinosum - light sensitivity and evidence for direct interaction with hydrogen.* FEBS Letters, 1985. **179**(2): p. 271-277.
2. Medina, M., E.C. Hatchikian, and R. Cammack, *Studies of light-induced nickel epr signals in hydrogenase: Comparison of enzymes with and without selenium.* Biochimica Et Biophysica Acta-Bioenergetics, 1996. **1275**(3): p. 227-236.
3. Medina, M., et al., *Studies of light-induced nickel epr signals in desulfovibrio-gigas hydrogenase.* Journal of the Chemical Society, Faraday Transactions, 1994. **90**(19): p. 2921-2924.
4. Fichtner, C., M. van Gastel, and W. Lubitz, *Wavelength dependence of the photo-induced conversion of the ni-c to the ni-l redox state in the [nife] hydrogenase of desulfovibrio vulgaris miyazaki f.* Physical Chemistry Chemical Physics, 2003. **5**(24): p. 5507-5513.
5. Brecht, M., et al., *Direct detection of a hydrogen ligand in the [nife] center of the regulatory h-2-sensing hydrogenase from ralstonia eutropha in its reduced state by hyscore and endor spectroscopy.* Journal of the American Chemical Society, 2003. **125**(43): p. 13075-13083.
6. Kellers, P., et al., *Ftir study on the light sensitivity of the nife hydrogenase from desulfovibrio vulgaris miyazaki f: Ni-c to ni-l photoconversion, kinetics of proton rebinding and h/d isotope effect.* Physical Chemistry Chemical Physics, 2009. **11**(39): p. 8680-8683.
7. Bagley, K.A., et al., *Infrared-detectable groups sense changes in charge-density on the nickel center in hydrogenase from chromatium-vinosum.* Biochemistry, 1995. **34**(16): p. 5527-5535.
8. Pierik, A.J., et al., *Carbon monoxide and cyanide as intrinsic ligands to iron in the active site of nife - hydrogenases - nife(cn)(2)co, biology's way to activate h-2.* Journal of Biological Chemistry, 1999. **274**(6): p. 3331-3337.
9. Schroeder, O., et al., *Characterization of a cyanobacterial-like uptake nife hydrogenase: Epr and ftir spectroscopic studies of the enzyme from acidithiobacillus ferrooxidans.* Journal of Biological Inorganic Chemistry, 2007. **12**(2): p. 212-233.
10. Davidson, G., et al., *Structural examination of the nickel site in chromatium vinosum hydrogenase: Redox state oscillations and structural changes accompanying reductive activation and co binding.* Biochemistry, 2000. **39**(25): p. 7468-7479.
11. Foerster, S., et al., *Single crystal epr studies of the reduced active site of nife hydrogenase from desulfiovibrio vulgaris miyazaki f.* Journal of the American Chemical Society, 2003. **125**(1): p. 83-93.
12. Foerster, S., et al., *An orientation-selected endor and hyscore study of the ni-c active state of desulfovibrio vulgaris miyazaki f hydrogenase.* Journal of Biological Inorganic Chemistry, 2005. **10**(1): p. 51-62.
13. Lubitz, W., E. Reijerse, and M. van Gastel, *[nife] and [fefe] hydrogenases studied by advanced magnetic resonance techniques.* Chemical Reviews, 2007. **107**(10): p. 4331-4365.
14. Higuchi, Y., et al., *Removal of the bridging ligand atom at the ni-fe active site of nife hydrogenase upon reduction with h-2, as revealed by x-ray structure analysis at 1.4 angstrom resolution.* Structure with Folding & Design, 1999. **7**(5): p. 549-556.
15. Kampa, M., et al., Journal of Biological Inorganic Chemistry, 2012.
16. Neese, F., *Orca, an ab initio, dft and semiempirical scf-mo package*. 2011: University of Bonn.
17. Becke, A.D., *Density-functional exchange-energy approximation with correct asymptotic-behavior.* Physical Review A: Atomic, Molecular, and Optical Physics, 1988. **38**(6): p. 3098-3100.
18. Perdew, J.P., *Density-functional approximation for the correlation-energy of the inhomogeneous electron-gas.* Physical Review B: Condensed Matter, 1986. **33**(12): p. 8822-8824.
19. Buehl, M. and H. Kabrede, *Geometries of transition-metal complexes from density-functional theory.* Journal of Chemical Theory and Computation, 2006. **2**(5): p. 1282-1290.
20. Buehl, M., et al., *Geometries of third-row transition-metal complexes from density-functional theory.* Journal of Chemical Theory and Computation, 2008. **4**(9): p. 1449-1459.
21. Bubacco, L., et al., *Spectroscopic characterization of the electronic changes in the active site of streptomyces antibioticus tyrosinase upon binding of transition state analogue inhibitors.* Journal of Biological Chemistry, 2003. **278**(9): p. 7381-7389.
22. Pipek, J. and P.G. Mezey, *A fast intrinsic localization procedure applicable for abinitio and semiempirical linear combination of atomic orbital wave-functions.* Journal of Chemical Physics, 1989. **90**(9): p. 4916-4926.

23. Neese, F., *Metal and ligand hyperfine couplings in transition metal complexes: The effect of spin-orbit coupling as studied by coupled perturbed kohn-sham theory.* Journal of Chemical Physics, 2003. **118**(9): p. 3939-3948.
24. Brecht, M. 2001, Technische Universität Berlin: Berlin.
25. Jonas, V. and W. Thiel, *Theoretical-study of the vibrational-spectra of the transition-metal carbonyls m(co)(6) m=cr, mo, w , m(co)(5) m=fe, ru, os , and m(co)(4) m=ni, pd, pt.* Journal of Chemical Physics, 1995. **102**(21): p. 8474-8484.
26. Jonas, V. and W. Thiel, *Density functional study of the vibrational spectra of octahedral transition-metal hexacarbonyls: Neutral molecules (m = cr, mo, w) and isoelectronic ions (m = v, nb, ta; mn, re; fe, ru, os; co, rh, ir; pt; au).* Organometallics, 1998. **17**(3): p. 353-360.
27. Fichtner, C., et al., *Spectroelectrochemical characterization of the nife hydrogenase of desulfovibrio vulgaris miyazaki f.* Biochemistry, 2006. **45**(32): p. 9706-9716.
28. FontecillaCamps, J.C., et al., in *Hydrogen as a fuel*, R. Cammack, M. Frey, and R. Robson, Editors. 2001, Taylor & Francis: London. p. 93-109.
29. Matias, P.M., et al., *Nife hydrogenase from desulfovibrio desulfuricans atcc 27774: Gene sequencing, three-dimensional structure determination and refinement at 1.8 angstrom and modelling studies of its interaction with the tetrahaem cytochrome c(3).* Journal of Biological Inorganic Chemistry, 2001. **6**(1): p. 63-81.
30. Amara, P., et al., *A hybrid density functional theory molecular mechanics study of nickel-iron hydrogenase: Investigation of the active site redox states.* Journal of the American Chemical Society, 1999. **121**(18): p. 4468-4477.
31. Sellmann, D., F. Geipel, and M. Moll, *Ni(nhpnpr(3))('s-3') , the first nickel thiolate complex modeling the nickel cysteinate site and reactivity of nife hydrogenase.* Angewandte Chemie-International Edition, 2000. **39**(3): p. 561-+.
32. Goldman, C.M. and P.K. Mascharak, *Reactions of h-2 with the nickel site(s) of the feni and fenise hydrogenases: What do the model complexes suggest?* Comments on Inorganic Chemistry, 1995. **18**(1): p. 1-25.
33. Bleijlevens, B., B.W. Faber, and S.P.J. Albracht, *The nife hydrogenase from allochromatium vinosum studied in epr-detectable states: H/d exchange experiments that yield new information about the structure of the active site.* Journal of Biological Inorganic Chemistry, 2001. **6**(8): p. 763-769.
34. Maroney, M.J. and P.A. Bryngelson, *Spectroscopic and model studies of the ni-fe hydrogenase reaction mechanism.* Journal of Biological Inorganic Chemistry, 2001. **6**(4): p. 453-459.
35. Ogata, H., et al., *Structural studies of the carbon monoxide complex of nife hydrogenase from desulfovibrio vulgaris miyazaki f: Suggestion for the initial activation site for dihydrogen.* Journal of the American Chemical Society, 2002. **124**(39): p. 11628-11635.
36. Volbeda, A., et al., *High-resolution crystallographic analysis of desulfovibrio fructiosovorans nife hydrogenase.* International Journal of Hydrogen Energy, 2002. **27**(11-12): p. 1449-1461.
37. De Gioia, L., et al., *Ni-fe hydrogenases: A density functional theory study of active site models.* Inorganic Chemistry, 1999. **38**(11): p. 2658-2662.
38. Dole, F., et al., *Nature and electronic structure of the ni-x dinuclear center of desulfovibrio gigas hydrogenase. Implications for the enzymatic mechanism.* Biochemistry, 1997. **36**(25): p. 7847-7854.

5.4. The EPR–active and EPR–silent CO–inhibited states

An unusual bent coordination of the inhibiting CO ligand and the influence of the second coordination shell

Abstract

We have studied CO inhibition of [NiFe] hydrogenase by using large cluster models, which include, in addition to the bimetallic core and the first coordination shell, amino acid fragments of the complete second coordination shell. Both, the EPR–active and the EPR–silent Ni–CO state, have been studied. Computational results have been compared to experimental data in order to come up with reliable structures for the EPR–active and EPR–silent Ni–CO states. In addition, we have investigated in detail the binding of the CO ligand and studied the influence of the second coordination shell. A unique electronic ground state with a d_{y^2} singly occupied orbital was identified as consequence of CO binding in the EPR active state. Additionally, according to the similar electronic features of the nickel–H_2 and nickel–CO bonds, insights from the Ni–CO state valuable for shedding light on the details of H_2 coordination in the course of the catalytic mechanism.

4.4.1. Introduction

Carbon monoxide is a competitive inhibitor of [NiFe] hydrogenases [1], which, upon binding to the active site of [NiFe] hydrogenase, gives rise to an EPR–active or an EPR–silent Ni–CO state. EPR spectroscopy of the enzyme gave first evidence for the binding of a CO molecule to the active site and, hence, the presence of an EPR–active Ni–CO state in [NiFe] hydrogenases [2-3]. Happe *et. al.* found that CO binding to the Ni–C state does not take place in the dark but can be induced by illumination at 30 K followed by dark adaptation at 200K [4]. The kinetics of CO binding was studied by stopped–flow FTIR spectroscopy with *Allochromatium vinosum* hydrogenase and with *Desulfovibrio fructosovorans* hydrogenase immobilized on electrons [5].

The binding of an exogenous CO ligand to an EPR–silent state of catalytically active [NiFe] hydrogenase after treatment with excess amounts of CO [6] was discovered by FTIR investigations. FTIR data of inhibited *D. frutosovorans* enzyme [7] revealed the presence of an additional large CO stretching frequency which does not couple to the stretching mode of the Fe–bound CO ligand. Hence, it was concluded that the exogenous CO ligand binds to the terminal nickel site and that the metal–CO bond is weak. Consistently, EXAFS results obtained with *A. vinosum* [NiFe] hydrogenase [8] indicate that CO–binding takes place at the terminal nickel site. Unambiguous evidence finally came from the crystal structure of CO-incubated *D. vulgaris* Miyazaki F hydrogenase [9], which shows the coordination of the CO ligand at the terminal nickel site. Intriguingly, according to the X–Ray structure, the CO ligand coordinates to the metal in a bent conformation. Pandelia *et al.* [10] investigated CO–inhibition in more detail by means of electrochemical and spectroscopic methods and identified two EPR–silent CO–inhibited states. The two EPR–silent states are formed upon binding of the CO molecule to the Ni–SI_a state of the catalytic cycle differing in the redox–state of the proximal [4Fe4S] cluster.

Binding of carbon monoxide to the active site of hydrogenase was investigated In DFT–studies. The computational studies employed models, as compared, which contained in addition to the nickel and iron core, the four cysteines of the active site, the two Fe coordinating CN^- ligands and the Fe–coordinating CO ligand as well as the additional CO ligand. Stein and Lubitz investigated the paramagnetic Ni–CO state [11] as part of a computational study, which focused on the magnetic and structural properties of the EPR–observable states of [NiFe] hydrogenase. Several cluster models were employed in which the additional CO molecule was bound either to the terminal nickel site or to the bridging position, with the nickel atom featuring either a formal Ni^{1+} or Ni^{3+} doublet state. The computed properties were most compatible with the experimental data for a formal Ni^{1+} doublet state with the CO ligand modeled at the terminal nickel site. In the context of a general study on the reaction mechanism of [NiFe] hydrogenase, Pardo *et al.* investigated the structure and the stretching

frequencies of the diamagnetic CO–inhibited state [12]. The employed cluster models were fully geometry–optimized and no constraints were imposed. Based on the comparison of computed and experimental CO stretching frequencies, they concluded that the EPR–silent Ni–CO state features most likely a Ni^{2+} high–spin state.

We have studied the paramagnetic and the diamagnetic Ni–CO states by DFT and compared spectroscopic and geometric parameters to the available experimental data to make a reliable structural assignment for the EPR–silent and EPR–active CO–inhibited states. For the first time, we employed a cluster model for the study of the Ni–CO state, which includes amino acid fragments of the complete second coordination shell. We also investigated the details of a bent CO–coordination focusing on the influence of the second coordination shell.

4.4.2. Model systems

The various Ni–CO models were derived from the HisHε model for the Ni–C state (chapter 4.2.), which includes, in addition to the first coordination shell, amino acid fragments of the complete second coordination shell. Most notably, HisHε model was found to successfully reproduce a large body of experimental data of the Ni–C state. Inclusion of the second coordination shell of the enzyme is particularly important for the computation of IR–frequencies, since the stretching frequency of the intrinsic CO and CN^- ligands coordinated to the Fe^{2+} center were found to be highly sensitive to the hydrogen bonds formed with the two cyanide ligands (chapter 4.2.). The models were subdivided into EPR–silent and EPR–active models in line with the corresponding experimental identification of two CO–inhibited states.

The EPR–active models feature a doublet spin state. The hydride ligand, which binds to the bridging position in the Ni–C state, is either retained (^{2}Ni–CO/H^- model) or modeled as a proton, which binds to one of the cysteine ligands. When the proton is bound to one of the terminal cysteine residues Cys81 or Cys546, two different orientations of the hydrogen–sulfur bond are possible (chapter 4.3), which were designated as A and B. The corresponding cluster models for the EPR active Ni–CO state are termed ^{2}Ni–CO H^+81–A, ^{2}Ni–CO H^+81–B, ^{2}Ni–CO H^+84, ^{2}Ni–CO H^+546–A, ^{2}Ni–CO H^+546–B and ^{2}Ni–CO H^+549. In addition, the cluster model in which the hydride has been completely removed is termed ^{2}Ni–CO.

The models of the EPR–silent Ni–CO state feature either a singlet or a triplet nickel spin state. The models with a vacant bridging position are designated ^{1}Ni–CO and ^{3}Ni–CO, while those models with a hydride ligand occupying the bridging position are named ^{1}Ni–CO/H^- and ^{3}Ni–CO/H^-. If not stated otherwise, the CO ligand was modeled at the terminal nickel site (Figure 1a) and not at the bridging position (Figure 1b). For some of the calculations small models were used, which contain the first

coordination shell, i.e. the nickel and iron cores, the four cysteines, the three Fe–coordinating two–atomic ligands and the exogenous CO ligand.

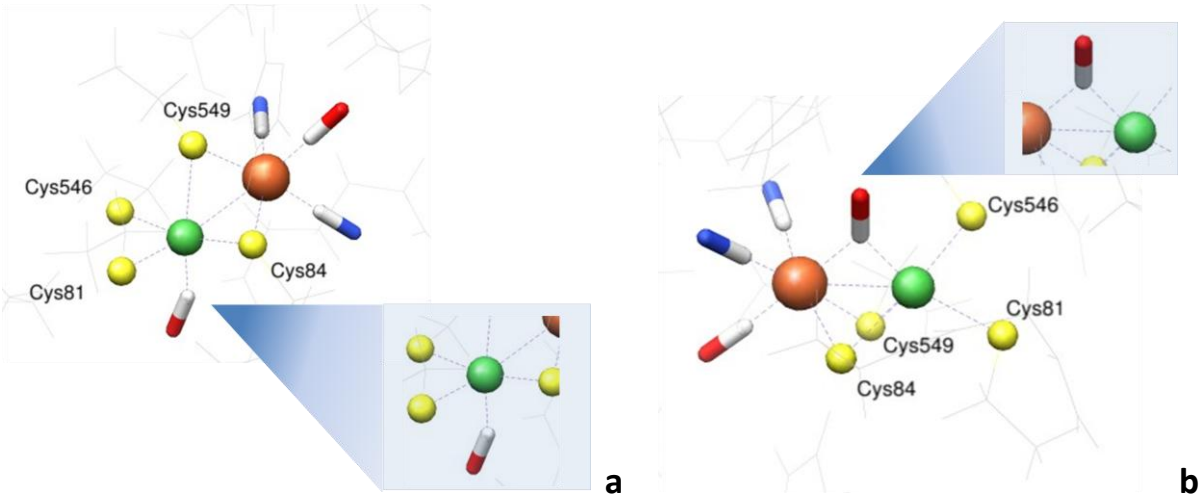

Figure 1: First coordination shell of [NiFe] hydrogenase with CO bound to (a) the terminal nickel site and (b) the bridging site. CO–coordination is highlighted by the blue boxes.

Total charge, spin multiplicity, number of atoms and contracted basis functions, as well as the spin contamination of the EPR–active models are collected in Table 1. The number of atoms and number of basis functions of the respective EPR–silent models equal those of the ^{2}Ni–CO/H^{-} model and the ^{2}Ni–CO model. With a maximum value of 0.06 for the ^{2}Ni–CO/H^{-} model, spin contaminations are negligible. For the triplet ^{3}Ni–CO/H^{-} and ^{3}Ni–CO models spin contaminations are 0.03 and 0.04, respectively.

	H^{+}81–A	**H^{+}81–B**	**H^{+}84**	**H^{+}546–A**	**H^{+}546–B**	**H^{+}549**	**^{2}Ni–CO/H^{-}**	**^{2}Ni–CO**
spin cont.	0.03	0.03	0.03	0.04	0.04	0.03	0.06	0.03
Atoms	167	167	167	167	167	167	167	166
basis	1472	1472	1472	1472	1472	1472	1472	1466
charge	2–	2–	2–	2–	2–	2–	2–	3–
Multiplicity	2	2	2	2	2	2	2	2

Table 1: Spin contamination, number of atoms, number of contracted basis functions, total charge and multiplicity of the EPR–active models.

4.4.3. Geometries – binding of the CO ligand in a bent conformation.

Geometric parameters of the EPR–silent Ni–CO cluster models and the corresponding data from the X–Ray structure are collected in Table 1. The Ni–S distances of the singlet cluster models are in reasonable overall agreement with those from the X–Ray structure. An exception is clearly the Ni–Sγ(Cys549) distance in the ^{1}Ni–CO/H^{-} model. The Ni–Sγ(Cys549) distance of 3.20 Å is significantly larger than Ni–Sγ(Cys549) distance of 2.34 Å in the X–Ray structure and indicates that the Ni–S bond is broken in the ^{1}Ni–CO/H^{-} model. Except for the Ni–Sγ(Cys546) distance, which is in accurate agreement with experiment, the Ni–S distances in the triplet ^{3}Ni–CO/H^{-} model are generally larger than the Ni–S distances from the X–Ray structure. In particular, the Ni–Sγ(Cys549) distance is in poor agreement with experiment. The Ni-S bond lengths in ^{3}Ni–CO are in better agreement with experiment but the Ni–Sγ(Cys84) is by more than 0.1 Å larger than the value from the crystal structure. The Fe–Sγ(Cys84) and Fe–Sγ(Cys549) bond lengths in the ^{1}Ni–CO/H^{-}, ^{1}Ni–CO and ^{3}Ni–CO models match the experimental values well. In contrast, the Fe–Sγ(Cys84) distance is too large in the ^{3}Ni–CO/H^{-} model. In the ^{1}Ni–CO model, the Ni–Fe distance is in excellent agreement with the distance observed in the X–Ray structure. The corresponding values from the triplet models, ^{3}Ni–CO/H^{-} and ^{3}Ni–CO, can be considered satisfactory while the Ni–Fe bond length is too large in ^{1}Ni–CO/H^{-}. ^{1}Ni–CO model is the only model, which gives a reasonable bond length for the Ni–C bond. Conclusively, the best overall agreement of the various computed bond distances with the distances from the X–Ray structure is clearly achieved with the ^{1}Ni–CO cluster model.

X–Ray structures of the Ni–CO state [9] have been obtained from three single crystals which were incubated with CO in the dark. In contrast to the bond distances, the Ni–C–O bond angles in these structures differ markedly since values of 136.2°, 159.9° and 157.5° are found for different light intensities. The angle of 136.2° cannot be reproduced by either of the EPR–silent models. The values from the triplet models are in good agreement with the experimental angles of 159.9° and 157.5° while the angles from the two singlet models, ^{1}Ni–CO and ^{1}Ni–CO/H^{-}, are by about 10° too large and too small, respectively. The dihedral angle C–O–Ni–Sγ(Cys546) in ^{1}Ni–CO also deviates significantly from the corresponding value in the X–Ray structure while the the EPR–silent cluster models exhibit better agreement with experiment. For the small ^{1}Ni–CO model a Ni–C–O bond angle of 175° and a dihedral angle of –63° are found.

	^{1}Ni–CO/H^{-}	^{3}Ni–CO/H^{-}	^{1}Ni–CO	^{3}Ni–CO	X–Ray [9]
Ni–Sγ (Cys81)	2.31	2.42	2.36	2.33	2.29
Ni–Sγ (Cys84)	2.24	2.41	2.26	2.45	2.31
Ni–Sγ(Cys546)	2.24	2.31	2.24	2.23	2.30
Ni–Sγ(Cys549)	3.20	2.58	2.29	2.39	2.34
Fe–Sγ(Cys84)	2.27	2.36	2.27	2.26	2.25
Fe–Sγ(Cys549)	2.35	2.34	2.26	2.28	2.30
Ni–Fe	2.77	2.70	2.61	2.68	2.62
Ni–C (Co_{ex})	1.86	1.82	1.76	1.84	1.72
C–O (CO_{ex})	1.17	1.16	1.16	1.16	1.14
dihedral angle θ	–43.7	–35.9	–79.5	–56.3	–49.8
Ni–C–O angle	149.6	161.9	169.5	157.0	136.2

Table 2: Selected geometric parameters of the EPR–silent Ni–CO cluster models. The dihedral angle O_{CO}–C_{CO}–Ni–Sγ(Cys546) is designated as θ. X–Ray structure: 1UBH from [9].

4.4.4. Energies of CO coordination and the influence of the second coordination shell

In the present section, energy values are analyzed in detail. In particular, the influence of Arg479 and Asp123 of the second coordination shell is explored. Firstly, the energy change upon bending of the CO ligand and its rotation about the C_{CO}-Ni axis is explored. Then, the energies of formation of the CO-inhibited states are discussed. To round the discussion off, it is investigated by means of two dimensional energy surface scans whether binding to the bridging site or the terminal nickel site is energetically favored.

The energies of CO bending

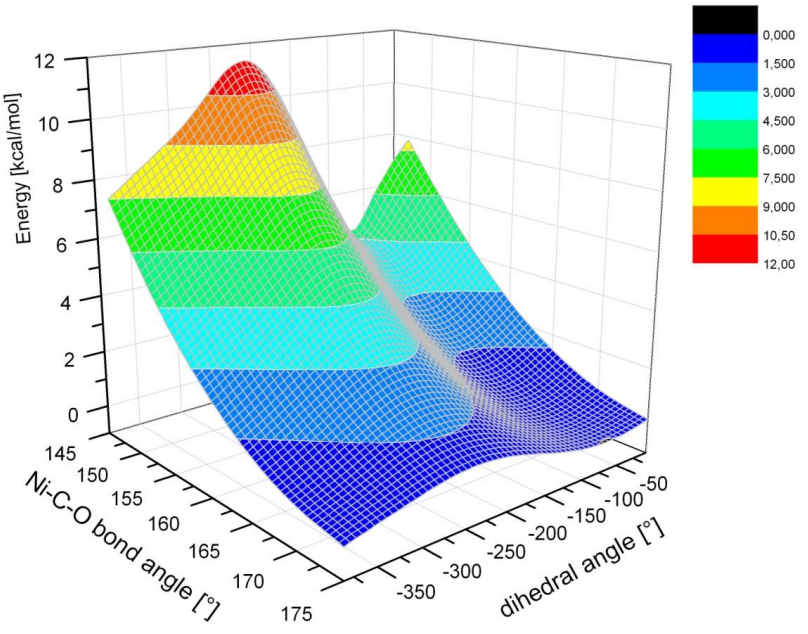

a

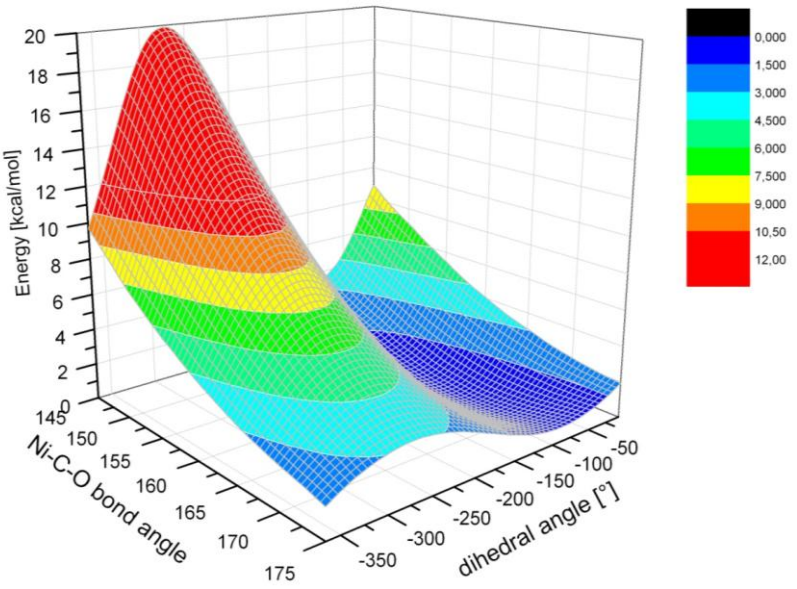

b

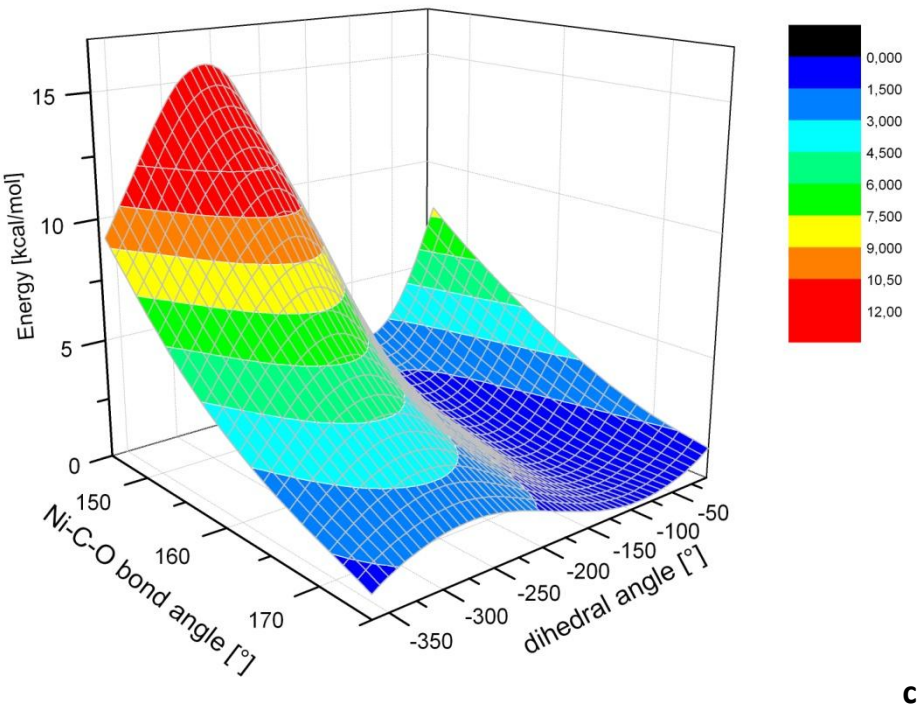

c

Figure 2: Two–dimensional relaxed surface scans. The energy [kcal/mol] is plotted as a function of the Ni–C_{CO}–O_{CO} bond angle [°] and the O_{CO}–C_{CO}–Ni–Sγ(Cys546) dihedral angle [°]. The energy at the global minimum has been set to zero. The calculations have been carried out with the (a) small ^{1}Ni–CO model and (b) the small ^{1}Ni–CO model supplemented with Arg479 and Asp123 (c) the small ^{2}Ni–CO model supplemented with Arg479 and Asp123.

In Figure 2, the energy is plotted as a function the Ni–C_{CO}–O_{CO} bond angle [°] and the O_{CO}– C_{CO}–Ni–Sγ(Cys546) dihedral angle. The relaxed surface scans were performed with the small model (Figure 2a) and the small model (Figure 2b) supplemented with the Arg479 and Asp123 residues. The Ni–C_{CO}–O_{CO} bond angle [°] was chosen as variable parameter in order to investigate the energy change upon bending of the CO ligand as observed in X–Ray and in the geometry–optimized structures. Variation of the O_{CO}–C_{CO}–Ni–Sγ(Cys546) dihedral angle corresponds to a rotation of the CO ligand about the C_{CO}–Ni bond and was chosen in order to understand the different O_{CO}–C_{CO}–Ni–Sγ(Cys546) dihedral angles found for the geometry–optimized structures (Table 2).

With respect to the dihedral angle, one energy maximum and one minimum is present in both plots. However, for the maximum of the dihedral angle, the *increase* of the energy with *decreasing* Ni–C_{CO}–O_{CO} angle is steeper in (b). For the energy minimum of the dihedral angle the opposite behavior is found. As apparent from (b), for dihedral angle between -50° to -200°, the energy does not change by more than 1.5 kcal/mol. This readily explains the different O_{CO}– C_{CO}–Ni– Sγ(Cys546) dihedral angles in the geometry optimized structures. Within this range of dihedral angles, the energy in (b) varies only slightly for different bond angles whereas in (a) the energy increases slowly but continuously. The plot for the small ^{2}Ni–CO model supplemented with Arg479 and Asp123 (Figure 2c) is very similar to that of the ^{1}Ni–CO model and, hence, the binding mode of the CO ligand is apparently not significantly different in the doublet relative to the singlet state. In summary, it can be concluded that the inclusion of the Arg479 and Asp123 residues leads to a flattening of the energy profile for dihedral angle between -50° to -200° while, at more negative dihedral angles, the energy change is more pronounced for different bond angles.

Energies for CO coordination at the terminal nickel site

	ΔE_{CO}	ΔE_{Prot}	ΔE_{sites}
^{2}Ni–CO/H^{-}	–15	0	–
^{2}Ni–CO	–26	–	0
^{2}Ni–CO H^{+}81–A	–24	5	2
^{2}Ni–CO H^{+}81–B	–25	2	2
^{2}N^{i}–CO H^{+}84	–31	9	1
^{2}Ni–CO H^{+}546–A	–25	–6	2
^{2}Ni–CO H^{+}546–B	–27	–2	–1
^{2}Ni–CO H^{+}549	–31	12	1

a

	ΔE_{CO}	$\Delta E_{trip/singl}$	ΔE_{sites}
^{1}Ni–CO	–27	17	–
^{3}N^{i}–CO	–4	–	–11
^{1}Ni–CO/H^{-}	–6	–7	–
^{3}Ni–CO/H^{-}	–11	–	–

b

Table 3: Energies [kcal/mol] of the (a) EPR–active and (b) EPR–silent Ni–CO models. ΔE_{CO} has been computed with the BP86 functional, since using the B3LYP functional results in significant spin contamination in the case of an unoccupied terminal nickel site (chapter 3). ΔE_{prot} designates the energy for both, removing the hydride of Ni–CO/H^{-} from the bridging position and subsequent binding to one of the terminal cysteines as a proton. ΔE_{sites} is the energy for moving the CO ligand from the terminal nickel position to the bridging position. $\Delta E_{trip/singl}$ designates the energy difference between triplet and singlet state.

As evident from Table 3a, the CO–binding energy ΔE_{CO} [kcal/mol] is negative for all models ranging from –15 kcal/mol for ^{2}Ni–CO/H^{-} to –31 kcal/mol for ^{2}Ni–CO H^{+}549 and ^{2}Ni–CO H^{+}84. Upon photo–conversion of the Ni–C to the Ni–L state, the hydride leaves the bridging position [13] and eventually binds to one of the cysteine sulfur atoms (chapter 4.3). The negative ΔE_{CO} values for the models indicate that the EPR–active Ni–CO state is energetically accessible by incubation of the Ni–L state under CO atmosphere as described by Pandelia and co–workers [10, 14].

Inspection of Table 3a reveals that the ΔE_{Prot} values are negative only for ^{2}Ni–CO H^{+}546–A and ^{2}Ni–CO H^{+}546–B, which shows that only the conversion of Ni–CO/H^{-} to ^{2}Ni–CO H^{+}546–A or ^{2}Ni–CO H^{+}546–B would be energetically favorable. Only the models with negative ΔE_{Prot} energies are thermodynamically stable with respect to dissociation of the cysteine–bound proton and formation of a bridging hydride. ΔE_{site} is the energy, which is required for the transfer of the CO molecule from the terminal nickel site to the bridging site of the bimetallic core. For coordination of the CO ligand at the bridging position an energy minimum was only found for μ–type binding, where the carbon atom

of the CO ligand coordinates to both metals. For the EPR–active Ni–CO cluster models, ΔE_{site} is only slightly positive and with –1 kcal/mol becomes even negative for ^{2}N–CO H^{+}546–B. Thus, binding to the terminal nickel position is only slightly favored over binding to the bridging position.

For the EPR–silent Ni–CO models, the energy values ΔE_{CO}, ΔE_{Prot} and ΔE_{site} are presented in Table 3b. All four models exhibit negative ΔE_{CO} values but, for ^{3}Ni–CO and ^{1}Ni–CO/H^{-}, CO–binding to the active site is relatively weak as indicated by ΔE_{CO} values of only –4 kcal/mol and –6 kcal/mol. ^{3}Ni–CO binding to the bridging site is favored by –11 kcal/mol relative to the terminal nickel site as indicated by the corresponding value for ΔE_{site}. In the case of the ^{1}Ni–CO model, no energy minimum has been found at the bridging position and the exogenous CO ligand binds exclusively to the terminal nickel position. In the Ni–CO/H^{-} models, the bridging site is occupied by the hydride ligand and, hence, only the terminal nickel–site is available for binding. For ^{1}Ni–CO and ^{3}Ni–CO, which feature a vacant bridging position, the triplet state is by 17 kcal/mol higher in energy. On the other hand, the $^{3}Ni^{II}$–CO/H^{-} model is favored over the corresponding singlet model, $^{1}Ni^{II}$–CO/H^{-}, by 7 kcal/mol.

Influence of Arg479 and Asp123 on CO binding at the terminal site and the bridging site

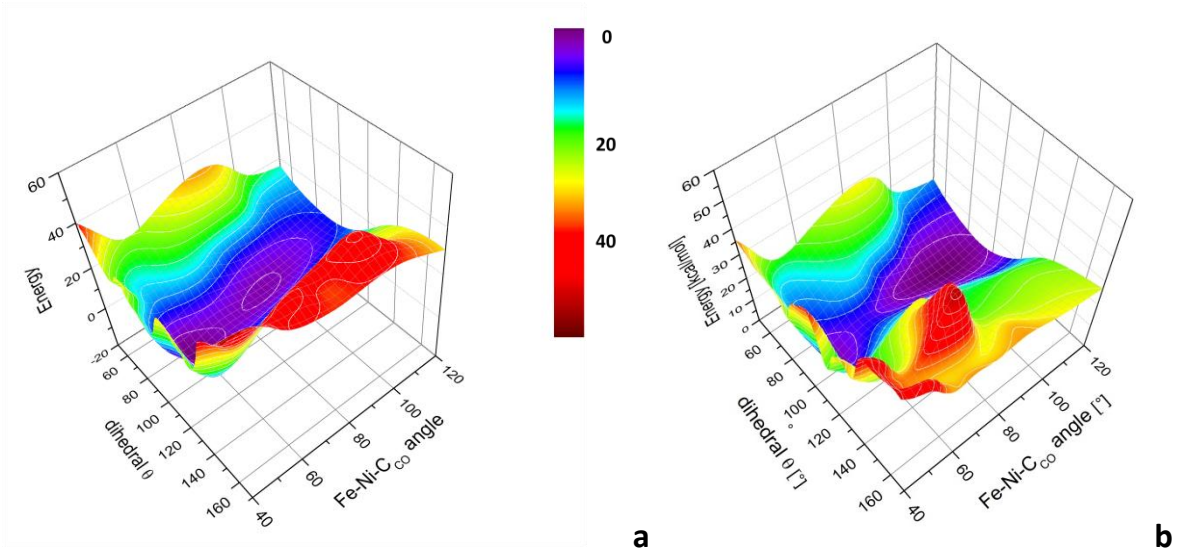

Figure 3: Two–dimensional relaxed surface scans computed with the ^{2}Ni–CO model. The energy [kcal/mol] is plotted as a function of the Fe–Ni–C_{CO} angle [°] and the Sγ(Cys84)–Ni–Fe–C_{CO} dihedral angle [°]. The energy at the global minimum has been set to zero. The calculations have been performed with the (a) small ^{2}Ni–CO model and (b) the small ^{2}Ni–CO model supplemented with the Arg479 and Asp123 amino acid fragments taken.

In order to study the potential energy surface of exogenous CO binding in more detail, two–dimensional relaxed surface scans have been performed. The energy [kcal/mol] has been plotted as a function of the Fe–Ni–C_{CO} bond angle [°] and the S(Cys84)–Ni–Fe–C_{CO} dihedral angle θ [°]. The two variable internal coordinates are equivalent to those of the corresponding scan of the Ni-C state (section 4.2) and were chosen to explore the transition from the structure with CO-coordinated at the bridging site to the structure where the CO is bound at the terminal nickel site.The plot in Figure 3a has been obtained with the small ^{2}Ni–CO cluster model. Two energy minima can be identified on the potential energy surface, which are both found at a dihedral angle of 95°. The first minimum at the Fe–Ni–C_{CO} bond angle of 100° corresponds to the coordination of the CO ligand to the terminal nickel site. The second minimum is located at a smaller bond angle of about 55° and, consistently, corresponds to a μ–type coordination of the CO ligand at the bridging position. The two minimum structures as well as the geometries which are adopted in the course of the interconversion of the minimum structures form a nearly iso-energetic surface. Accordingly, the CO ligand can equilibrate almost unrestrictedly between the two binding sites. For the computation of the plot in Figure 3b, the small ^{2}Ni–CO model has been supplemented with the amino acid fragments of Arg479 and Asp123, which are positioned nearby the two binding sites. With these two amino acids from the second coordination shell included, the two energy minima are separated by an energetically higher

lying energy barrier, which amounts to about 9 kcal/mol. Thus, Arg479 and Asp123 restrict the nearly free equilibration of the CO ligand between the two binding sites and might be responsible for trapping the CO ligand at the terminal nickel site in a meta–stable state.

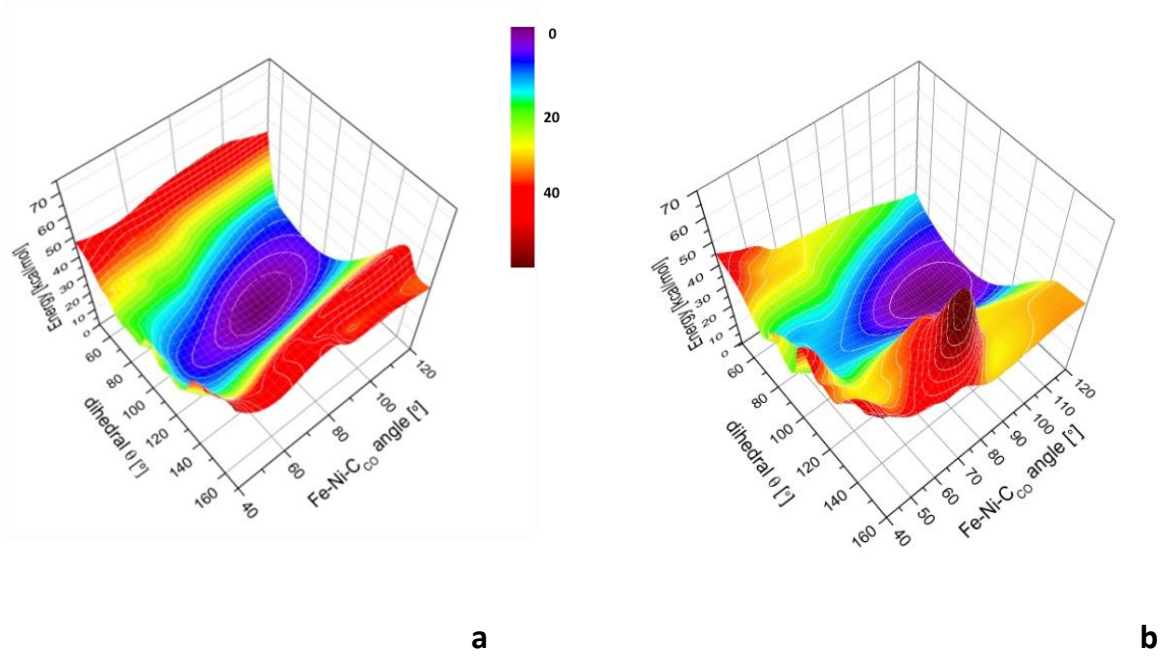

Figure 4: Two–dimensional relaxed surface scans carried out with the ^{1}Ni–CO model. The energy [kcal/mol] is plotted as a function of the Fe–Ni–C_{CO} angle [°] and the Sγ(Cys84)–Ni–Fe–C_{CO} dihedral angle [°]. The energy at the global minimum has been set to zero. The calculations have been performed with the (a) ^{1}Ni–CO small model and (b) the ^{1}Ni–CO small model supplemented with the Arg479 and Asp123 amino acid fragments taken from the large model.

The two–dimensional relaxed surface scans in Figure 4a have been obtained with the small ^{1}Ni–CO model. It is evident from the plot that the bridging position is by 7–9 kcal/mol higher in energy than the terminal nickel site. At the bridging position no energy minimum can be identified and, therefore, only a minimum is present at the terminal nickel site. The plot in Figure 4b has been computed using the small ^{1}Ni–CO model supplemented with the amino acid fragments Arg479 and Asp123. As in Figure 4a, no energy minimum is found at the bridging position. By inclusion of Arg479 and Asp123 fragments in Figure 4b, the energy difference of the terminal nickel site and the bridging position increases. Hence, the amino acids Arg479 and Asp123 of the second coordination shell reinforce the energetic preference of CO–coordination to the terminal nickel site over binding to the bridging site.

In summary, as indicated by the negative CO–binding energies, coordination of the CO molecule to the terminal nickel site is energetically feasible for all cluster models. In the case of the EPR–silent

models, the singlet ^{1}Ni–CO model is more stable than the triplet ^{3}Ni–CO model, while the triplet ^{3}Ni–CO/H^{-} is favored over the singlet ^{1}Ni–CO/H^{-}. In the case of the ^{1}Ni–CO model, no energy minimum has been found at the bridging site while in the ^{3}Ni–CO model, coordination to the bridging site is favored. For the EPR–active Ni–CO models, the structures with the CO ligand coordinated to the bridging position and the terminal nickel position exhibit nearly identical energies. Two–dimensional relaxed surface scans reveal that the two amino acids Arg479 and Asp123 destabilize the binding of the CO ligand to the bridging position relative to the terminal nickel site and increase the energy barrier for the respective interconversion.

4.4.5. Electronic structure of the EPR–observable Ni–CO models

In this section, the electronic structure, of the EPR–observable states, is discussed. As coordinate system, the g tensor principal axes system of the Ni–C state has been chosen. In this axes system the z–axis points approximately along the Ni–Sγ(Cys549) bond and the x–axis points along Ni–Sγ(Cys81). In the Ni–C state the spin density is present in the Ni d_{z^2} orbital.

Most notably, in the EPR–active ^{2}Ni–CO H^{+}546 states (Figure 5), the $d_{x^2-y^2}$ orbital and the d_{z^2} orbitals mix and thereby re–hybridize to a $d_{x^2-z^2}$ orbital and a d_{y^2} orbital. Hence, the electronic structure of the ^{2}Ni–CO H^{+}546 states differs markedly from that of the Ni–C state and should thereby feature different spectroscopic properties. Upon the photo–induced formation of the Ni–L state from the Ni-C state, the nickel $d_{x^2-y^2}$ orbital and the d_{z^2} orbitals rehybridize (chapter 4.3) to a $d_{y^2-z^2}$ and a d_{x^2} orbital. The EPR active Ni–CO state is most likely formed by a two–step mechanism [10], i.e. firstly formation of the Ni–L state from the Ni–C state by photo–conversion and, secondly, binding of the CO ligand to the nickel site. The coordination of the CO molecule in the second step then results in another rehybridization of the orbitals from $d_{y^2-z^2}$ /d_{x^2} to $d_{x^2-z^2}$ /d_{y^2}. A corresponding orbital scheme is presented in Figure 5 for ^{2}Ni–CO H^{+}546–A (^{2}Ni–CO H^{+}81–A, ^{2}Ni–CO H^{+}81–B, ^{2}Ni–CO H^{+}546–B and ^{2}Ni–CO feature similar electronic structures). As in Ni–L, in the Ni–CO state, the hydride ligand binds as a proton to one of the cysteines, which results in a formal reduction of the nickel center from a 3+ to a 1+ oxidation state. However, a sizable amount of electron density is transferred into the unoccupied π^*–orbital of the CO ligand by a ligand–metal back–bonding interaction with the nickel $d_{x^2-z^2}$ orbital (inset, Figure 5). The back–bonding contributes to a lowering of the $d_{x^2-z^2}$ orbital energy below that of the d_{y^2} orbital leading to the presence of the unpaired electron in the d_{y^2} orbital instead of the $d_{x^2-z^2}$ orbital (Figure 6).

In the Ni–L state, electron density is transferred from the nickel to the iron center by means of a nickel–iron bond. Transfer of electron density to the iron, and thereby formation of a metal–metal

bond, is also observed in Ni–CO but to a somewhat smaller extend than in Ni–L. This is demonstrated by the Ni–Fe Mayer bond orders, which amount to 0.4 in Ni–L and 0.3 in the ^{2}Ni–CO H^{+}546-A model (BP86). The smaller bond order in Ni–CO with respect to Ni–L presumably results from the transfer of electron density from the metal–metal bond to the CO ligand by means of back–bonding.

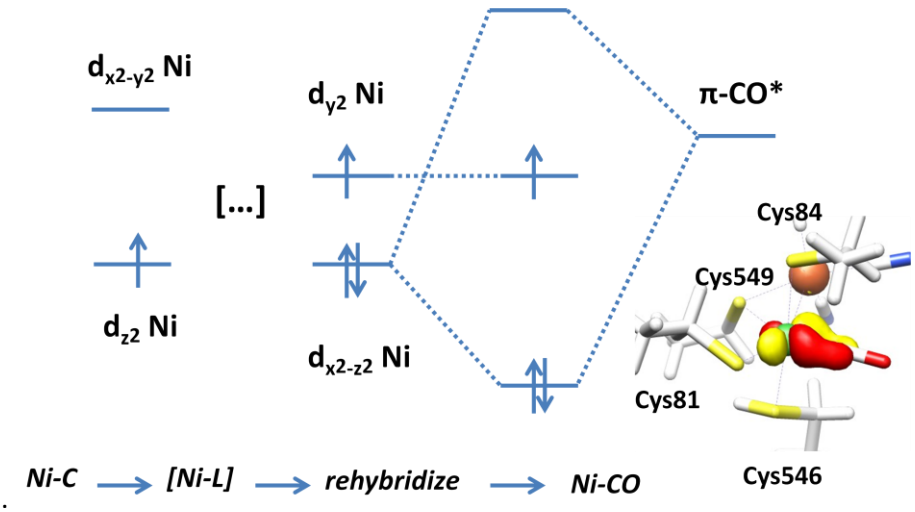

Figure 5: MO scheme for ^{2}Ni–CO H^{+}546. Upon Ni–L formation (not shown explicitly) the d_{z^2} and the $d_{x^2-y^2}$ orbitals rehybridize to d_{x^2} and $d_{y^2-z^2}$ orbitals which in turn rehybridize to d_{y^2} and the $d_{x^2-z^2}$ orbitals in Ni–CO. The energy of the $d_{x^2-z^2}$ is stabilized with respect to the d_{y^2} orbital by back–bonding with the π*–CO ligand

A SOMO of d_{y^2} type is unique in [NiFe] hydrogenases. The spin density in the d_{y^2} orbital results, by means of σ–bonding interactions, in a spin delocalization into the p orbitals of Sγ(Cys546) and Sγ(Cys84) as shown for ^{2}Ni–CO H^{+}546–A in Figure 6. For ^{2}Ni–CO H^{+}546–A, the Mulliken spin population of Sγ(Cys84) is by 0.04 larger than the one of Sγ(Cys546), which is in line with the stabilization of the Sγ(Cys546) p–orbital due to protonation. The spin population of C_{CO} is with 0.02 relatively small. Conclusively, As ^{2}Ni–CO H^{+}81–A, ^{2}Ni–CO H^{+}81–B and ^{2}Ni–CO exhibit similar electronic structures as ^{2}Ni–CO H^{+}546–A and ^{2}Ni–CO H^{+}546–B, one can expect these models to be hardy distinguishable by means of their magnetic properties such as g–tensors and hyperfine couplings.

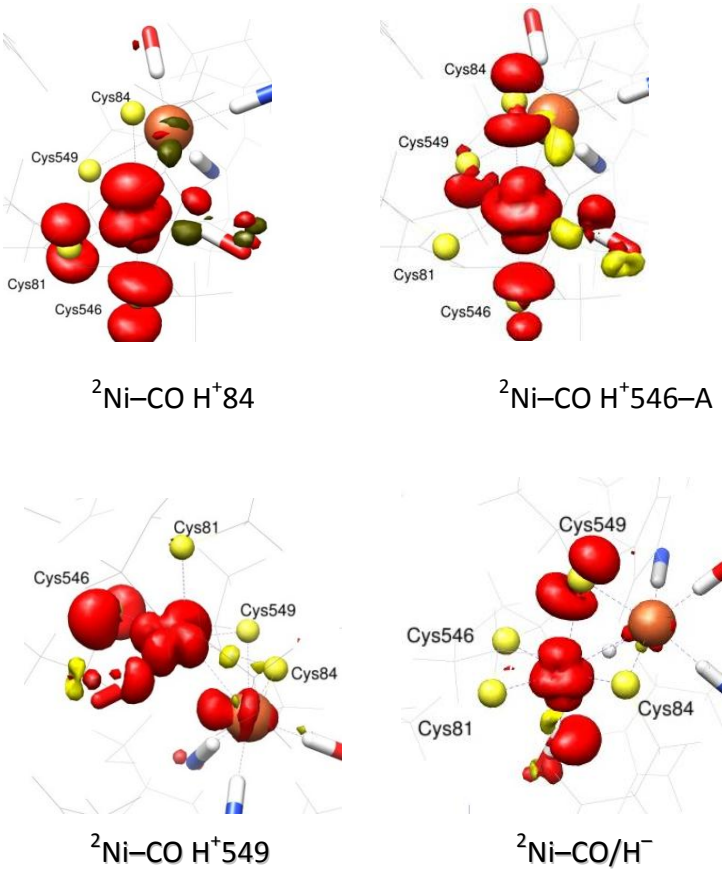

Figure 6: Spin density plots ^{2}Ni–CO H$^+$84, ^{2}Ni–CO H$^+$546–A, ^{2}Ni–CO H$^+$549 and ^{2}Ni–CO/H$^-$. The plots for ^{2}Ni–CO H$^+$81–A, ^{2}Ni–CO H$^+$81–B, ^{2}Ni–CO H$^+$546–B and ^{2}Ni–CO are similar to the plot for ^{2}Ni–CO H$^+$546–A and, therefore, are not shown.

In ^{2}Ni–CO/H$^-$, the spin density at the metal is found in a nickel d_{z^2} orbital and is markedly delocalized into a p–orbital of Sγ(Cys549) (Figure 6b). The spin density distribution of ^{2}Ni–CO/H$^-$ is thereby similar to that of the Ni–C state (chapter 4.2), which is readily understood by considering that the bridging hydride of Ni–C is also present in ^{2}Ni–CO/H$^-$. In addition, since the ligand–metal bond of the CO ligand is oriented approximately along the z–axis, the sp orbital of the C_{CO} atom can efficiently overlap with the spin carrying d_{z^2} orbital of the nickel atom. This results in significant amounts of spin density at the C_{CO} atom. The delocalization of spin density is reflected by the Mulliken spin populations (Table 4), which are 0.2 for Sγ(Cys546) and 0.11 for C_{CO}. Conclusively, due to the sizable amount of spin density at the carbon of the CO ligand, the ^{2}Ni–CO/H$^-$ should be clearly distinguishable from the other EPR-active models by the possibly large ^{13}C hyperfine coupling.

In ^{2}Ni–CO H^{+}549, the spin carrying nickel orbital forms a π–bonding interaction with the p–orbital of Sγ(Cys546) which contains the free electron pair. Interaction with an unoccupied Fe d–orbital leads to the transfer of spin density from nickel to iron as evidenced by a positive Fe spin population of 0.15. The spin population at the C_{CO} amounts to 0.05.

In the case of ^{2}Ni–CO H^{+}84, a π–bonding interaction of the spin carrying nickel d–orbital with the doubly occupied Sγ(Cys81) p–orbital and a σ–bonding interaction with the doubly occupied p–orbital of Sγ(Cys546) lead to significant amounts of spin density at these two sulfur atoms, while the spin density at C_{CO} is rather small as evidenced by a spin population of only 0.01. In line with the almost vanishing spin density at the carbon atom, ^{2}Ni–CO H^{+}84 should be distinguishable from the other models by means of a probably small ^{13}C hyperfine coupling constant of the ^{13}CO ligand.

	S_{Cys81}	S_{Cys84}	S_{Cys546}	S_{Cys549}	Ni	Fe	C_{CO}	O_{CO}
^{2}Ni–CO/H^{-}	–0.02	–0.02	0.01	0.20	0.68	0.00	0.11	0.00
^{2}Ni–CO	0.05	0.13	0.15	0.04	0.78	–0.15	0.02	–0.02
^{2}Ni–CO H^{+}81–A	0.03	0.14	0.15	0.05	0.71	–0.08	0.03	–0.02
^{2}Ni–CO H^{+}81–B	0.03	0.13	0.15	0.04	0.71	–0.08	0.04	–0.01
^{2}Ni–CO H^{+}84	0.11	0.00	0.19	0.00	0.72	–0.05	0.01	–0.01
^{2}Ni–CO H^{+}546–A	0.04	0.14	0.09	0.07	0.78	–0.11	0.02	–0.02
^{2}Ni–CO H^{+}546–B	0.04	0.14	0.10	0.08	0.78	–0.11	0.02	–0.02
^{2}Ni–CO H^{+}549	0.00	–0.02	0.16	0.00	0.67	0.15	0.05	–0.02

Table 4: Mulliken spin populations.

4.4.6. Magnetic spectroscopy

g–tensor

	g_1	g_2	g_3	g_{iso}
^{2}Ni–CO/H$^-$	2.03	2.07	2.09	2.06
^{2}Ni–CO	2.02	2.08	2.10	2.07
^{2}Ni–CO H$^+$81–A	2.02	2.07	2.09	2.06
^{2}Ni–CO H$^+$81–B	2.02	2.06	2.09	2.06
^{2}Ni–CO H$^+$84	2.03	2.08	2.16	2.09
^{2}Ni–CO H$^+$546–A	2.02	2.08	2.10	2.07
^{2}Ni–CO H$^+$546–B	2.02	2.07	2.10	2.06
^{2}Ni–CO H$^+$549	2.05	2.06	2.15	2.08
exptl. [3]	2.02	2.07	2.12	2.07

Table 5: g–values of the EPR–active Ni–CO models.

In Table 5, g–values are presented for the EPR–active models. The ^{2}Ni–CO H$^+$81–A, ^{2}Ni–CO H$^+$81–B, ^{2}Ni–CO H$^+$546–A, ^{2}Ni–CO H$^+$546–B, ^{2}Ni–CO/H$^-$ and ^{2}Ni–CO models feature similar g–values. For a g_3 value of 2.09, the corresponding experimental value of 2.12 is underestimated by about 25%. Such an underestimation of the g–tensor in nickel transition metals is well documented [15], and, given this underestimation, the ^{2}Ni–CO H$^+$81–A, ^{2}Ni–CO H$^+$81–B, ^{2}Ni–CO H$^+$546–A, ^{2}Ni–CO H$^+$546–B, ^{2}Ni–CO/H$^-$ and ^{2}Ni–CO models with g_3 values ranging from 2.09 to 2.10 suitably reproduce the experimental value. However, the computed g_2 values and thereby also the g_{iso} values seem to be slightly too large.

According to their markedly different spin density distribution, the ^{2}Ni–CO H$^+$549 and the ^{2}Ni–CO H$^+$84 models are exceptions, which exhibit g_3 values of 2.15 and 2.16, respectively, which are clearly too large with respect to experiment.

The ^{2}Ni–CO/H$^-$ model features a d_{z^2} orbital as singly occupied orbital with the axis of the g_1 component of the g–tensor pointing along the z–axis. On the other hand, the d_{y^2} orbital is the spin–containing nickel orbital in the ^{2}Ni–CO H$^+$81–A, ^{2}Ni–CO H$^+$81–B, ^{2}Ni–CO H$^+$546–A, ^{2}Ni–CO H$^+$546–B and ^{2}Ni–CO models and the axis of the g_1 component points along the y–axis. Although they feature similar g–values, it should be possible to distinguish ^{2}Ni–CO/H$^-$ from ^{2}Ni–CO H$^+$81–A, ^{2}Ni–CO H$^+$81–B, ^{2}Ni–CO H$^+$546–A, ^{2}Ni–CO H$^+$546–B and ^{2}Ni–CO by means of the different orientations of their g–tensor axes. Unfortunately, single crystal EPR measurements and, hence, experimentally determined orientations of the g–tensor axes have not been reported for the EPR–active Ni–CO state, yet.

^{13}C hyperfine couplings

	A_1	A_2	A_3	A_{iso}
Ni–CO/H^-	200	204	225	210
Ni–CO	67	75	86	76
Ni–CO H^+81–A	65	70	82	72
Ni–CO H^+81–B	70	74	87	77
Ni–CO H^+84	3	11	18	11
Ni–CO H^+546–A	84	89	99	91
Ni–CO H^+546–B	85	89	99	91
Ni–CO H^+549	127	131	139	132
exptl. [3]	–	–	–	85

Table 6: ^{13}C hyperfine couplings of exogenously bound ^{13}CO. Experimental values for A_1, A_2 and A_3 were not determined.

In Table 6, ^{13}C hyperfine coupling constants of ^{13}CO are presented. Experimentally, an isotropic ^{13}C hyperfine coupling constant of 85 MHz has been reported [3]. With A_{iso} values between 72 and 77 MHz, the EPR–active models ^{2}Ni–CO H^+81–A, ^{2}Ni–CO H^+81–B and ^{2}Ni–CO feature isotropic hyperfine couplings that match the experimental value suitably. The experiment is also satisfactorily reproduced by ^{2}Ni–CO H^+546–A and ^{2}Ni–CO H^+546–B, of which the A_{iso} values are only 6 MHz larger than the experimentally observed one. The similar hyperfine couplings found for these four models are in line with their similar Mulliken spin populations of C_{CO}. On the other hand, ^{2}Ni–CO/H^- and, to a smaller degree, ^{2}Ni–CO H^+549, both exhibit isotropic hyperfine coupling constants, which are significantly larger than the experimental values. The large A_{iso} values are in line with the relatively large Mulliken spin populations found for C_{CO} in the two models. Most notably, a spin–carrying d_{z^2} orbital can be clearly excluded and, hence, according to the ^{13}C hyperfine couplings the EPR–active Ni–CO state necessarily features an electronic ground state which markedly differs from that of the Ni–C state.

4.4.7. CN^- and CO stretching frequencies

	ν(CO)	ν(CO_{ex})	ν(CN^-)	ν(CN^-)
^{1}Ni–CO /H^-	1900	1929	2022	2049
^{3}Ni–CO/H^-	1906	1952	2018	2046
^{1}Ni–CO	1946	2016	2054	2074
^{3}Ni–CO	1946	1972	2051	2080
exptl. [16]	1931	2056	2070	2083

Table 7: IR frequencies [cm^{-1}]; CO_{ex} refers to the exogenous carbon monoxide. The computed frequencies have been up–shifted by an additive constant of 29 cm^{-1} [17-18] since CO stretching frequencies are systematically underestimated by DFT.

Experimental CO and CN^- stretching frequencies have only been reported for the EPR-silent state. The experimental values along with the calculated ones from the EPR–silent models are collected in Table 7. The experimentally determined frequency of the Fe–bound CO ligand is by 30 cm^{-1} smaller than the corresponding value found for the Ni–C state [19]. This reduction of the CO stretching frequency is reproduced by all models. However, in absolute terms, the computed value is most compatible with the experimental data for the ^{1}Ni–CO model and the ^{3}Ni–CO model. Contrarily, the frequencies obtained with the models which feature a bridging hydride, namely the ^{1}Ni–CO /H^- and ^{3}Ni–CO /H^- models, are significantly too small.

It is evident from Table 7 that the experimentally determined CO frequency which corresponds to the exogenous CO_{ex} is by more than 100 cm^{-1} larger than that of the Fe–bound CO, which indicates that the Ni–CO back–bonding is markedly reduced in the case of the Ni–bound CO. The observation of a single CO stretching frequency instead of a broad spectrum in the Ni–CO state might indicate that the energy minimum is energetically well defined and that than the potential energy surface in Figure2b might be somewhat too flat. However, it should be kept in mind that, according to the Bolzmann distribution, an energy difference between two structures of only 1 kcal/mol results in a fivefold larger population of the more stable structure. All computed CO frequencies significantly underestimate the experimental value of 2056 cm^{-1}. Amongst the various models, the ^{1}Ni–CO gives the largest frequency and, hence, reproduces the experimental frequencies best. The difference of experimental and computed frequency is relatively large. Nevertheless, in qualitative terms, the ^{1}Ni–CO model reproduces a markedly larger CO frequency of the exogenous CO ligand relative to the Fe–bound CO ligand. For the Fe–bound CO ligand, the accuracy of the CO frequency calculation has been evaluated for the well–characterized Ni–C state while, unfortunately, the quality of the frequency calculations of the nickel–bound CO ligand cannot be assessed. An underestimation of the frequency

of the exogenous CO ligand is however not very surprising as the covalency of the sulfur-nickel bonds tends to be overestimated by DFT.

The CN^- frequencies obtained with the ^{1}Ni–CO model are smaller than the experimental values. However, at least for the antisymmetric stretching frequency a smaller value is also found for the structurally well-characterized Ni-C state.

4.4.8. Conclusion

We have studied CO inhibition of [NiFe] hydrogenase by using large cluster models, which include, in addition to the first coordination shell, i.e. the exogenous CO ligand, the bimetallic core, the four coordinating cysteines and the three Fe–coordinating two–atomic ligands, amino acid fragments of the complete second coordination shell. Computed results of the EPR–active Ni–CO state are most compatible with experimental parameters for structures, in which the active site features a vacant bridging position with the former hydride being bound to one of the terminal cysteine residues Cys546 or Cys81 (^{2}Ni–CO H^+546–A, ^{2}Ni–CO H^+546–B, ^{2}Ni–CO H^+81–A, ^{2}Ni–CO H^+546–B) while the exogenous CO ligand binds to the terminal nickel site opposite to Sγ(Cys549). Similarly, in a computational Ni–L study (chapter 4.3), the terminal cysteines were also found to bind the bridging hydride as a proton upon photo–conversion from Ni–C to Ni–L. Most notably, the electron density is present in d_{y^2} orbital, which corresponds to a unique electronic ground state in [NiFe] hydrogenase, The rehyridized $d_{x^2-z^2}$ forms a back–bonding interaction with the exogenous CO ligand.

With respect to the EPR–silent Ni–CO state, the cluster model which is most compatible with the experimental data is the singlet ^{1}Ni–CO model. The ^{1}Ni–CO model features a vacant bridging position and the exogenous CO ligand is bound to the terminal nickel site. Based on the poor agreement of the computed results with experimental data, the corresponding triplet state can be safely excluded. The X–Ray structure of the enzyme clearly shows that the CO ligand binds to the nickel site in a bent conformation, which is reproduced by our calculations. Furthermore, we could demonstrate that the Arg479 and Asp123 residues play an important role in CO–coordination to the nickel site, since they seemingly increase the barrier for binding of the CO ligand to the bridging site and are apparently responsible for the flat energy surface is found for bending of the exogenous CO ligand. As initial H_2 coordination also takes place by a ligand–metal back–bonding interaction (chapter 4.6) and thereby its binding mode is similar to that of the CO ligand, the results obtained from the study of the EPR-silent CO–inhibited state might have interesting implications for the catalytic mechanism. Firstly, coordination of the H_2 substrate is likely to also take place at the nickel center and, secondly, the state of the catalytic cycle where H_2 binds to the active site is also singlet spin state [20].

In summary, the present study reveals some important features of inhibition of [NiFe] hydrogenase by carbon monoxide, such as an electronic ground state with a d_{y^2} singly occupied orbital in the EPR–active Ni–CO state and a singlet spin state in the EPR–silent Ni–CO state. Moreover, the present investigation of the CO–inhibited states, may contribute to a better understanding of the catalytic mechanism as the electronic features of CO and H_2 binding to the active site are very similar.

References

1. Fauque, G., et al., *The 3 classes of hydrogenases from sulfate-reducing bacteria of the genus desulfovibrio.* Fems Microbiology Reviews, 1988. **54**(4): p. 299-344.
2. Vanderzwaan, J.W., et al., *Electron-paramagnetic-res evidence for direct interaction of carbon-monoxide with nickel in hydrogenase from chromatium-vinosum.* Biochimica Et Biophysica Acta, 1986. **872**(3): p. 208-215.
3. Vanderzwaan, J.W., et al., *Effect of o-17(2) and (co)-c-13 on epr-spectra of nickel in hydrogenase from chromatium-vinosum.* Biochimica Et Biophysica Acta, 1990. **1041**(2): p. 101-110.
4. Happe, R.P., W. Roseboom, and S.P.J. Albracht, *Pre-steady-state kinetics of the reactions of nife - hydrogenase from chromatium vinosum with h-2 and co.* European Journal of Biochemistry, 1999. **259**(3): p. 602-608.
5. George, S.J., et al., *Reactions of h-2, co, and o-2 with active [nife]-hydrogenase from allochromatium vinosum. A stopped-flow infrared study.* Biochemistry, 2004. **43**(21): p. 6808-6819.
6. Bagley, K.A., et al., *Infrared studies on the interaction of carbon-monoxide with divalent nickel in hydrogenase from chromatium-vinosum.* Biochemistry, 1994. **33**(31): p. 9229-9236.
7. DeLacey, A.L., et al., *Ir spectroelectrochemical study of the binding of carbon monoxide to the active site of desulfovibrio fructosovorans ni-fe hydrogenase.* Journal of Biological Inorganic Chemistry, 2002. **7**(3): p. 318-326.
8. Davidson, G., et al., *Structural examination of the nickel site in chromatium vinosum hydrogenase: Redox state oscillations and structural changes accompanying reductive activation and co binding.* Biochemistry, 2000. **39**(25): p. 7468-7479.
9. Ogata, H., et al., *Structural studies of the carbon monoxide complex of [nife]hydrogenase from desulfovibrio vulgaris miyazaki f: Suggestion for the initial activation site for dihydrogen.* Journal of the American Chemical Society, 2002. **124**(39): p. 11628-11635.
10. Pandelia, M.E., et al., *Inhibition of the [nife] hydrogenase from desulfovibrio vulgaris miyazaki f by carbon monoxide: An ftir and epr spectroscopic study.* Biochimica Et Biophysica Acta-Bioenergetics, 2010. **1797**(2): p. 304-313.
11. Stein, M. and W. Lubitz, *Relativistic dft calculation of the reaction cycle intermediates of nife hydrogenase: A contribution to understanding the enzymatic mechanism.* Journal of Inorganic Biochemistry, 2004. **98**(5): p. 862-877.
12. Pardo, A., et al., *Density functional study of the catalytic cycle of nickel-iron [nife] hydrogenases and the involvement of high-spin nickel(ii).* Journal of Biological Inorganic Chemistry, 2006. **11**(3): p. 286-306.
13. Fichtner, C., M. van Gastel, and W. Lubitz, *Wavelength dependence of the photo-induced conversion of the ni-c to the ni-l redox state in the [nife] hydrogenase of desulfovibrio vulgaris miyazaki f.* Physical Chemistry Chemical Physics, 2003. **5**(24): p. 5507-5513.
14. Pandelia, M.E., H. Ogata, and W. Lubitz, *Intermediates in the catalytic cycle of [nife] hydrogenase: Functional spectroscopy of the active site.* Chemphyschem, 2010. **11**(6): p. 1127-1140.
15. Neese, F., *Prediction of electron paramagnetic resonance g values using coupled perturbed hartree-fock and kohn-sham theory.* Journal of Chemical Physics, 2001. **115**(24): p. 11080-11096.
16. deLacey, A.L., et al., *Infrared spectroelectrochemical characterization of the nife hydrogenase of desulfovibrio gigas.* Journal of the American Chemical Society, 1997. **119**(31): p. 7181-7189.
17. Jonas, V. and W. Thiel, *Theoretical-study of the vibrational-spectra of the transition-metal carbonyls m(co)(6) [m=cr, mo, w], m(co)(5) [m=fe, ru, os], and m(co)(4) [m=ni, pd, pt].* Journal of Chemical Physics, 1995. **102**(21): p. 8474-8484.

18. Jonas, V. and W. Thiel, *Density functional study of the vibrational spectra of octahedral transition-metal hexacarbonyls: Neutral molecules (m = cr, mo, w) and isoelectronic ions (m = v, nb, ta; mn, re; fe, ru, os; co, rh, ir; pt; au).* Organometallics, 1998. **17**(3): p. 353-360.
19. Fichtner, C., et al., *Spectroelectrochemical characterization of the [nife] hydrogenase of desulfovibrio vulgaris miyazaki f.* Biochemistry, 2006. **45**(32): p. 9706-9716.
20. Montet, Y., et al., *Gas access to the active site of ni-fe hydrogenases probed by x-ray crystallography and molecular dynamics.* Nature Structural Biology, 1997. **4**(7): p. 523-526.

Appendix

Electronic structure

	Ni–Fe	Ni–CO	C–O
^{2}Ni–CO/H^{-}	0.26	0.79	2.06
^{2}Ni–CO	0.28	0.91	1.91
^{2}Ni–CO H^{+}81–A	0.23	0.90	1.97
^{2}Ni–CO H^{+}81–B	0.25	0.88	1.99
^{2}Ni–CO H^{+}84	0.26	0.97	1.92
^{2}Ni–CO H^{+}546–A	0.24	0.87	2.00
^{2}Ni–CO H^{+}546–B	0.25	0.90	2.00
^{2}Ni–CO H^{+}549	0.23	0.95	1.98
^{3}Ni–CO/H^{-}	0.22	0.84	1.96
^{1}Ni–CO /H^{-}	0.20	0.75	2.00
^{3}Ni–CO	0.15	0.76	2.07
^{1}Ni–CO	0.23	0.86	2.02

Table A1: Selected Mayer bond orders of the EPR–active and EPR–silent Ni–CO models.

Energies

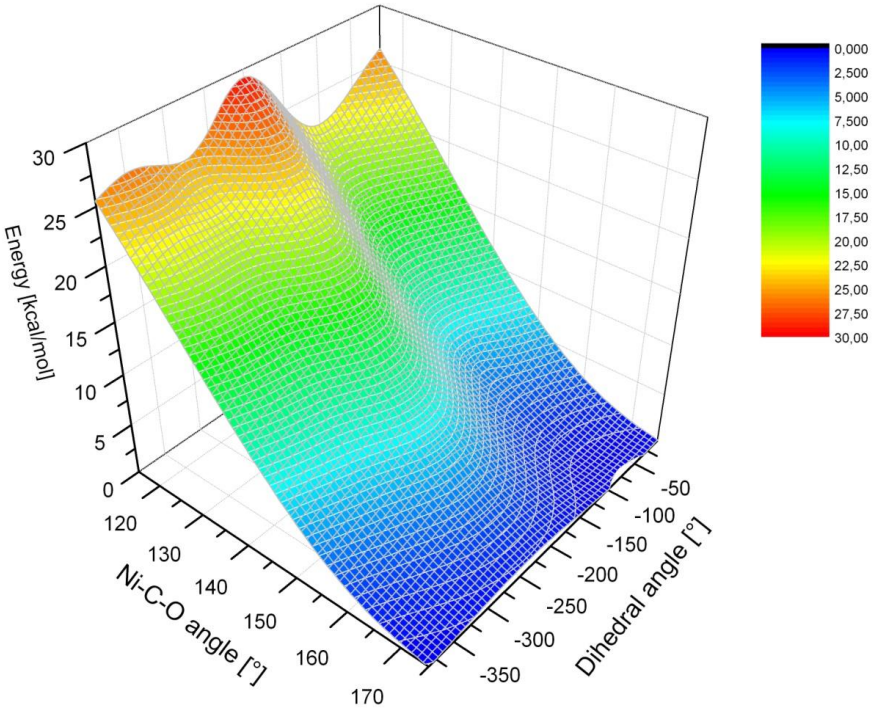

Figure A1: Two–dimensional relaxed surface scan computed with the ^{1}Ni–CO model for extended bond angles of 120°–175°. The energy [kcal/mol] is plotted as a function of the Ni–C_{CO}–O_{CO} bond angle [°] and the C_{CO}–O_{CO}–Ni– Sγ(Cys546) dihedral angle [°]. The energy at the global minimum has been set to zero. The calculations have been performed with the small ^{1}Ni–CO model.

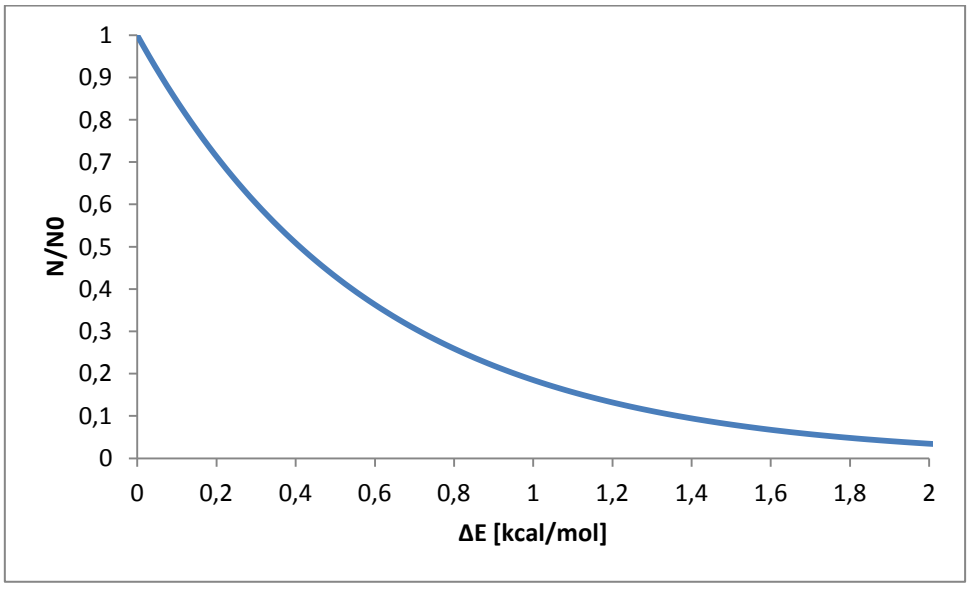

Figure A2: Bolzmann distribution at 25°

^{61}Ni	A_1	A_2	A_3	A_{iso}
^{2}Ni–CO/H^{-}	42	–53	–184	–93
^{2}Ni–CO	10	–77	–170	–86
^{2}Ni –CO H^{+}81–A	11	–60	–163	–70
^{2}Ni –CO H^{+}81–B	14	–61	–162	–70
^{2}Ni –CO H^{+}84	21	–87	–169	–93
^{2}Ni –CO H^{+}546–A	20	–92	–170	–81
^{2}Ni –CO H^{+}546–B	23	–95	–164	–79
^{2}Ni –CO H^{+}549	26	–121	–146	–80

Table A2: ^{61}Ni hyperfine coupling tensor

^{57}Fe	A_1	A_2	A_3	A_{iso}
^{2}Ni–CO/H^{-}	1	2	–2	0
^{2}Ni–CO	–2	–3	–10	–5
^{2}Ni–CO H^{+}81–A	–1	–2	–5	–3
^{2}Ni–CO H^{+}81–B	–1	–2	–5	–3
^{2}Ni–CO H^{+}84	0	–2	–4	–2
^{2}Ni–CO H^{+}546–A	–1	–2	–7	–3
^{2}Ni–CO H^{+}546–B	–1	–2	–7	–3
^{2}Ni–CO H^{+}549	0	2	11	4

Table A3: ^{57}Fe hyperfine coupling tensor

^{33}S(Cys81)	A_1	A_2	A_3	A_{iso}
^{2}Ni–CO/H^{-}	3	8	9	6
^{2}Ni–CO	9	9	23	14
^{2}Ni–CO H^{+}81–A	13	14	22	16
^{2}Ni–CO H^{+}81–B	11	11	21	14
^{2}Ni–CO H^{+}84	4	7	37	16
^{2}Ni–CO H^{+}546–A	3	4	16	8
^{2}Ni–CO H^{+}546–B	3	3	14	7
^{2}Ni–CO H^{+}549	0	–5	5	0

^{33}S(Cys84)	A_1	A_2	A_3	A_{iso}
^{2}Ni–CO/H^{-}	2	9	9	7
^{2}Ni–CO	16	19	50	28
^{2}Ni–CO H^{+}81–A	14	15	51	27
^{2}Ni–CO H^{+}81–B	14	16	51	27
^{2}Ni–CO H^{+}84	17	18	20	18
^{2}Ni–CO H^{+}546–A	13	15	50	26
^{2}Ni–CO H^{+}546–B	13	15	49	25
^{2}Ni–CO H^{+}549	1	8	10	6

^{33}S(Cys546)	A_1	A_2	A_3	A_{iso}
^{2}Ni–CO/H^{-}	0	5	15	7
^{2}Ni–CO	19	20	61	33
^{2}Ni–CO H^{+}81–A	10	11	53	25
^{2}Ni–CO H^{+}81–B	13	14	56	28
^{2}Ni–CO H^{+}84	3	1	56	20
^{2}Ni–CO H^{+}546–A	43	43	68	51
^{2}Ni–CO H^{+}546–B	29	29	57	39
^{2}Ni–CO H^{+}549	–2	3	51	17

^{33}S(Cys549)	A_1	A_2	A_3	A_{iso}
^{2}Ni–CO/H^{-}	12	14	70	32
^{2}Ni–CO	14	16	24	18
^{2}Ni–CO H^{+}81–A	16	18	29	21
^{2}Ni–CO H^{+}81–B	15	16	26	19
^{2}Ni–CO H^{+}84	0	–1	2	0
^{2}Ni–CO H^{+}546–A	20	22	38	27
^{2}Ni–CO H^{+}546–B	21	23	42	29
^{2}Ni–CO H^{+}549	5	5	6	5

Table A4: ^{33}S hyperfine coupling tensors of Cys81, Cys84, Cys546 and Cys

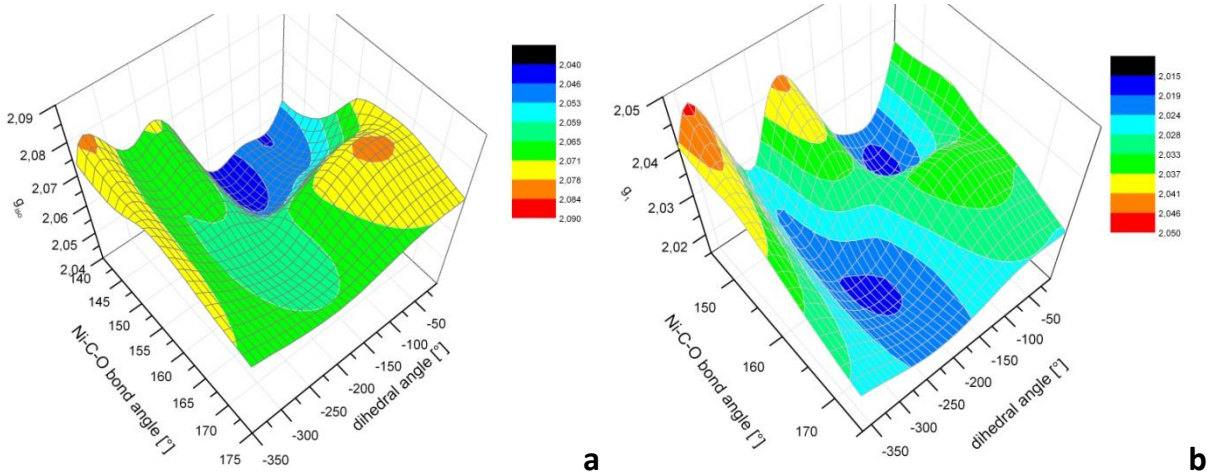

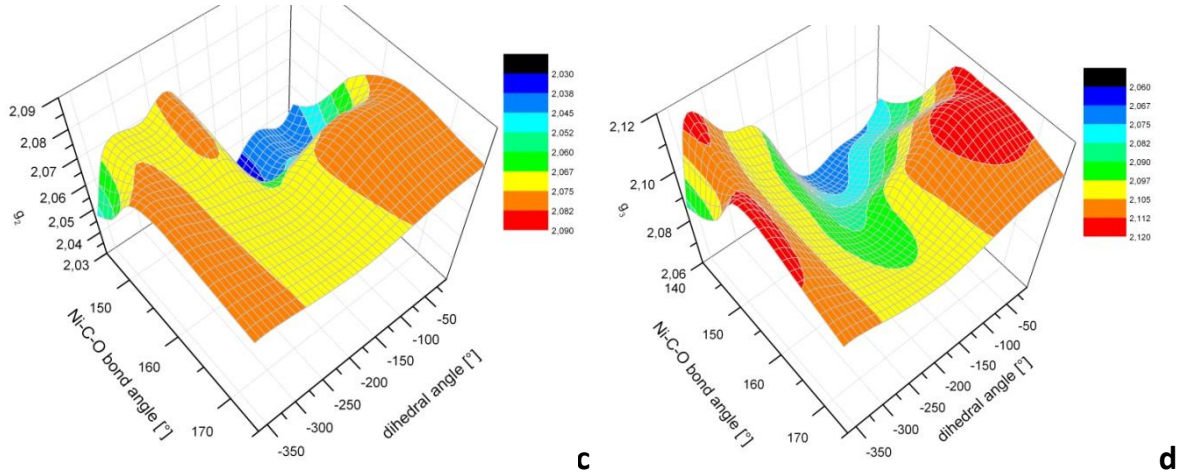

Figure A3: (a) g–iso (b) g_1 (c) g_2 and (d) g_3 values from single–point calculations of the structures from a two–dimensional relaxed surface scan computed with the ^{2}Ni–CO model. The g–values are plotted as a function of the Ni–C_{CO}–O_{CO} bond angle [°] and the C_{CO}–O_{CO}–Ni– Sγ(Cys546) dihedral angle [°]. The small model supplemented with the amino acids Arg479 and Asp123 has been employed.

4.5. The inactive oxidized states

Theoretical IR–frequency calculations corroborate the presence of an OH^- ligand in Ni–A and Ni–B

Abstract

Oxygen inhibition of [NiFe] hydrogenases is considered as one of the fundamental problems in the application of the enzyme for large scale H_2–production from biomass by immobilization in bioreactors. Unfortunately, counter–strategies have not been very successful so far since the molecular principles of oxygen intolerance of [NiFe] hydrogenases are still elusive. Two oxygen–inhibited redox–states have been identified Ni–A and Ni–B and pronouncedly differ in their reactivation behavior. Although studied experimentally and computationally in detail, the structures of the two states are still under debate. In a recent ^{1}H-ENDOR study, a hydroxo ligand OH^- was proposed as ligand for both oxygen–inhibited states, with different orientations of the O–H bond in Ni–A and Ni–B. In the present DFT study, we investigated the orientation dependence of a hydroxyl anion bound to the enzyme´s active site by comparing calculated spectroscopic parameters and geometries with a large body of experimental data. The used large cluster models includes the complete second coordination shell of the enzyme, which is particularly important for the correct description of the stretching frequencies of the iron–bound CN^- and CO ligands, due to the presence of hydrogen bonds to the CN^- ligands. Most strikingly, it turns out that the CO stretching frequencies clearly corroborates a hydroxo ligand in both states, Ni–A and Ni–B. Strong evidence for different orientations of the OH^- ligand in Ni–A and Ni–B comes from the ^{1}H hyperfine coupling constant of the exchangeable proton.

4.5.1. Introduction

[NiFe] hydrogenase becomes inhibited upon full oxidation. Two different oxidized states have been identified, namely the Ni–A state and the Ni–B state. Ni–A and Ni–B are both paramagnetic and thereby susceptible to electron paramagnetic resonance investigations.

One–electron–reduction of Ni-A and Ni-B leads to the activation of the enzyme and the formation of the EPR-silent intermediate states Ni-SU and Ni-SIr, respectively. The activation process [1] differs markedly for Ni–A and Ni–B. Ni–B is readily activated and thus often referred to as "ready–state". In contrast, since the reductive activation of the Ni–A state may take few minutes up to several hours, Ni–A has been termed the "unready–state".

The nature of the ligand at the bridging position between the nickel and the iron centers in the Ni–B state and, in particular, in the Ni–A state is still not known with certainty. X–Ray diffraction experiments of the oxidized states of [NiFe] hydrogenase from various microorganisms [2-7] show electron density between the nickel and iron atoms, which can be associated with a bridging ligand containing a non–hydrogen atom. ^{17}O–ENDOR and EPR investigations [8-9] have revealed that the bridging ligand in both, Ni–A and Ni–B, is oxygen–based. As an alternative to an oxygen–based bridging ligand, a sulfur species was proposed as initial interpretation of the data from X–Ray diffraction experiments of the oxidized states in *Desulfovibrio vulgaris* Miyazaki F. [5]. However, DFT calculations showed that an oxygen–based ligand is more compatible with the crystal structure than a sulfur–containing species [10]. In the X–Ray structure of the [NiFe] hydrogenase from *Desulfovibrio fructosovorans* [11] and *D. vulagaris* Miyazaki F. [6], an OOH^- ligand was modeled at the bridging site.

In sharp contrast to the pronouncedly different activation kinetics, the Ni–A and Ni–B states exhibit rather similar spectroscopic properties [12]. For example, the CN^- and CO stretching frequencies determined by FTIR spectroscopy are virtually equal for both states. In contrast, the g–tensor of the two states exhibits a prominent difference. While the g_1 and g_3 components are very similar, the g_2 component of the Ni–A state is larger than the respective value of Ni–B, which renders the Ni–A g–tensor more axial than the Ni–B tensor. Also the isotropic ^{1}H hyperfine coupling constant of the exchangeable proton is different for the two states.

Several DFT studies were conducted to reveal the identity of the bridging ligand in Ni–A and Ni–B. In most studies a relatively small cluster model was employed as compared to present day standards, which contained the two metal centers, the bridging ligand, the four cysteine residues and the three two–atomic ligands at the iron. An exception is the QM/MM study by Amara and co–workers, who

suggested [13] the presence of an O^{2-} ligand for Ni–A based on energy values. In an earlier contribution, Niu et al. proposed [14] a vacant bridging site for Ni–B, which is in contrast to the identification of electron density in the bridging position by X–Ray crystallography. By comparing calculated magnetic properties with experiment, Stein *et al.* came to the conclusion that in the Ni–B state the bridging ligand is OH^-, while an oxo O^{2-} was proposed for Ni–A . Stadler and co–workers [15] also used a small model for the calculation of magnetic properties. In contrast to the similar study by Stein *et al.*, it was suggested that OH^- is the bridging ligand in both, Ni–A and Ni–B. Pardo *et al.* [16] compared computed g–tensors and IR–frequencies using a small model with experimental data and suggested an μ–OH^- ligand for Ni–B and a hydroperoxo bridging ligand for Ni–A. In 2006, van Gastel *et al.* [17] reported a single–crystal ^{1}H–ENDOR study of the exchangeable proton in the Ni–B state. The interpretation of the experimental results was supported by DFT calculations. A cluster model was used, which included, in addition to the bimetallic core and the first coordination shell, the His88 residue of the second coordination shell. As a result, it was concluded that an OH^- molecule with different orientations of the O–H bond is present as bridging ligand in the Ni–A and Ni–B states.

In this DFT–study, we have investigated the oxygen–inhibited states of [NiFe] hydrogenase. We have focused on the orientation dependence of the hydroxo ligand in the oxidized states and compared computed spectroscopic properties with experiment. In this way, the present contribution is similar to that by van Gastel and co–workers [17]. However, we have employed large cluster models, in order to assess the influence of the entire second coordination shell on the energies and spectroscopic properties of the two OH conformers. In particular, for the calculation of the stretching frequencies of the iron–bound CO and CN^- ligands, the inclusion of the second coordination shell in the cluster model is indispensible due to the presence of hydrogen bonds to the cyanides ligands (see Chapter 4.2). In addition to the evaluation of spectroscopic parameters, we have investigated the interconversion of the two hydroxyl conformers in terms of reaction and transition state energies.

4.5.2. Cluster Models

The cluster models investigated in the present study are displayed in Figure 1. The cluster models with an OH^- ligand in two different conformations are designated as hydroxo–A and hydroxo–B. Models with an H_2O ligand and an O^{2-} ligand are designated aquo model and oxo model, respectively. In Table 1, spin–multiplicity, charge, the number of atoms, the number of basis functions and the spin–contamination of the cluster models are presented.

	hydroxo–A	hydroxo–B	oxo	aquo
spin cont.	0.03	0.03	0.03	0.04
atoms	1693	1693	1687	1699
basis functions	166	166	165	167
charge	–2	–2	–3	–1
multiplicity	2	2	2	2

Table 1: Spin contaminations, number of atoms and contracted basis functions, charge and multiplicity of the cluster models

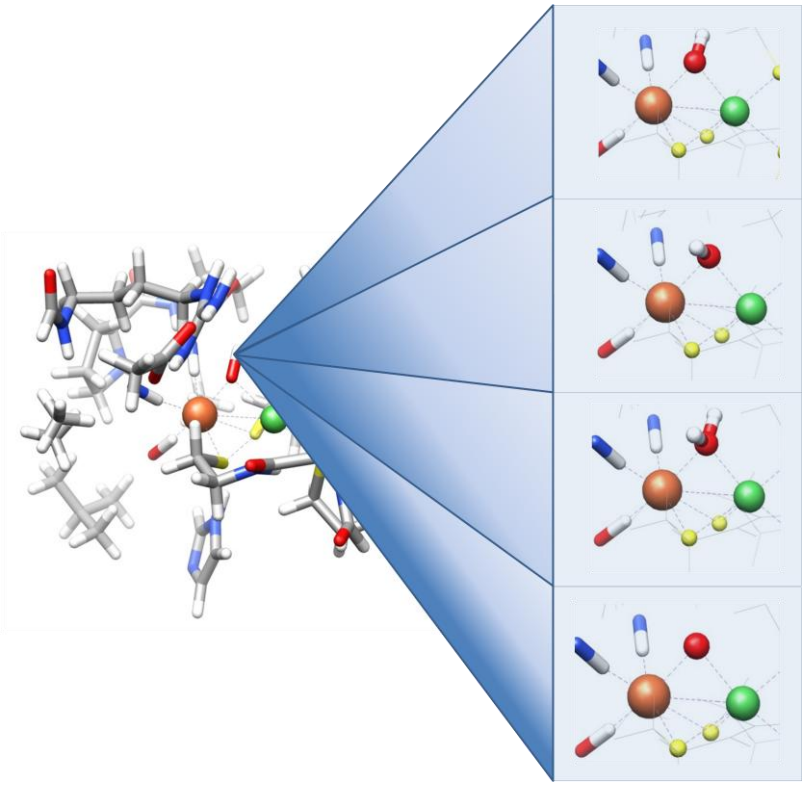

Figure 1: Cluster models (X refers to the variable bridging ligand), from top to bottom: hydroxo–A (X = OH^-), hydroxo–B (X = OH^-), aquo (X = H_2O) and oxo (X = O^{2-}). Suffixes A and B in the hydroxo–A and hydroxo–B models designate the two differently oriented O–H bonds of the hydroxo ligand. There is no intended relation of these designations to the redox–states Ni–A and Ni–B.

4.5.3. Energies of two hydroxyl conformers

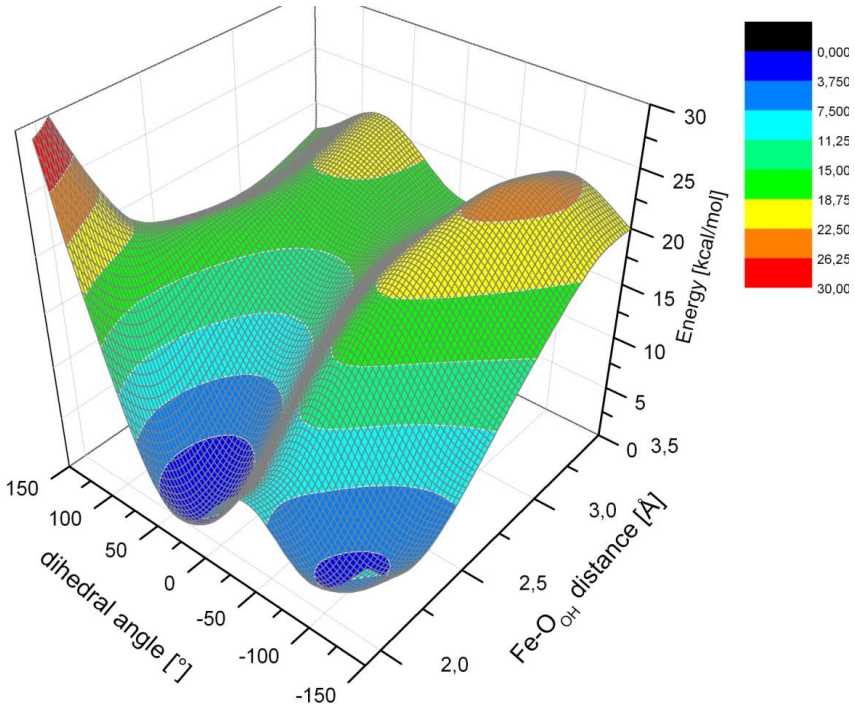

Figure 2: Two–dimensional relaxed surface scans for a hydroxo ligand bound to the active site in the Ni^{3+} doublet state. The energy [kcal/mol] is plotted as a function of the Fe–O_{OH} distance [Å] and the Sγ(Cys546)–Ni–O_{OH}–H_{OH} dihedral angle [°]. The energy at the global minimum has been set to zero.

A two–dimensional relaxed surface scan for an OH^- ligand bound to the active in the Ni^{3+} doublet state is shown in Figure 2. The energy is plotted as a function of the Fe–O_{OH} distance [Å] and the Sγ(Cys546)–Ni–O_{OH}–H_{OH} dihedral angle [°]. The Sγ(Cys546)–Ni–O_{OH}–H_{OH} dihedral angle was chosen as variable parameter in order to explore the rotational interconversion of hydroxyl-A and hydroxyl-B. In addition, the Fe–O_{OH} distance enables to explore the rotational movement of OH^- not only at the bridging position but to also move the ligand towards the terminal nickel site.

The two energy minima, which correspond to the hydroxo–A and hydroxo–B structures, are found at dihedral angles of 28° and –113°, respectively, and at a Fe–O distance of 2.1 Å. The hydroxo–A structure is by 2.4 kcal/mol more stable than the hydroxo–B structure (small cluster model) while with the large cluster model an only slightly smaller value of 1.8 kcal/mol is found. Hence, also additional protonation of the His88 residue at Nδ does not significantly change the energy difference between the two structures (2 kcal/mol).

Starting from hydroxo–A, the dihedral angle may be changed in two different directions to get to the hydroxo–B structure and, hence, two pathways are possible for the conversion of hydroxo–A to hydroxo–B. The same applies of course also to the conversion from hydroxo–B to hydroxo–A. First, by *decreasing* the dihedral angle, the energy barrier for the conversion from Ni–A to Ni–B amounts to 8 kcal/mol (BP86). The energy of the transition state is 7 kcal/mol when B3LYP is used. Second, if the dihedral angle at a constant Fe-O distance is increased, the reaction barrier exceeds 30 kcal/mol as the rotation of the O–H group is hindered by the iron atom. By raising the Fe–O distance, the hydroxo ligand moves away from the iron center and the second pathway becomes energetically more favorable but still amounts to almost 19 kcal/mol. Hence, the first pathway is the energetically preferred one.

At larger Fe-O distances, the hydroxyl ligand is positioned at the terminal nickel site. However, from Figure 2, it is apparent that no energy minimum is present at the terminal nickel position. Also in geometry optimizations of the large cluster model, no stable minimum structure was found for binding of the OH^- ligand to the terminal nickel site. As evident from Figure 2, the energy at the nickel site is by 15–16 kcal/mol larger than that at the bridging position. Hence, in the oxidized nickel 3+ state, the hydroxo ligand is trapped in the bridging position, which is in line with the experimental finding that the ligand cannot be removed from the bimetallic core of the enzyme prior to reduction of the nickel center. In contrast, in the aquo model, only with the large but not with the small model, it was possible to find an energy minimum with H_2O at the bridging position which indicates a weak coordination of H_2O in line with the neutral charge of the ligand. The weak binding of the H_2O ligand is also reflected by the long metal-oxygen bonds in the aquo model, *vide infra*.

In summary, the energies of hydroxo–A and hydroxo–B are similar. One of the two interconversion pathways between the two structures features a reaction barrier of nearly 20 kcal/mol, which even amounts to more than 30 kcal/mol larger when the OH^- ligand in not moved out of the bridging position. For the other pathway a still discernible reaction barrier of 7–9 kcal/mol is found. Given the limited accuracy of DFT (see chapter 2.1) for larger molecular systems, the energy barrier might actually be large enough to prevent the interconversion of hydroxo–A and hydroxo–B.

4.5.4. Geometries

	hydroxo–B	hydroxo–A	Oxo	aquo	exptl. (1h2a)	exptl. (1YRQ)
Ni–S(Cys81)	2.21	2.21	2.29	2.19	2.22	2.15
Ni–S(Cys84)	2.37	2.36	2.36	2.35	2.38	2.54
Ni–S(Cys546)	2.18	2.20	2.22	2.20	2.33	2.21
Ni–S(Cys549)	2.39	2.39	2.44	2.31	2.37	2.29
Fe–S(Cys84)	2.40	2.39	2.44	2.35	2.14	2.29
Fe–S(Cys549)	2.35	2.35	2.44	2.32	2.37	2.28
Ni–Fe	2.86	2.86	2.80	2.83	2,55	2,82
Ni–O	1.91	1.89	1.79	2.08	2,17	1,86
Fe–O	2.04	2.03	1.92	2.27	2,25	1,91

Table 2: Selected bond lengths [Å].

Selected bond lengths are presented in Table 2. Experimental values have been obtained from the crystal structures of *D. vulgaris* hydrogenase (0.18 Å resolution, 1h2a) [5] and *D. fructosovorans* hydrogenase (0.21 Å resolution, 1YRQ) [18]. Spectroscopic properties have been found to change only insignificantly for "standard" [NiFe] hydrogenases from different organisms [12] and, hence, larger structural differences between the respective active sites are not likely. The sulfur–metal distances from the X–Ray structure of *D. vulgaris* hydrogenase and *D. fructosovorans* differ by a mean value of about 0.11 Å and, hence, one cannot expect the geometric parameters from the two structures to be more accurate than 0.1 Å. The various calculated sulfur–metal bond lengths do not change by more than 0.05 Å and the computed values from all models are in agreement with the corresponding parameters from one of the X–Ray structures. For the metal–oxygen distances and the nickel–iron distance, the differences between the values from the two crystal structures amount to a mean value of 0.3 Å. The large discrepancy is possibly due to the modeling of a sulfur atom at the bridging position in the case of the *D. vulgaris* enzyme instead of an oxygen ligand as in *D. fructosovorans* hydrogenase. However, the presence of an oxygen–based ligand has been evidenced clearly by ^{17}O–ENDOR spectroscopy, and is nowadays generally accepted. The Ni–O and Fe–O distances obtained with the oxo and the two hydroxo models reproduce the values of the *D. fructosovorans* enzyme satisfactorily. The Ni–O and Fe–O values from the aquo model are on the other hand too large. This is in particular true for the Fe–O distance. The computed Ni–Fe distances of all four models are in very good agreement with the values from the X–Ray structure of the *D. fructosovorans* enzyme. In the Ni–C state, the experimental (PDB: 1h2r) and the computed Ni–Fe distance are 2.54 Å and 2.60 Å, respectively, and thereby significantly smaller than the computed and experimental values of the oxidized states.

4.5.5. Electronic structure

In this section, we provide a detailed analysis of the electronic structure of the oxygen inhibited state focussing on the two OH^-–bound structures, hydroxo–A and hydroxo–B. In the spectroscopy section we will compare theoretical and experimental spectroscopic results for the oxidized states to the corresponding values obtained for the well–characterized Ni–C state (see chapter 4.2). Therefore, we analyze in this section the differences in the electronic structure for an OH^- and a hydride ligand in bridging position. First, a simple ligand field scheme is derived from the experimentally available g–tensor orientations. Then, the fundamentally different metal–ligand bonds of a hydroxo–ligand and a hydride ligand are analyzed in detail. Finally, the electronic structure of the transition state for interconversion of hydroxo–A and hydroxo–B is discussed.

Ligand field scheme

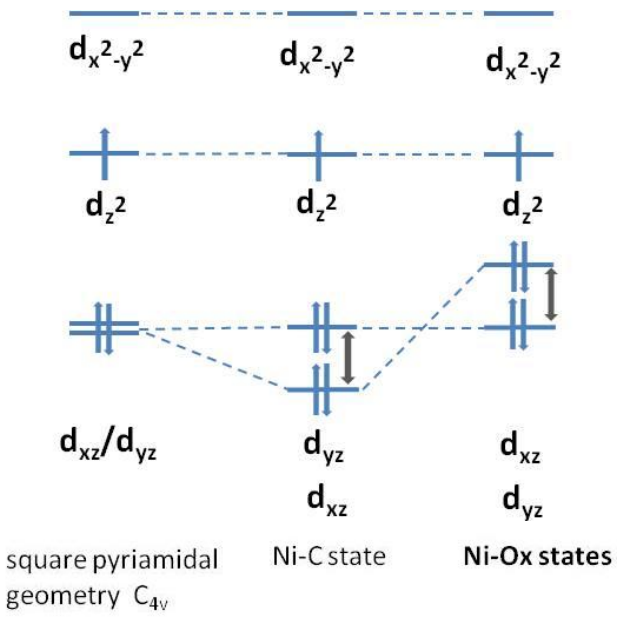

Figure 3: Ni^{3+} ligand field scheme for the oxidized states. The d_{xy} orbital has been omitted.

A ligand field scheme for the Ni^{3+} center (d^7 electronic configuration) of the oxidized states is presented in Figure 3. The d_{yz} and d_{xz} orbitals, which are degenerate in a pyramidal ligand field of C_{4v} symmetry, split in the Ni–C, Ni–A and Ni–B states. The ordering of the energies of the d_{xy} and d_{xz} orbitals were derived from the orientations of the g–tensor principal axes (see Chapter 2.2). In the Ni–C state (see Chapter 4.2), the d_{xz} orbital is found to be lower in energy than the d_{yz} orbital. In the oxidized states, the orientation of the g_2 and g_3 axes are interchanged relative to the respective orientations in Ni–C (vide infra), which is associated with an inversion of the d_{xz} and d_{yz} orbital energies. In conclusion, according to the ligand field schemes, the Ni–C state and the oxidized states

show pronounced similarities, such as a singly occupied nickel d_{z^2} orbital (Figure 4). However, in contrast to Ni–C, the d_{xz} orbital is higher in energy than the d_{yz} orbital, which is possibly due to repulsive interactions of the d_{xz} orbital with the free electron pairs of the oxygen ligand. Hence, it can be expected that the spectroscopic parameters of the oxidized states which depend to first order on the spin density are similar to those in Ni–C, while second order properties, such as the g–tensor or the SOC contribution to the hyperfine coupling contant, should diverge more pronouncedly.

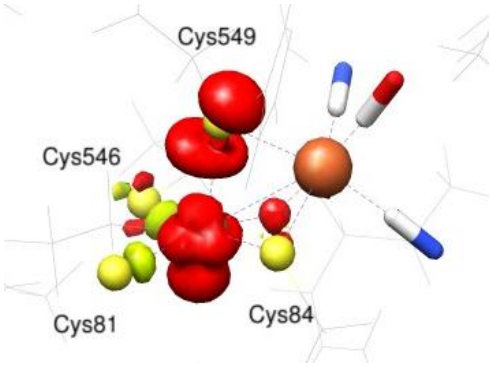

Figure 4: Spin density plot for hydroxo–A.

The oxygen–metal bond at the bridging position:

As shown in Figure 5a, the OH^- ligand forms a two–center bond with the nickel and the iron atoms. One of the oxygen–based p–orbitals interacts with the nickel $d_{x^2-y^2}$ orbital (Figure 5a, left) while another oxygen p–orbital interacts with the iron d_{z^2} (Figure 5a, middle). In the Ni–C state (Figure 5a, right), the bonding situation is markedly different. Most notably, the hydride ligand forms *one* three–center bond with nickel $d_{x^2-y^2}$ orbital and iron d_{z^2} orbital instead of *two* genuine two–center bonds.

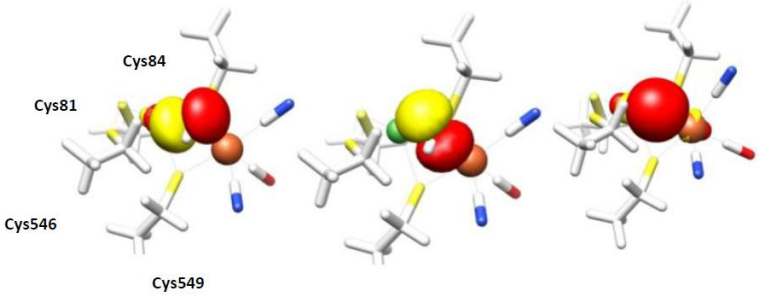

a

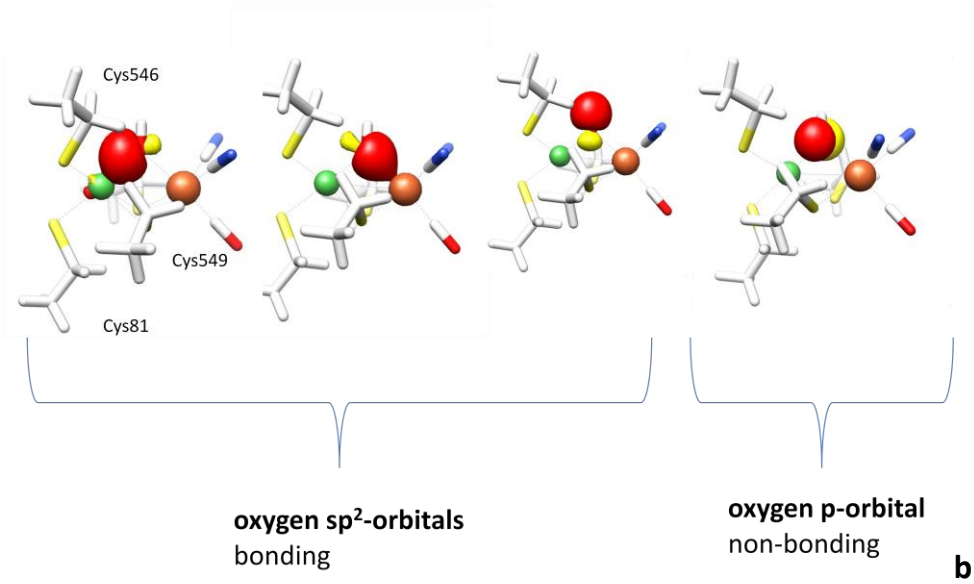

Figure 5: (a) Localized quasi–restricted orbitals of the Ni–OH^- (left) and Fe–OH^- (middle) bonds and of the three–center bond of the hydride (right). (b) Localized quasi–restricted orbitals of the transition state for the interconversion of hydroxo–A and hydroxo–B. Shown are the three bonding oxygen sp^2–orbitals and the non–bonding oxygen p–orbital.

Central to the different binding properties of the hydride and the hydroxo ligands is the presence of two free electron pairs in the case of the oxygen atom and only one free electron pair in the hydride. The free electron pairs of the hydroxyl oxygen are harbored in two p–orbitals, which point towards the iron and nickel atoms, respectively, and are therefore capable of forming two localized metal–ligand bonds. In contrast, since the 1s orbital in the hydride is of spherical symmetry, it is suitable for the formation of a multicenter–bond including nickel and iron d–orbitals. Furthermore, the oxygen atom of the hydroxyl molecule is a relatively hard ligand. This results in the formation of ionic metal–oxygen bonds in [NiFe] hydrogenase, as evidence by the small nickel and iron contributions to the localized orbitals of only 0.1 and 0.14, respectively. On the other hand, the hydride is a soft ligand forming covalent bonds as reflected by nickel and iron contributions to the three–center orbital, of 0.37 and 0.2. The larger ionicity of the oxygen–metal bonds relative to the hydride–metal bond has further implications for the electronic structure of the bimetallic site. Firstly, the spin populations (Table 3) of the oxygen atoms are positive, which is in contrast to the negative spin populations of the hydride due to spin polarization mediated by the covalent Ni–H bond in Ni–C. Secondly, Mulliken charge populations (Table 3) of about –0.5 are computed for the oxygen atom of the hydroxyl group, while the charge population of the hydride in Ni–C is nearly zero. Thirdly, the charge population of the nickel atom in Ni–C is negative but positive for hydroxo–A and hydroxo–B. Fourth, the presence of the three–center bond in the case of Ni–C is reflected by the Mayer bond orders. Formally an order of 0.23 is found for the Ni–Fe bond in Ni–C, which can be viewed as the respective metal–metal

contribution to the Ni–H–Fe three center bond. On the other hand for the hydroxo–A and hydroxo–B models no Ni–Fe bond order is present. The absence of a covalent three–center bond and thereby a metal–metal contribution to the bonding of the bridging ligand is reflected by the pronouncedly larger nickel–iron distance in the oxidized states as found theoretically and experimentally (Table 2).

In summary, the bonding properties of the hydroxo ligands in the oxygen inhibited states differ markedly from those of the hydride ligand in the Ni–C state. The presence of ionic two–center bonds instead of a covalent three–center bond is a striking difference to the Ni-C state and results in a pronounced widening of the Ni–Fe distance in the oxidized states relative to the corresponding value in Ni-C (section 4.2).

	oxo		**hydroxo–A**		**Hydroxo–B**		**aquo**	
	charge	**spin**	**charge**	**spin**	**charge**	**Spin**	**Charge**	**spin**
S Cys81	–0.48	–0.01	–0.38	–0.03	–0.39	–0.02	–0.34	0.02
S Cys84	–0.32	0.01	–0.24	–0.02	–0.23	–0.02	–0.17	–0.03
S Cys546	–0.32	–0.02	–0.24	–0.02	–0.23	0.00	–0.17	–0.01
S Cys549	–0.33	0.18	–0.23	0.25	–0.23	0.25	–0.15	0.20
Ni	0.16	0.83	0.07	0.80	0.06	0.79	0.04	0.80
Fe	0.36	–0.03	0.32	–0.01	0.33	–0.01	0.32	0.01
O_{bridge}	–0.59	0.03	–0.49	0.02	–0.55	0.00	–0.52	0.01
H_{bridge}	–	–	0.23	0.00	0.23	0.00	0.29	0.00
H_{bridge}	–	–	–	–	–	–	0.28	0.00

Table 3: Mulliken charge and spin populations of selected atoms.

Interconversion of Ni–A and Ni–B

Localized quasi–restricted orbitals of the trigonal transition state for the interconversion of hydroxo–A and hydroxo–B are shown in Figure 5b. At the oxygen, one finds three bonding and one non–bonding p–orbital. The bonding orbitals are sp^2 hybrid orbitals, of which two form bonds with the metals and one forms a bond with the hydrogen of the hydroxyl group. The non–bonding orbital is the oxygen p–orbital which is perpendicular to the three other bonding orbitals. When proceeding along the reaction coordinate, the Fe–O–Ni, Fe–O–H and Ni–O–H bond angles first increase, then become maximal at the transition state, with values of 97°, 131° and 132°, and finally decrease (Figure 6). The increase in energy in the transition state with respect to hydroxo–A/hydroxo–B can be easily understood in the framework of the simple Valence Shell Electron Pair Repulsion (VSEPR) model, which predicts a trigonal geometry to be energetically disfavored with respect to a tetrahedral arrangement of the Ni-OH-Fe group due to the repulsive interactions stemming from the free electron pair. In the case of a H_3O^+ hydronium cation, a corresponding rehybridization and

concomitant adoption of a planar structure with angles of 120° is with 2–3 kcal/mol (B3LYP) energetically less costly. However, in contrast to H_3O^+, the OH^- ligand is bound to the bridging position of the active site of [NiFe] hydrogenase. A larger Fe–O–Ni bond angle requires an energetically unfavorable elongation of the Fe–O, Ni–O and/or Fe–Ni bond distances, which is reflected by the distorted structure of the planar transition state: the Ni–O–Fe bond angle is smaller than 120°, which in turn is accommodated by the larger Ni–O–H and Fe–O–H bond angles. The Ni–O and the Ni–Fe bond distances increase relative to hydroxo–A each by about 0.05 Å while the Fe–O bond length remains constant.

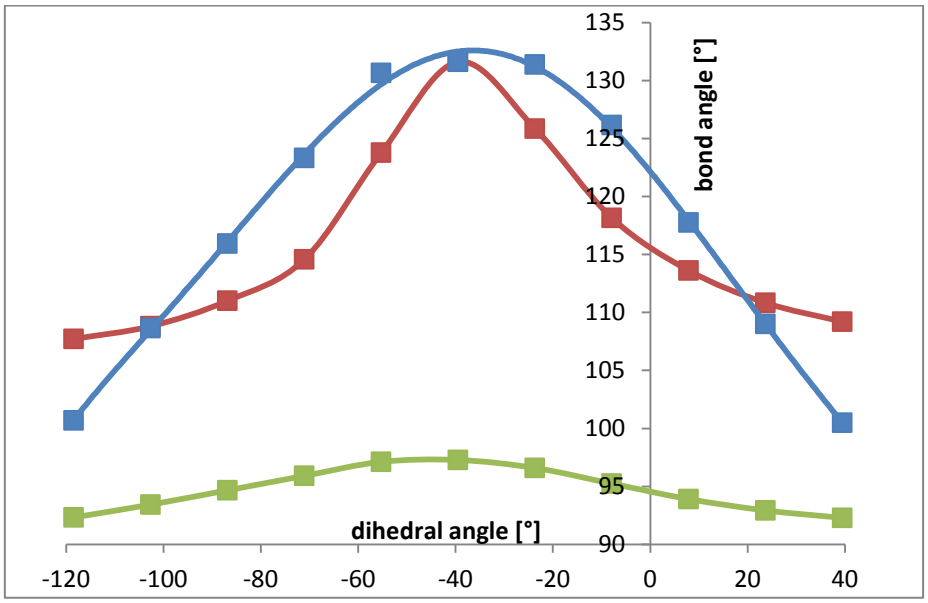

Figure 6: Dependence of the Ni–O–Fe (green), Ni–O–H (blue) and Fe–O–H (red) bond angles on the Sγ(Cys546)–Ni–O_{OH}–H_{OH} dihedral angle [°] (small model).

4.5.6. Magnetic spectroscopy

In the following section, calculated magnetic parameters are compared to a large body of experimental data. First g–values and then hyperfine couplings are discussed. The ^1H hyperfine coupling of the exchangeable proton of the hydroxo ligand is of particular interest as a comparison with experiment allows in principle an assignment of the hydroxo–A and hydroxo–B structures to the Ni–A and Ni–B redox states [17]. Finally, computed IR frequencies are compared to the respective experimental values.

g–tensor

	g_1	g_2	g_3	g_{iso}
oxo	2.04	2.2	2.22	2.15
hydroxo–A	2.04	2.15	2.2	2.13
hydroxo–B	2.04	2.14	2.2	2.13
aquo	2.06	2.11	2.2	2.12
HisHε	2.03	2.12	2.16	2.1
exptl Ni–A [19]	2.01	2.24	2.32	2.19
exptl Ni–B [19]	2.01	2.16	2.33	2.17
exptl Ni–C [20]	2.01	2.15	2.22	2.13

Table 4: g–tensor components.

The g–values of the Ni–C state are in good agreement with the experimental values. The calculated g_1 component is by 0.2 larger than the experimental g_1 value, whereas g_2 and g_3 underestimate the experimentally determined values (by 20–30%) as usual for nickel metal complexes (section 2.1).

In all models of the oxidized states, the g_1 components are by 0.03 larger than the experimentally determined g_1 components of Ni–A and Ni–B, which is only slightly larger than the overestimation in Ni–C. However, the aquo model exhibits a g_1 value of even 2.06 and, hence, is by 0.05 larger than the experimental value. The experimental g_1 and g_3 components of Ni–A and Ni–B are nearly equal. In contrast, g_2 is slightly larger in the case of Ni–A as compared to Ni–B and, thereby, the experimental g–tensor of the Ni–A state is somewhat more axial. The g_2 value of the oxo model is too large, given a systematic underestimation of the g–tensor by 20–30%. The hydroxyl and the aquo models are overall in suitable agreement with g_2 and g_3 of Ni–A and Ni–B. However, the g_1 value of the aquo model seems to be markedly too large relative to experiment. Hydroxo–A and hydroxo–B are reasonable candidates for Ni–A while for Ni–B g_2 seems somewhat too large given the expected underrepresentation of the g-values. The difference in the g_2 value of Ni–A and Ni–B is not reproduced by hydroxo–A and hydroxo–B since both structure yield almost identical g–values. However, speculatively, structural and electronic features, which differentiate g_2 and g_3 in Ni–A and Ni–B, are either not correctly described by DFT or are not covered by the used cluster model, such as long–range interactions with the [FeS] clusters.

As revealed by EPR measurements of single crystals, the g_1 axes of the of the g–tensor points approximately along the Ni–Sγ(Cys549) bond, g_2 along the Ni– Sγ(Cys81) bond and g_3 along the Ni–Sγ(Cys546) bond. Accordingly, the principal axes of the two larger components of the g–tensor, g_2 and g_3, are interchanged as compared to the Ni–C state. This is reproduced by the two hydroxo

models and by the aquo model while orientations of the g_2 and g_3 components in the oxo model are similar to those in the Ni–C state.

^{1}H hyperfine coupling tensor of the β–CH_2 group of Cys549

^{1}H(1)	A'_1	A'_2	A'_3	A_{iso}
oxo	–3	–2	4	10
hydroxo–A	–3	–1	4	14
hydroxo–B	–3	–1	4	13
aquo	–2	–1	4	9
HisHε (Ni-C)	–3	–1	4	13
exptl, Ni–A*	–2	–1	4	11
exptl, Ni–B [17]	–2	–2	4	13
exptl, Ni–C [21]	–2	-2	4	14

^{1}H(2)	A'_1	A'_2	A'_3	A_{iso}
oxo	–1	–1	3	6
hydroxo–A	–2	–1	3	10
hydroxo–B	–2	–1	3	10
aquo	–2	–1	2	12
HisHε (Ni-C)	–2	–1	3	10
exptl. Ni–A*	–1	–1	2	11
exptl. Ni–B [17]	–1	–1	2	11
exptl. Ni–C [21]	–2	–1	3	12

Table 5: ^{1}H hyperfine coupling tensors [MHz] of the β–CH_2 group of Cys549. A'_1, A'_2 and A'_3 are the anisotropic contribution to the hyperfine coupling tensor. *Ogata, H., personal communication.

In the Ni–C state, the hyperfine couplings are mainly isotropic and generally in good agreement with experiment. The first hyperfine coupling constant exhibits an isotropic hyperfine coupling constant which is by about 2 MHz larger than that of the second which is correctly reproduced by the computations for Ni-C.

The hyperfine coupling constant of the Cys549 β–CH_2 group in the oxidized states are collected in Table 5. The experimental values for the two protons in Ni–B are similar to those in Ni–C with the coupling of H(1) being smaller than that of H(2) by 2 MHz. The coupling constant for H(1) in Ni–A however is similar to that of H(2) and therefore slightly smaller than the corresponding one in Ni–B. The hyperfine coupling constants are dominated by the isotropic contribution with the anisotropic contribution being nearly axial.

Computationally, the isotropic coupling of H(1) is by 1 MHz larger in the hydroxo–A model as compared to the hydroxo–B model while both models show the same value for H(2). This is in agreement with an assignment of hydroxo–A and hydroxo–B to Ni–B and Ni–A, respective. In the aquo model, the larger value is found for H(2) rather than H(1). The oxo model exhibits smaller isotopic values than the hydroxo models with H(1) amounting to 10 MHz and H(2) only to 6 MHz.

^{1}H hyperfine coupling tensor of the β–CH_2 group of Cys546

^{1}H (1)	A'_1	A'_2	A'_3	A_{iso}
oxo	–2	–2	3	0
hydroxo–A	–1	–2	3	1
hydroxo–B	–2	–2	3	2
aquo	–2	–1	3	3
HisHε (Ni-C)	-2	-1	3	9
exptl. Ni–C	-2	-2	3	9

^{1}H (2)	A'_1	A'_2	A'_3	A_{iso}
oxo	–2	–2	4	3
hydroxo–A	–2	–1	3	4
hydroxo–B	–2	–1	3	5
aquo	–2	–1	3	3
HisHε (Ni-C)	-1	-1	3	6

Table 6: ^{1}H hyperfine coupling tensor[MHz] of the β–CH_2 group of Cys546. A'_1, A'_2 and A'_3 are the anisotropic contribution to the hyperfine coupling tensor.

Experimentally, no hyperfine couplings were found for the β–CH_2 Cys546 protons. This is in contrast to the Ni–C state where a coupling constant for one of the two non–exchangeable protons of the β–CH_2 group in Cys546 was detected. This difference of the oxidized states relative to Ni–C can be considered correctly reproduced by all models as the computed values for Cys546 are, firstly, significantly smaller than the values found for Cys549 and, secondly, also markedly smaller than the corresponding values in Ni–C.

^{1}H hyperfine coupling tensor of the exchangeable proton

^{1}H	A'_1	A'_2	A'_3	A_{iso}
hydroxo–A	–4	–6	10	–2
hydroxo–B	–5	–6	10	2
aquo H(1)	–4	–4	8	0
aquo H(2)	–4	–3	7	4
exptl. Ni–A [17]	–4	–4	7	3
exptl. Ni–B [17]	–4	–3	8	–4

Figure 7: ^{1}H hyperfine coupling tensor [MHz] of the exchangeable proton. A'_1, A'_2 and A'_3 are the anisotropic contribution to the hyperfine coupling tensor.

Experimental and computed ^{1}H hyperfine couplings of the exchangeable proton are presented in Table 7. The experimentally determined ^{1}H hyperfine coupling tensor for the exchangeable proton in Ni–B is nearly axial and features a negative isotropic hyperfine coupling constant of –4 MHz. In the case of Ni–A, the anisotropic contribution to the hyperfine coupling tensor of the exchangeable proton is almost equal to that of the Ni–B state. However, with a value of +2.6 MHz, the isotropic component exhibits a similar magnitude but differs from the corresponding value determined for Ni–B by sign. Since the oxo model does not feature an exchangeable proton at all, it can be excluded as possible candidate for Ni–A and Ni–B. The computed anisotropic components of hydroxo–A, hydroxo–B and of the two exchangable protons of the aquo model are in line with the corresponding experimental anisotropic contributions of Ni–A and Ni–B. In terms of the isotropic contribution, assigning the hydroxo–A model to the Ni–B state and the hydroxo–A model to the Ni–A state is most compatible with experiment. The computed isotropic contributions of hydroxo–A and hydroxo–B are by 1–3 MHz smaller than the corresponding values obtained by van Gastel and thereby are in even slightly better agreement with experiment and clearly confirm the assignment of the two OH^- conformers to the Ni–A and Ni–B redox–states.

4.5.7. IR–frequencies – evidence for the same type of ligand in Ni–A and Ni–B

	CO	CN^-	CN^-
oxo	1898	2061	2086
hydroxo–A	1952	2095	2115
hydroxo–B	1951	2093	2116
aquo	1989	2093	2128
HisHε (Ni-C)	1957	2062	2083
exptl. Ni–A	1956	2084	2094
exptl. Ni–B	1955	2081	2090
exptl. Ni–C	1961	2074	2085

Table 8: CO and CN^- stretching frequencies [cm^{-1}] [22]. The collected CO frequencies correspond to the computed values shifted by an additive correction constant of 28 cm^{-1} [23-24].

CO and CN^- stretching frequencies are presented in Table 8. All CO vibrations have been up–shifted by a correction constant of 28 cm^{-1} according to the systematic underestimation of the CO frequencies in transition metals by DFT [23-24]. The experimental CO frequencies are similar for Ni–A and Ni–B and slightly smaller than the values found for the N–C state. The hydroxo–A and hydroxo–B models give very similar CO frequencies. Both models are in good agreement with the experimentally obtained values for Ni–A and Ni–B. The slight lowering of the CO frequency in Ni–A and Ni–B with respect to Ni–C is also correctly reproduced. In the case of the oxo model the CO frequency is by almost 60 cm^{-1} underestimated with respect to experiment. On the other hand, the aquo model overestimates the CO stretching frequency by 20–30 cm^{-1}.

The experimental CN^- stretching frequencies are larger than the corresponding values of the Ni–C state. This is reproduced by the two hydroxo models, which have almost equal CN^- frequencies. However, the computed CN^- frequencies are larger than the experimental values of Ni–A and Ni–B. In the case of the aquo model, the overestimation of the CN^- frequencies is even more pronounced than in the hydroxo models whereas for the oxo model an underestimation of the experimental values is found.

In summary, different ligands in the active site, as an aquo, oxo and hydroxo ligand feature very different computed IR stretching frequencies. Hence, the experimental observation of almost equal IR frequencies gives strong evidence that in *both* redox–states the same bridging ligand is present. The bridging ligand is most likely a hydroxyl ion as, in contrast to the aquo and oxo models, the values of the CO stretching frequencies obtained with the hydroxo models are in excellent agreement with the experimentally determined values. The computed CN^- frequencies of the hydroxo models are too large. However, the values are also larger than the computed values for Ni–C

and thereby correctly reproduce the experimental finding of larger CN^- frequencies in Ni–A and Ni–B relative to Ni–C.

4.5.8. Conclusion

In the present DFT study, we have investigated the oxygen–inhibited states. In addition to a small cluster model, which only includes the bimetallic core and the first coordination shell of the enzyme, we have employed large cluster models which additionally include the complete second coordination shell. We have focused on the investigation of two cluster models which feature a hydroxo ligand bound to the bridging position with the O–H bond in two different orientations, in order to evaluate whether the OH^- conformers are related to the two experimentally observed oxidized states Ni–A and Ni–B is found. To this end, we have compared computed spectroscopic parameters with the corresponding experimental values. Overall very good agreement is found for a hydroxo ligand in both Ni–A and Ni–B. Most striking evidence in this respect comes from the IR–frequencies, as almost equal values were found experimentally for Ni–A and Ni–B. Since for different ligands such as OH^-, H_2O or O^{2-} the theoretical frequencies are significantly different, the important conclusion can be drawn that it is very likely that in *both,* Ni–A and Ni–B, the *same* ligand is present. Given the excellent agreement of the CO–frequencies from the two hydroxo models with the experimental values, the presence of an OH^- ligand in Ni–A and Ni–B is very likely. Furthermore, the ^1H hyperfine coupling constant of the exchangeable proton gives convincing evidence that the hydroxo ligands in Ni–A and Ni–B feature different orientations. The presence of an OH^- ligand is further corroborated experimentally by the recent X–Ray structure of [NiFe] hydrogenase from *Allochromatium vinosum* at 2.10 Å resolution (3MYR), which shows a single oxygen atom at the bridging position, instead of a peroxo–structure as found previously [6]. In addition to spectroscopic properties and geometries, we have calculated energies of the two hydroxyl conformers. Both structures are nearly iso–energetic with little difference whether the small or the large cluster model is used. However a discernible energy barrier is present between the two states as the Ni–OH–Fe structure adopts an energetically unfavorable trigonal–planar geometry in the transition state. Given the limited accuracy of DFT in the treatment of larger molecular systems, this could prevent the interconversion of the two structures as found experimentally. The presence of a hydroxyl ligand in both oxidized states has important implications for the reactivation mechanism. The pronouncedly different kinetics in Ni-A and Ni-B are not likely to be due to the different orientations of the OH^- ligand and, hence, need to be due to some sort of alterations of the proton or electron pathways.

References

1. Fernandez, V.M., E.C. Hatchikian, and R. Cammack, *Properties and reactivation of 2 different deactivated forms of desulfovibrio-gigas hydrogenase.* Biochimica Et Biophysica Acta, 1985. **832**(1): p. 69-79.
2. Volbeda, A., et al., *Crystal-structure of the nickel-iron hydrogenase from desulfovibrio-gigas.* Nature, 1995. **373**(6515): p. 580-587.
3. Volbeda, A., et al., *Structure of the [nife] hydrogenase active site: Evidence for biologically uncommon fe ligands.* Journal of the American Chemical Society, 1996. **118**(51): p. 12989-12996.
4. Volbeda, A., et al., *Structural differences between the ready and unready oxidized states of [nife] hydrogenases.* Journal of Biological Inorganic Chemistry, 2005. **10**(3): p. 239-249.
5. Higuchi, Y., T. Yagi, and N. Yasuoka, *Unusual ligand structure in ni-fe active center and an additional mg site in hydrogenase revealed by high resolution x-ray structure analysis.* Structure, 1997. **5**(12): p. 1671-1680.
6. Ogata, H., et al., *Activation process of [nife] hydrogenase elucidated by high-resolution x-ray analyses: Conversion of the ready to the unready state.* Structure, 2005. **13**(11): p. 1635-1642.
7. Montet, Y., et al., *Gas access to the active site of ni-fe hydrogenases probed by x-ray crystallography and molecular dynamics.* Nature Structural Biology, 1997. **4**(7): p. 523-526.
8. Vanderzwaan, J.W., et al., *Effect of o-17(2) and (co)-c-13 on epr-spectra of nickel in hydrogenase from chromatium-vinosum.* Biochimica Et Biophysica Acta, 1990. **1041**(2): p. 101-110.
9. Carepo, M., et al., *O-17 endor detection of a solvent-derived ni-(ohx)-fe bridge that is lost upon activation of the hydrogenase from desulfovibrio gigas.* Journal of the American Chemical Society, 2002. **124**(2): p. 281-286.
10. Stein, M. and W. Lubitz, *Dft calculations of the electronic structure of the paramagnetic states ni-a, ni-b and ni-c of nife hydrogenase.* Physical Chemistry Chemical Physics, 2001. **3**(13): p. 2668-2675.
11. Volbeda, A., et al., *Structural differences between the ready and unready oxidized states of nife hydrogenases.* Journal of Biological Inorganic Chemistry, 2005. **10**(3): p. 239-249.
12. Lubitz, W., E. Reijerse, and M. van Gastel, *[nife] and [fefe] hydrogenases studied by advanced magnetic resonance techniques.* Chemical Reviews, 2007. **107**(10): p. 4331-4365.
13. Amara, P., et al., *A hybrid density functional theory molecular mechanics study of nickel-iron hydrogenase: Investigation of the active site redox states.* Journal of the American Chemical Society, 1999. **121**(18): p. 4468-4477.
14. Niu, S.Q., L.M. Thomson, and M.B. Hall, *Theoretical characterization, of the reaction intermediates in a model of the nickel-iron hydrogenase of desulfovibrio gigas.* Journal of the American Chemical Society, 1999. **121**(16): p. 4000-4007.
15. Stadler, C., et al., *Density functional calculations for modeling the active site of nickel-iron hydrogenases. 2. Predictions for the unready and ready states and the corresponding activation processes.* Inorganic Chemistry, 2002. **41**(17): p. 4424-4434.
16. Pardo, A., et al., *Characterization of the active site of catalytically inactive forms of [nife] hydrogenases by density functional theory.* Journal of Biological Inorganic Chemistry, 2007. **12**(6): p. 751-760.
17. van Gastel, M., et al., *A single-crystal endor and density functional theory study of the oxidized states of the [nife] hydrogenase from desulfovibrio vulgaris miyazaki f.* Journal of Biological Inorganic Chemistry, 2006. **11**(1): p. 41-51.
18. Volbeda, A., et al., *Structural differences between the ready and unready oxidized states of [nife] hydrogenases (vol 10, pg 239, 2005).* Journal of Biological Inorganic Chemistry, 2005. **10**(5): p. 591-591.
19. Gessner, C., et al., *Single crystal epr study of the ni center of nife hydrogenase.* Chemical Physics Letters, 1996. **256**(4-5): p. 518-524.
20. Foerster, S., et al., *Single crystal epr studies of the reduced active site of nife hydrogenase from desulfiovibrio vulgaris miyazaki f.* Journal of the American Chemical Society, 2003. **125**(1): p. 83-93.
21. Foerster, S., et al., *An orientation-selected endor and hyscore study of the ni-c active state of desulfovibrio vulgaris miyazaki f hydrogenase.* Journal of Biological Inorganic Chemistry, 2005. **10**(1): p. 51-62.
22. Fichtner, C., et al., *Spectroelectrochemical characterization of the [nife] hydrogenase of desulfovibrio vulgaris miyazaki f.* Biochemistry, 2006. **45**(32): p. 9706-9716.
23. Jonas, V. and W. Thiel, *Theoretical-study of the vibrational-spectra of the transition-metal carbonyls m(co)(6) [m=cr, mo, w], m(co)(5) [m=fe, ru, os], and m(co)(4) [m=ni, pd, pt].* Journal of Chemical Physics, 1995. **102**(21): p. 8474-8484.

24. Jonas, V. and W. Thiel, *Theoretical study of the vibrational spectra of the transition-metal carbonyl hydrides hm(co)(5) (m=mn, re), h(2)m(co)(4) (m=fe, ru, os), and hm(co)(4) (m=co, rh, ir).* Journal of Chemical Physics, 1996. **105**(9): p. 3636-3648.

4.6. The catalytic cycle

The reaction mechanism of [NiFe] hydrogenase featuring H_2–coordination at the nickel center and homolytic H_2–cleavage.

Abstract

[NiFe] hydrogenases efficiently catalyze the splitting of molecular H_2 into two protons and two electrons. In this DFT study, we present a corresponding reaction mechanism of the enzyme using a large cluster model which includes up to the second coordination shell of the enzyme. Comparison of the CO and CN^- stretching frequencies with the corresponding experimental values corroborate the validity of the proposed mechanism. Most strikingly, we find that H_2 binds to the nickel instead of the iron center, and that hydrogen cleavage is homolytic as opposed to the so far assumed heterolytic mechanism. By studying the reaction mechanism in detail, we have shed light on some of the intriguing structural and electronic features of the active site in [NiFe] hydrogenases.

4.6.1. Introduction

The experimentally observable Ni–SIa, Ni–C and Ni–R redox–states of [NiFe] hydrogenase form part of the catalytic cycle of the enzyme. A fundamental reaction scheme was derived from the redox–properties and the associated pH dependency of these three states [1-3] (Figure 1). Hydrogen uptake in the Ni–SIa state leads to the formation of the Ni–R state, which in turn is converted into the paramagnetic Ni–C state by one–electron oxidation and removal of one proton. The catalytic cycle is closed by a second one–electron oxidation and proton–removal step. There is no experimental evidence for another paramagnetic state in the catalytic mechanism besides Ni–C. Both, hydrogen cleavage *and* biosynthesis are catalyzed by hydrogenases. However, H_2–cleavage is mainly performed by [NiFe] hydrogenases whereas [FeFe] hydrogenases usually carry out hydrogen synthesis [1].

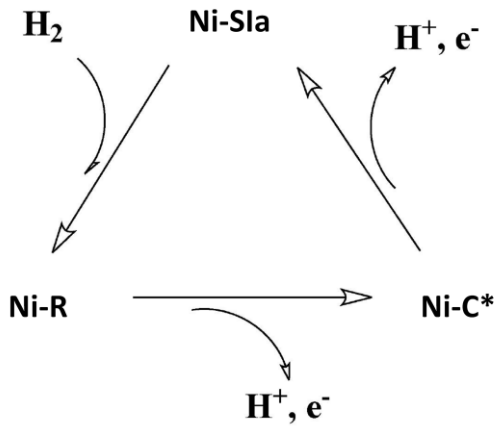

Figure 1: Interconversion of the experimentally characterized Ni–SIa, Ni–R and Ni–C redox–states. The Ni–C state is paramagnetic while the two other states are diamagnetic.

Electron transport is mediated by the three iron–sulfur cluster of the enzyme. In several experimental and computational studies, the terminal cysteine 546 (*Desulfovibrio vulgaris* Miyazaki F numbering is used throughout) was identified as first proton acceptor [4-11]. Particularly convincing evidence for this assignment comes from the spectroscopic and kinetic characterization of a Glu34 mutant of *Desulfovibrio fructosovorans* [NiFe] hydrogenase [12] as Glu34 is positioned in close proximity to Cys546.

Usually, the reaction surface in transition metal enzymes is highly complex featuring multiple intermediate and transition states [13-15]. Accordingly, the reaction mechanism of [NiFe] hydrogenase with its complex bimetallic structure probably not only comprises the three isolated redox–states but in addition several short–lived intermediates elusive to experimental observation.

By computational methods such as DFT, it is possible to gain insights into the structure and electronic features of experimentally inaccessible intermediate and transition states [15-16].

Several DFT studies have been devoted to the elucidation of the mechanistic steps of hydrogen conversion in [NiFe] hydrogenases (for reviews see [17-22]). In most of the earlier studies [19, 23-28], a relatively small cluster model, compared to present day standards, was used, which includes only the first coordination sphere of the active site in addition to the bimetallic core.

It is still elusive whether the enzymatic reaction takes place on a singlet or a triplet surface. Fan *et al.* argued that a high–spin Ni^{2+} state is more likely since a low–spin Ni^{2+} preferably adopts a planar arrangement [29]. Experimental evidence for a high spin state comes from an L–edge X–ray absorption study [30]. In a QM/MM study, Jayapal and co–workers [31] addressed the question of the spin state in Ni–SI and Ni–R. As part of their investigation, it was evaluated whether the hybrid functional B3LYP or the GGA functional BP86 yields better geometries of the active intermediate states. By additionally taking into account MP2 calculations, the conclusion was drawn that BP86 is more suitable for geometries in this respect and, furthermore, that a low–spin is more likely than a high–spin state. The assignment of singlet ground state is in line with parallel mode EPR and UV–visible MCD studies [11, 32-33].

A DFT–study of the reaction mechanism of [NiFe] hydrogenase was performed by Siegbahn [18, 34] using a cluster model which, in addition to the first coordination shell, contained the residues His88, Arg479, Asp123 and Glu34. The iron center was proposed as site for initial hydrogen binding despite the finding that this step is endergonic. In this respect, it was argued that endergonic substrate binding is feasible if the complete reaction energy is exergonic such that reaction at later stages compensates for this endergonic first step [18]. According to Siegbahn, H_2–binding is followed by heterolytic hydrogen cleavage with Cys546 acting as a nucleophile. Two electron and two proton transfer steps, which involve Cys546 and Glu34, follow H_2–cleavage. In another extensive study on the topic, Pardo *et al.* [35] investigated a large number of structures focusing on the calculation of geometries, energies and IR frequencies. A small cluster model was used and, most notably, no constraints were imposed on the coordinating cysteines. As in the study by Siegbahn, an energy minimum for H_2–coordination was found only at the iron center and the proposed reaction mechanism features H_2–coordination to the iron site followed by heterolytic cleavage by Cys546. A different mechanism was proposed by Stein and Lubitz, who suggested that an H_2O molecule binds to the terminal iron site in the doublet Ni^{3+} state and acts as a nucleophile, which dissociates away from the active site as H_3O^+ after heterolytic cleavage of the H_2 substrate [36-37]. In their model of

the reaction mechanism, H_2 diffuses into the bimetallic active site and, without prior coordination to one of the metal centers, is cleaved by the water molecule.

Experimental evidence is in agreement with initial H_2–binding at the nickel center. Most notably, a hydrophobic gas channel, which ends exactly at the free coordination position of the nickel, has been identified by xenon binding experiments [38-39]. In addition, as demonstrated unambiguously by the corresponding X–Ray structure, the competitive inhibitor CO binds to the terminal nickel coordination position [40], which corroborates the assumption that H_2–binding also takes place at the nickel center. In all computational studies, H_2–cleavage was found to be heterolytic and mediated by either one of the active site cysteines or an exogenous H_2O molecule. In a very recent contribution, Nilsson Lill and Siegbahn performed calculations of a high spin reaction mechanism using in addition to a DFT cluster model of 137 atoms, and two QM/MM models with a QM region of 30 atoms [41]. They employed a QM region of 30 atoms, which contained the first coordination shell in addition to the hetero–bimetallic core of the enzyme. As a result of their investigation, an autocatalytic mechanism in a reduced doubled Ni^{+1} state was presented, which includes hydrogen cleavage at the nickel center without pre–coordination. The reaction barriers for the autocatalytic H_2–cleavage reaction were found to range between 17 kcal/mol and 22 kcal/mol when the QM/MM model was used depending on the corrections employed for the calculations. A barrier of 18 kcal/mol was found with the DFT model. Recalculation of the heterolytic reaction mechanism gave an energy barrier between 15 kcal/mol and 17 kcal/mol depending on whether the DFT or one of the two QM/MM models were used.

In this contribution, we have investigated the reaction mechanism of [NiFe] hydrogenases. A large cluster model was used which contained amino acid fragments of the entire second coordination shell. The proposed reaction mechanism for H_2–cleavage features initial coordination of H_2 at the nickel site followed by homolytic cleavage, which results in a stable intermediate state with both hydrogen atoms forming covalent bonds with the metal atoms. According to the computed energies the reaction sequence in the low–spin state is kinetically and thermodynamically highly favorable. Computed CO and CN^- stretching frequencies are compared to the corresponding experimentally determined FTIR frequencies of the SIa, SI–R and Ni–C redox–states and corroborate the proposed mechanism.

4.6.2. Mechanistic steps of hydrogen cleavage in [NiFe] hydrogenases

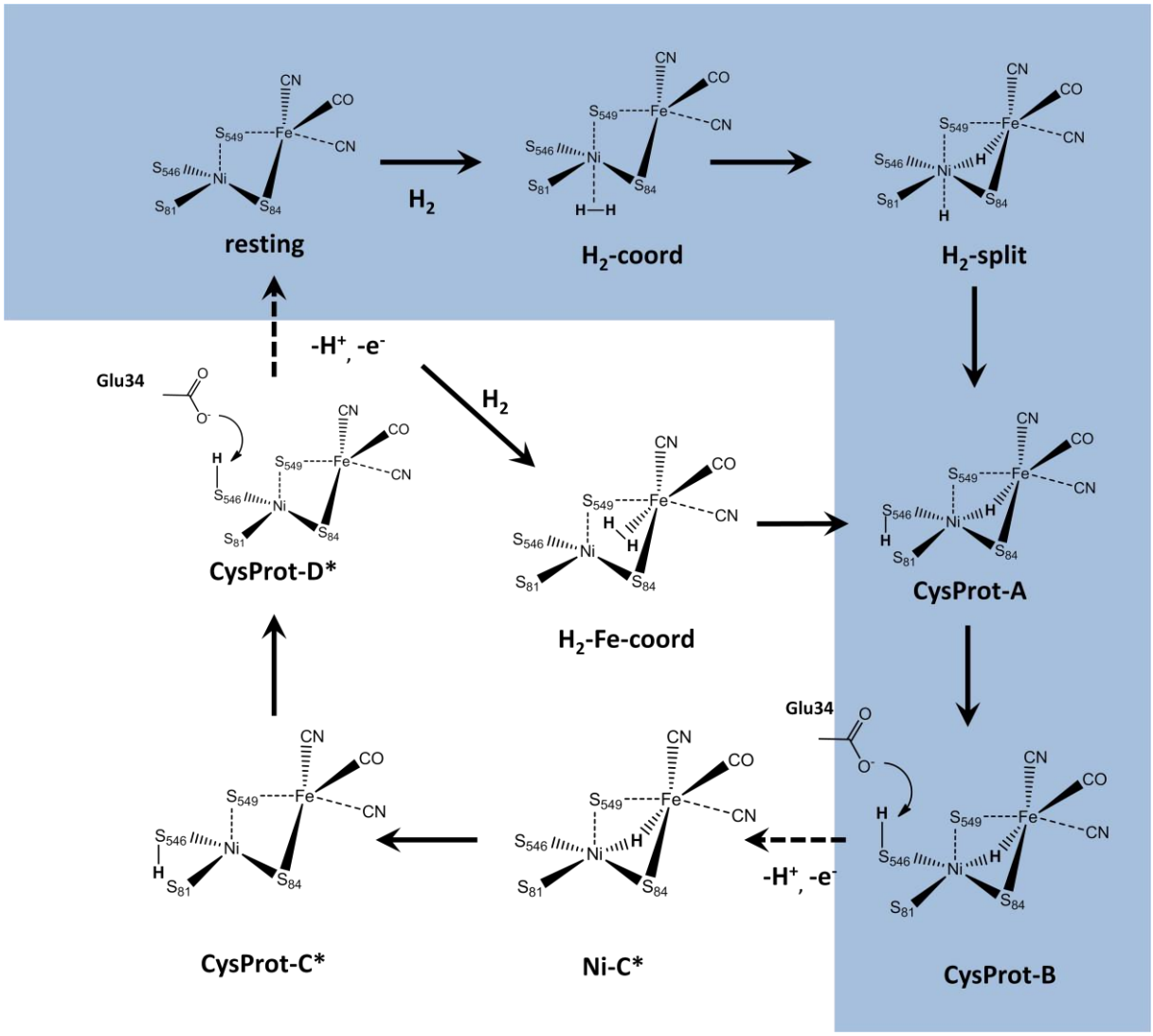

Figure 2: Proposed catalytic cycle of [NiFe] hydrogenases. The EPR–inactive states were computed as singlet and triplet states. Electron/proton transfer steps are highlighted with dashed arrows but might not necessarily take place at the indicated position in the cycle. In the present study, we have focused on the steps highlighted in blue, which correspond to H_2–binding and cleavage and the first electron/proton transfer step.

The reaction mechanism we propose for [NiFe] hydrogenase is presented in Figure 2. In the first reaction step, the H_2 substrate binds to the terminal nickel site of the enzyme (resting state) leading to the formation of the H_2-enzyme complex (H_2-coord state). Coordination might alternatively take place at the iron atom (H_2–Fe–coord state). In the second catalytic step, the H–H bond of the H_2 molecule is broken. As outcome of the H_2–cleavage reaction, hydrogen atom H(1) remains at the terminal nickel site while the other one, H(2), binds to the bridging position (H_2–split state).

The enzymatic reaction then proceeds with the abstraction of H(1) from the terminal nickel site by the sulfur atom of Cys546 leading to the CysProt–A state, in which Sγ(Cys546) is protonated and H(2)

remains at the bridging position. From the H_2-Fe-coord state, CysProt–A is formed in a single reaction step. Next, CysProt–A converts into CysProt–B, which corresponds to a conformational change of the Sγ(Cys546)–H(1) bond. In CysProt–B, the proton adopts a suitable position to be abstracted by Glu34 and to move via the amino acid proton transfer chain away from the active site. In addition to the proton removal, an electron transfer step takes place resulting in the formation of the paramagnetic Ni–C state. Proton and electron transport might proceed simultaneously in the form of a proton coupled electron transfer step [42]. Another proton/electron transfer sequence then restores the resting state and thereby closes the catalytic cycle.

The models for the multiple structures employed in this study were derived from the HisHε cluster model, which successfully reproduces the spectroscopic and geometric data of the Ni–C state (see chapter 4.2). The cluster model includes the two metals and the first coordination shell, i.e. the four cysteine residues, the iron–coordinating diatomic ligands and, in the Ni–C state, a hydride ligand in bridging position. In addition, amino acid fragments of the complete second coordination sphere were included in the model. In HisHε, the ε–nitrogen atom of His88 is protonated and forms a hydrogen bond with Sγ(Cys549), while the δ–nitrogen is deprotonated. Glu34, which is positioned in direct vicinity to Cys546, is modeled as propionic acid. Also HisHεHδ, which features protons at both His88 nitrogens δ and ε, has been shown to be in reasonable agreement with experiment.

A set of six cluster models was investigated for each of the structures highlighted in blue in Figure 2. (1) HisHε: The HisHε model without modifications (2) HisHδHε: The HisHε model with an additional proton at the δ nitrogen of His88, (3) HisHεGlu: The HisHε model with the Glu34 residue modeled as propionate instead of a propionic acid moiety (4) HisHεSe: The HisHε model with the sulfur atom of Cys546 being replaced by a selenium atom (5) Small model: a model which only contains the first coordination shell in addition to the bimetallic [NiFe] core (6) Ni–only: a cluster models which only includes the nickel atom and the coordinating cysteines but not the iron center. Constraints at the cysteines are conserved.

The influence of the protonation state of His88 and Glu34 on the reaction energies was investigated with models (1)–(3). With model (4), it was studied whether H_2–cleavage in [NiFeSe] hydrogenases [43] differs from that in standard [NiFe] hydrogenases. By comparison of calculations using the small model (5) with calculations using the larger models (1)–(3), the overall influence of the second coordination shell on the mechanism was evaluated. Furthermore, the small cluster model was used for the relaxed surface scans. By comparison of model (6) with the small model, we shed some light on the role of the iron center in the reaction.

4.6.3. Energies of the intermediate states of the catalytic cycle

In the following section, we discuss the energies of the reaction intermediates, presented in Figure 2, for the singlet spin and the triplet spin states. Spin contaminations of the triplet states are below 0.05 and are therefore negligible. For H_2–coord of the HisHεSe model a somewhat more elevated value of nearly 0.07 is found. Then, we analyze the singlet and triplet energy surface by two–dimensional relaxed surface scans in order to study the homolytic cleavage reaction in more detail and to explore whether alternative pathways are possible for H_2–splitting after coordination at the nickel atom. The section is rounded off by a short discussion of the Ni^{3+} reaction surface.

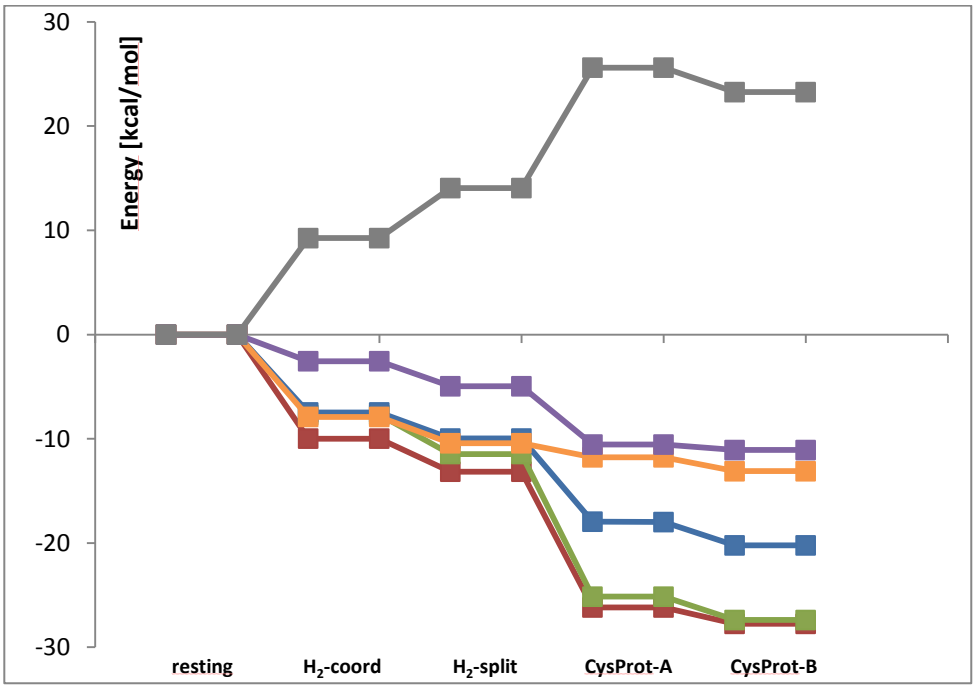

a

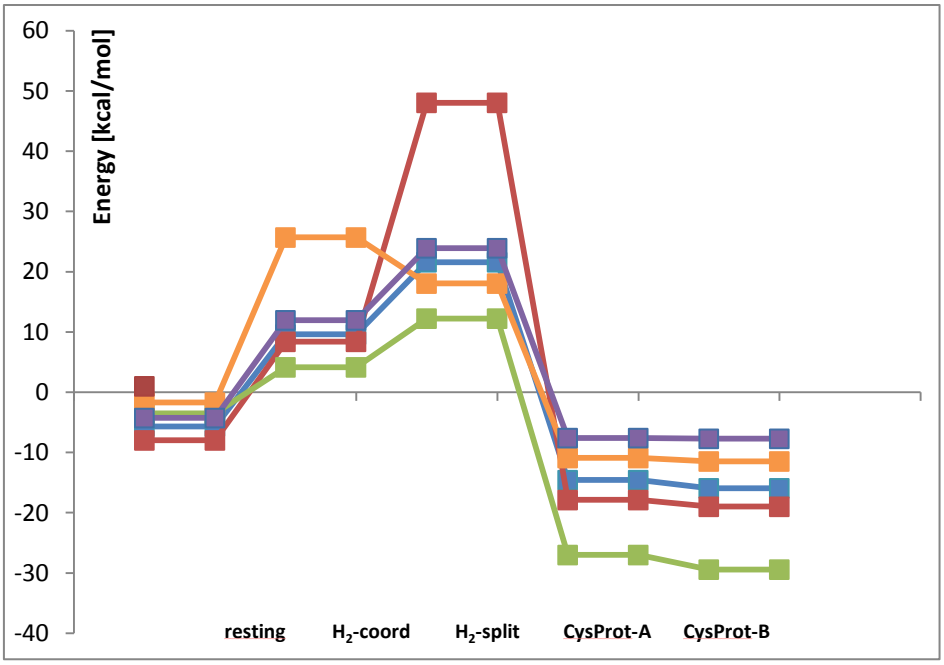

Figure 3: Computed (a) singlet and (b) triplet energies (B3LYP) of the reaction intermediates. Color code: HisHε (blue), HisHεHδ (red), HisHεGlu (green), HisHεSe (orange), small (violet), Ni–only (grey). The energy of the singlet resting state was chosen as zero point energy.

For all models (except for the triplet Ni–only model), an energy minimum has been found for H_2–coordination at the nickel site by optimization of suitable starting structures. On the other hand, an energy minimum for H_2–coordination at the iron is identified only with the small model. With +4 kcal/mol coordination at the iron is energetically not favorable in the singlet state while for the triplet state a value of –2.7 kcal/mol is calculated. In contrast to the present study, an energy minimum for H_2–coordination at the nickel site has not been found in previous mechanistic studies [18, 34-35]. However, these studies employed different cluster models and the B3LYP functional instead of BP86. Therefore, in order to evaluate the influence of the density functional and the size of the cluster model on the coordination site of H_2, we performed geometry optimizations with the B3LYP functional using the small and the HisHε models. For the singlet state, an energy minimum can be identified at the nickel center, but for the triplet no mimimum could be found at the terminal nickel site in the case of the small and the HisHε model, which is in agreement with the results from Nilsson Lill and Siegbahn [41].

Conclusively, the question whether an energy minimum for H_2 coordination is present at the nickel center or at the iron center of the bimetallic active site of [NiFe] hydrogenase is apparently governed by the spin state, the choice of the cluster model, the basis set and the energy functional employed. As H_2–coordination at the terminal nickel site is clearly in agreement with experiment, we are

confident that the used computational methodology and the employed cluster models are generally well suited for studying the reaction mechanism of [NiFe] hydrogenase.

In Figure 3, calculated (a) singlet and (b) triplet energies of the intermediate states are presented. For the resting state, the triplet is favored over the singlet spin state. With –8 kcal/mol, the lowest energy is found for the triplet HisHεHδ model while, with only about –2 kcal/mol, the energy of the triplet HisHεSe model is similar to that of the corresponding singlet state. Numerical energy values are collected in Table 1A of the appendix.

The singlet reaction energy is negative in all steps. The energy for the complete sequence is most negative for the HisHεHδ and the HisHεGlu models amounting to –28 kcal/mol in both cases. With –8 kcal/mol, the reaction is less favorable for the small model. Especially, the energy of CysProt–A depends on the protonation state of the two amino acids His88 and Glu34. For the HisHεSe model, it is found that CysProt–A is energetically only slightly favored over the H_2–split state. This is in line with the larger acidity of the Se–H bond compared to the S–H bond. For the triplet state, the energy of formation of H_2–coord and H_2–split is positive in contrast to the singlet state. Especially, the H_2–split state of the HisHεHδ model is pronouncedly destabilized with respect to the resting state. However, the CysProt–A and CysProt–B states feature a negative energy for all models.

In the case of the Ni–only model, only the energies of the singlet intermediate states are shown, since for H_2–split and H_2–coord no stable energy minima could be identified. In sharp contrast to the other singlet models, the energy of the singlet Ni–only model is positive for all reaction steps. Therefore, the reaction energy of the entire sequence is positive. Conclusively, the finding of a qualitatively different energy profile for the Ni–only model clearly indicates that iron center plays an important role in the catalytic cycle, even though it does not change its redox–state in the course of the reaction.

Transition states were calculated for the small model. The transition state energy for the reaction leading from the singlet H_2–coord to the H_2–split state amounts to 2.5 kcal/mol (B3LYP). The reaction from H_2–split to CysProt–A exhibits a transition state energy only 0.5 kcal/mol (B3LYP). Conclusively, energy barriers for hydrogen cleavage and abstraction are very small. For the two reactions on the triplet spin surface, the transition states virtually coincide with the H_2–split and the CysProt–A structures, which is in line with the respective large reaction energies.

In conclusion, due to the energetically unfavorable triplet H_2–coord and H_2–split states, the singlet reaction sequence is clearly favored. However, in the resting state, for all models, the triplet energies are lower than the respective energies of the singlet state. It is possible that the enzyme features a

high–spin nickel center in the resting state while upon H_2–coordination the singlet state could be adopted by spin–crossing. By comparison of the cluster models, we have demonstrated that the second coordination shell has a significant influence on the energies of the catalytic cycle. In particular, the protonation states of Glu34 and His88 show a marked influence on the energies. In this respect, hydrogen bond formation of His88 with Sγ(Cys546) has been shown to play an important role (see chapter 4.2.). By fine–tuning the catalytic activity as a function of the pH–value, Glu34 and His88 might be crucial for the enzyme being functional in a wide range of environments.

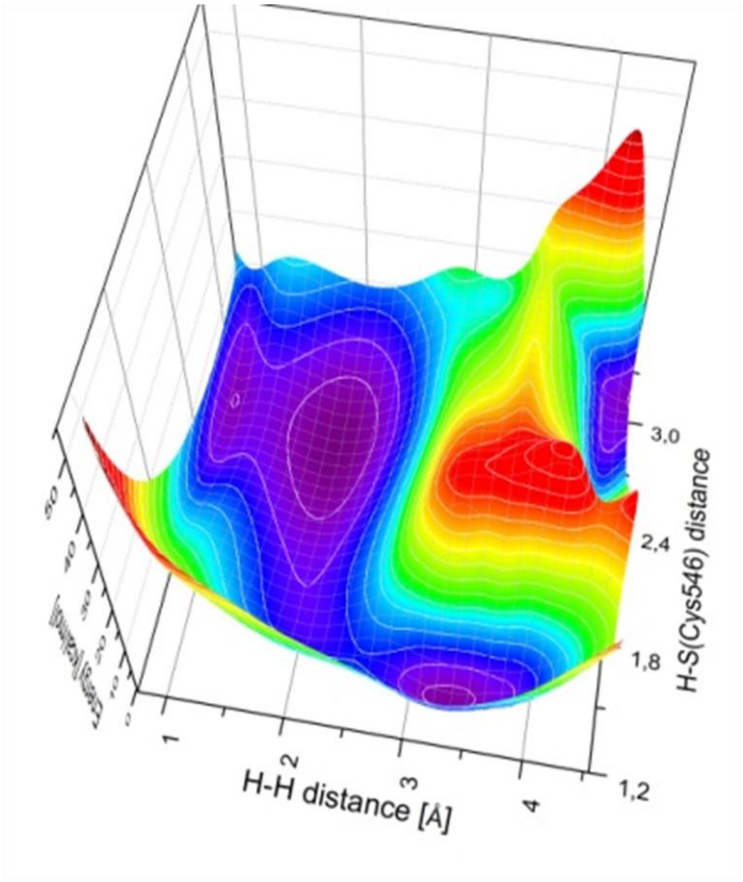

a

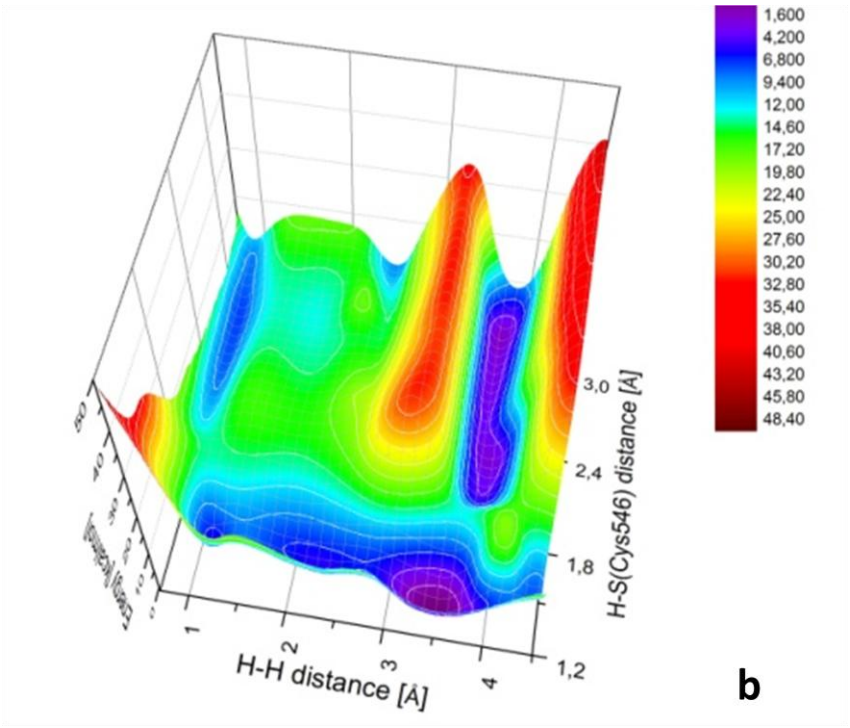

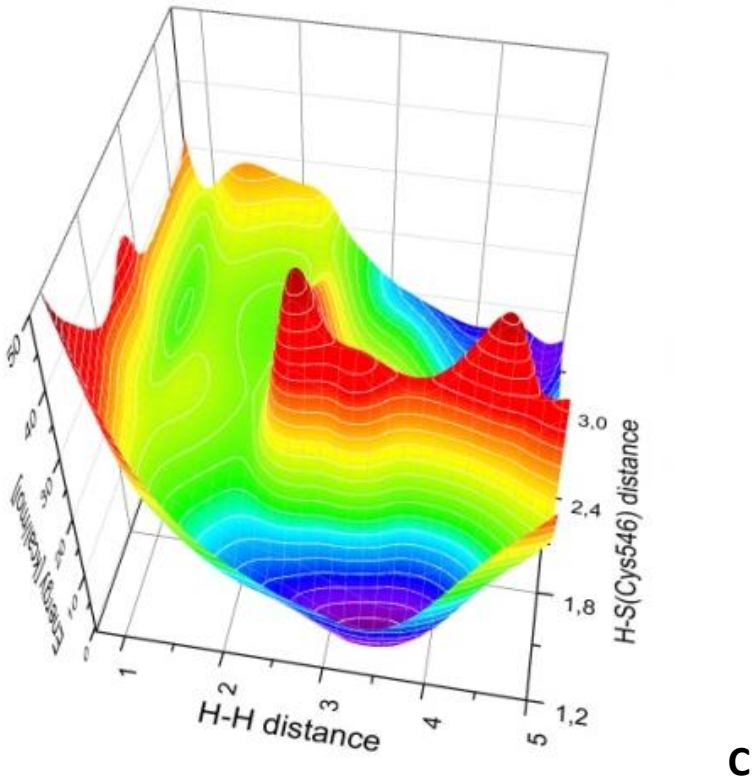

Figure 4: Two–dimensional relaxed surface scans of the hydrogen substrate bound to the active site for the Ni^{2+} (a) singlet and (b) triplet as well as (c) the Ni^{3+} doublet. The energy [kcal/mol] (BP86) is plotted as a function of the H–H distance [Å] and the H–Sγ(Cys546) distance [Å]. The energy at the global minimum of each plot has been set to zero.

In Figure 4, two–dimensional potential energy plots are presented for the (a) triplet and the (b) singlet state. The energy is plotted as a function of the H–H distance [Å] and the H–Sγ(Cys546) distance [Å]. The two variable parameters have been chosen in a way to ensure that the intermediates of the reaction sequence form part of the relaxed surface scan. In this respect, the variation of the H–H distances covers the H_2–coord and H_2–split states while, with the H–Sγ(Cys546) distance as second variable parameter, CysProt–A and CysProt–B are included in the scan.

In the singlet state, the energy minimum corresponding to the H_2–coord structure is found at a H–H distance of 0.9 Å and a H–Sγ(Cys546) distance of 2.7 Å. By increasing the H–H distance, the H_2–split state is formed. It is evident from the Figure 4a that the singlet energy surface around the minimum is relatively broad, i.e. for smaller changes of the H–Sγ(Cys546) and the H–H bond distances the energy varies only slightly. Increasing the H–Sγ(Cys546) bond distance leads to the CysProt–A state. Then, an additional lengthening of the H–H bond distance results in the final CysProt–B structure. Direct abstraction of H(1) by Sγ(Cys546) is energetically less favorable than proton abstraction after formation of the H_2–split state and subsequent proton abstraction by Cys546. This becomes evident from Figure 4a by careful inspection of how the energy changes when the H–Sγ(Cys546) distance in the H_2–coord state is decreased. Furthermore, as evident from the figure, no stationary point is present for direct abstraction. For the triplet state, the energy minimum corresponding to the H_2–coord structure is identified at 0.8 Å and 2.8 Å. In contrast to the singlet state, the H_2–split structure is energetically unfavorable. Formation of the H_2–split state might be avoided by heterolytic cleavage of the H_2 molecule in the triplet state as evident from Figure 4b. Minima at larger H–H distances correspond to the protonation of other cysteine residues but are separated from the H_2–coord and H_2–split structures by significant energy barriers in the triplet and singlet spin states.

A two–dimensional relaxed surface scan of H_2–cleavage on a doublet Ni^{3+} surface, of which however no experimental evidence has been reported, is given in Figure 4c. The energy surface is similar to that of the singlet Ni^{2+} state. Accordingly, also for the doublet it is evident that direct proton abstraction by Cys546, i.e. heterolytic cleavage, is disfavored over a two–step cascade of homolytic H_2–cleavage and subsequent proton abstraction by Cys546. Despite the vast similarities between the doublet and the singlet surface, the CysProt states are significantly more stabilized in the case of the Ni^{3+} doublet relative to the Ni^{2+} singlet.

4.6.4. CN^- and CO stretching frequencies

Ni–SIa, Ni–C and Ni–R are the redox–states of the catalytic cycle which were isolated and experimentally characterized. In this section, we compare calculated CO and CN^- stretching frequencies with the experimentally determined values. For the reliable computation of CO and CN^-

stretching frequencies, the inclusion of the second coordination shell is indispensible due to the presence of hydrogen bonds with the CN^- ligands (see chapter 4.2.).

	resting singl.	**resting trip.**	**H_2–coord singl.**	**H_2–coord trip.**	**H_2–coord doubl.**	**H_2–split singl.**
CO	1928	1941	1942	1937	1966	1960
CN^-	2052	2055	2052	2051	2073	2033
CN^-	2071	2075	2076	2072	2086	2062

	H_2–split tripl.	**H_2–split doubl.**	**CysProt–A singl.**	**CysProt–A trip**	**CysProt–A doubl.**	**CysProt–B singl.**
CO	1935	1974	1949	1936	1993	1950
CN^-	1992	2001	2047	2045	2088	2048
CN^-	2057	2076	2072	2067	2105	2072

	CysProt–B trip.	**CysProt–B doubl.**	**NiC doubl.**	**CysProt–C singl.**	**CysProt–C tripl.**	**CysProt–C doubl.**
CO	1935	1991	1958	1968	1970	1915
CN^-	2044	2088	2062	2077	2078	2034
CN^-	2066	2105	2083	2094	2094	2056

	CysProt–D singl.	**CysProt–D trip.**	**CysProt–D doubl.**	**NiSIa exptl.**	**Ni–C exptl.**	**NI–R exptl.**
CO	1966	1970	1916	1943	1961	1948
CN^-	2077	2078	2033	2075	2074	2061
CN^-	2093	2094	2055	2086	2084	2074

Table 1: Computed and experimental and CO and CN stretching frequencies [cm^{-1}] [44]. A constant of 28 cm^{-1} was added to the CO frequencies [45-47].

CO and CN^- stretching frequencies are presented in Table 1. CO frequencies were shifted by an additive constant of 28 cm^{-1} in order to compensate for the systematic DFT error observed for computed CO frequencies [45-47]. In general, the CO stretching frequencies of the doublet Ni^{3+} states are larger than those for the singlet and triplet Ni^{2+} states. The reduced electron density in the doublet state results in reduced back–bonding and a larger CO frequency. By comparison of the computed frequencies of CysProt–A with CysProt–B (and CysProt–C with CysProt–D), it is apparent that the values are nearly similar. Hence, the different orientation of the S(Cys546)–H bond has apparently no influence on the electronic structure at the iron center and thereby the CO frequency.

According to the experimentally derived scheme presented in Figure 1, it seems reasonable to assign the resting state to the Ni–SIa redox state. Ni–R is formed upon H_2–uptake and might therefore correspond either to the H_2–coord, the H_2–split or the CysProt–A and CysProt–B states. For the structurally well–known Ni–C state, accurate agreement of the computed and experimental CO

frequency was found and interpreted with regard to the formation of hydrogen bonds to the cyanide ligands (see chapter 4.2.). The symmetric CN stretching frequency is also well reproduced while the antisymmetric frequency is underestimated about by 10 cm^{-1}.

For the triplet resting state, the CO frequency is in suitable accordance with the experimental value for the Ni–SIa state. However, the calculated symmetric and antisymmetric CN^- frequencies are by around 10 cm^{-1} and 20 cm^{-1} too small, respectively. For the singlet resting state, similar CN^- frequencies are calculated. In contrast, the CO frequency is by more than 10 cm^{-1} smaller than in the triplet state and therefore in worse accordance with experiment. Hence, based on the comparison of computed and experimental CO frequencies, it is very likely that Ni–SIa corresponds to the triplet resting state, which is also agreement with the more favorable triplet energy values (*vide supra*). The experimentally determined CO frequency for the Ni–R state is in best agreement with the singlet H_2–coord and the CysProt-A states. Contrarily, the CO stretching frequency of the H_2–split state seems too large. The symmetric CN^- stretching frequency of the H_2–coord state is also in suitable agreement with experiment whereas the antisymmetric CN^- frequency is underestimated by about 10 cm^{-1} which however is also found for Ni-C. Unfortunately, according to the very similar frequencies for the singlet and the triplet H_2–coord states, it is not feasible to discriminate between the two spin states by means of frequency calculations.

4.6.5. The nickel center – an electronically favorable position for H_2-coordination

In the following section, we discuss the binding mode of the H_2 substrate and analyze why H_2–binding to the nickel site is energetically favored over binding to the iron center. The g–tensor principal axes system of the Ni–C state (see chapter 4.2.) has been chosen as coordinate system with the z–axis pointing approximately along the Ni–Sγ(Cys549) bond and the x–axis along the Ni–Sγ(Cys81) bond.

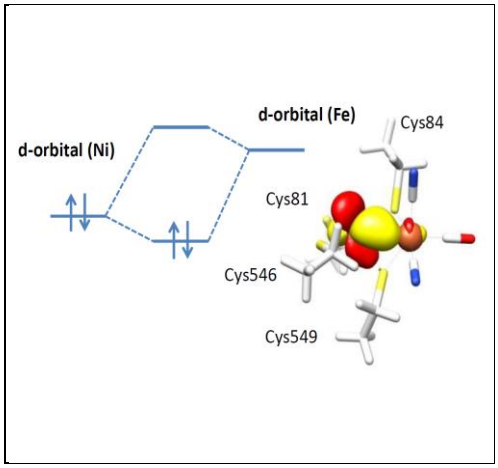

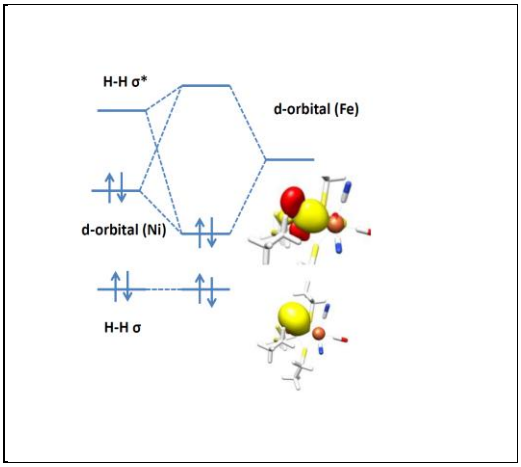

a **b**

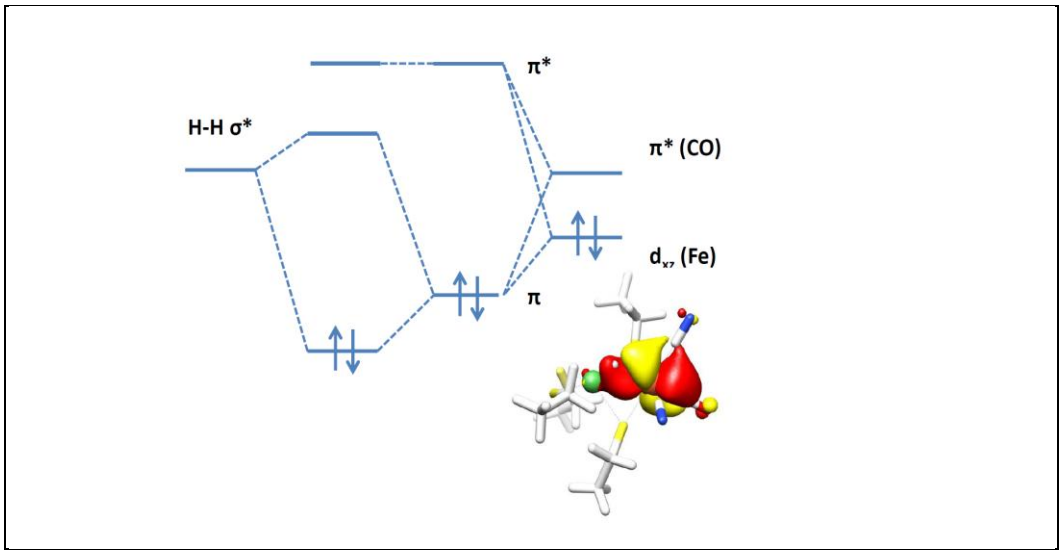

c

Figure 5: Orbital scheme in the intermediates of the singlet (a) resting, (b) H_2–coord (c) Fe–H_2–coord states. Localized quasi–restricted orbitals are shown as insets.

In the H_2–coord state (Figure 5b), the nickel $d_{x^2-z^2}$ orbital, which arises from rehybridization of the $d_{x^2-y^2}$ and d_{z^2} orbitals, forms a bonding interaction with the unoccupied anti–bonding orbital of the H_2 ligand. The corresponding orbital is shown as inset in Figure 5b along with the H_2–bonding orbital. From the figure it is apparent that the orbital also contains smaller contributions from the empty d_{x^2} iron orbital, which indicates the presence of a partial iron–nickel bond. Electron density is transferred from the nickel to the anti–bonding H_2 orbital, which results in a weakening of the substrate H_2 bond and concomitant formation of partial Ni–H bonds. This is reflected by bond orders of 0.38, 0.40 and 0.58 for the two hydrogen–nickel bonds and for the H–H bond, respectively. Hence, as the unbound H_2 substrate features a bond order of unity, the H–H bond is significantly weakened upon binding to the nickel site of hydrogenase. Further evidence for partial breaking of the H–H bond comes from the elongation of the H–H distance by 0.13 Å. The Ni–H bonds lengths are 1.59 Å and 1.60 Å. The nickel–iron bond order is, with 0.21, smaller than the bond order of 0.24 in the resting state (Figure 5a), which apparently reflects the transfer of electron density from the Ni–Fe bond to the hydrogen anti–bonding orbital of H_2. In summary, the H_2–ligand binds via a back–bonding interaction to the nickel center and therefore, binding of the H_2 ligand is similar to the coordination of the CO ligand in CO–inhibited [NiFe] hydrogenase. By elucidation of the X–Ray structure of CO–inhibited hydrogenase, it has been demonstrated unambiguously that the CO ligand binds to the terminal nickel site [48] which, given the similar binding modes of H_2 and CO, corroborates hydrogen coordination to the terminal nickel site.

The pronounced covalency characteristic of the Ni–S bonds results in the transfer of significant amounts of electron density to the nickel center. This, in turn, facilitates substrate coordination by a strengthening of the metal–ligand back–bonding interaction with the H_2 ligand. The significant transfer of electron density is reflected by an even negative Mulliken charge population of –0.17 at the formally two–valent nickel atom. Hence, for the formation of a stable H_2–complex, coordination of the nickel by soft sulfur atoms is apparently crucial. Experimentally, it was tried to replace the active site cysteines of [NiFe] hydrogenases from *Alcaligenes eutrophus* and *Ralstonia eutropha* with serine residues, which resulted in the compelte inactivation of the enzyme [49-50]. The corresponding *in silico* experiment leads to a disassembly of the bimetallic core when all cysteines are replaced by serines. In contrast, when only the terminal cysteines are replaced, the structural integrity of the active site is retained but H_2–coordination becomes highly unfavorable amounting to +19 kcal/mol. This result is in full agreement with harder oxygen ligands and the formation of less covalent nickel oxygen bonds, which tend to donate electron density to the nickel center to a much smaller degree and thereby prevent the formation of a stable metal–ligand back–bonding complex.

As an alternative to H_2–coordination at the nickel center, the substrate hydrogen may bind to the iron center of the bimetallic core. An orbital scheme for the interaction of H_2 substrate with the iron center is presented in Figure 5c. The doubly–occupied iron d_{xz} orbital forms a back–bonding interaction with an empty π^* orbital of the CO ligand. This leads to a stabilization of the d_{xz} orbital. Due to this stabilization, the interaction of the iron d_{xz} with the σ^* orbital of the H–H bond, which is high in energy, can be expected comparatively weak and, hence, energetically less stable as compared to H_2 coordination at the nickel center. The preferred binding at the terminal nickel site is corroborated by the bond order of the H–H bond, which is, with 0.66 for the iron, by about 0.1 larger than the corresponding bond order of H_2 coordinated to the nickel site (small models). Mayer bond orders for Fe–H(1) and Fe–H(2) are 0.19 and 0.29, respectively, which is in line with the different Fe–H distances of 1.70 and 1.84. From the orbital picture, shown as inset in Figure 5c, it is evident that, small contributions to the orbital arise from a nickel–centered orbital, which is reflected by an Ni–H(1) bond order of 0.15. The small contribution of the nickel center seems to be, at least partly, responsible for the two unequal Fe–H bond orders. . When the CO ligand at the iron center is replaced by a CN^- ligand, which is a potent π–donor, H_2–coordination to the iron site becomes more favorable by –6 kcal/mol. This corroborates that coordination of the H_2 ligand to the iron site proceeds by metal–ligand back–bonding. In addition, it highlighted that it actually is the CO ligand, which prevents stable H_2 coordination at the iron.

4.6.6. The crucial role of nickel and iron in the homolytic cleavage of the H_2 bond

[NiFe] hydrogenases manage to cleave the enormously stable H–H single bond, which features a bond–energy of 104 kcal/mol. We have investigated the reaction step of homolytic hydrogen cleavage in detail in order to shed light on the foundations of the catalytic efficiency of the enzyme. We have focused on the role of the iron center by comparing results for the small model with the corresponding calculations obtained with the Ni–only model.

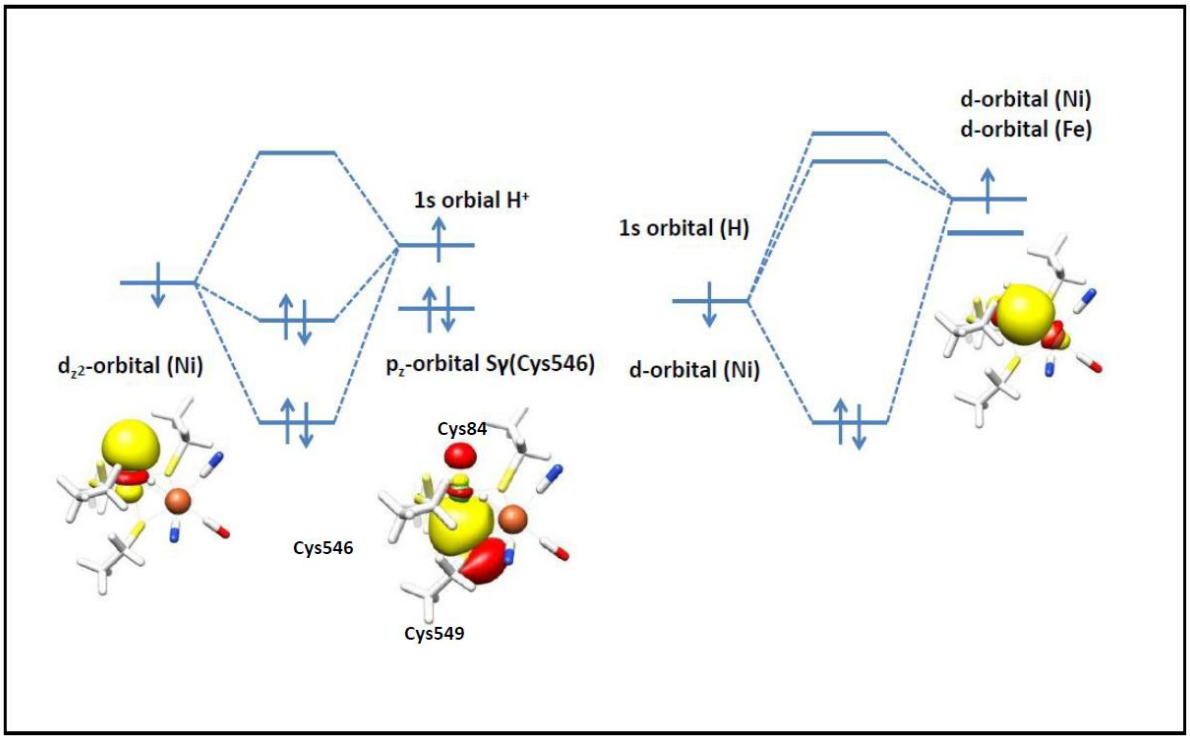

Figure 6: Orbital interactions of the two hydrogen atoms H(1) (left) and H(2) (right) with the hetero–bimetallic active site in the H_2–split state. Localized quasi–restricted orbitals are shown as insets.

An orbital scheme for the H_2–spit state is presented in Figure 6. The d_{z^2} orbital forms a bonding interaction with the hydrogen atom H(1). The sulfur p_z orbital of Sγ(Cys549) has more non–bonding character than the H(1)–Ni bond but nevertheless exhibits contributions from the nickel d_{z^2} / H(1) 1s antibonding combination. The second substrate hydrogen atom, H(2), forms part of a three–center bond which, in addition to the 1s orbital of the hydrogen in bridging position, includes contributions from iron and nickel orbitals. Formally, the two substrate hydrogen atoms are present as hydride ions. This would imply a nickel oxidation state of 4+ instead of 2+. However, in the H_2–split state, the Mulliken charge populations of the hydrogen atoms are nearly zero and the charge population of the nickel is, with a value of –0.25, even negative. Mayer bond orders of the two Ni–H bonds are 0.78 for

H(1) and 0.44 for H(2). These findings indicate that the nickel–hydrogen bonds are better described as two highly covalent Ni^{2+}–H bonds rather than ionic Ni^{4+}–H^- bonds.

Formation of the triplet state requires promotion of one of the non–bonding electrons into an anti–bonding orbital. The promotion energy gets larger with number and covalency of the metal–ligand bonds as the antibonding character of the respective orbitals increases. Hence, formation of the triplet state is energetically more costly in the case of the H_2–split state where, in addition to the four sulfur–nickel bonds, two highly covalent nickel–hydrogen bonds are present.

According to the electronic structures of the H_2–coord and the H_2–split states, one can view hydrogen cleavage formally as a two–step process. The initial step is the homolytic cleavage of the H_2 bond, which arises from the transfer of electron density into the antibonding H_2 orbital, while in the second step the respective metal–hydrogen bonds are formed. The actual process of H_2–cleavage is rather concerted as described in detail in the following section.

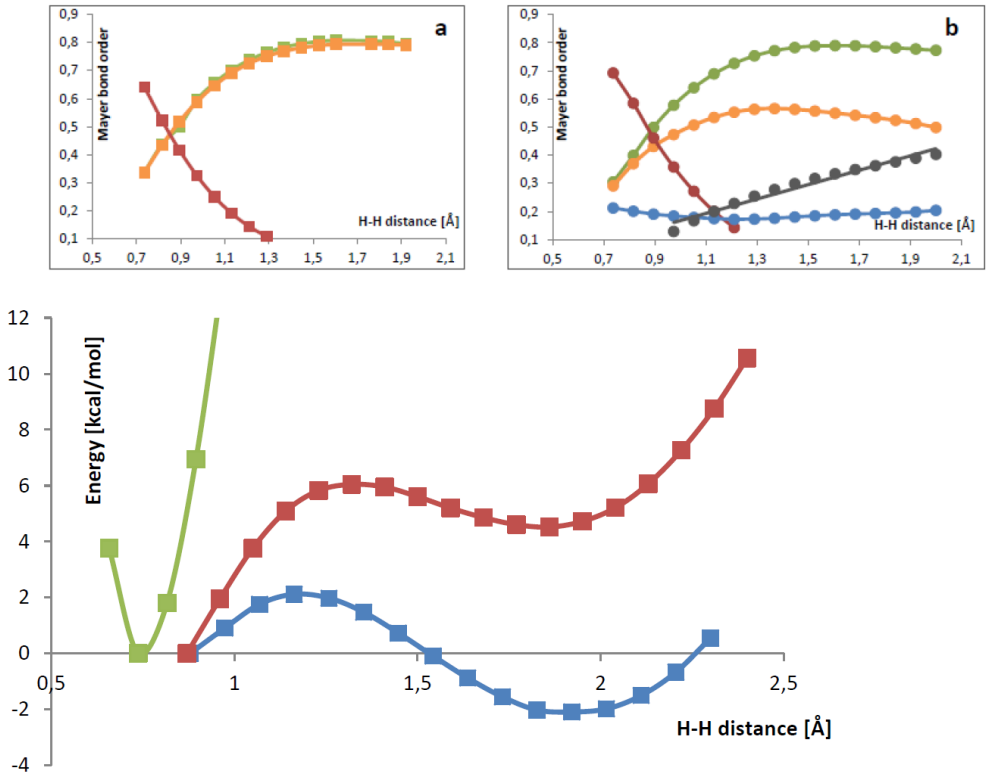

Figure 7: Energy [kcal/mol] as a function of the H–H distance [Å] for the singlet spin state. Color code: small cluster model (blue), Ni–only cluster model (red), H_2 molecule (green). The energy at 2.9 Å was set to zero which approximately corresponds to the H–H distance at the minimum of the H_2–coord state of the Ni–only and the small model. For the H_2 molecule the minimum was chosen as energy zero point at about 0.7 Å. Insets: Mayer bond orders obtained with the (a) singlet small cluster model and the (b) singlet Ni–only model are

shown as a function of the H–H distance [Å]. Color code: Ni–Fe bond (blue), H–H bond (red), Ni–H(1) (green), Ni–H(2) (orange) , Fe–H(2) (grey)

In Figure 7, energies are plotted as a function of the H–H distance of the H_2 substrate in the singlet state. Relaxed surface scans were performed with the small model (blue), the Ni–only model (red) and an unbound H_2 molecule (green). The increase of the energy upon enlargement of the H–H distance is steepest in the case of an unbound H_2 molecule, which is in line with the high stability of the H–H single bond. In the small model the increase of the energy with the H–H distance is much less pronounced and the energy maximum is found at a H–H distance of about 1.2 Å. In agreement with Figure 3a, the reaction energy is negative in the small model whereas for the Ni–only model the reaction energy is found to be positive. As shown as insets in Figure 7, Mayer bond orders are plotted against the H–H distance of the (a) small and (b) the Ni–only singlet models. In both, the small model *and* the Ni–only model, the bond order of the H–H bond decreases, from a value of about almost 0.7 at 0.7 Å to a value of about nearly 0.1 at 1.2 Å. Therefore at distances larger than 1.3 Å the H–H bond can be considered as entirely broken. In both models the increase of the Ni–H(1) bond order with H–H distance is most pronounced at small H–H distances, but gets less steep at larger H–H bond lengths. From an H–H distance of about 1.3 Å on, the bond order nearly remains constant. In the Ni–only model, the Ni–H(2) bond order is very similar to the Ni–H(1) bond order over the complete range of H–H distances. In contrast, in the small model, the increase of the Ni–H(2) bond order is less pronounced as compared to Ni–H(1) and, from a H–H distance of about 1.4 Å on, the bond order even decreases slightly but continuously. Despite the weaker Ni–H(2) bond, in the case of the small model, stabilization of the H_2–splitting reaction arises from the Fe–H(2) bond, which starts to form at a H–H distance of 1 Å and increases nearly linearly with H–H bond length. Apparently, formation of the Fe–H(2) bond overcompensates the presence of a weaker Ni–H(2) bond in the small model such that H_2–cleavage becomes energetically favorable in the small but not in the Ni–only model. It should be remembered that there is no genuine Fe–H(2) two–center bond in the active site of [NiFe] hydrogenase as evident from Figure 6. Instead, a Ni–H–Fe three–center bond is formed and the Fe–H(2) bond order represents the corresponding contribution to the Ni–H–Fe three–center bond. The formation of the three–center bond readily explains the significantly lower Ni–H(2) bond order with respect to Ni–H(1) in the small model. In the context of the presence of a three–center bond, the more favorable energy found for the small model is due the increased stability of the Ni–H–Fe bond as compared to the Ni–H(2) two–center bond in the Ni–only model.

In summary, the energy barrier of the reaction arises from the breaking or the H_2 bond. Bond–cleavage in an unbound H_2 molecule is energetically highly unfavorable. In [NiFe] hydrogenases, it becomes energetically favorable due to the formation of metal–hydrogen bonds, which compensate

for the energetically “costly” breaking of the H–H bond. In this respect, the presence of the iron center is of fundamental importance as a stable Ni–H–Fe three–center bond can be formed.

4.6.7. Hydrogen abstraction – kinetic control by the Cys546 side chain conformation

In this section, we shed light on the details of H(1) abstraction in the H_2–split state by Cys546, which leads to the formation of the CysProt–A state. It has been shown previously for the Ni–C state (see chapter 4.2.) that the spin density at Sγ(Cys546) strongly depends on the Cβ(Cys546)–Sγ(Cys546)–Ni–Sγ(Cys549) dihedral angle. Therefore we have studied the influence of the orientation of the Cys546 sidechain on the energy barrier of hydrogen abstraction by Cys546 through systematic variation of the Cβ(Cys546)–Sγ(Cys546)–Ni–Sγ(Cys549) dihedral angle. It turns out that the corresponding dihedral angles of Cys546 and Cys81 are responsible for the preference of hydrogen abstraction by Cys546 instead of Cys81.

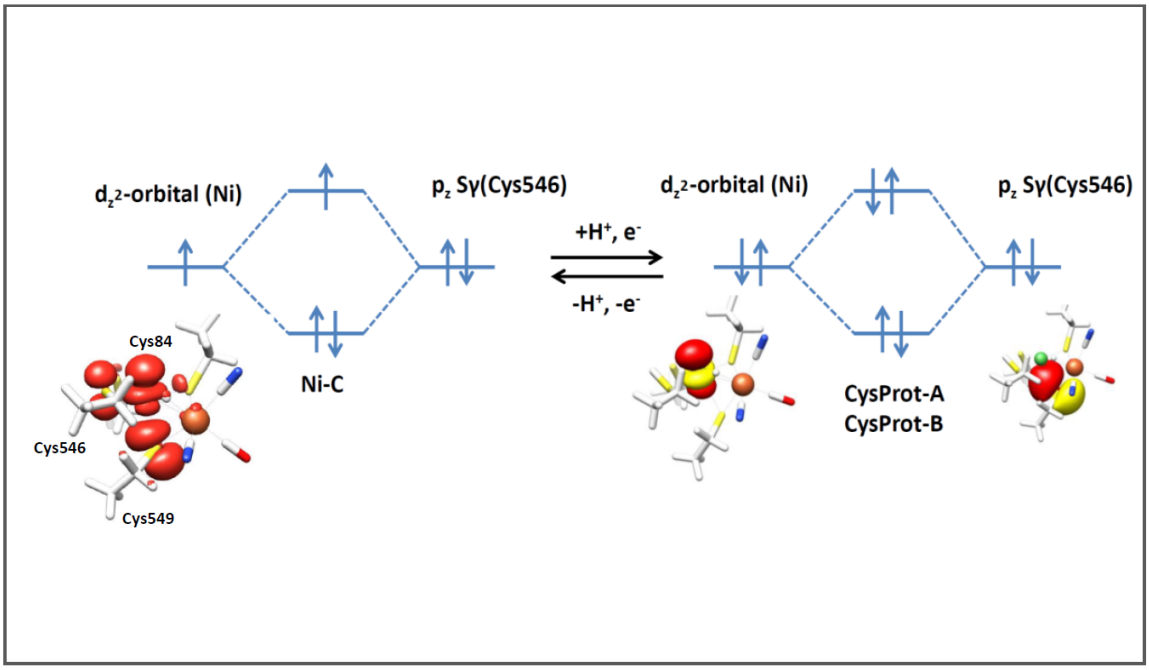

Figure 8: Orbital scheme for the Ni–C (left) and the CysProt states (right). Quasi–restricted orbitals are shown as insets.

In the Ni–C state, interaction of the doubly occupied p_z orbital of Sγ(Cys549) with the singly occupied d_{z^2} nickel orbital leads to the formation of a Ni–S bond with formal bond order of 0.5 since two electrons are in the bonding orbital combination and one electron in the antibonding orbital combination (Figure 8). The resulting spin density in Ni–C is pronouncedly delocalized. By one–electron reduction of Ni–C, which leads to CysProt–A, the antibonding orbital combination becomes doubly occupied which corresponds to the breaking of the Ni–S bond. This is evidenced by the

significantly lower Ni–Sγ(Cys549) bond order in CysProt–A (0.24) relative to Ni–C (0.61). Furthermore, the Ni–Sγ(Cys549) distance is pronouncedly longer in CysProt–A (2.52 Å) as compared to Ni–C (2.34 Å). Hence, the structure of CysProt–A and CysProt–B is probably characterized best as square planar, which is the usually preferred coordination geometry in nickel d^8 complexes and, according to Fan *et al.* [29], should be prerequisite for the presence of a stable low–spin state. As a consequence of the broken Ni–Sγ(Cys549) bond in CysProt–A and CysProt–B, the Fe–Sγ(Cys549) bond is strengthened, which is reflected by a Fe–S bond order of 0.63 in CysProt–A relative to 0.55 in Ni–C. This explains why the conversion of H_2–split to CysProt–A is energetically unfavorable in the case of the Ni–only model where the breaking of the nickel–sulfur bond cannot be compensated. In summary, Ni–Sγ(Cys549) bond breaking upon formation the CysProt–A state is compensated by the strengthening of the Fe–Sγ(Cys549) bond, which once more highlights the crucial role of the iron center for the catalytic activity of [NiFe] hydrogenase.

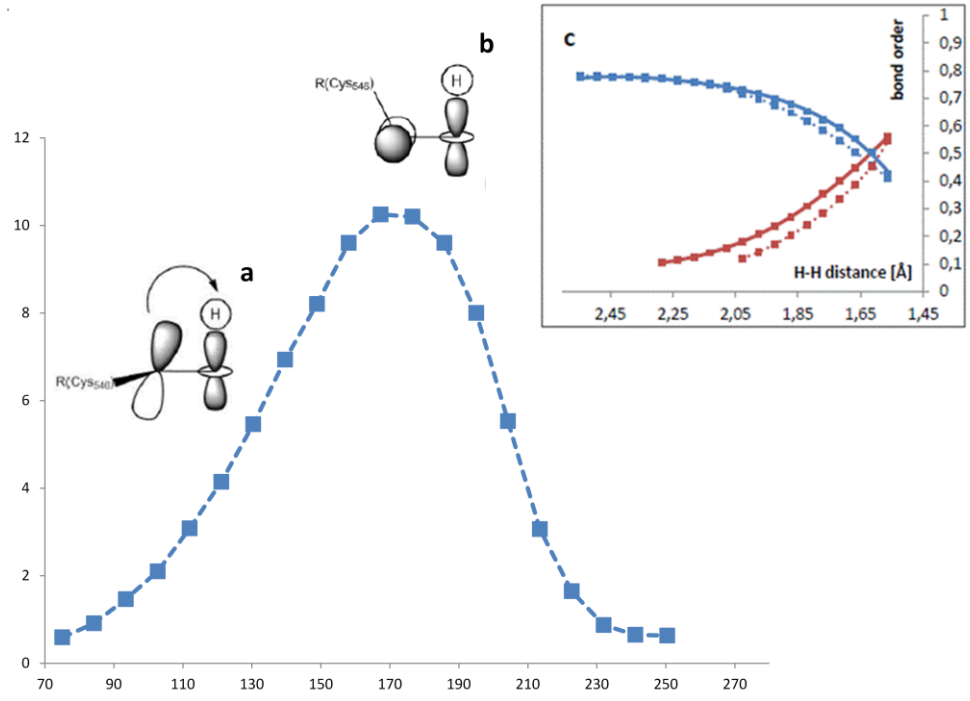

Figure 9: The energy barrier [kcal/mol] (BP86) for the abstraction of H(1) by Sγ(Cys546) is plotted against the Cβ(Cys546)–Sγ(Cys546)–Ni–Sγ(Cys549) dihedral angle [°]. A truncated small model was used, in which the ethyl–thiolate side chain of Cys546 was replaced by a methyl–thiolate. Constraints of Cys546 were reestablished by freezing the γ–sulfur atom. The minimum energy of the H_2–split state at the respective dihedral angles was set to zero. Insets: Orbital schemes for the abstraction of H(1) by Sγ (Cys546) for Cβ(Cys546)–Sγ(Cys546)–Ni–Sγ(Cys549) dihedral angles of (a) 90° and (b) 180°. (c) Mayer bond orders plotted as a function of the Sγ(Cys546)–H(1) distance [Å] for a Cβ(Cys546)–Sγ(Cys546)–Ni–Sγ(Cys549) dihedral angle of 90° (straight lines) and 180° (dotted lines). Color code: Sγ(Cys546)–H(1) (blue) and Ni–H(1) (red).

In Figure 9, the energy barrier for H(1) abstraction by Cys546, which results in the formation of CysProt–A, is displayed as a function of the Cβ(Cys546)–Sγ(Cys546)–Ni–Sγ(Cys549) dihedral angle. The reaction corresponds mainly to a contraction of the Sγ(Cys546)–H(1) distance [Å]. The minimum energy of the H_2–split state at the respective dihedral angles was set to zero. From the figure it is evident, that the energy at 70° amounts to less than 1 kcal/mol and then rises until a maximum is reached at a dihedral angle of 170°–180°. The plot then decreases again to an energy value of nearly zero at 250°.

For dihedral angles of 90° and 180°, Mayer bond orders of the Sγ(Cys546)–H(1) and Ni–H(1) bonds are plotted as a function of the Sγ(Cys546)–H(1) distance in Figure 9c. In the course of the proton abstraction reaction, the Sγ(Cys546)–H(1) bond order increases while the bond–order of Ni–H(1) decreases. The Sγ(Cys546)–H(1) bond starts to form at a Sγ(Cys546)–H(1) distance of about 2.0 Å (bond order threshold 0.1) in the case of a dihedral angle of 180°. Most notably, bond formation is observed already at about 2.3 Å for a dihedral angle of 90°. The Ni–H(1) bond order decreases somewhat more pronouncedly in the case of an angle of 180° from a Sγ(Cys546)–H(1) distance of 2.3 Å on.

The dependence of the activation barriers on the Cβ(Cys546)–Sγ(Cys546)–Ni–Sγ(Cys549) angle arises from different orientations of the non–bonding p–orbital of Cys546 at the two dihedral angles. For 90° and 180°, orbital schemes are displayed in Figure 9, as insets (a) and (b), respectively. At a dihedral angle of 90°, the sulfur p–orbital can readily overlap with the empty σ* anti–bonding orbital formed by the nickel d_{z^2} and the hydrogen 1s orbital. Thereby electron density is transferred into the respective orbital, which results in a weakening of the Ni–H bond and the concomitant formation of a partial Sγ(Cys546)–H bond as required for the formation of CysProt–A. On the other hand, for an angle of 180°, the non–bonding p–orbital is oriented nearly perpendicular to the C_∞ axis of the σ* orbital. In this orientation, there is no net–overlap of the non–bonding p–orbital of Sγ(Cys546) with the Ni–H σ* anti–bonding orbital. Consequently, in the case of a dihedral angle of 180° the Ni–H bond has to undergo a destabilizing distortion in order to initialize S–H bond formation. This is reflected by the later formation of the S–H bond and translates into a higher reaction barrier at a dihedral angle of 180°.

In summary, the dependence of the reaction barrier on the Cβ(Cys546)–Sγ(Cys546)–Ni–Sγ(Cys549) dihedral angle is due to different orientations and thereby a different net–overlap of the non–bonding sulfur Sγ(Cys546) p–orbital and the Ni–H σ* anti–bonding orbital. An equilibrium Cβ(Cys546)–Sγ(Cys546)–Ni–Sγ(Cys549) dihedral angle of 86° ensures that abstraction of the hydrogen atom from the terminal nickel site proceeds nearly at optimal rates and is thereby a prominent example for an enzymatic structure–function relationship.

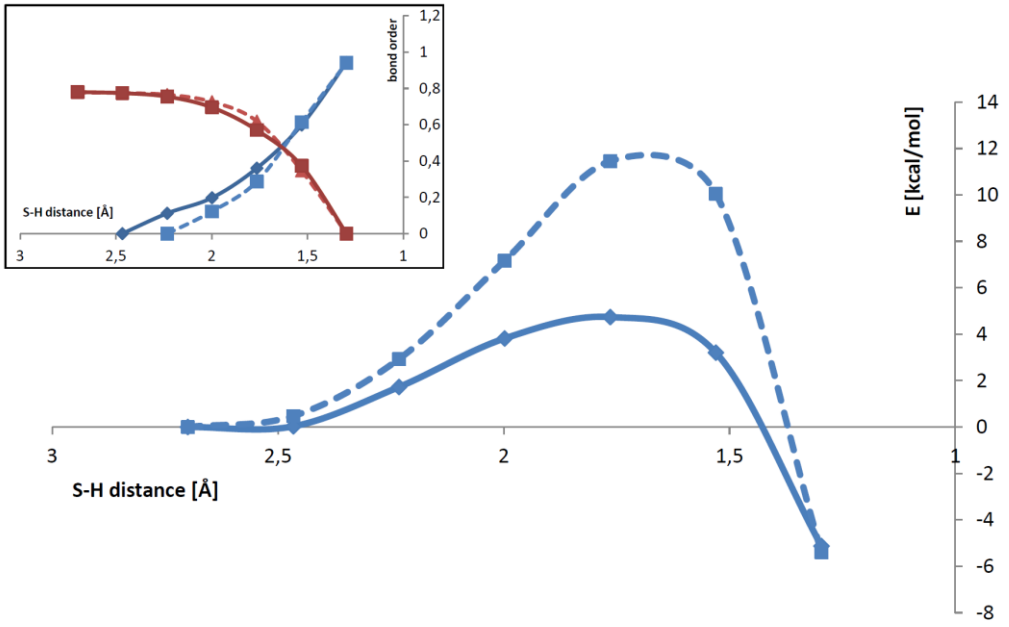

Figure 10: Energy (B3lYP) as a function of the distance [Å] (up to a value of 1.3 Å) between H(1) and γS of Cys546 (straight line) and Cys81 (dashed line). The energy of the H_2–split state was set to zero. Inset: Dependence of the Ni–H(1) (red) and the H(1)– γS bond order (blue) on the γS–H(1) distance for Cys546 (straight line) and cys81 (dashed line).

In contrast to the sulfur atoms of the bridging cysteines, the terminal Sγ(Cys81) features a free electron pair and, therefore, could also perform hydrogen abstraction of H(1). The energy barrier (Figure 10) for Sγ(Cys81)–H(1) is by about 7 kcal/mol (B3LYP) higher than the value found for Sγ(Cys546). Hence, H(1) should react almost predominantly with Sγ(Cys546). A Cβ(Cys81)–Sγ(Cys81)–Ni–Sγ(Cys549) dihedral angle of –21° is identified for Cys81, which translates into a rather similar orientation of the Sγ(Cys81) p–orbital as the one of Cys546 for 180°, shown in Figure 9b. In analogy to the case of a Cβ(Cys546)–Sγ(Cys546)–Ni–Sγ(Cys549) dihedral angle of 180°, hydrogen abstraction by Sγ(Cys81) takes place at a late point on the reaction coordinate. This is reflected by the Sγ(Cys81)–H(1) Mayer bond order, which starts to form at a Sγ(Cys81)–H(1) distance of 2.0 Å rather than at 2.2–2.3 Å as found for Sγ(Cys546)–H(1) (Figure 10, inset). Conclusively, the preference for hydrogen abstraction by Sγ(Cys546) rather than by Sγ(Cys81) is, at least to a large part, due to different conformations of the side chains of Cys546 and Cys549 and thereby different orientations of the corresponding sulfur p–orbitals. Stated differently, selective hydrogen abstraction by Cys546 instead

of Cys81 is ensured by the conformations of the side–chains of the two residues. No proton transfer chain is present close to Cys81 and the selective abstraction by Cys546 could be paramount, as abstraction by Cys81 would trap H(1) at Sγ(Cys81) thereby changing the electronic properties and possibly the activity of the active site.

4.6.8. Conclusion

In this contribution, we have reported a mechanism for the first electron/proton transfer step in [NiFe] hydrogenases, which features the nickel center as initial H_2–binding site and homolytic H_2–cleavage on a singlet spin surface. Calculations were performed using large cluster models, which include, in addition to the two metals and the ligands of the first coordination shell, amino acids from the complete second coordination shell. Coordination of the H_2 substrate to the nickel site is clearly corroborated by the experimental identification of a hydrophobic pathway which ends at the nickel [38-39]. Furthermore, the proposed mechanism is supported by the favorable calculated reaction energies and by the comparison of theoretical with experimental stretching frequencies.

As revealed by comparison of the results from the large cluster models with those from the small model, which only includes the first coordination shell in addition to the bimetallic [NiFe] core, the second coordination shell has a discernible influence on the energies of the intermediate states by lowering the overall energy of the reaction sequence. In particular, the energies are highly sensitive to the protonation states of His88 and Glu34 and the two residues might eventually fine–tune the catalytic activity as a function of the pH–value.

In addition, by studying the reaction steps in detail, important structure–function relationships of the active site have been revealed. First, the presence of the highly covalent Ni–Sγ(Cys) bonds seem evolutionarily tailored for the formation of a stable H_2–complex at the nickel by means of a back–bonding interaction. At the same time, the electron withdrawing CO ligand at the iron center destabilizes binding of the H_2 substrate at the iron. Second, although iron does not change its redox–state, the low–spin Fe^{2+} center plays a crucial in the catalytic mechanism. It lowers the transition barrier and the energy of the homolytic cleavage reaction by enabling the formation of a stable Ni–H–Fe three center bond. Furthermore, upon formation of CysProt–A, the strengthening of the Fe–Sγ(Cys549) bond compensates for the breaking of the Ni–Sγ(Cys549) bond. Third, in the catalytic intermediates which feature a vacant bridging position, we have identified the presence of a genuine two center nickel–iron bond, which possibly stabilizes the structural integrity of the bimetallic core in the absence of a bridging ligand. Fourth, the selectivity and the high efficiency of hydrogen abstraction by the sulfur atom of Cys546 from the nickel site is due to the orientation of the non–bonding sulfur p–orbital, which in turn is controlled by the side chain confirmation of the cysteine.

In summary, in this contribution, we have presented a reaction mechanism for the important first electron/proton transfer step of the [NiFe] hydrogenase catalytic mechanism. As opposed to previous computational studies but in agreement with experiment, the proposed mechanism involves H_2–coordination to the terminal nickel site and homolytic cleavage of the H_2 substrate. The study has shed light on some of the unique features of the active site of the enzyme, such as the presence of CO and CN^- ligands at the iron site. By aiding the development of biomimetic H_2-evolving compounds, an in-depth knowledge of the mechanistic details of hydrogenases might in the long run eventually be beneficial for mastering some of the challenges of a putative future "hydrogen–economy".

References

1. De Lacey, A.L., et al., *Activation and inactivation of hydrogenase function and the catalytic cycle: Spectroelectrochemical studies.* Chemical Reviews, 2007. **107**(10): p. 4304-4330.
2. De Lacey, A.L., J. Moiroux, and C. Bourdillon, *Simple formal kinetics for the reversible uptake of molecular hydrogen by [ni-fe] hydrogenase from desulfovibrio gigas.* European Journal of Biochemistry, 2000. **267**(22): p. 6560-6570.
3. Leger, C., et al., *Enzyme electrokinetics: Hydrogen evolution and oxidation by allochromatium vinosum [nife]-hydrogenase.* Biochemistry, 2002. **41**(52): p. 15736-46.
4. Amara, P., et al., *A hybrid density functional theory molecular mechanics study of nickel-iron hydrogenase: Investigation of the active site redox states.* Journal of the American Chemical Society, 1999. **121**(18): p. 4468-4477.
5. Matias, P.M., et al., *Nife hydrogenase from desulfovibrio desulfuricans atcc 27774: Gene sequencing, three-dimensional structure determination and refinement at 1.8 angstrom and modelling studies of its interaction with the tetrahaem cytochrome c(3).* Journal of Biological Inorganic Chemistry, 2001. **6**(1): p. 63-81.
6. Sellmann, D., F. Geipel, and M. Moll, *Ni(nhpnpr(3))('s-3') , the first nickel thiolate complex modeling the nickel cysteinate site and reactivity of nife hydrogenase.* Angewandte Chemie-International Edition, 2000. **39**(3): p. 561-+.
7. Goldman, C.M. and P.K. Mascharak, *Reactions of h-2 with the nickel site(s) of the feni and fenise hydrogenases: What do the model complexes suggest?* Comments on Inorganic Chemistry, 1995. **18**(1): p. 1-25.
8. Bleijlevens, B., B.W. Faber, and S.P.J. Albracht, *The nife hydrogenase from allochromatium vinosum studied in epr-detectable states: H/d exchange experiments that yield new information about the structure of the active site.* Journal of Biological Inorganic Chemistry, 2001. **6**(8): p. 763-769.
9. Maroney, M.J. and P.A. Bryngelson, *Spectroscopic and model studies of the ni-fe hydrogenase reaction mechanism.* Journal of Biological Inorganic Chemistry, 2001. **6**(4): p. 453-459.
10. Volbeda, A., et al., *High-resolution crystallographic analysis of desulfovibrio fructiosovorans nife hydrogenase.* International Journal of Hydrogen Energy, 2002. **27**(11-12): p. 1449-1461.
11. Dole, F., et al., *Nature and electronic structure of the ni-x dinuclear center of desulfovibrio gigas hydrogenase. Implications for the enzymatic mechanism.* Biochemistry, 1997. **36**(25): p. 7847-7854.
12. Dementin, S., et al., *A glutamate is the essential proton transfer gate during the catalytic cycle of the [nife] hydrogenase.* Journal of Biological Chemistry, 2004. **279**(11): p. 10508-10513.
13. Siegbahn, P.E.M. and M.R.A. Blomberg, *Transition-metal systems in biochemistry studied by high-accuracy quantum chemical methods.* Chemical Reviews, 2000. **100**(2): p. 421-437.
14. Siegbahn, P.E.M. and M.R.A. Blomberg, *Density functional theory of biologically relevant metal centers.* Annual Review of Physical Chemistry, 1999. **50**: p. 221-249.

15. Neese, F., et al., *Dealing with complexity in open-shell transition metal chemistry from a theoretical perspective: Reaction pathways, bonding, spectroscopy, and magnetic properties.* Advances in Inorganic Chemistry: Theoretical and Computational Inorganic Chemistry, Vol 62, 2010. **62**: p. 301-349.
16. Siegbahn, P.E.M., *Modeling aspects of mechanisms for reactions catalyzed by metalloenzymes.* Journal of Computational Chemistry, 2001. **22**(14): p. 1634-1645.
17. Bruschi, M., et al., *Dft investigations of models related to the active site of nife and fe hydrogenases.* Coordination Chemistry Reviews, 2005. **249**(15-16): p. 1620-1640.
18. Siegbahn, P.E.M., J.W. Tye, and M.B. Hall, *Computational studies of [nife] and [fefe] hydrogenases.* Chemical Reviews, 2007. **107**(10): p. 4414-4435.
19. Siegbahn, P.E.M., et al., *The mechanism of the ni-fe hydrogenases: A quantum chemical perspective.* Journal of Biological Inorganic Chemistry, 2001. **6**(4): p. 460-466.
20. Fan, H.J. and M.B. Hall, *Recent theoretical predictions of the active site for the observed forms in the catalytic cycle of ni-fe hydrogenase.* Journal of Biological Inorganic Chemistry, 2001. **6**(4): p. 467-473.
21. Lubitz, W., et al., *Epr and theoretical investigations of nife hydrogenase: Insight into the mechanism of biological hydrogen conversion.* Epr in the 21st century: Basics and applications to material, life and earth sciences, ed. A. Kawamori, J. Yamauchi, and H. Ohta. 2002, Amsterdam: Elsevier Science Bv. 437-445.
22. Stein, M. and W. Lubitz, *Quantum chemical calculations of nife hydrogenase.* Current Opinion in Chemical Biology, 2002. **6**(2): p. 243-249.
23. Niu, S.Q., L.M. Thomson, and M.B. Hall, *Theoretical characterization, of the reaction intermediates in a model of the nickel-iron hydrogenase of desulfovibrio gigas.* Journal of the American Chemical Society, 1999. **121**(16): p. 4000-4007.
24. Li, S.H. and M.B. Hall, *Modeling the active sites of metalloenzymes. 4. Predictions of the unready states of [nife] desulfovibrio gigas hydrogenase from density functional theory.* Inorganic Chemistry, 2001. **40**(1): p. 18-24.
25. Pavlov, M., M.R.A. Blomberg, and P.E.M. Siegbahn, *New aspects of h-2 activation by nickel-iron hydrogenase.* International Journal of Quantum Chemistry, 1999. **73**(2): p. 197-207.
26. Pavlov, M., et al., *Mechanism of h-h activation by nickel-iron hydrogenase.* Journal of the American Chemical Society, 1998. **120**(3): p. 548-555.
27. De Gioia, L., et al., *Ni-fe hydrogenases: A density functional theory study of active site models.* Inorganic Chemistry, 1999. **38**(11): p. 2658-2662.
28. De Gioia, L., et al., *Ab initio investigation of the structural and electronic differences between active-site models of nife and nifese hydrogenases.* International Journal of Quantum Chemistry, 1999. **73**(2): p. 187-195.
29. Fan, H.J. and M.B. Hall, *High-spin ni(ii), a surprisingly good structural model for [nife] hydrogenase.* Journal of the American Chemical Society, 2002. **124**(3): p. 394-395.
30. Wang, H.X., et al., *Nickel l-edge soft x-ray spectroscopy of nickel-iron hydrogenases and model compounds - evidence for high-spin nickel(ii) in the active enzyme.* Journal of the American Chemical Society, 2000. **122**(43): p. 10544-10552.
31. Jayapal, P., et al., *Qm/mm studies of ni-fe hydrogenases: The effect of enzyme environment on the structure and energies of the inactive and active states.* Physical Chemistry Chemical Physics, 2008. **10**(29): p. 4249-4257.
32. Wang, C.P., et al., *The nickel site in active desulfovibrio-baculatus nifese hydrogenase is diamagnetic - multifield saturation magnetization measurement of the spin state of ni(ii).* Journal of Biological Chemistry, 1992. **267**(11): p. 7378-7380.
33. Kowal, A.T., et al., *Electronic and magnetic-properties of nickel-substituted rubredoxin - a variable-temperature magnetic circular-dichroism study.* Inorganic Chemistry, 1988. **27**(7): p. 1162-1166.
34. Siegbahn, P.E.M., *Proton and electron transfers in nife hydrogenase.* Advances in Inorganic Chemistry - Including Bioinorganic Studies, Vol 56, 2004. **56**: p. 101-125.
35. Pardo, A., et al., *Density functional study of the catalytic cycle of nickel-iron [nife] hydrogenases and the involvement of high-spin nickel(ii).* Journal of Biological Inorganic Chemistry, 2006. **11**(3): p. 286-306.

36. Bandsma, R.H.J., et al., *Increased lipogenesis and resistance of lipoproteins to oxidative modification in two patients with glycogen storage disease type 1a.* Journal of Pediatrics, 2002. **140**(2): p. 256-260.
37. Stein, M. and W. Lubitz, *Relativistic dft calculation of the reaction cycle intermediates of nife hydrogenase: A contribution to understanding the enzymatic mechanism.* Journal of Inorganic Biochemistry, 2004. **98**(5): p. 862-877.
38. Volbeda, A. and J.C. Fontecilla-Camps, *The active site and catalytic mechanism of nife hydrogenases.* Dalton Transactions, 2003(21): p. 4030-4038.
39. Montet, Y., et al., *Gas access to the active site of ni-fe hydrogenases probed by x-ray crystallography and molecular dynamics.* Nature Structural Biology, 1997. **4**(7): p. 523-526.
40. Ogata, H., et al., *Structural studies of the carbon monoxide complex of nife hydrogenase from desulfovibrio vulgaris miyazaki f: Suggestion for the initial activation site for dihydrogen.* Journal of the American Chemical Society, 2002. **124**(39): p. 11628-11635.
41. Lill, S.O.N. and P.E.M. Siegbahn, *An autocatalytic mechanism for nife-hydrogenase: Reduction to ni(i) followed by oxidative addition.* Biochemistry, 2009. **48**(5): p. 1056-1066.
42. Weinberg, D.R., et al., *Proton-coupled electron transfer.* Chemical Reviews, 2012. **112**(7): p. 4016-4093.
43. Garcin, E., et al., *The crystal structure of a reduced [nifese] hydrogenase provides an image of the activated catalytic center.* Structure, 1999. **7**(5): p. 557-566.
44. Fichtner, C., et al., *Spectroelectrochemical characterization of the [nife] hydrogenase of desulfovibrio vulgaris miyazaki f.* Biochemistry, 2006. **45**(32): p. 9706-9716.
45. Jonas, V. and W. Thiel, *Theoretical-study of the vibrational-spectra of the transition-metal carbonyls m(co)(6) [m=cr, mo, w], m(co)(5) [m=fe, ru, os], and m(co)(4) [m=ni, pd, pt].* Journal of Chemical Physics, 1995. **102**(21): p. 8474-8484.
46. Jonas, V. and W. Thiel, *Density functional study of the vibrational spectra of octahedral transition-metal hexacarbonyls: Neutral molecules (m = cr, mo, w) and isoelectronic ions (m = v, nb, ta; mn, re; fe, ru, os; co, rh, ir; pt; au).* Organometallics, 1998. **17**(3): p. 353-360.
47. Jonas, V. and W. Thiel, *Theoretical study of the vibrational spectra of the transition-metal carbonyl hydrides hm(co)(5) (m=mn, re), h(2)m(co)(4) (m=fe, ru, os), and hm(co)(4) (m=co, rh, ir).* Journal of Chemical Physics, 1996. **105**(9): p. 3636-3648.
48. Ogata, H., et al., *Structural studies of the carbon monoxide complex of [nife]hydrogenase from desulfovibrio vulgaris miyazaki f: Suggestion for the initial activation site for dihydrogen.* Journal of the American Chemical Society, 2002. **124**(39): p. 11628-11635.
49. Massanz, C. and B. Fliedrich, *Amino acid replacements at the h-2-activating site of the nad-reducing hydrogenase from alcaligenes eutrophus.* Biochemistry, 1999. **38**(43): p. 14330-14337.
50. Burgdorf, T., A.L. De Lacey, and B. Friedrich, *Functional analysis by site-directed mutagenesis of the nad(+)-reducing hydrogenase from ralstonia eutropha.* Journal of Bacteriology, 2002. **184**(22): p. 6280-6288.

Appendix

Energies

HisHε	**Singl**	**Trip**
resting	0.0	–5.7
H_2–coord	–7.5	9.6
H_2–split	–10.0	21.6
CysProt–A	–18.0	–14.6
CysProt–B	–20.2	–15.9

HisHεHδ	**Singl**	**Trip**
resting	0.0	–8.0
H_2–coord	–10.0	8.4
H_2–split	–13.2	48.1
CysProt–A	–26.2	–17.9
CysProt–B	–27.7	–19.0

HisHεGlu	**Singl**	**Trip**
resting	0.0	–3.5
H_2–coord	–7.7	4.1
H_2–split	–11.5	12.2
CysProt–A	–25.1	–27.0
CysProt–B	–27.4	–29.4

HisHεSe	**Singl**	**Trip**
resting	0.0	–1.7
H_2–coord	–7.9	
H_2–split	–10.4	18.1
CysProt–A	–11.8	–10.9
CysProt–B	–13.1	–11.5

Small	**Singl**	**Trip**
resting	0.0	–4.3
H_2–coord	–2.6	12.0
H_2–split	–5.0	23.9
CysProt–A	–10.5	–7.6
CysProt–B	–11.1	–7.7

Ni–only	**Singl**
ohne	0.0
H_2–coord	9.3
H_2–split	14.1
CysProt–A	25.6
CysProt–B	23.3

Table 1A: B3LYP single point energies of geometries optimized with BP86. The singlet resting state has been chosen as energy zero point.

Small B3LYP	**Singl**	**Trip**
resting	0.0	–8.1
H_2–coord	–3.0	–10.4
H_2–split	–4.0	15.3
CysProt–A	–5.6	–9.2
CysProt–B	–8.4	–9.7

Large B3LYP	**Singl**	**Trip**
resting	0.0	–6.5
H_2–coord	–6.4	–9.0
H_2–split	–8.2	16.7
CysProt–A	–17.1	–19.2
CysProt–B	–19.5	–20.8

Small BP	**Singl**	**Trip**
resting	0.0	6.9
H_2–coord	–10.7	5.9
H_2–split	–14.0	9.7
CysProt–A	–7.6	0.2
CysProt–B	–9.8	–0.4

Large BP	**Singl**	**Trip**
resting	0.0	6.8
H_2–coord	–13.2	5.0
H_2–split	–16.3	15.1
CysProt–A	–16.6	–9.0
CysProt–B	–19.2	–10.6

Table 2A: B3LYP energies of geometries optimized with B3LYP. The singlet resting state has been chosen as energy zero point.

Geometries

	HisHε Singlet	**HisHε Trip**	**HisHε Singl** (B3LYP)	**HisHε Trip** (B3LYP)	**HisHδHε Singl**	**HisHδHε Trip**	**HisHεGu Singl**	**HisHεGlu Trip**
Ni–S(Cys81)	2.30	2.27	2.30	2.29	2.30	2.26	2.30	2.28
Ni–S(Cys84)	2.26	2.29	2.32	2.40	2.26	2.29	2.26	2.30
Ni–S(Cys546)	2.16	2.16	2.18	2.18	2.16	2.16	2.15	2.16
Ni–S(Cys549)	2.15	2.28	2.20	2.36	2.16	2.30	2.15	2.26
Fe–S(Cys84)	2.32	2.24	2.36	2.28	2.32	2.24	2.32	2.25
Fe–S(Cys549)	2.21	2.31	2.25	2.35	2.21	2.31	2.22	2.31
C–O	1.17	1.17	1.15	1.15	1.18	1.17	1.18	1.17
C–N	1.18	1.18	1.16	1.16	1.18	1.18	1.18	1.18
C–N	1.18	1.18	1.16	1.16	1.18	1.18	1.18	1.18
Fe–CO	1.72	1.71	1.73	1.73	1.71	1.71	1.72	1.71
Fe–CN^-	1.86	1.86	1.89	1.89	1.86	1.86	1.86	1.86
Fe–CN^-	1.88	1.87	1.91	1.90	1.88	1.87	1.88	1.87
Ni–Fe	2.67	2.78	2.80	2.93	2.66	2.75	2.66	2.72

	HisHεSe Singl	**HisHεSe Trip**	**Small Singl**	**Small Trip**	**Small Singl** (B3LYP)	**Small Trip** (B3LYP)	**Ni–Only**
Ni–S(Cys81)	2.27	2.25	2.30	2.28	2.30	2.31	2.26
Ni–S(Cys84)	2.24	2.24	2.25	2.32	2.32	2.42	2.29
Ni–S(Cys546)	2.27	2.27	2.19	2.19	2.24	2.23	2.24
Ni–S(Cys549)	2.15	2.27	2.20	2.31	2.25	2.39	2.22
Fe–S(Cys84)	2.32	2.25	2.32	2.27	2.38	2.32	–
Fe–S(Cys549)	2.21	2.31	2.21	2.32	2.27	2.37	–
C–O	1.17	1.17	1.18	1.18	1.16	1.16	–
C–N	1.18	1.18	1.18	1.18	1.16	1.16	–
C–N	1.18	1.18	1.18	1.18	1.16	1.16	–
Fe–CO	1.72	1.71	1.71	1.69	1.72	1.72	–
Fe–CN^-	1.86	1.86	1.89	1.89	1.93	1.93	–
Fe–CN^-	1.88	1.87	1.89	1.89	1.93	1.93	–
Ni–Fe	2.66	2.73	2.64	2.78	2.89	3.11	–

Table 3A: Selected bond distances from the resting state models.

	HisHε Singl	HisHε Trip	HisHε Singl (B3LYP)	HisHε Trip (B3LYP)	HisHδHε Singl	HisHδHε Trip	HisHεGlu Singl
Ni–S(Cys81)	2.31	2.31	2.32	2.31	2.27	2.31	2.30
Ni–S(Cys84)	2.28	2.44	2.32	2.45	2.29	2.39	2.29
Ni–S(Cys546)	2.25	2.20	2.24	2.20	2.24	2.19	2.25
Ni–S(Cys549)	2.29	2.32	2.34	2.32	2.37	2.36	2.29
Fe–S(Cys84)	2.31	2.30	2.34	2.30	2.31	2.28	2.31
Fe–S(Cys549)	2.25	2.26	2.27	2.26	2.28	2.27	2.26
C–O	1.17	1.17	1.15	1.17	1.17	1.18	1.17
C–N	1.18	1.18	1.16	1.18	1.18	1.18	1.18
C–N	1.18	1.18	1.16	1.18	1.18	1.18	1.18
Fe–CO	1.71	1.71	1.73	1.71	1.71	1.71	1.71
Fe–CN^-	1.86	1.86	1.89	1.86	1.86	1.86	1.86
Fe–CN^-	1.87	1.87	1.91	1.87	1.87	1.87	1.87
Ni–Fe	2.60	2.66	2.69	2.66	2.57	2.64	2.60
Ni–H(2)	1.60	1.77	1.65	1.76	1.57	1.82	1.60
Ni–H(1)	1.59	1.76	1.62	1.75	1.52	1.84	1.58

	HisHεSe Singl	HisHεSe Trip	Small Singl	Small Trip	Small Singl (B3LYP)	Small Trip (B3LYP)	Ni–Only Singl
Ni–S(Cys81)	2.28		2.31	2.28	2.33	n.c.	2.33
Ni–S(Cys84)	2.27		2.28	2.51	2.31	n.c.	0.23
Ni–S(Cys546)	2.35		2.26	2.27	2.26	n.c.	2.26
Ni–S(Cys549)	2.29		2.32	2.29	2.38	n.c.	2.36
Fe–S(Cys84)	2.32		2.31	2.33	2.36	n.c.	–
Fe–S(Cys549)	2.26		2.26	2.26	2.29	n.c.	–
C–O	1.17		1.18	1.18	1.16	n.c.	1.63
C–N	1.18		1.18	1.18	1.16	n.c.	1.62
C–N	1.18		1.18	1.18	1.16	n.c.	–
Fe–CO	1.71		1.70	1.70	1.72	n.c.	–
Fe–CN^-	1.86		1.89	1.90	1.93	n.c.	–
Fe–CN^-	1.87		1.89	1.89	1.93	n.c.	–
Ni–Fe	2.58		2.61	2.69	2.73	n.c.	–
Ni–H(2)	1.60		1.61	1.76	1.68	n.c.	–
Ni–H(1)	1.58		1.58	1.67	1.64	n.c.	–

Table 4A: Selected bond distances from the H_2–coord models. Geometry optimizations of the triple small model have not converged (n.c) with B3LYP.

	HisHε Singlet	HisHε Trip	HisHε Singl (B3LYP)	HisHε Trip (B3LYP)	HisHδHε Singl	HisHδHε Trip	HisHεGlu Singl	HisHεGlu Trip
Ni–S(Cys81)	2.26	2.33	2.27	2.29	2.26	2.84	2.26	2.33
Ni–S(Cys84)	2.27	2.42	2.30	2.54	2.27	2.25	2.28	2.43
Ni–S(Cys546)	2.23	2.19	2.23	2.28	2.22	2.23	2.23	2.19
Ni–S(Cys549)	2.37	2.27	2.40	2.32	2.41	2.37	2.38	2.27
Fe–S(Cys84)	2.29	2.36	2.33	2.39	2.29	2.43	2.31	2.37
Fe–S(Cys549)	2.31	2.29	2.33	2.33	2.31	2.38	2.31	2.30
C–O	1.17	1.17	1.15	1.15	1.17	1.19	1.17	1.17
C–N	1.18	1.18	1.16	1.16	1.18	1.19	1.18	1.18
C–N	1.18	1.18	1.16	1.16	1.18	1.19	1.18	1.18
Fe–CO	1.73	1.76	1.75	1.76	1.72	1.76	1.73	1.75
Fe–CN^-	1.86	1.87	1.90	1.90	1.87	1.85	1.86	1.86
Fe–CN^-	1.87	1.87	1.90	1.90	1.87	1.86	1.87	1.87
Ni–Fe	2.55	2.60	2.58	2.59	2.55	2.67	2.55	2.60
Ni–H(2)	1.57	1.65	1.54	1.59	1.57	1.65		
Ni–H(1)	1.45	1.46	1.43	1.45	1.44	1.45	1.45	1.46

	HisHεSe Singl	HisHεSe Trip	Small Singl	Small Trip	Small Singl (B3LYP)	Small Trip (B3LYP)	Ni–Only Singl
Ni–S(Cys81)	2.24	2.35	2.27	2.26	2.29	2.36	2.38
Ni–S(Cys84)	2.26	2.34	2.27	2.62	2.30	2.47	2.27
Ni–S(Cys546)	2.32	2.29	2.24	2.28	2.25	2.28	2.25
Ni–S(Cys549)	2.37	2.28	2.39	2.28	2.43	2.45	2.37
Fe–S(Cys84)	2.31	2.37	2.29	2.34	2.34	2.39	–
Fe–S(Cys549)	2.31	2.30	2.32	2.31	2.36	2.39	–
C–O	1.17	1.17	1.18	1.17	1.16	1.14	–
C–N	1.18	1.18	1.18	1.18	1.16	1.16	–
C–N	1.18	1.18	1.18	1.18	1.16	1.16	–
Fe–CO	1.73	1.76	1.72	1.74	1.74	1.85	–
Fe–CN^-	1.86	1.86	1.90	1.91	1.93	1.95	–
Fe–CN^-	1.87	1.87	1.89	1.90	1.93	1.95	–
Ni–Fe	2.53	2.59	2.55	2.56	2.60	2.64	–
Ni–H(2)	1.57	1.66	1.57	1.59	1.54	1.69	1.45
Ni–H(1)	1.45	1.46	1.45	1.46	1.43	1.42	1.46

Table 5A: Selected bond distances from the H_2–split models.

Mayer bond orders:

	resting singl	**resting trip**	**H_2–coord singl**	**H_2–coord trip**	**H_2–split singl**	**H_2–split trip**
Ni–S(Cys81)	0.66	0.72	0.66	0.66	0.73	0.64
Ni–S(Cys84)	0.67	0.60	0.67	0.49	0.68	0.54
Ni–S(Cys546)	1.00	1.02	0.89	1.06	0.88	0.81
Ni–S(Cys549)	0.75	0.63	0.59	0.57	0.48	0.58
Fe–S(Cys84)	0.63	0.78	0.61	0.71	0.60	0.61
Fe–S(Cys549)	0.71	0.59	0.66	0.64	0.59	0.57
Ni–H(2)	–	–	0.38	0.26	0.52	0.44
Ni–H(1)	–	–	0.40	0.25	0.80	0.78
Fe–H(2)	–	–	–	–	0.36	0.46
H(1)–H(2)	–	–	0.58	0.73	–	–
Ni–Fe	0.24	0.11	0.21	0.15	0.22	0.22

Table 6A: Selected Mayer bond orders for the singlet and triplet resting. the H_2–coord and the H_2–split states.

Mulliken charge and spin populations:

	resting	H_2–coord	H_2–split	CysProt–A	CysProt–B
S(Cys81)	–0.48	–0.44	–0.35	–0.49	–0.49
S(Cys84)	–0.22	–0.17	–0.13	–0.19	–0.19
S(Cys546)	–0.23	–0.23	–0.19	0.01	0.00
S(Cys549)	–0.10	–0.18	–0.24	–0.37	–0.36
Ni	–0.05	–0.17	–0.25	–0.08	–0.10
Fe	0.20	0.26	0.04	0.08	0.10
H(2)	–	0.00	0.08	–0.04	–0.06
H(1)	–	0.02	–0.01	0.09	0.10

a

	resting	H_2–coord	H_2–split	CysProt–A	CysProt–B
S(Cys81)	–0.48	–0.48	–0.44	–0.54	–0.55
S(Cys84)	–0.20	–0.25	–0.26	–0.31	–0.30
S(Cys546)	–0.30	–0.22	–0.02	–0.04	–0.05
S(Cys549)	–0.26	–0.21	–0.19	–0.27	–0.27
Ni	0.07	–0.03	–0.16	0.05	0.05
Fe	0.19	0.23	0.02	0.12	0.14
H(2)	–	–0.02	0.04	–0.07	–0.10
H(1)	–	0.05	–0.02	0.09	0.11

b

	resting	H_2–coord	H_2–split	CysProt–A	CysProt–B
S(Cys81)	0.17	0.12	0.14	0.10	0.11
S(Cys84)	0.04	0.09	0.18	0.15	0.15
S(Cys546)	0.19	0.49	0.81	0.08	0.07
S(Cys549)	0.14	0.14	0.11	0.17	0.17
Ni	1.36	1.13	0.63	1.35	1.34
Fe	0.05	–0.04	0.09	0.09	0.09
H(2)	–	0.00	0.02	0.03	0.02
H(1)	–	0.03	–0.02	–0.01	0.00

c

Table 7A: Selected Mulliken charge populations of the (a) singlet and (b) triplet HisHε model and (c) Mulliken spin populations of the triplet HisHε model.

5. Summary and Conclusion

In this work, the electronic, geometric and mechanistic features of the redox–states of [NiFe] hydrogenase were studied by DFT. To this end, computed geometries and spectroscopic properties, i.e. magnetic parameters and IR–frequencies, were compared to the available experimental data of each redox–state.

In a first step, the reliability of DFT for the computation of synthetic Ni^{3+} complexes with square pyramidal and square planar metal coordination were studied by comparison of geometries and magnetic properties with experimental data. It was demonstrated that the quality of the DFT computations is highly dependent on the compound under investigation. It turns out that the DFT description of square planar Ni^{3+} complexes is of varying quality and, conclusively, DFT should be used for studies on this type of complexes only when comparison to reliable experimental data is possible. Magnetic properties are suitably reproduced for complexes with a square pyramidal arrangement of the ligands, which should be considered as fortunate, as the nickel coordination shell in most of the EPR–active states in [NiFe] hydrogenases is also a square pyramid.

A large cluster model was used for the present work, which includes not only the bimetallic core and the first coordination shell but also the amino acid residues from the complete second coordination shell. A principal motivation of this study was to establish the influence of the second coordination sphere on the computed geometries, spectroscopic properties and energies. In contrast, most of the previous DFT–studies on [NiFe] hydrogenases, especially those, which focused on theoretical spectroscopy, employed a relatively small model featuring only the two metals and the first coordination sphere. In order to evaluate the reliability of the cluster model, we performed investigations on the Ni–C state, which is the structurally best characterized redox–state of the enzyme. It is generally accepted that a hydride ligand is present at the bridging position in Ni–C. The calculated properties are overall in very good agreement with the experimental values which confirms the suitability of the enzyme cluster model for the study of [NiFe] hydrogenase.

The Ni–L state is formed from the Ni–C state by a photoreaction. There is strong experimental evidence that the hydride ligand dissociates from the bridging site upon Ni–L formation. In our study of the Ni–L state we could show that the hydride leaves the bridging position as a proton and binds to one of the terminal cysteines. The electronic structure of the Ni–L state is unique. In particular, we have demonstrated the presence of a covalent bond between the two metal centers, which is in full agreement with a large body of experimental values.

Carbon monoxide is a competitive inhibitor of [NiFe] hydrogenases. An EPR–active and an EPR–silent form of CO–inhibited [NiFe] hydrogenases were identified experimentally. The CO ligand was found to bind to the terminal nickel position in a bent conformation as evidenced by the corresponding X–Ray structure. We have revealed that the EPR–active CO–inhibited state, which is formed from the Ni–C state, is similar to the Ni–L state as it features a vacant bridging position and protonation of one of the terminal cysteine residues. Most notably, binding of the CO ligand leads to an unique electronic ground state, which is neither found in the Ni–C nor in the Ni–L state. The EPR–inactive CO–inhibited state is found to be most compatible with a singlet spin state, which corroborates that H_2–cooridnation in the course of the catalytic cycle takes place in a low–spin state.

[NiFe] hydrogenases are readily inhibited by oxidation of the bimetallic core. Several X–Ray structures and ^{17}O–ENDOR experiments have revealed the presence of an oxygen–based ligand at the bridging position in the two experimentally characterized oxidized states, Ni–A and Ni–B. From a previous, combined DFT/ENDOR study, it was concluded that an OH^- ligand is present in both, Ni–A and Ni–B, but with different orientations of the O–H bond. Our study has confirmed the presence of a hydroxyl ligand in both oxidized redox–states according to the evaluations of geometries, energies and spectroscopic parameters. Particularly convincing evidence in this respect comes from the study of the CO stretching frequencies. The experimental values are nearly identical for Ni–A and Ni–B, which, according to our calculations can only be reproduced correctly if the same type of ligand is present in the bridging position of both states.

Finally, the reaction mechanism of hydrogen splitting was investigated by computation of the energies of the intermediate states and by comparison of computed with experimental stretching frequencies. It turns out that H_2 binding takes place at the nickel center and not at the iron as proposed in the context of previous mechanistic DFT–studies. Most notably, H_2–cleavage is probably homolytic as opposed to the so far suggested heterolytic mechanism. In addition, we have demonstrated that the iron center is indispensible for the catalytic activity and, furthermore, that the second coordination shell has a discernible influence on the reaction energies. We have also shed light on some of the remarkable structural features of the active site, such as the unusual coordination shell at the iron and the presence of the cysteine thiolates at the nickel center.

The author hopes that the insights obtained by the present work provide fruitful and inspiring input for further studies on hydrogenases and the development of biomimetic H_2–catalysts.